

Magnons, worms and nanogratings in artificial magnetic quasicrystals

Présentée le 16 juin 2021

Faculté des sciences et techniques de l'ingénieur
Laboratoire des matériaux magnétiques nanostructurés et magnoniques
Programme doctoral en science et génie des matériaux

pour l'obtention du grade de Docteur ès Sciences

par

Sho WATANABE

Acceptée sur proposition du jury

Prof. D. Damjanovic, président du jury
Prof. D. Grundler, directeur de thèse
Prof. Y. Otani, rapporteur
Dr U. Ebels, rapporteuse
Prof. F. Sorin, rapporteur

To my parents...

Acknowledgements

This work emerged in four and a half years of my PhD at the Laboratory of Nanoscale Magnetic Materials and Magnonics (LMGN) at EPFL. It would not be possible without the help of many people who I would like to thank. These are in particular:

- **Prof. Dirk Grundler**, my thesis supervisor, for the great support, his enthusiasm for science, the numerous ideas, and for his guidance. I thank him for accepting me as a PhD student at LMGN, a multinational team consisting of highly motivated researchers. Through the tremendous number of scientific discussions with you, I have learned how to go beyond the horizon of the research. I also thank his advice to improve my working condition in terms of the time management and the productivity.
- **Prof. Yoshichika Otani**, **Dr. Ursula Ebels** and **Prof. Fabien Sorin** for taking time to evaluate my PhD study as examiners. **Prof. Dragan Damjanovic** for his acceptance as a president of my examination committee.
- **Dr. Vinayak Shantaram Bhat**, my co-supervisor, for the great support. I thank him for his guidance of my PhD study regarding the magnetic properties of artificial magnetic quasicrystals. His depth understanding toward the artificial quasicrystals as well as artificial spin ices enriched the outcome of my experimental works. I also acknowledge him for his work regarding the sample fabrication of artificial spin ices and data collection for the investigation of their magnetization reversal.
- **Korbinian Baumgärtl**, a colleague at BM 3143. He helped me for the experiment using Brillouin light scattering spectroscopy to obtain high-quality data. Discussions with you at BM 3143 often provided me with new awareness of science on my research.
- **Maria Carmen Giordanao**, a colleague at BM 3143. She advised me a lot concerning sample fabrications. I was motivated by her passion to accomplish her work professionally.
- **Ping Che**, a colleague who started PhD work at the same time. I thank her fruitful discussions about work, especially the magnonic grating coupler study. I was always motivated by her enthusiasm toward science.
- **Dr. An Kyongmo** for his support to establish a new broadband SW spectroscopy setup as well as a time domain reflectometry setup.

Acknowledgements

- **Anna Kúkolóvá**, a colleague who also belongs to LMSC. A time management skill learned from her makes my PhD study more productive. We always had fun time with LMSC people, whom she kept me connected with.
- **Mohammad Hamdi** for his theoretical support. His accuracy in science improved my work, especially on the exploration of the magnonic band structure of the magnonic crystal/quasicrystal.
- **Andrea Muchietto** for his simulation support. His inputs toward the simulation strengthened the outcome of our work, especially, the magnonic grating coupler study. I also thank him to improve the magnetic force microscopy setup concerning the noise reduction.
- **Dr. Jian Rui Soh, Cagri Ozdilek** and **Le Yu** for their comments on my thesis work during the LMGN group meeting.
- **Yuko Kagata Spitteler** for administration support. I always had enjoyable talks with her in Japanese. She provided me with her mental support for my work at LMGN.
- **Sebastian Wintz, Johannes Förster, Thomas Rauch, Markus Weigand, Joachim Gräfe, Gisela Schütz** for the fruitful collaboration on X-ray-based nanoimaging of worm-like nanochannels in the artificial magnetic quasicrystal.
- **Florian Kronast** for the fruitful collaboration on the imaging of artificial spin ice for the investigation of magnetization reversal using X-ray photoemission electron microscopy.
- **Evi Athanasopoulou** and **Anna Murello** for the technical support for the usage of the atomic force microscopy setup belonging to Supramolecular Nano-Materials and Interfaces Laboratory (SuNMIL) led by **Prof. Francesco Stellacci**
- **CMi team** for maintaining the class cleanroom facility at EPFL. Special thanks for the electron-beam writing support to **Zdenek Benes**, for the support concerning wet etching process to **Joffrey Pernollet** and **Cyrille Hibert**, for the electrically bonding support to **Corradini Giancarlo** and **Adrien Toros**, and to **Patrick Alain Madliger** who ensured safe operation in CMi.
- **Shan Shixuan**, a master thesis student, for the simulation support of the magnonic grating coupler study. **Elif Nur Dayi**, an EEE internship student, for the fabrication support of the magnonic grating coupler samples. **Richa Agrawal, Clément Jean-Michel Patrice Cardon, Julien Gay**, and **Qi Huang**, semester project students, for the support of the improvement of the magnetic force microscopy setup.
- **LMSC people**, especially, **Akshay Balgarkashi, Didem Dede, Simon Robert Escobar Steinvall, Lea Ghisalberti, Andrea Giunto, Lucas Güniat, Wonjong Kim, Jean-Baptiste Leran, Nicholas Paul Morgan, Rajrupa Paul, Valerio Piazza, Santhanu Panikar Ramanandan, Elias Zsolt Stutz, Nicolas Tappy, Mahdi Zamani, Luca Francaviglia, Dmitry**

Mikulik, Martin Friedl from the Laboratory of Semiconductor Materials (LMSC) led by **Prof. Anna Fontcuberta i Morral** for their time together with me afterwork at SAT.

- **Mintae Chung**, my flat mate, for his support. He helped me control myself mentally in busy time due to a lot of work, and provided me with enjoyable time at home.
- **All my friends** in Switzerland, in Europe, in Japan and all over the world. I enjoyed meetings during my holiday, weekend, and afterwork, which for sure makes my PhD life better.
- **My family** for providing me with the possibility to study science in Japan and Germany, and even in Switzerland. Without their help I could not have accomplished the part of my work at EPFL for four and a half years.

Hontoni domo arigatou gozaimashita.

Lausanne, May 4, 2021

S. W.

Abstract

Magnons (spin waves, SWs) are elementary spin excitations in magnetically ordered materials. They are the promising quanta for the transmission and processing of information. Magnons can be coupled to the electromagnetic waves utilized for the wireless communication technologies. A wavelength of magnons is orders of magnitude shorter than that of electromagnetic waves at the same frequency. Therefore, wave-based computing with magnons would be promising for the next generation information technology. For the optimized information processing, artificial magnetic media have the potential to offer advanced controls of SWs. A magnonic crystal, consisting of a periodically arranged nanomagnets, provides a tailored magnon band structure due to the formation of artificially introduced Brillouin zone. Periodic magnonic grating couplers (MGCs) efficiently convert centimeter-scaled microwaves to sub-100 nm wavelength SWs. Artificial spin ices (ASIs) are expected to offer reprogrammable magnetization configurations. However, the studies on artificial magnetic materials based on the quasicrystalline and aperiodic arrangement are in their infancy. A quasicrystal, a long range ordered material with a lack of translational invariance, exhibits manifold rotational symmetry. The reciprocal vectors associated with the quasicrystal densely fill out all reciprocal space. These exotic properties would be advantageous for the control of SWs.

During my PhD study, I explored SW properties in two dimensional (2D) artificial magnetic quasicrystals (AMQs) to understand the effect of aperiodicity on magnetic properties by means of broadband SW spectroscopy, inelastic light scattering spectroscopy, X-ray magnetic circular dichroism and micromagnetic simulation. By nanofabrication, AMQs made of different magnetic materials were created based on 2D analogues of quasicrystals such as Penrose P2, P3 and Ammann tilings.

First, we fabricated AMQs based on aperiodically arranged nanoholes etched into ferromagnetic thin films of CoFeB. Angular-dependent SW spectra exhibited tenfold rotational symmetry reflecting the lattice symmetry of the quasicrystalline nanohole arrangement. Intriguingly, worm-like nanochannels, each exhibiting different SW states, were generated in the AMQs. Our findings imply that the nanohole-based AMQ would become a new class of dense-wavelength division multiplexer. AMQs based on low damping Yttrium iron garnet (YIG) allowed for omnidirectional SW emission thanks to the unconventional rotational symmetry of the quasicrystal. Absorption spectra exhibited forbidden frequency gap openings and a corresponding modification of the magnon density of states, indicating the formation

Abstract

of a magnonic band structure. MGCs, prepared from aperiodically arranged ferromagnetic nanopillars on YIG thin films, allowed also for omnidirectional SW emission with a broad range of wave vectors. SWs with a wavelength below 100 nm were simultaneously excited by two emitters, and their constructive/destructive interference allowed for a binary 1/0 output operation. ASIs composed of interconnected ferromagnetic nanobars were found to show non-stochastic switching relevant for reconfigurable functionalities. An ASI integrated on a YIG film showed MGC modes and SW channeling with the presence of an external field. The SW spectra at remnant state exhibited reprogrammable characteristics depending on the magnetic field history.

Our study and findings on AMQs are important for the fundamental understanding of quasicrystals as well as fabrication of future magnonic devices targeting at information processing by wave-based computing system on the nanoscale.

Keywords: Magnonics, Spin wave, Worm, Grating coupler, Magnetic material, Quasicrystal, Microwave electronics

Zusammenfassung

Magnonen (Spinwellen) sind elementare Spin-Anregungen in magnetisch geordneten Materialien. Sie sind vielversprechend für die Übermittlung und Verarbeitung von Informationen. Magnonen können an elektromagnetische Wellen gekoppelt werden, welche für drahtlose Kommunikationstechnologien verwendet werden. Die Wellenlänge von Magnonen ist um Größenordnungen kürzer als die von elektromagnetischen Wellen bei derselben Frequenz. Wellenbasiertes Rechnen mit Magnonen wäre daher für die Informationstechnologie der nächsten Generation vielversprechend. Für die optimierte Informationsverarbeitung könnten künstliche magnetische Medien eine fortgeschrittene Steuerung von Spinwellen ermöglichen. Ein magnonischer Kristall, der aus periodisch angeordneten Nanomagneten besteht, bietet aufgrund der Bildung einer künstlichen Brillouin-Zone eine maßgeschneiderte Magnonenbandstruktur. Periodische magnonischen Gitterkoppler (MGCs) wandeln zentimeterskalige Mikrowellen effizient in Spinwellen mit Wellenlängen unter einhundert Nanometer um. Es wird erwartet, dass künstliches Spin-Eis (ASIs) reprogrammierbare Magnetisierungskonfigurationen bieten. Die Forschung an künstlichen magnetischen Materialien mit quasikristalliner und aperiodischer Anordnung steckt jedoch noch in den Kinderschuhen. Ein Quasikristall, ein Material mit Fernordnung und fehlender Translationsinvarianz, weist eine unkonventionelle Rotationssymmetrie auf. Die reziproken Gittervektoren des Quasikristalls füllen den gesamten reziproken Raum dicht aus. Diese exotischen Eigenschaften wären für die Kontrolle von SWs vorteilhaft.

Während meiner Doktorarbeit untersuchte ich die Eigenschaften von Spinwellen in zweidimensionalen (2D) künstlichen magnetischen Quasikristallen (AMQs) mithilfe von Breitband-Spinwellenspektroskopie, Brillouin-Spektroskopie, Röntgendiffraktion und mikromagnetischer Simulation um den Einfluss der Aperiodizität auf die magnetischen Eigenschaften zu verstehen. Durch Nanofabrikation wurden AMQs aus verschiedenen magnetischen Materialien basierend auf 2D-Analoga von Quasikristallen wie Penrose P2, P3 und Ammann-Fliesen hergestellt.

Zuerst haben wir AMQs hergestellt, die auf aperiodisch angeordneten Nanolöchern basieren, die in ferromagnetische Dünnschichten aus CoFeB geätzt wurden. Winkelabhängige Spinwellenspektren zeigten eine zehnfache Rotationssymmetrie, die die Gittersymmetrie der quasikristallinen Nanolochanordnung widerspiegelte. Interessanterweise wurden in den AMQs wurmartige Nanokanäle erzeugt, die jeweils unterschiedliche Spinwellenzustände aufweisen. Unsere

Ergebnisse deuten darauf hin, dass der AMQ auf Nanolochbasis eine neue Klasse von dichten Wellenlängen-Multiplexverfahren wird. AMQs, die auf Yttrium-Eisengranat (YEG) mit geringer Dämpfung basieren, ermöglichten dank der unkonventionellen Rotationssymmetrie des Quasikristalls eine omnidirektionale Spinwellenemission. Absorptionsspektren zeigten verbotene Frequenzlücken und eine entsprechende Modifikation der Magnon-Zustandsdichte, was auf die Bildung einer Magnonenbandstruktur hinweist. MGCs, die aus aperiodisch angeordneten ferromagnetischen Nanopillen auf YIG-Filmen hergestellt wurden, ermöglichten auch eine omnidirektionale Spinwellenemission mit einem breiten Bereich von Wellenvektoren. Spinwellen mit einer Wellenlänge unter 100 nm wurden gleichzeitig von zwei Emitttern angeregt, und ihre konstruktive / destruktive Interferenz ermöglichte eine binäre 1/0 Ausgangsoperation. Es wurde gefunden, dass ASIs, die aus miteinander verbundenen ferromagnetischen Elementen bestehen, nicht stochastisches Schalten zeigen, das für rekonfigurierbare Funktionalitäten relevant ist. Ein ASI, das in einen YEG-Film integriert war, zeigte MGC-Moden und Spinwellenkanalbildung bei Vorhandensein eines externen Feldes. Die Spinwellenspektren im Restzustand zeigten in Abhängigkeit von der Magnetfeldhistorie reprogrammierbare Eigenschaften.

Unsere Studie und Ergebnisse zu AMQs sind wichtig für das grundlegende Verständnis von Quasikristallen sowie für die Herstellung zukünftiger magnonischer Geräte, die auf die Informationsverarbeitung durch ein wellenbasiertes Computersystem im Nanobereich abzielen.

Stichwörter: Magnonik, Spinwelle, Wurm, Gitterkoppler, Quasikristall, Magnetisches Material, Mikrowellenelektronik

Résumé

Les magnons (ondes de spin) sont des excitations de spins élémentaires pouvant se propager dans des matériaux magnétiquement ordonnés. Ce sont des quantas prometteurs pour la transmission et le traitement d'informations. Les magnons peuvent être couplés à des ondes électromagnétiques compatibles avec les technologies de télécommunication. La longueur d'onde d'un magnon est un ordre de grandeur plus courte que celle des ondes électromagnétiques à la fréquence équivalente. Par conséquent, de l'informatique à base d'ondes de spins serait prometteur pour la prochaine génération des technologies de l'information. Pour traiter de l'information de manière optimisée, les supports magnétiques artificiels ont le potentiel d'offrir un grand contrôle des ondes de spin. Un cristal magnonique, constitué de nanoaimants disposés périodiquement, fournit une structure de bande de magnons adaptée par l'introduction artificielle d'une zone de Brillouin. Les coupleurs de réseaux magnétiques (MGCs) périodiques convertissent efficacement des micro-ondes à l'échelle du centimètre en ondes de spin dont la longueur d'onde est inférieure à 100 nm. On s'attend à ce que les glaces magnétiques artificielles (ASIs) offrent la possibilité de reprogrammer les magnétisations. Cependant, les études concernant les matériaux magnétiques artificiels basés sur l'arrangement de quasi-cristaux et aperiodique en sont à leurs balbutiements. Un quasi-cristal est un réseau ordonné à longue-portée, mais avec une non-conservation de la symétrie de translation. Il présente cependant une symétrie de rotation multiple. Les vecteurs réciproques associés au quasi-cristal remplissent densément tout l'espace réciproque.

Ces propriétés uniques seraient avantageuses pour le contrôle des ondes de spin. Au cours de mon doctorat, j'ai exploré les propriétés des ondes de spin dans les quasi-cristaux magnétiques artificiels (AMQs) bidimensionnels dans le but de comprendre l'effet de l'apériodicité sur les propriétés magnétiques. Pour ce faire, j'ai utilisé la spectroscopie à ondes de spin à large bande, la spectroscopie Brillouin, le dichroïsme circulaire magnétique à rayons X et des simulations micromagnétiques. Des AMQ constitués de différents matériaux magnétiques ont été nanofabriqués et forment des quasi-cristaux bidimensionnels tels que les pavages Penrose P2, P3 et Ammann.

Tout d'abord, nous avons fabriqué des AMQ basés sur des nano-trous disposés aperiodiquement gravés dans des couches minces ferromagnétiques de CoFeB. Les spectres à dépendance angulaire des ondes de spins ont présenté une symétrie de rotation décuplée reflétant la symétrie du réseau de nano-trous quasi-cristallins. Curieusement, des nanocanaux de type

Résumé

vers, chacun présentant des états d'onde de spin différents, ont été générés dans les AMQ. Nos résultats impliquent que l'AMQ à base de nanotrous deviendrait une nouvelle classe de multiplexage en longueur d'onde dense. Les AMQ basés sur un grenat de fer et d'yttrium (YIG) à faible amortissement ont permis une émission d'onde de spin omnidirectionnelle grâce à la symétrie de rotation non conventionnelle du quasi-cristal. Les spectres d'absorption présentaient des ouvertures d'intervalle de fréquence interdites et une modification correspondante de la densité d'états de magnons, indiquant la formation d'une structure de bande magnonique. Les MGC, préparés à partir de nanopiliers ferromagnétiques disposés aperiodiquement sur des films minces YIG, ont également permis une émission d'ondes de spin omnidirectionnelle avec une large gamme de vecteurs d'ondes. Les ondes de spin avec une longueur d'onde inférieure à 100 nm étaient simultanément excitées par deux émetteurs, et leur interférence constructive / destructive permettait une opération de sortie binaire 1/0. Les ASI composés de nano-barres ferromagnétiques interconnectées ont montré une commutation non-stochastique intéressantes pour des applications à fonctionnalités reconfigurables. Un ASI intégré sur un film YIG a montré des modes MGC et une canalisation des ondes de spins avec la présence d'un champ externe. Les spectres d'onde de spin à l'état résiduel ont pu être reprogrammés en fonction de l'historique du champ magnétique.

Notre étude et nos résultats sur les AMQ sont importants pour la compréhension du comportement fondamental des quasi-cristaux ainsi que pour la fabrication de futurs dispositifs magnoniques ciblant le traitement de l'information par un système informatique basé sur les ondes à l'échelle nanométrique.

Mots clés : Magnonique, Onde de spin, Ver, Coupleur de réseau, Quasi-cristal, Electronique micro-ondes

Contents

Acknowledgements	i
Abstract (English/Français/Deutsch)	v
Introduction	1
I Introductory chapter	5
1 Theory	7
1.1 Introduction to magnetism	7
1.2 Effective field approximation	8
1.3 Magnetization dynamics	10
1.3.1 Ferromagnetic resonance	10
1.3.2 Spin wave dispersion	12
1.4 Artificial magnetic materials	15
1.4.1 Magnonic crystal	17
1.4.2 Magnonic grating coupler	17
1.4.3 Artificial spin ice	19
2 Method	21
2.1 Broadband SW spectroscopy	21
2.1.1 S-parameters	21
2.1.2 Experimental setup	22
2.1.3 SW excitation and detection	24
2.2 Brillouin light scattering microscopy	25
2.2.1 Theory	25
2.2.2 Experimental setup	26
2.3 X-ray magnetic circular dichroism microscopy	28
2.3.1 Background	28
2.3.2 Techniques	29
2.4 Micromagnetic simulation	30
3 Sample fabrication	31
3.1 Magnetic materials	31

Contents

3.2	Nanofabrication	32
3.3	Process flow	33
3.3.1	Etching process	33
3.3.2	Lift-off processing	35
II	Results and Discussion	39
4	Worms and magnonic motifs in artificial ferromagnetic quasicrystals	41
4.1	Direct Observation of Worm-Like Nanochannels and Emergent Magnon Motifs in Artificial Ferromagnetic Quasicrystals	41
5	Magnon band structure in magnonic Penrose quasicrystal	57
5.1	Direct observation of multiband transport in magnonic Penrose quasicrystals via broadband and phase-resolved spectroscopy	58
5.2	Magnons in aperiodic worm-like nanochannels of 2D artificial magnetic qua- sicrystals	75
6	Magnonic nanogratings arranged on quasicrystalline lattice	81
6.1	Broadband nanograting coupler of multiple magnetic resonances approaching 5G telecommunication	81
7	Engineering of artificial spin ice for magnonics	97
7.1	Non-stochastic Switching in Aperiodic Nanomagnet Lattices Forming Repro- grammable Artificial Quasicrystals	97
7.1.1	Conclusion	105
7.2	Toward reconfigurable magnonic waveguide based on artificial spin ice inte- grated YIG film	106
7.2.1	Method	107
7.2.2	Result and discussion	108
8	Summary and Outlook	113
A	Appendix	117
A.1	SI-Direct Observation of Worm-Like Nanochannels and Emergent Magnon Mo- tifs in Artificial Ferromagnetic Quasicrystals	117
A.2	SI-Direct observation of multiband transport in magnonic Penrose quasicrystals via broadband and phase-resolved spectroscopy	124
A.3	SI-Broadband magnonic nanograting coupler approaching 5G telecommunica- tion	132
	Bibliography	149
	Curriculum Vitae	151

Introduction

A spin wave (SW, magnon) is a collective spin excitation in magnetically ordered materials [1]. SWs are coupled to electromagnetic waves in a frequency regime which covers the one conventionally used for telecommunication devices in modern technologies [2]. The wavelength of electromagnetic waves in air is on the centimetre scale while the wavelength of SWs is one the few micrometre scale or even below on the sub-100 nm scale at the same frequency. The propagation of SWs is not associated with a flow of electrons and results in the reduction of Joule heating. Therefore, a such wave-based computing system utilizing phase information of SWs would be advantageous for efficient data processing at high speed [3]. Furthermore, the wave-based data processing units, which are scaled down by the wavelength of the exploited magnon, enable devices to be significantly miniaturized [3]. Hence the realization of logic circuits based on nanoscaled SWs as an alternative of conventional electron-based devices is of special importance.

Toward fabrication of magnon-based computing system, advanced control of SWs is needed for optimized information processing. In the research field of magnonics the generation and manipulation of SWs is explored [4, 5] and artificial magnetic materials with properties varied in space have been investigated. A magnonic crystal (MC) based on periodically arranged nanomagnets tailors the magnon band structure [6, 7]. The Brillouin zone of the band structure is characterized by the newly introduced periodicity, which designs the allowed minibands (SW transmission bands) and forbidden frequency gaps (stop bands). Thanks to the advancements in nanofabrication technologies, one dimensional (1D) and two dimensional (2D) MCs [8, 9] have been explored in experiment [10, 11, 12, 13]. The advantage of 2D MCs is the large degree of freedom associated with the direction of the SW propagation. A 2D MC based on an antidot lattice (ADL) allowed SWs to extend between the nanoholes over its entire surface [10]. Still, the propagation direction was controlled by rotating an in-plane magnetic field [14, 15]. Magnonic grating couplers (MGCs) consisting of periodically arranged magnetic nanoelements on a magnetic underlayer, efficiently converted the long-wavelength microwaves to the sub-100 nm wavelength SWs by adding reciprocal vector \mathbf{G} of the gratings to the transferred wave vector [16, 17, 18, 19]. An artificial spin ice, a 2D array of magnetically coupled nanoislands or nanowires, exhibited emergent frustration properties, which led to particular magnetization states [20, 21]. Their magnetization configurations controlled by a global magnetic field would be of interest in the perspective of reprogrammable magnonics [22].

The static and dynamic properties of the artificial magnetic materials are strongly influenced by their arrangement, such as square lattice [10, 13, 16, 17, 20, 22, 23], hexagonal lattice [14, 24, 25, 26] and even quasicrystalline Penrose lattice [27, 28, 29, 30, 31]. Penrose tiling, invented by Roger Penrose, is an aperiodically arranged pattern consisting of several prototiles, e.g., an acute and obtuse rhombi for Penrose P3 tiling [32, 33]. The Penrose tiling is considered as a 2D analogue of a natural quasicrystal, which exhibits long range order but lacks translational invariance [34]. Therefore constituents in quasicrystals possess non-identical local environments. A quasicrystal possesses manifold rotational symmetry, e.g., tenfold rotational symmetry for the Penrose tiling [32, 33], which is forbidden in crystalline structures. Bragg diffraction patterns of quasicrystalline structures provide a dense set of sharp Bragg peaks, corresponding to their reciprocal vectors [35]. The reciprocal vectors of the Penrose tiling form a decagonal pseudo-Brillouin zone [36], which is more isotropic than the Brillouin zone of a periodic lattice. In photonic quasicrystals composed of aperiodically arranged dielectric elements, a perfect photonic band gap was observed thanks to their high-rotational symmetry [36, 37, 38]. These aspects would be equally advantageous for the advanced control of SWs in artificial magnetic materials, but studies on quasiperiodic arrangements of magnets are in their infancy.

In this thesis, I explored SW properties in artificial magnetic quasicrystals (AMQs) to understand the effect of aperiodicity on magnetic properties using a material-by-design approach. This PhD thesis is organized as follows: First, we give an overview about magnetostatics and spin dynamics in Chapt. 1. Then, the Landau-Lifshitz-Gilbert equation is introduced, and uniform spin precessions (ferromagnetic resonance) as well as spin waves with non-zero wave vectors are explained. Several types of artificial magnetic materials are also introduced. In Chapt. 2, we present experimental techniques such as broadband spin wave spectroscopy using a Vector Network Analyzer, inelastic light scattering (BLS) for SW imaging, and X-ray circular dichroism for the exploration of magnetization configuration as well as spin dynamics on the nanoscale. Micromagnetic simulations for comparison with experimental results are also described. In Chapt. 3, the sample fabrication techniques crucial for the material-by-design approach are discussed. First, important parameters of the investigated magnetic materials from the magnonic application perspective are introduced. Then the sample fabrication processes with used equipment in the clean room facility at EPFL are listed in a step-by-step manner. Results and discussion are formed in Chapt. 4 to 7. In Chapt. 4, spin wave properties in nanohole-based 2D artificial ferromagnetic quasicrystals fabricated for the first time in the field of magnonics are reported. The aperiodic sequence of bends gave rise to different wavelengths in discovered nanochannels and enabled the quasicrystal to become a dense-wavelength division multiplexer. In Chapt. 5, the backfolding and grating coupler effect of a magnonic quasicrystal made of insulating yttrium iron garnet are studied. The lattice symmetry of the quasicrystal allowed SWs to be transmitted omnidirectionally. The formation of a band structure modified the magnon density of states, resulting in forbidden frequency gap openings. Chapt. 6 describes a study on an advanced magnonic grating coupler with which a SW wavelength of 52 nm is realized at small field. The quasicrystalline arrangement allows for the excitation of SWs in a broad range of wave vectors. SWs excited from two different emitters

interfered constructively/destructively, allowing for a wave-based 1/0 binary operation. This study is key for the miniaturization of magnonic devices. In Chapt. 7, a magnetization reversal mechanism of artificial magnetic quasicrystals consisting of ferromagnetic nanobars with different spacings is explained. Interconnected ferromagnetic nanobars were found to have a reprogrammable feature. A hybrid nanostructure of interconnected ferromagnetic nanobars combined with an insulating ferrimagnetic thin layer exhibited reprogrammable properties of SWs. As a conclusion, we summarize our studies and give an outlook for the future experiments in Chapt. 8.

This work was supported by Swiss National Science Foundation via Grant No. 163016.

Introductory chapter

Part I

1 Theory

This chapter presents the theoretical background of ferromagnetism as well as spin dynamics. We first present the overview of magnetic properties of solids. Next, we describe a classical model of the macroscopic magnetization dynamics in an external field and introduce the Landau Lifshitz Gilbert (LLG) equation for ferromagnetic resonance (FMR). We then turn to the spin precessional motion in a magnetic thin film with non-zero wave vectors, called spin waves, and discuss their dispersion relation. Finally, we introduce different kinds of artificially modified nanomagnets such as a magnonic crystal, magnonic grating coupler and artificial spin ice.

1.1 Introduction to magnetism

Magnetic materials [39, 40] made of single element such as Cobalt (Co), Iron (Fe) and Nickel (Ni) as well as an alloy NiFe (Py) are ferromagnets, where magnetic moments are aligned parallel, and a spontaneous magnetization emerges (Fig. 1.1a). An antiferromagnet, where neighboring magnetic moments align anti-parallel (Fig. 1.1b), exhibits no net magnetic moment in the absence of an external field (e.g., NiO). One can also consider that there are two polarized lattices whose magnetizations align anti-parallel. For a ferrimagnet (Fig. 1.1c), the amplitudes of the magnetic moments for the two lattices are not equal. In this thesis, Yttrium Iron Garnet (YIG) is actively utilized as an insulating ferrimagnet. Its macroscopic magnetization is about an order of magnitude smaller compared to Co or Fe. Paramagnet does not exhibit a net magnetic moment as the magnetic moments are randomly oriented (Fig. 1.1d). The alignment of magnetic moments is caused by the quantum mechanical exchange interaction. This interaction is called exchange interaction, and the exchange energy for neighboring spins \mathbf{S}_i and \mathbf{S}_j is expressed as [39]

$$E_{\text{exch}} = -2 \sum_{i>j} J_{\text{exch}} \mathbf{S}_i \cdot \mathbf{S}_j \quad (1.1)$$

where J_{exch} is the exchange constant given by the material. The material with $J_{\text{exch}} > 0$ ($J_{\text{exch}} < 0$) where spins tend to align parallel (anti-parallel) gives rise to ferromagnetic (antiferromagnetic) characteristics.

A spin \mathbf{S}_i gives rise to a microscopic magnetic moment \mathbf{m}_i which leads to the magnetization

$$\mathbf{M} = \frac{\sum_i \mathbf{m}_i}{V} \quad (1.2)$$

where V is the volume. The relation of magnetization \mathbf{M} and a magnetic field \mathbf{H} is expressed as

$$\mathbf{M} = \chi \mathbf{H} \quad (1.3)$$

where χ is the dimension-less susceptibility. The susceptibility represents the response of the material toward the magnetic field \mathbf{H} . The magnetic flux density \mathbf{B} with a unit of Tesla (T) is expressed as

$$\mathbf{B} = \mu_0 (\mathbf{H} + \mathbf{M}) \quad (\text{SI-unit}). \quad (1.4)$$

where μ_0 is a permeability in vacuum. The unit of \mathbf{H} and \mathbf{M} is Ampere/meter (A/m). In this thesis, we use Tesla to describe the magnetic field via $\mu_0 \mathbf{H}$ and magnetization via $\mu_0 \mathbf{M}$, which is conventionally accepted in the field of magnetism.

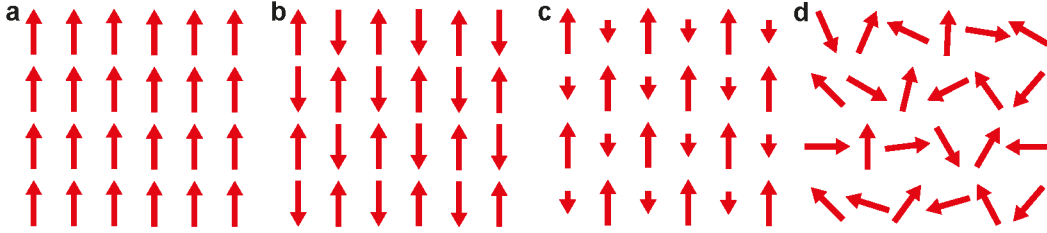


Figure 1.1: Schematic images of magnetic moments (arrows) in a (a) ferromagnet, (b) antiferromagnet, (c) ferrimagnet and (d) paramagnet. The length of arrows represents the amplitude of magnetic moments. The state shown in (d) is relevant for a ferromagnet at a temperature above the critical temperature.

1.2 Effective field approximation

The characteristic feature of ferromagnetic and ferrimagnetic materials is their spontaneous magnetization M_0 . The magnetic order occurs due to the quantum mechanical exchange interaction. Beyond the exchange energy, further energy terms contribute to the total energy E_{tot} of a magnet such as the Zeeman energy, demagnetization energy, and magnetic anisotropy energy. The sum E_{tot} of those energies determine the equilibrium state of magnetization \mathbf{M} , by considering the effective magnetic field via [41]

$$\mathbf{H}_{\text{eff}} = -\frac{1}{\mu_0} \frac{d}{d\mathbf{M}} \frac{dE_{\text{tot}}}{dV}. \quad (1.5)$$

In the presence of an effective magnetic field \mathbf{H}_{eff} , a torque exerted on the magnetic moment \mathbf{m} is considered as $\boldsymbol{\tau} = \mu_0 \mathbf{m} \times \mathbf{H}_{\text{eff}}$. Thereby the magnetization \mathbf{M} tends to align to \mathbf{H}_{eff} and the torque exerted on \mathbf{M} vanishes. In the following, relevant energies are explained.

Zeeman energy

A magnetic moment \mathbf{m} tends to align toward an external field \mathbf{H}_{ext} . The alignment is defined by introducing a potential energy, called Zeeman energy:

$$E_z = -\mu_0 \int_V \mathbf{H}_{\text{ext}} \cdot \mathbf{M} dV \quad (1.6)$$

Note that there is no net force on a magnetic moment in a uniform magnetic field as the potential energy is not position dependent.

Demagnetization energy

Demagnetization energy is a magnetostatic energy, which involves the self-energy of the specimen with the field created by itself. The self-induced field is called demagnetization field \mathbf{H}_d [42], and the demagnetization energy is described by

$$E_d = -\frac{\mu_0}{2} \int_V \mathbf{H}_d \cdot \mathbf{M} dV. \quad (1.7)$$

The demagnetization field $\mathbf{H}_d = -\hat{N}\mathbf{M}$ is proportional to \mathbf{M} and sensitive to the shape of the specimen. \hat{N} is the 3×3 demagnetization tensor. It is symmetric and becomes diagonal in the axes coinciding with the axes of an ellipsoid. The components of \hat{N} in these axes, N_x , N_y and N_z are called demagnetization factors with the relation $N_x + N_y + N_z = 1$ [1]. The demagnetization energy is also called dipolar energy.

Magnetic anisotropy energy

Magnetic anisotropy induces an easy axis and hard axis for magnetically ordered materials. The tendency of the magnetization lying along an easy axis is described by the energy density:

$$\epsilon_a = K_u \sin^2 \theta, \quad (1.8)$$

where K_u is an anisotropy constant, and θ is an angle between magnetization \mathbf{M} and the easy axis. One of the major anisotropies is magnetocrystalline anisotropy, originating from spin-orbit interaction. The easy axis depends upon the magnetic material, e.g., the c-axis [001] of single-crystalline hexagonal Co [39].

Exchange energy

Neighboring spins are coupled via exchange interaction. This exchange energy is parameterized by a position dependent magnetization $\mathbf{M}(\mathbf{r})$ as [43]

$$E_{\text{exch}} = \int A_{\text{exch}} (\nabla \mathbf{e}_{\mathbf{M}})^2 dV \quad (1.9)$$

where $\mathbf{e}_{\mathbf{M}} = \mathbf{M}(r)/M_0$. A_{exch} is the exchange stiffness, and proportional to the exchange constant J_{exch} . The exchange stiffness constant A_{exch} characterizes an exchange length l_{exch} , a length scale over which the direction of magnetization can adapt to a dipolar field via a competition of exchange energy and dipolar energy, described as [44]

$$l_{\text{exch}} = \sqrt{\frac{2A_{\text{exch}}}{\mu_0 M_s^2}}. \quad (1.10)$$

The exchange length is typically 2-5 nm for ferromagnetic materials.

1.3 Magnetization dynamics

In quantum mechanics, spin \mathbf{S} intrinsically possesses an angular momentum. Therefore, the magnetic moment misaligned with a constant magnetic field \mathbf{H}_0 experiences a torque and starts precessing. This is so called Larmor precession. This precessional motion is described with magnetization \mathbf{M} in terms of the Landau–Lifshitz equation [45] as follows:

$$\frac{d\mathbf{M}}{dt} = -|\gamma| \mathbf{M} \times \mu_0 \mathbf{H}_0, \quad (1.11)$$

where γ is the gyromagnetic ratio $\gamma = g\mu_B/\hbar$. μ_B and \hbar are the Bohr magneton and the reduced Planck constant, respectively. Note that the value of g is substance-specific, for example, the g -value of electrons is $g = -2.0023$ [46]. Thus, the gyromagnetic ratio over 2π for an isolated electron is $|\gamma/2\pi| = 28.024$ GHz/T.

In the following, spin dynamics is discussed based on the equation above. We first consider uniformly precessing magnetic moments in a magnetic material, called ferromagnetic resonance. We then discuss the spin precessional motion with a phase shift between neighboring spins, forming spin waves with non-zero wave vectors.

1.3.1 Ferromagnetic resonance

Equation 1.11 describes that the magnetization precesses infinitely around the magnetic field once excited. However, in a real sample these oscillations of the magnetization are accompanied by energy relaxation as illustrated in Fig. 1.2a. To take into account the relaxation, Gilbert [47] added a phenomenological damping term to the Landau–Lifshitz equation, referred to as

the Landau–Lifshitz–Gilbert (LLG) equation [1]:

$$\frac{d\mathbf{M}}{dt} = -\gamma(\mathbf{M} \times \mu_0 \mathbf{H}) + \frac{\alpha}{|\mathbf{M}_0|}(\mathbf{M} \times \frac{d\mathbf{M}}{dt}), \quad (1.12)$$

where α is the dimensionless (Gilbert) damping constant. The damping constant α describes how precession in a system decays (see Fig. 1.2a). In order to solve the LLG equation analytically, we consider that the microwave magnetic field $\mathbf{h}(t)$ acts as a time dependent small perturbation on the equilibrium magnetization \mathbf{M} , resulting in dynamic components $\mathbf{m}(t)$. The magnetic field and magnetization are separated in static and time dependent components

$$\mathbf{M} = \begin{pmatrix} m_x(t) \\ m_y(t) \\ M_0 \end{pmatrix} = \mathbf{m}(t) + \mathbf{M}_0, \quad \mathbf{H} = \begin{pmatrix} h_x(t) \\ h_y(t) \\ H_0 \end{pmatrix} = \mathbf{h}(t) + \mathbf{H}_0. \quad (1.13)$$

where we assume $|\mathbf{m}(t)| \ll |\mathbf{M}_0|$ and $|\mathbf{h}(t)| \ll |\mathbf{H}_0|$. A harmonic precession is expressed as $\mathbf{m}(t) \propto e^{i\omega t}$ where ω is the angular frequency of the microwave magnetic field. One has $d\mathbf{m}(t)/dt = i\omega\mathbf{m}(t)$, and inserting Eq. (1.13) into Eq.(1.12) results in

$$\begin{aligned} \mathbf{m}(t) &= \frac{\gamma M_0}{(\omega_0 + i\omega\alpha)^2 - \omega^2} \begin{pmatrix} \omega_0 + i\omega\alpha & i\omega \\ -i\omega & \omega_0 + i\omega\alpha \end{pmatrix} \mu_0 \mathbf{h}(t) \\ &= \begin{pmatrix} \chi_{11} & \chi_{12} \\ \chi_{21} & \chi_{22} \end{pmatrix} \mu_0 \mathbf{h}(t). \end{aligned} \quad (1.14)$$

where $\omega_0 = \gamma\mu_0 H_0$, corresponding to the Larmor frequency. In case of $\mathbf{h}(t) = (h_x(t), 0, 0)$, the x -component of dynamic magnetization is $m_x(t) = \chi_{11} h_x(t)$. The susceptibility χ_{11} separated in real and imaginary part is described as

$$\chi_{11} = \frac{\gamma M_0 \omega_0 (\omega_0^2 - \omega^2 (1 - \alpha^2))}{(\omega_0^2 - \omega^2 (1 + \alpha^2))^2 + 4\omega_0^2 \omega^2 \alpha^2} - i \frac{\gamma M_0 \omega (\omega_0^2 + \omega^2 (1 + \alpha^2)) \alpha}{(\omega_0^2 - \omega^2 (1 + \alpha^2))^2 + 4\omega_0^2 \omega^2 \alpha^2}, \quad (1.15)$$

and is illustrated in Fig. 1.2c. Around the resonant frequency ω_0 (Larmor frequency), the real part of χ_{11} consists of a dispersion-like function (anti-symmetric Lorentzian function), while the imaginary part of χ_{11} is composed of an absorption-like function (symmetric Lorentzian function).

Until now, we only consider Zeeman interaction for the calculation of magnetization dynamics. However, in ferromagnets, the effective field \mathbf{H}_{eff} including demagnetization energy as well as magnetic anisotropy energy is relevant (Sect. 1.2). Since this thesis work focuses on the nanopatterning of magnetic materials, we consider the internal field generated by the dipolar interaction to investigate ferromagnetic resonance (FMR) [1]. The undamped system with $\alpha = 0$ is used to calculate the precession frequency. For that, the magnetization is projected onto the axes of a Cartesian coordinate system in which the z -axis coincides with the direction of the external magnetic field and the static magnetization. In this scenario, the effective

magnetic field \mathbf{H}_{eff} is described as

$$\mathbf{H} = \mathbf{H} + \mathbf{H}_d = \begin{pmatrix} -N_x m_x(t) \\ -N_y m_y(t) \\ H_0 - N_z M_0 \end{pmatrix}, \quad (1.16)$$

and with Eq. 1.11 one gets the two linear equations,

$$\begin{aligned} i\omega m_x + \gamma\mu_0[H_0 + (N_y - N_z)M_0]m_y &= 0, \\ -\gamma\mu_0[H_0 + (N_x - N_z)M_0]m_x + i\omega m_y &= 0. \end{aligned} \quad (1.17)$$

The condition of the compatibility of these equations gives the expression for the eigenfrequency (FMR):

$$\omega = \gamma\mu_0 \sqrt{[H_0 + (N_x - N_z)M_0][(H_0 + (N_y - N_z)M_0)]}. \quad (1.18)$$

Equation (1.18) is the famous formula obtained by Kittel [48]. The FMR frequency can be further simplified for the limiting cases (i) a sphere, (ii) a rod oriented along the z -axis and (iii) a thin film in the xz plane: (i) For the sphere, $N_x = N_y = N_z = 1/3$ so that $\omega = \gamma\mu_0 H_0$, which coincides with the Larmor frequency. (ii) The demagnetization factor of the rod is $N_x = N_y = 1/2, N_z = 0$, and the Kittel formula is $\omega = \gamma\mu_0 H_0 + M_0/2$. The FMR frequency corresponds to the Larmor frequency with an offset $M_0/2$. (iii) The resonance frequency of a thin film with the demagnetization factor $N_x = N_z = 0, N_y = 1$ is expressed as $\omega = \gamma\mu_0 \sqrt{H_0(H_0 + M_0)}$. The resonance curve starts from 0 GHz and converges to the FMR plot for the rod in a high external field range. All the FMR frequency evolution is depicted in Fig. 1.2d.

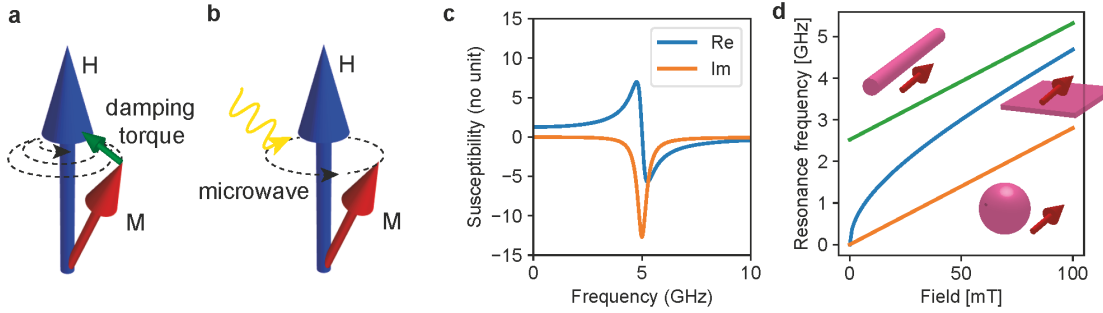


Figure 1.2: (a) A schematic image of magnetization \mathbf{M} precessing around the field \mathbf{H} with energy relaxation (damping). (b) Magnetization precesses around the field with a constant cone angle due to irradiation with microwaves at the resonance frequency. (c) Susceptibility with real (blue) and imaginary parts (orange). (d) Field-dependent FMR frequency for a rod (green), a sphere (orange) and a thin film (blue). Insets indicate the direction of the magnetization \mathbf{M} associated with the field \mathbf{H} .

1.3.2 Spin wave dispersion

Apart from the uniformly excited spin precession (FMR), the neighboring magnetic moments could precess with a phase difference, and form a wave-like excitation, called spin wave

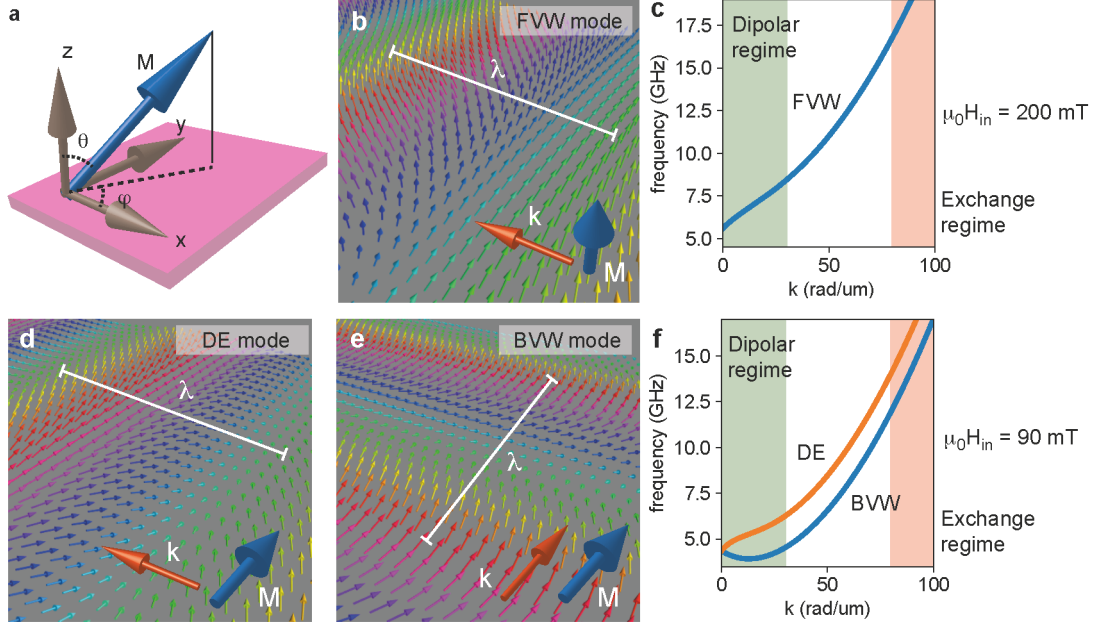


Figure 1.3: (a) The geometry and the orientation of magnetization \mathbf{M} in the Cartesian coordinate system. (b) A schematic image of FVW and (c) its dispersion relation for a 100-nm-thick YIG film with an out-of-plane internal field of $\mu_0 H_{in} = 200$ mT. Schematic images of (d) DE-type SW and (e) BVW and (f) their dispersion relations for the 100-nm-thick YIG film with an in-plane internal field of $\mu_0 H_{in} = 90$ mT.

(SW, magnon). SWs can be dominated by (long-range) dipolar interaction and (short-range) exchange interaction. The SW characteristics are defined by a wave vector \mathbf{k} and the magnetization configuration. Kalinikos and Slavin [49] established a theoretical approach for the calculation of SW dispersion relations in a thin film. Assuming that the magnetization \mathbf{M} in a magnetic thin film orients by an angle θ with respect to the z -direction, and \mathbf{M} projected onto the xy plane forms an angle φ with the x -direction as shown in Fig. 1.3a. One defines k and κ as a wave number for in-plane direction and out-of-plane direction, respectively. Thus, the magnitude of the wave vector is expressed as $k_n = \sqrt{k^2 + \kappa^2}$. If a standing wave vertical to the film (thickness: t) is formed, $\kappa = n\pi/t$ ($n = 1, 2, \dots$) for the wave pinned at the film surface. This standing wave is called perpendicular standing spin wave (PSSW). Using $\omega_H = \gamma\mu_0 H_{in}$, where H_{in} is the internal field, and $\omega_M = \gamma\mu_0 M_0$, the resonance frequency of the SW is described as follows [49]:

$$\omega = \sqrt{[\omega_H + l_{ex}^2 \omega_M k_n^2][\omega_H + l_{ex}^2 \omega_M k_n^2 + \omega_M F_n]} \quad (1.19)$$

where

$$F_n = P_n + \sin^2 \theta (1 - P_n (1 + \cos^2 \varphi)) + \omega_M \frac{P_n (1 - P_n) \sin^2 \varphi}{\omega_H + l_{ex}^2 \omega_M k_n^2} \quad (1.20)$$

and

$$P_n = \frac{k^2}{k_n^2} + \frac{k^2 \kappa^2}{k_n^4} \frac{2}{kL} [1 - (-1)^n \exp(-kt)]. \quad (1.21)$$

This is a dispersion relation of SWs, which enables us to extract a SW group velocity $v_g = \partial\omega/\partial k$. In the large wavelength regime ($kt \ll 1$), the dipolar interaction term $\omega_M F_n$ dominates the characteristic of the SWs. On the contrary, the exchange interaction term $l_{\text{ex}}^2 \omega_M k_n^2$ plays a dominant role for SWs at large k . In the exchange regime, the group velocity of SWs is always positive.

The SW properties are changed depending on the magnetization configuration as well as the angle between magnetization \mathbf{M} and wave vector \mathbf{k} (Fig. 1.3a). SWs with out-of-plane magnetization are called forward volume waves (FVWs) as illustrated in Fig. 1.3b. The group velocity of FVW is positive in the dipolar regime (Fig. 1.3c). The dispersion relation of FVWs is isotropic in-plane, and therefore SWs generated from a point source propagate omnidirectionally. On the contrary, the dispersion relation of SWs for an in-plane magnetization exhibits an anisotropic feature. SWs with $\mathbf{M} \perp \mathbf{k}$ as shown in Fig. 1.3d are called Damon-Eshbach modes (DE modes), whose group velocity is positive in the dipolar regime (Fig. 1.3f). For $\mathbf{M} \parallel \mathbf{k}$ (Fig. 1.3e), SWs are so-called backward volume waves (BVWs) with a negative group velocity. The wavelength λ of SWs in an unpatterned thin film is generally given by the geometrical parameters of a SW excitation waveguide, to which microwaves are applied. Artificially created magnetic nanostructures can modify the wavelength of SWs characterized by their geometrical parameters.

Laterally confined spin wave modes: Standing SWs would be confined in a magnetic structure similar to the PSSW mode. We assume that there is a ferromagnetic nanopillar made of Py with a thickness of 100 nm and diameter of 95 nm, and it is saturated along its axis by an external field of -500 mT (Fig. 1.4a). The standing wave can be formed in the lateral direction at the top and bottom surfaces (Fig. 1.4b) and the axial direction (Fig. 1.4c). By considering the magnetization direction, the laterally confined SW and axially confined SW possess a FVW-like and BVW-like characteristics, respectively.

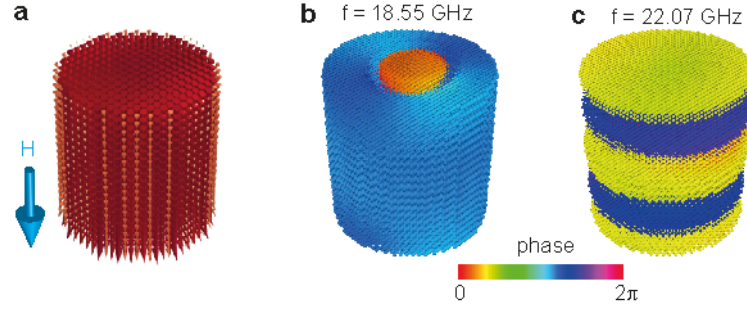


Figure 1.4: (a) A simulated 3D image of magnetization in a Py nanopillar. Red cones indicate the direction of magnetic moments. An external field (sky blue arrow) is applied along the axis of the nanopillar. Simulated SW images of the nanopillar at (b) 18.55 GHz and (c) 22.07 GHz. The size of spheres indicates the amplitude and hue represents the phase of the standing SWs.

1.4 Artificial magnetic materials

In the previous sections, we discussed about spin dynamics in an unpatterned film and single elements. Apart from these structures, artificially modulated magnetic nanostructures with periodic/apperiodic arrangements give rise to new static and dynamics properties, and therefore the understanding of the crystalline/quasicrystalline properties is important. Below, characteristics of periodic/apperiodic structures in real space and reciprocal space are discussed.

Periodic structures such as Bravais lattices and a honeycomb structure possess translational invariance, exhibiting two-fold, three-fold, four-fold and six-fold rotational symmetries. Due to their periodic nature, the periodic lattices in reciprocal space also exhibit periodically arranged sharp peaks. For example, a square lattice with a periodicity a exhibits a four-fold rotational symmetry in real and reciprocal spaces as depicted in Fig. 1.5a and c, respectively. Reciprocal lattice vectors (RLVs) \mathbf{G} are expressed as

$$\mathbf{G}_{m,n} = \frac{2\pi}{a} \begin{pmatrix} m \\ n \end{pmatrix} \quad (m, n = 0, \pm 1, \pm 2, \dots). \quad (1.22)$$

A Brillouin zone boundary, inside which the wave properties are completely described in a periodic medium, is formed at half of $\mathbf{G}_{\pm 1,0}$ and $\mathbf{G}_{0,\pm 1}$. One can investigate (periodic-)crystal properties using X-ray/electron scattering by observing Bragg peaks. The width of the reciprocal peaks would be broader by deviating lattice positions, and therefore a randomized structure does not provide sharp peaks in reciprocal space anymore in analogy with an amorphous material.

A quasicrystal, reported by Dan Shechtman in 1984 [34], is not classified as either crystal or amorphous. A quasicrystal exhibits no translational invariance but possesses long-range order. Therefore, constituents in quasicrystals possess non-identical local environments. Penrose tiling is a 2D analogue of a natural quasicrystal [33]. Unlike periodic tilings, the Penrose tiling consists of several prototiles. For example, Penrose P3 tiling is composed of an acute and

obtuse rhombi, which fill out the space infinitely (Fig. 1.5b). Quasicrystals exhibit unconventional rotational symmetries such as eight-fold [29, 50], ten-fold [32, 36], twelve-fold [37, 51] and more [51, 52], which are forbidden in periodic crystals [53]. The infinite Penrose tiling exhibits ten-fold rotational symmetry. Due to the long-range order and aperiodic properties of quasicrystals, a Bragg diffraction pattern provides sharp peaks, which densely fill reciprocal space (Fig. 1.5d) and coincide with reciprocal vectors (RVs) \mathbf{F} . Especially the prominent peaks which are close to the inverse of the characteristic length a of the Penrose tiling, are called basic RVs. The basic RVs for the Penrose P3 tiling are described as [36]

$$\mathbf{F}_n^{(1)} = \frac{2\pi}{a \cos(\pi/10)} \begin{pmatrix} \cos(n\pi/5) \\ \sin(n\pi/5) \end{pmatrix} \approx 1.051 \times \frac{2\pi}{a} \begin{pmatrix} \cos(n\pi/5) \\ \sin(n\pi/5) \end{pmatrix}, \quad (n = 0, 1, \dots, 9). \quad (1.23)$$

A decagon defined by lines bisecting the basic RVs is called pseudo-Brillouin zone (p-BZ). The shape of the p-BZ is more isotropic as compared with the BZ of a 2D Bravais lattice, which is advantageous for the formation of a band structure for wave-like states with complete band gaps in artificial materials.

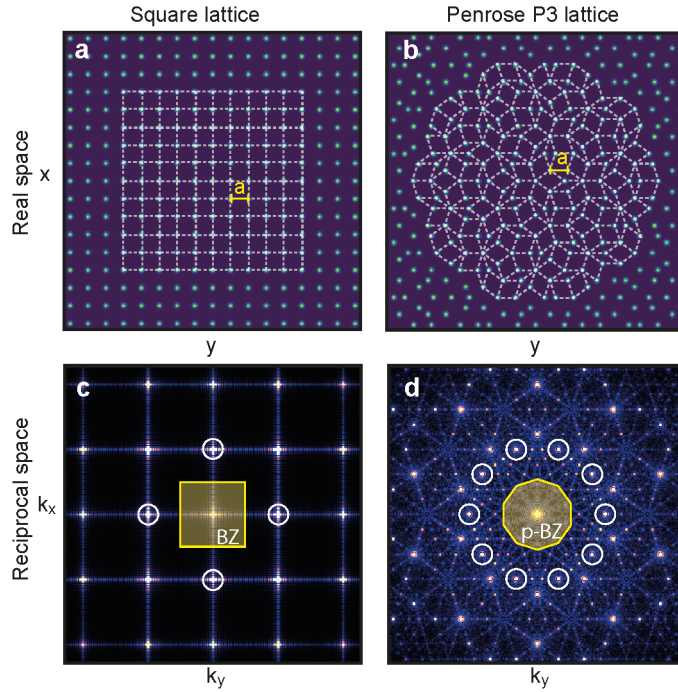


Figure 1.5: Illustrations of (a) a square lattice and (b) a Penrose P3 lattice with a characteristic length of a . Dots of the lattices are positioned at the vertex of the tilings indicated by white dashed lines. (c) Square lattice and (d) Penrose P3 lattice in reciprocal space by performing fast Fourier transformation on (a) and (b), respectively. Yellow transparent square and decagon represent a (pseudo-) Brillouin zone based on the responsible reciprocal vectors (white circles) in the square and the Penrose lattice, respectively.

1.4.1 Magnonic crystal

Periodically arranged magnetic structures provide tailored band structures for spin waves in one (1D) [54, 55, 56, 57, 58, 59], two (2D) [9, 10, 11, 12, 13] and three dimensions (3D) [8, 60]. These so-called magnonic crystals (MCs) are expected to realize the full control of spin waves [6, 7]. Figure 1.6a shows an example design of a 1D magnonic crystal made of 100-nm-thick YIG. Periodic nanogrooves with a depth of 20-nm are introduced with a periodicity of $a = 900$ nm. An external field of 90 mT is applied along the long axis of the 1D MC. Figure 1.6b shows the dispersion relation of the 1D MC for DE-type SWs ($\mathbf{M} \perp \mathbf{k}$) following the calculation method of Refs. [56, 61]. The back-folded dispersion curves with $G = 2\pi n/a$ ($n = 0, \pm 1, \pm 2, \dots$) form a band structure inside the Brillouin Zone (BZ). The opened gap at the 1st BZ boundary (inset of Fig. 1.6b) can be considered as a stop band of SWs [59].

A backfolding effect of SWs is also reported in 2D MCs (Fig. 1.6c). A periodically arranged antidot lattice (ADL) based MC formed a miniband of specific SW modes [10] by induced inhomogeneous internal fields due to the demagnetization effect [62]. Bragg reflection was directly measured by resolving wave vectors of SWs in the 2D MC [11]. The formation of a complete (omnidirectional) band gap is however challenging due to the anisotropic characteristics of SWs (Fig. 1.6c). Quasicrystalline structures, where the circularly shaped p-BZ might be formed, would however realize the complete band gap for SW filtering. So far photonic quasicrystals in which dielectric materials are arranged with long-range quasiperiodic order exhibit a perfect photonic band gap [36].

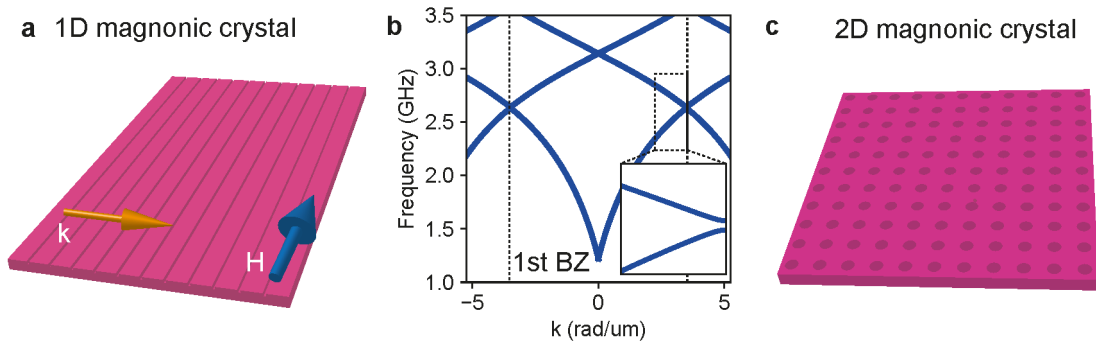


Figure 1.6: A schematic image of (a) 1D MC made of YIG with periodically introduced nanogrooves with a depth of 20-nm. The periodicity amounts to 900 nm. (b) Band structure of SWs for the 1D MC shown in (a). The inset shows a gap opening of SWs at the 1st BZ boundary. (c) A schematic image of a 2D magnonic crystal based on nanoholes (antidot lattice).

1.4.2 Magnonic grating coupler

In photonics and plasmonics, grating couplers have been demonstrated as a powerful method for the control of light propagation [63, 64, 65]. In magnonics, H. Yu *et al.* proved a magnonic grating coupler (MGC) effect on SWs [16, 17, 18]. They have fabricated MGC samples with periodically arranged ferromagnetic CoFeB nanodisks on top of a ferrimagnetic YIG thin film as illustrated in Fig. 1.7a. The CoFeB nanodisks and YIG film served as nanograting elements

and SW propagation medium, respectively. Microwaves were applied to an integrated coplanar waveguide (CPW) on the MGC sample in order to excite SWs. The wavelength and propagation direction of the SWs were found to be precisely controlled by reciprocal lattice vectors \mathbf{G} of the periodic structures. As explained in Sec. 1.3.2, geometrical parameters of the CPW are expected to define the wave vectors of excited SWs \mathbf{k}_{cpw} in a plane magnetic film. Due to the magnetization precession in the grating elements, dynamic dipolar fields and exchange bias from the grating elements modulate SW properties in the YIG film, and thus the spin precessional amplitudes of grating coupler induced modes $\mathbf{k}_{\text{cpw}} \pm n\mathbf{G}$ ($n = 1, 2, \dots$) are found to be largely enhanced compared with the original excitation strength from the microwave antennas (Fig. 1.7a).

The grating coupler modes are most effectively enhanced when the magnetization inside the grating elements precesses at their resonance frequency. Figure 1.7b describes the dispersion relation of a 100-nm thick YIG film with the field of 90 mT applied in-plane and the FMR frequency of ferromagnetic nanodisk made of Py. Considering the full width at half maximum (FWHM) of the FMR, SW mode $\mathbf{k} + 4\mathbf{G}$ would be effectively excited (on-resonant grating coupler mode [17, 18, 19, 66]). Since the magnetization is susceptible to a microwave magnetic field even at off resonance, grating coupler modes at the different frequencies could be also excited but inefficiently (off-resonant grating coupler mode [16]). Conventional grating coupler modes with periodic nanogratings could only be excited with specific wave vectors due to the discrete nature of reciprocal lattice vectors \mathbf{G} as shown in Fig. 1.5c. However aperiodically arranged nanograting element might solve this issue as the reciprocal vectors of quasicrystals densely fill out the reciprocal space [36].

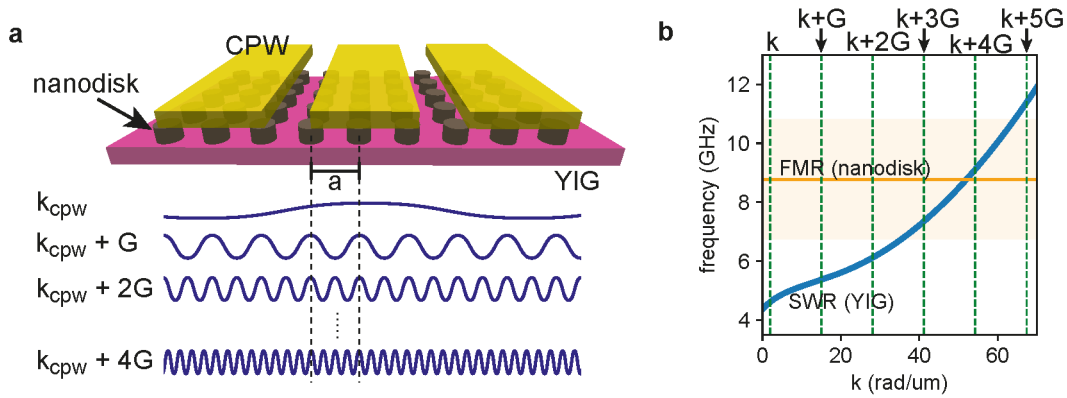


Figure 1.7: (a) Magnonic grating coupler sample with CPW. Nanodisks made of ferromagnet are arranged periodically on top of a YIG thin film. Due to the magnetization precession inside the grating elements, specific grating coupler modes $\mathbf{k}_{\text{cpw}} \pm n\mathbf{G}$ ($n = 1, 2, \dots$) could be resonantly enhanced. (b) Dispersion relation of a 100 nm thick YIG film and FMR frequency of the nanodisk made of Py. A field of 90 mT is applied in-plane.

1.4.3 Artificial spin ice

Using nanotechnology, one can create single domain nanomagnets if their size is below or comparable to the minimum domain size. A ferromagnetic nanobar would form a single domain with a bi-stable property due to its shape anisotropy. We assume a ferromagnetic nanobar with a length l , width w and thickness t . The nanobar is considered as a dumbbell of length l with two equal charges of opposite polarity, $\pm q = \pm ml = \pm Mtwl/l = \pm Mtw$, at the dumbbell's ends as shown in Fig. 1.8a (Dumbbell model) [67]. This dumbbell would behave as a giant Ising spin.

Now we assume that three magnetic nanobars A, B and C are arranged in a way that their edges meet as illustrated in Fig. 1.8b, and the magnetization of nanobars A and B points in their favored directions. Then the magnetization direction of nanobar C can be only favorable for either nanobar A or B (frustration). One can imagine this frustration over a large area by allocating those interacting nanobars with an arrangement of a periodic 2D lattice, e.g., a kagome lattice (Fig. 1.5c). This array of frustrated ferromagnetic nanobars is called artificial spin ice (ASI). The magnetization configurations of ASIs are investigated via magnetic imaging techniques such as magnetic force microscopy (MFM) [20, 68] and X-ray magnetic circular dichroism (XMCD) [69, 70, 71] concerning magnetic charges at the vertex of the lattice (Charge model) [67]. Their frustrations are studied by modifying lattice and geometrical parameters of the nanobars.

Unlike periodic structures, quasicrystalline tilings possess no translational invariance, and thus vertices in such tilings possess non-identical local environments. Figure 1.8d shows magnetic nanobars arranged on a Penrose P3 tiling. A finite Penrose P3 tiling [32] possesses coordination numbers (CNs) of 2, 3, 4, 5, and 7 at its vertices while vertices of a kagome lattice have a CN of 3. For the saturated case along y -direction, absolute values of magnetic charge numbers can exceed 1 for a Penrose P3 tiling-based ASI while this is not the case for the kagome-ASI (Fig. 1.8c and d). These interesting properties of the quasicrystalline arrangement attract more attention in the field of artificial spin ice. V. Bhat *et al.* fabricated ferromagnetic artificial quasicrystals consisting of interconnected Py nanobars arranged in the Penrose P2 tiling [32]. Characteristic knee anomalies, i. e., drastic jumps of the magnetization value were observed in the magnetic hysteresis curve at several fields in experiment and simulation [27]. They were argued to indicate the systematic switching of Py nanobar groups. The magnetic charge model suggested that the non-identical local environment strongly influenced the magnetization reversal by affecting exchange and dipolar interactions and caused the switching to be non-stochastic. Reproducible FMR was reported in the hysteretic regime where the knee anomalies occurred [27]. In this work we will analyze the reversal of different quasicrystal-based ASIs in terms of the charge model.

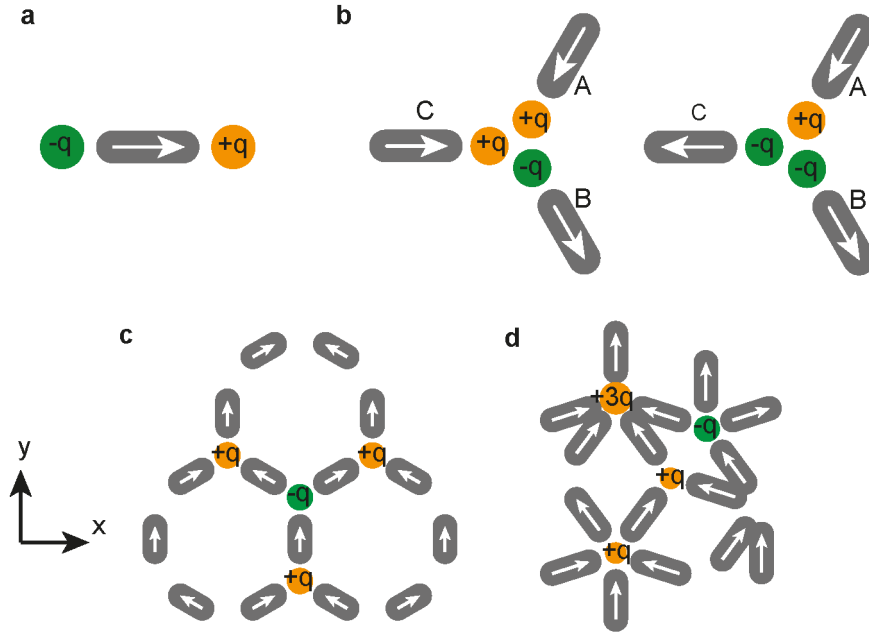


Figure 1.8: (a) Schematic image of a ferromagnetic nanobar behaving as a giant Ising spin. At the edges of the nanobar, magnetic charges $\pm q$ are defined. (b) Frustrated ferromagnetic nanobars. Nanobar C cannot satisfy the lowest energy state with nanobar A and nanobar B, simultaneously. Artificial spin ice consisting of ferromagnetic nanobars arranged on a (c) kagome lattice (left) and (d) Penrose P3 tiling (right). Orange and green represent positive and negative magnetic charges, respectively. The dotted circle indicate

2 Method

In this chapter, experimental methods to characterize the static and dynamic properties of the prepared magnetic nanostructures are discussed: Broadband spin wave spectroscopy, inelastic (Brillouin) light scattering (BLS) and X-ray magnetic circular dichroism (XMCD). Via broadband spectroscopy, spin waves excited by continuous-wave microwaves are detected by coplanar waveguides and induced voltages. BLS spectroscopy is based on the magnon-photon scattering, which allows us to image SWs with micro-focused light. Static magnetic properties are imaged using absorption of circularly polarized X-rays via magnetic circular dichroism. Spin wave microscopy with X-rays is also performed offering a higher spatial resolution than the light-based microscopy technique.

2.1 Broadband SW spectroscopy

We study spin precessional motion of standing and propagating spin waves by applying microwaves to coplanar waveguides (CPWs) integrated on top of the magnetic nanostructures [10, 12, 16, 59, 72, 73]. Since the spin precessional motion generates an induced voltage in CPWs via Faraday's induction law, the spin dynamics are detected electrically. This technique is also called all-electrical spin wave spectroscopy (AESWS), since all the measurement processes are completed electrically unlike light-involved BLS and X-ray-involved STXM.

2.1.1 S-parameters

We use a Vector Network Analyzer (VNA), a test system which enables the reflection and transmission of microwave devices to be characterized up to 26.5 GHz in our case. The VNA possesses multiple ports where microwave voltage signals are emitted and detected. The electrical behavior of the device under test (DUT) is described by Scattering parameters

(S-parameters):

$$\begin{pmatrix} b_1 \\ b_2 \\ b_3 \\ b_4 \end{pmatrix} = \begin{pmatrix} S_{11} & S_{12} & S_{13} & S_{14} \\ S_{21} & S_{22} & S_{23} & S_{24} \\ S_{31} & S_{32} & S_{33} & S_{44} \\ S_{41} & S_{42} & S_{43} & S_{44} \end{pmatrix} \begin{pmatrix} a_1 \\ a_2 \\ a_3 \\ a_4 \end{pmatrix} \quad (2.1)$$

where $a_i = A_i e^{i\phi_i}$ ($i = 1, 2, 3, 4$) represents incident microwave signals from port i and $b_i = B_i e^{i\phi_i}$ represents detected signals at port i . A (B) and ϕ indicate the amplitude and phase, respectively, of the microwave. The S-parameters are complex values, and normally a microwave source of one port is switched "ON" while the microwave sources of the other ports are switched "OFF", and therefore, S_{ij} is defined as

$$S_{ij} = \frac{b_i}{a_j} = \frac{B_i e^{i\phi_i}}{A_j e^{i\phi_j}} = \frac{B_i}{A_j} e^{i(\phi_i - \phi_j)} \text{ with } i, j = 1, 2, 3, 4. \quad (2.2)$$

Here S_{ii} ($S_{ij}, i \neq j$) parameters represent the reflection (transmission) coefficients of microwave signal. Figure 2.1 illustrates the definition of S-parameters for a 2-port VNA, which is mostly used in the thesis.

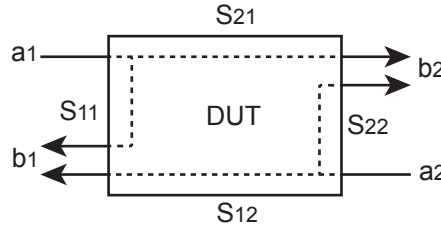


Figure 2.1: Schematic image of the S-parameters used for a 2-port VNA.

2.1.2 Experimental setup

For the characterization of the magnetic nanostructures, a DUT (CPWs with integrated magnetic nanostructures) is mounted in a 2D vector field application unit. In our laboratory, an in-plane field (x, y -direction) and out-of-plane field configurations (z -direction) are available as described in Fig. 2.2a and b, respectively. The VNA is connected to the DUT via microwave cables with microwave probes. We sweep the frequency of the applied microwave signal and provide a variable field \mathbf{H} at a fixed field orientation φ (field-dependent spectroscopy) or vary the angle φ for a specific field value H (angular dependent spectroscopy). For the SW excitation, two types of CPWs are considered: THRU-CPW and SHORT-CPW. In case of the THRU-CPW, tens of nominally identical artificial magnetic quasicrystal samples are embedded underneath the signal line of the CPW (Fig. 2.2c). Since the microwave field is almost homogeneous with respect to the quasicrystal samples, standing SWs are characterized. If the CPW and samples are perfectly symmetric with respect to the vertical axis of the CPW, all the S-parameters both in reflection and transmission will provide a same microwave response toward the excitation of SWs (SW absorption spectra). This THRU-CPW is used in

Sec. 4.1. A SHORT-type CPW will provide inhomogeneous microwave field to a large sample, and therefore excited SWs underneath the CPW will obtain a wave vector defined by the CPW. Transmitted SWs induce voltages in the neighboring CPW, and SW propagation spectra are detected in the transmission parameter. Similar to the THRU-CPW, SW absorption spectra are observed in reflection configuration. Note that a calibration is performed before the measurement in order to minimize the influence of the microwave cables on the results.

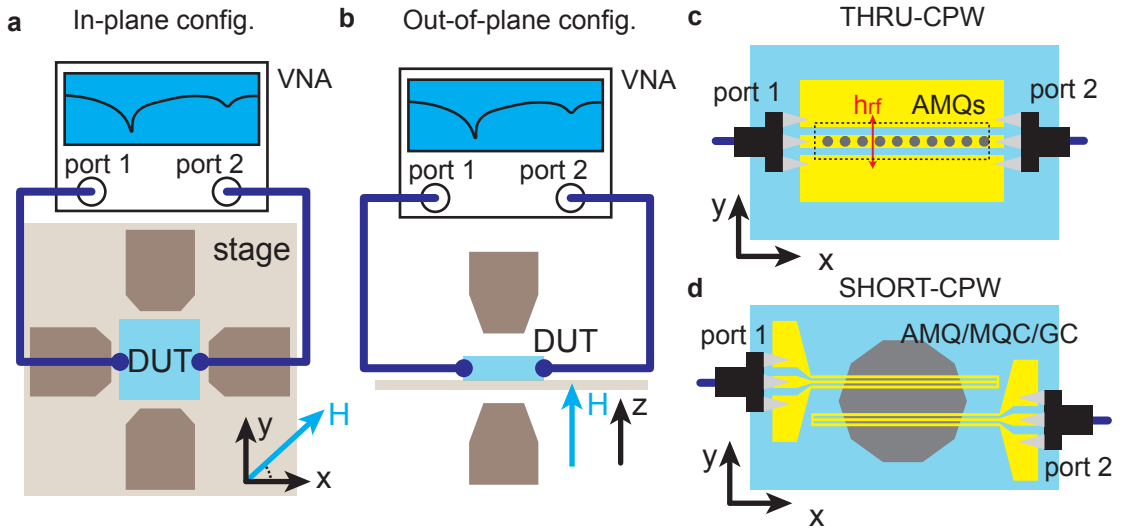


Figure 2.2: Schematic images of experimental setups for broadband SW spectroscopy with (a) in-plane and (b) out-of-plane external magnetic fields. A DUT connected with VNA via SMA cables is located between magnetic yokes. (c) THRU-type CPW and (d) SHORT-type CPWs are used for the excitation of spin waves.

Phase control mode: A VNA, PNA N5222A from Keysight can provide two output voltages with a defined phase difference from two ports simultaneously. One source is selected as a control source and the other is a reference source. As a result, phase sweep measurements at a fixed frequency and frequency sweep measurements at a fixed phase difference are available. In addition the relative power of the controlled port as compared to the reference power amplitude can be set. Under phase control, the microwave stimuli from port 1 and port 3 ($A_3 e^{i\phi_3}$) are detected at port 2 as shown in Fig. 2.3a, and transmission parameter S_{21}^* under phase control is detected. In our setup, the microwave from port 1 is referenced by port 3, and therefore the relative amplitude A_3/A_1 and the phase difference $\phi_3 - \phi_1$ can be set.

We consider that the VNA is connected to three CPWs integrated on a sample (Fig. 2.3b). SWs are excited at CPW 1 and CPW 3 connected to port 1 and port 3, and propagate to CPW 2 connected to port 2. The transmitted SWs would interfere underneath CPW 2, and induce a voltage, which would be modified by the relative amplitude and the phase difference. In Sec. 6.1, a relative amplitude is always set to 0 dBc for this type of measurements ($A_3/A_1 = 1$).

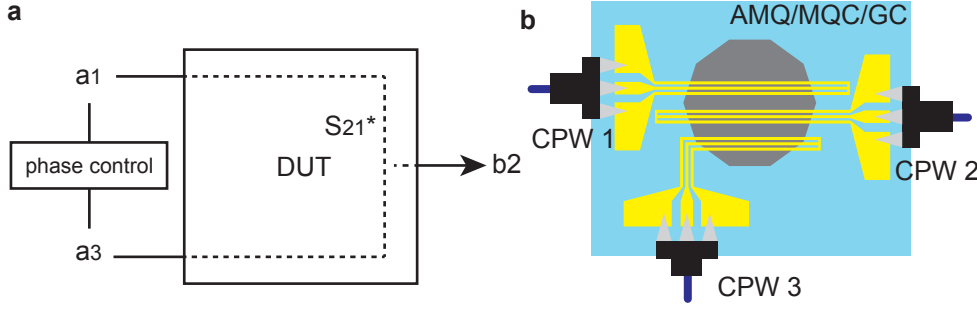


Figure 2.3: (a) Schematic image of the S-parameters used for a 4-port VNA under phase control. The amplitude and phase of the microwave inputs a_1 and a_3 are controlled. (b) A schematic image of an experiment with a three terminal DUT under phase control. Three CPWs are integrated on a magnetic nanostructure. Spin waves emitted from two CPWs are detected at the third CPW as an interference signal.

2.1.3 SW excitation and detection

Some of the SW modes observed in SW spectra reflect the inhomogeneity of the microwave magnetic field, which will be discussed in the following. Geometrical parameters of SHORT-CPWs used in this thesis are as follows: the width of signal and ground lines is 800 nm or $2\ \mu\text{m}$ and a gap between the signal and ground lines is 640 nm or $1.6\ \mu\text{m}$, respectively. Typically the CPWs are made of Au with a thickness of 100 to 200 nm with a 5 nm thick adhesive Ti layer. Microwave current directions in the signal line and ground lines for the SHORT-CPW are opposite. Figure 2.4a shows a simulated result of a microwave magnetic field distribution underneath a CPW along the y -direction of the CPW in Fig. 2.2d. Here the cross section of the CPW (yellow) is also shown simultaneously. Due to the inhomogeneity of the field, excited SWs possess non-zero wave vectors \mathbf{k} if a magnetic film extends beyond the CPW. Figure 2.4b shows a Fourier transformed result of Fig. 2.4a, exhibiting several broad peaks near local maxima k_1 , k_2 , k_3 , k_4 and k_5 . These wave vectors would be transferred with the SW modes. Figure 2.4c shows SW excitation spectra on a 100 nm thick YIG film with two SHORT-CPWs as illustrated in Fig. 2.2d. The distance s between the two signal lines of the CPWs amounted to $12\ \mu\text{m}$. The field of 90 mT was applied along the CPW axis ($+x$ -direction). S_{22} in real part shows an absorption spectrum of SWs excited in the YIG film. Three major peaks expected from the inhomogeneous field distribution of the microwave field are observed. In the transmission geometry (S_{21}), corresponding SW propagation signals are detected. The oscillations are caused by wave-vector dependent phase accumulation of SWs between the two CPWs [74, 75]. Taking into account the periodicity Δf of the oscillation signal, a group velocity v_g of SWs for each mode can be extracted as follows [15]:

$$v_g = \Delta f \cdot s. \quad (2.3)$$

The group velocity for the k_1 with the periodicity $\Delta f = 0.72\ \text{GHz}$ mode is calculated to 0.72 km/s. The higher frequency modes above 5.4 GHz in S_{21} are also associated with the

excitation spectrum of the CPW (k_4 and k_5), and corresponding modes in S_{22} are resolved (Inset of Fig. 2.4c).

In this work we will discuss both absorption spectra like the one shown as S_{22} in Fig. 2.4c and spectra with oscillations reflecting SW propagation (illustrated by S_{21} data in Fig. 2.4c). When using three CPWs for an interference experiment outlined before, we monitor the combined signal for two separately excited propagating SWs, i. e., the strength of the oscillating signal as a function of phase difference between the two emitter CPWs.

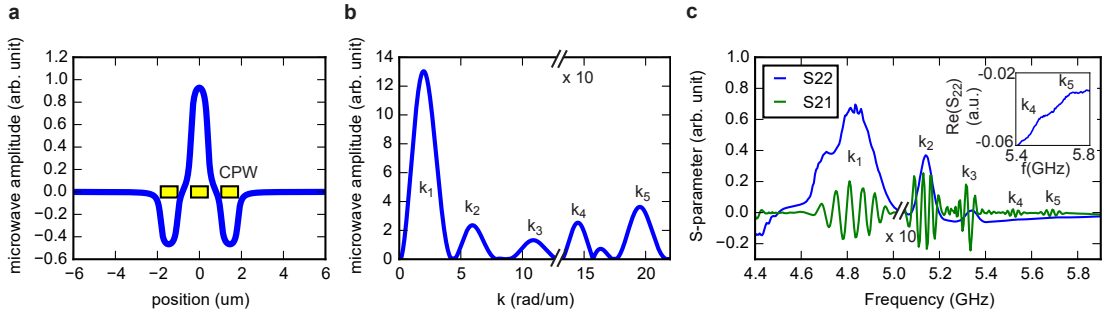


Figure 2.4: In-plane microwave magnetic field distribution at the bottom surface of a CPW in (a) real space and (b) reciprocal space. Main mode k_1 and satellite modes k_2, k_3, k_4 and k_5 are observed. (c) SW spectra of a 100-nm-thick YIG film in a reflection ($\text{Re}(S_{22})$ in blue) and transmission ($\text{Re}(S_{21})$ in green) geometry. A magnetic field of 90 mT was applied along the CPW (DE-mode). SW modes imposed by the CPW described in (b) are observed as peaks in $\text{Re}(S_{22})$, and corresponding modes as oscillations in $\text{Re}(S_{21})$ are detected. The inset shows magnified data of $\text{Re}(S_{22})$ for k_4 and k_5 modes.

2.2 Brillouin light scattering microscopy

The broadband SW spectroscopy technique presented in Sect. 2.1 provides global SW properties averaged over the relevant area of the measured sample. The Brillouin light scattering (BLS) technique allows us to characterize SWs with high spatial resolution in magnetic nanostructures [76, 77, 78, 79]. In addition we exhibit phase resolution [77, 78].

2.2.1 Theory

The magnon represents the quasi-particle of a SW, which could interact with other particles (quasiparticles) such as a photon. Thus SW imaging via inelastic photon-magnon scattering using focused laser light is possible [80, 81]. Figure 2.5 illustrates scattering processes of magnons, where a magnon is either annihilated or created by a photon. This scattering process, where energy and momentum are conserved, are described with an angular frequency ω and

wave vector \mathbf{k} as follows [81]:

$$\begin{aligned} h\omega_{\text{out}} &= h\omega_{\text{in}} + h\omega_{\text{sw}}, & h\mathbf{k}_{\text{out}} &= h\mathbf{k}_{\text{in}} + h\mathbf{k}_{\text{sw}}, & (\text{creation process}) \\ h\omega_{\text{out}} &= h\omega_{\text{in}} - h\omega_{\text{sw}}, & h\mathbf{k}_{\text{out}} &= h\mathbf{k}_{\text{in}} - h\mathbf{k}_{\text{sw}}, & (\text{annihilation process}) \end{aligned} \quad (2.4)$$

where h is the planck constant, and $_{\text{in}}$, $_{\text{out}}$ and $_{\text{sw}}$ denote the incident light, scattered light, and annihilated/created magnon, respectively. $|\omega_{\text{in}} - \omega_{\text{out}}|$ and $|\mathbf{k}_{\text{in}} - \mathbf{k}_{\text{out}}|$ corresponds to the annihilated/created SW frequency and wave vector. Since a number of annihilated/created magnons corresponds to the number of scattered photons, the intensity of the SWs is detected by counting the scattered photons. A scattered photon carries information of the annihilated/created magnon with its phase, and therefore the phase imaging of the corresponding SW modes are also possible by applying microwaves coherently [77, 78].

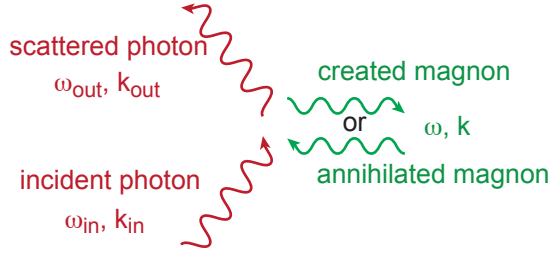


Figure 2.5: Inelastic magnon-photon scattering process. A magnon can be annihilated/created by an incident photon, and the energy and momentum of the scattered photon are gained/lost.

2.2.2 Experimental setup

The BLS system used in this work allows us to resolve the spatial distribution of SWs (space-resolved BLS). In this thesis, microwave-enhanced BLS microscopy (micro-BLS, μ -BLS) is used. Figure 2.6 contains a schematic image of the BLS setup with phase resolution. A CPW integrated to the magnetic nanostructure is placed on a sample stage with a xyz piezo electric positioning system, and the CPW is connected to a signal generator to excite SWs coherently as described in Sect. 2.1. A permanent magnet applies an in-plane magnetic field to the sample, and the amplitude of the field is controlled by a linear motor positioner integrated with the magnet. The polarization of the laser is horizontal in the beginning (s-polarized). An objective lens (Olympus LCPLFLN100xLCD) is installed to focus a laser beam with a wavelength of 473 nm on the sample surface. The polarization of photons is rotated by 90 deg in the inelastic magnon-photon scattering process, i. e., a part of the s-polarized light is rotated at the surface of the magnetic material, and in turn becomes vertically polarized light (p-polarized light). The back-reflected light at the sample surface is composed of s-polarized light and a fraction of p-polarized light due to the elastic and inelastic scattering, respectively. The s-polarized light is reflected by the Glan-Talor prism, and guided to a six path tandem Fabry-Pérot interferometer (table-stable TFPI) integrated with an avalanche photodiode detector. This system allows us to

count photons at specific frequencies shifted from a reference frequency of the laser. Finally, the counted photons are recorded and one obtains a SW spectrum at a specific position of the sample surface. Without applying microwaves, one can obtain the thermal magnon spectrum. By applying microwaves, one can obtain a large peak in the spectrum at the microwave frequency, if the spin precession is resonantly enforced by the microwave magnetic field. The sample is exposed by white light to image the sample surface by a camera. The position of the laser light is scanned in the region of interest (ROI) by moving the sample using the piezo electric positioner to explore SW mode profile [26] or the SW phase evolution. The attenuation length of SWs can be calculated by measuring the SW intensity as a function of position with respect to the SW emitter (i. e., the CPW where microwaves are applied).

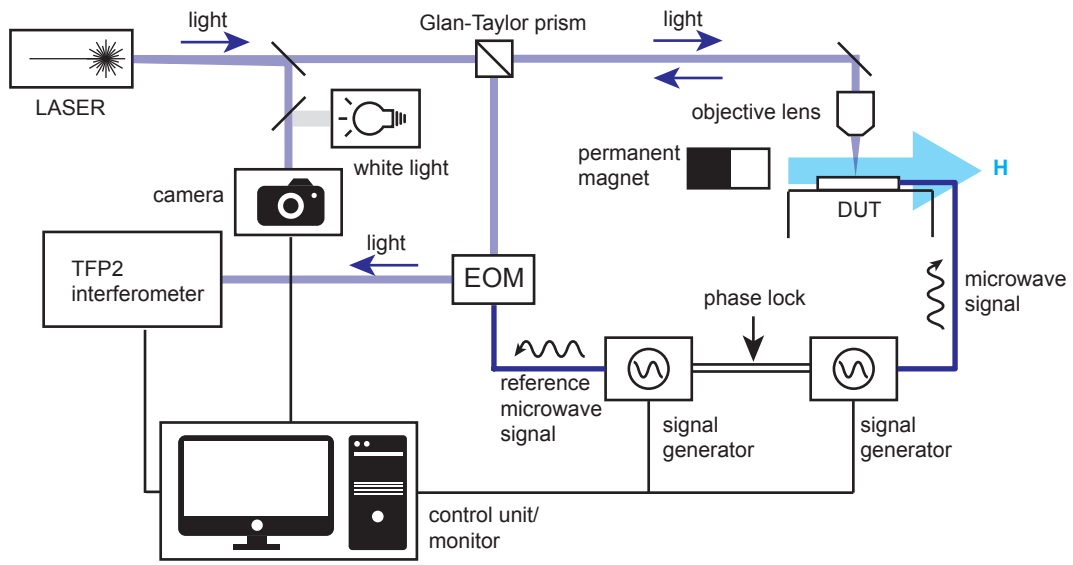


Figure 2.6: Schematic image of BLS experimental setup with phase resolution.

Phase detection: The scattered photon possesses the phase information of the annihilated/created magnon. Here we consider the wave interference between the reference laser light, modulated by an electro-optical modulator (EOM), and inelastically scattered light. The EOM can modulate a part of light at the frequency of the connected signal generator. If the both signal generators connected to the DUT for SW excitation and EOM operate at the same frequency and the phase of microwaves from the both signal generators is locked, the superposition of the modulated reference light I_{eom} and the inelastically scattered light I_{sw} is as follows [78]:

$$I_{\text{tot}}^2 = I_{\text{sw}}^2 + I_{\text{eom}}^2 + 2I_{\text{sw}}I_{\text{eom}}\cos(\phi). \quad (2.5)$$

where ϕ is a phase difference between the I_{sw} and I_{eom} . The phase $\phi(t)$ can be swept as a function of time t using a function generator connected to the signal generator for the EOM. The cosine function of the time-dependent SW spectrum is used for calculating the SW phase $\phi(t_0)$ [82]. The wave vector of SWs can be also calculated from the measured spatially varying SW phase [76, 77].

2.3 X-ray magnetic circular dichroism microscopy

Magneto-optics based techniques such as BLS and magneto-optic Kerr effect (MOKE) based on laser light in the optical regime [83, 84] are restricted in spatial resolution for microscopy to about 250 nm due to the diffraction limit of light. Thus magnetization configurations of magnetic nanostructures and properties of short-wave magnons in exchange interaction regime are hardly resolved or not detected at all. X-rays with a wavelength much smaller than visible light push the resolution for imaging down to about 20 nm when utilizing X-ray magnetic circular dichroism (XMCD) [85, 86].

2.3.1 Background

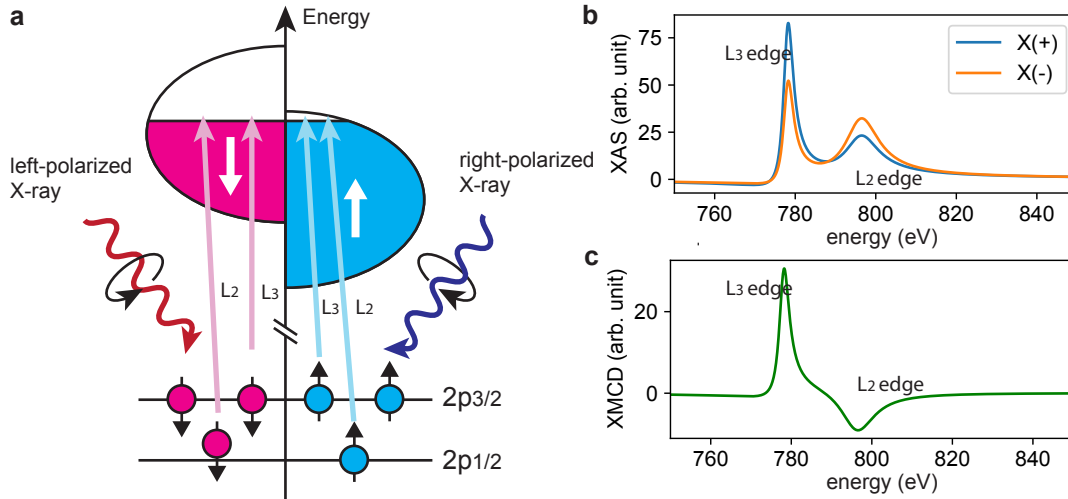


Figure 2.7: (a) Schematic image of electronic transition of up-spin and down-spin into valence states by applying circularly polarized X-ray. Schematic illustration of (b) XAS and (c) XMCD signal on Cobalt.

X-ray absorption spectroscopy (XAS) is a widely used technique to investigate the electronic structure of materials. Linearly polarized X-rays are injected into the material inside which the core electrons are excited into the valence state, and thus an element specific probe is available relevant to the energy of the X-ray. The final states excited by X-ray can decay via Auger electron emission or X-ray fluorescence. Therefore electron as well as ion and X-ray fluorescence yield can be also used to monitor X-ray absorption.

When an electronic band structure of a magnetically ordered material is spin splitted, there is a difference of the density of states at the Fermi level for up-spin and down-spin bands (Fig. 2.7a). Due to the momentum conservation, circularly polarized X-rays can excite either up or down spins, depending on the polarity of the X-rays. The difference of the absorption of circularly polarized X-rays is determined by which spins are dominantly excited into the valence state with respect to the X-ray application direction. Figure 2.7b shows a schematic representation of an XAS spectrum for Co using right- and left-circularly polarized X-rays

($X(+)$ and $X(-)$, respectively). The peaks correspond to the excitation of electrons from $2p_{1/2}$ (L_2 edge) and $2p_{3/2}$ (L_3 edge) orbits. There is a difference of the XAS absorption amplitude between $X(+)$ and $X(-)$. Figure 2.7c shows the XMCD data ($X(+)-X(-)$). For Co, the L_3 edge is useful to determine the direction of magnetization as the XMCD amplitude is large. In the next subsection techniques are discussed by which we investigated the properties of magnetic materials in this thesis.

2.3.2 Techniques

Photo electron emission microscopy: By utilizing Auger electrons, one can conduct photo electron emission microscopy (PEEM) by injecting X-rays on a sample surface. The Auger electrons are collected to image a magnetization configuration of a magnetic material (Fig. 2.8a). This is a surface-sensitive technique, and has a lateral resolution down to sub-100 nm. We performed XMCD-PEEM experiments using the UE49-PGM endstation at Helmholtz Zentrum Berlin to image magnetization configurations of artificial spin ice. The experiments were supported by Dr. Florian Kronast at Helmholtz Zentrum Berlin. The magnetic moments are aligned in-plane, so that the X-ray was applied to the sample with an angle with respect to the sample surface normal.

Scanning transmission X-ray microscopy: Here XMCD is combined with a scanning transmission X-ray microscopy (STXM) technique to spatially resolve the magnetization configuration on the nanometer scale as well as the spin dynamics with time resolution. Here SWs are pumped by applying continuous-wave microwaves into a CPW, and probed by X-ray flashes stroboscopically. X-rays passing through the sample for each point are detected by an avalanche diode (Fig. 2.8b). Sample thinning to form an X-ray transparent window is required. In our study, we collaborated with scientists from Max-Planck-institute and Helmholtz Zentrum Berlin for the X-ray window fabrication and STXM operation using MAXYMUS endstation at Helmholtz Zentrum Berlin. We applied in-plane magnetic fields to excite SWs. STXM detected the out-of-plane dynamic component.

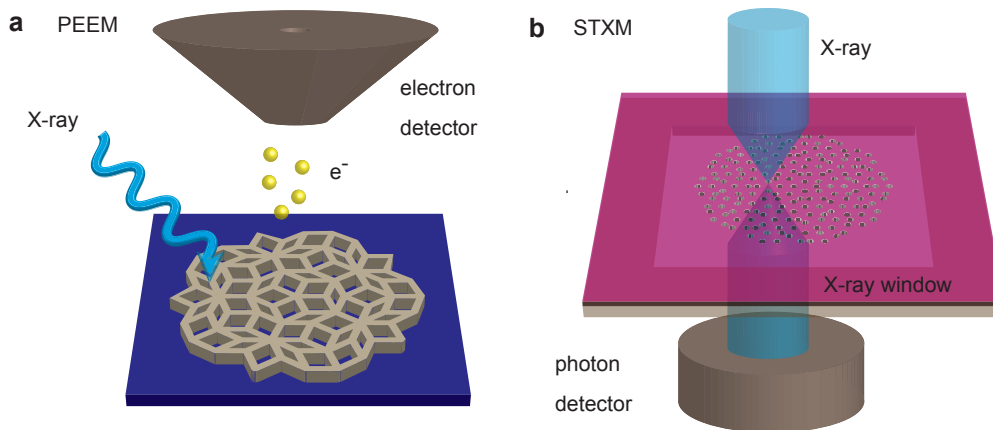


Figure 2.8: Schematic images of (a) PEEM and (b) STXM techniques.

2.4 Micromagnetic simulation

Micromagnetic simulation is a powerful tool to predict and investigate the static magnetic configuration of micro- and nanostructures as well as the spin dynamics [87]. In this thesis we employed two simulation software packages using a finite discretization method (FDM) in 2D and 3D: the Object Oriented MicroMagnetic Framework (OOMMF) [88] for Sect. 4.1 and Sect. 7.1 and MuMax3 [89] for Sect. 6.1. A discretized image corresponding to an investigated magnetic nanostructure is prepared, and material parameters such as saturation magnetization M_s , gyromagnetic ratio γ , exchange constant A_{ex} as well as a cell size are considered. Magnetic moments for each simulated cell are considered as a giant Ising spin, and thus the size of a cell should be smaller than the exchange length of the simulated material (typically a few nm - 10 nm). Within each cuboid cell, the magnitude of magnetization \mathbf{M} is assumed to be constant. The magnetization configuration can be either random or defined at first, and one collects the equilibrium magnetization with or without considering an applied magnetic field \mathbf{H} using the gradient descent method (GDM). In the GDM one assumes that a system evolves along a path which minimizes the total energy of the system. This process is iterated until the $\mathbf{M} \times (\mathbf{M} \times \mathbf{H}_{\text{eff}})$ goes below a certain value (e.g., 0.1 A/m for our simulation using the OOMMF software package).

The dynamics of magnetization can be recorded as a function of time t by calculating LLG equation (Eq. 1.12). One often applies a pulse of magnetic field instead of applying a continuous-wave microwave signal at a specific frequency in order to save simulation time in case of low computational power. The magnetization dynamics with a discrete step of Δt_{step} (e.g., 20 ps) is recorded after applying a pulse, and a fast Fourier transformation (FFT) in time is performed for each cell in order to obtain the amplitude and phase of the magnetization precession in the frequency domain. For the calculation of spin dynamics CoFeB based artificial magnetic quasicrystals (AMQs) in Sect. 4.1, we prepared a bitmap image of the quasicrystal with a discretized grid of 10 nm \times 10 nm \times 19 nm to import into OOMMF. We applied a global in-plane magnetic field of 90 mT, and equilibrium magnetization configuration was determined. Afterwards we applied a spatially homogeneous gaussian pulse $A \exp(-(t - t_0)^2 / (\Delta t)^2)$ with an amplitude $A = 20$ mT, an offset $t_0 = 100$ ps and a duration $\Delta t = 2.5$ ps for along out-of-plane direction. A FFT on the gaussian pulse provides an almost equal contribution of the field strength to all the frequencies up to 26.5 GHz. We performed FFT on the magnetization components for each pixel to obtain SW resonance spectrum and spatial distribution of SWs on the AMQs. Note that we set the temperature 0 K (thermal fluctuations were not considered.)

3 Sample fabrication

Nanofabrication techniques allow us to explore SW properties of artificially engineered magnetic nanostructures via a material-by-design approach. The functionality of a magnetic crystal/quasicrystal as well as artificial spin ice and grating couplers from the SW dynamics perspective strongly depends on (i) the material and (ii) the design of nanostructures. We first discuss the magnetic properties of important materials for the exploration of magnetic nanostructures, and then introduce fabrication techniques with equipment used in the Center of MicroNano Technology (CMi), the clean room facility at EPFL where we mostly fabricated samples. The detailed fabrication process for each nanostructure is also described.

3.1 Magnetic materials

Permalloy (Py) [90, 91], an alloy made of 81% nickel and 19% iron with saturation magnetization of 1 T, is commonly used in the field of magnonics. This soft magnetic material possesses no magnetocrystalline anisotropy as well as no magnetostriction at room temperature. On the contrary, Ni has a magnetostriction [92, 93, 94], which may induce a coupling of phonons with magnons. Ni has a saturation magnetization 0.6 T with a damping constant ~ 0.03 [92, 95], which is higher than the damping constant of Py ($\alpha = 0.008$) [91]. An amorphous alloy $\text{Co}_{20}\text{Fe}_{60}\text{B}_{20}$ (CoFeB) [72, 94, 96, 97] possesses higher saturation magnetization of $\mu_0 M_s = 1.8$ T. For the SW excitation in the dipolar regime where anisotropic dispersion relations are exhibited, well-distinguished SW resonances for different directional properties of SWs are expected in CoFeB due to its high saturation magnetization value. The amorphous CoFeB with low damping ($\alpha = 0.007$) ensures a long SW lifetime [72]. Single crystalline Yttrium iron garnet ($\text{Y}_3\text{Fe}_5\text{O}_{12}$, YIG) [5, 98, 99, 100] is difficult to be grown with high crystalline quality. We investigated the magnetic properties of the single crystalline YIG thin films grown on Gadolinium Gallium Garnet (GGG) substrate supplied from Matesy GmbH in Jena, Germany and INNOVENT e.V. in Jena, Germany using Liquid-phase epitaxy (LPE). Despite the challenging nanofabrication of the insulator YIG, it is considered as the promising material in the field of magnonics. High-quality single crystalline YIG ensures a small number of inhomogeneities, reducing scattering of spin waves. The damping coefficient of thin-film YIG is

very low ($\sim 10^{-4}$) and enables a long decay length of spin waves. This aspect boosts further development in magnonic circuit technologies for information processing. Due to its magnetostriction, magnons in YIG would be coupled to phonons [101]. The parameters of magnetic materials is summarized in Tab. 3.1. In this thesis work, both Py and Ni were grown by electron beam physical vapor deposition technique using Leybold Optics LAB 600H and CoFeB thin films were grown by magnetron sputtering using Alliance-Concept DP 650 installed in CMi.

Table 3.1: **Parameters of magnetic materials at room temperature**

material	saturation magnetization M_s (T)	damping constant α	Crystallinity
Ni	0.6 T	0.03 [95]	polycrystalline
Py	1.0 T	0.008 [91]	polycrystalline
CoFeB	1.8 T	0.007 [96]	amorphous
YIG	0.176 T	2.3×10^{-4} [98]	single crystalline

Summary of parameters of magnetic materials used in this thesis.

3.2 Nanofabrication

Nanopatterning of artificial magnetic materials is realized by electron beam (e-beam) lithography. The Raith EBPG5000 Ebeam tool allows for e-beam writing smaller than 10 nm and placing the patterns on a substrate with an accuracy less than 20 nm. This system uses a focused beam of electrons by which we expose an electron-sensitive resist with either positive tone or negative tone. A thickness of a positive resist bilayer MMA (methyl methacrylate)/PMMA (poly methyl methacrylate) on a substrate is defined by the rotation speed of the spin coating equipment. The focused e-beam breaks long polymer chains of carbon atoms in the MMA/PMMA bilayer, and the resist of the exposed patterns is dissolved by a development process using a developer consisting of methyl isobutyl ketone (MiBK) and isopropyl alcohol (IPA). After the metal evaporation process on the developed substrate, the substrate is washed by acetone, and patterned magnetic nanostructures such as artificial spin ice as well as grating coupler elements are fabricated. Oxygen plasma etching (equipment: Tepla GiGAbatch) is conducted to remove residuals of MMA after the development process as well as sample surface cleaning before the resist coating. Note that insulating substrates, e.g., a YIG thin film, need to have a conductive layer, e.g., 10 nm-thick Au, on the positive resist in order to avoid the surface charging and e-beam defocusing.

An etching process allows one to fabricate nanostructures from already deposited magnetic materials such as YIG thin films grown by external suppliers. Using the e-beam tool, we patterned a hard mask made of either positive resist CSAR-62 (main component: poly(α -methylstyrene-co-methyl chloroacrylate)) or negative resist (Hydrogen silsesquioxane, HSQ) on a substrate. The mask fabrication process using CSAR-62 was almost the same as the e-beam writing process on the MMA/PMMA. In contrast to the positive resist, exposed HSQ turned into SiO_2 and remained on the substrate after the development with an MF-CD-26 developer. This hard mask protected the substrate against ion-beam etching (equipment: Veeco Nexus IBE350) as well as material selective inductively coupled plasma (ICP) etching

(equipment: STS Multiplex ICP). The e-beam unexposed area was etched away. We used 1 % diluted Hydrogen fluoride (HF) for the removal of the hard mask.

3.3 Process flow

The type of fabrication of magnetic nanostructures is classified concerning etching process and lift-off processing. Via the etching process artificial magnetic quasicrystals made of CoFeB in Sec. 4.1 and magnonic quasicrystals made of YIG in Sec. 5.1 and Sec. 5.2 were fabricated. Grating elements made of Py on YIG thin films in Sec. 6.1, artificial spin ices made of Py nanobars on a Si wafer in Sec. 7.1 and Ni nanobars on YIG thin films in Sec. 7.2 were fabricated using lift-off processing. Below the sample fabrication steps are described.

3.3.1 Etching process

Nanohole-based artificial magnetic quasicrystal made of CoFeB

1. Sputter CoFeB (19 nm) using DP 650 sputter system for 600 sec on a Si wafer.
2. Spin coat HSQ on the Si wafer to obtain the thickness of 40 nm and bake it for 5 min at 180 deg.
3. Expose e-beam on the HSQ coated Si wafer (Fig. 3.1a).
4. Immerse the Si wafer into MF-CD-26 for 90 sec to develop HSQ, and rinse the substrate with DI water (Fig. 3.1b).
5. Mil the exposed HSQ/CoFeB pattern on the Si wafer using NEXUS IBE 350 (Fig. 3.1c).
6. Finish (Fig. 3.1d)

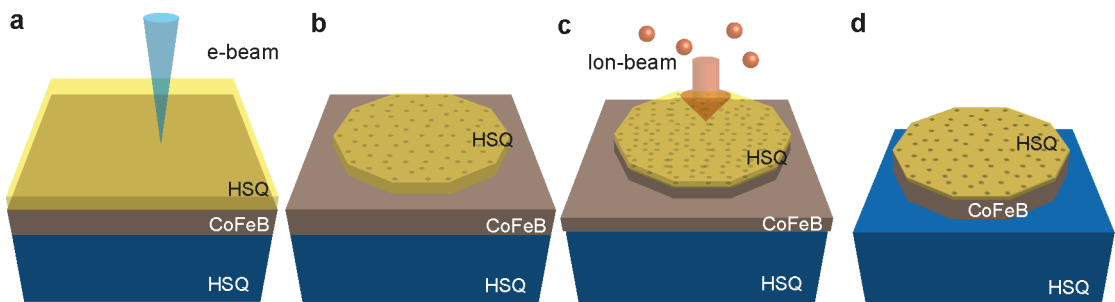


Figure 3.1: Schematic images of the fabrication process of nanohole-based artificial magnetic quasicrystals made of CoFeB. (a) E-beam exposure on an HSQ coated CoFeB thin film on a Si wafer. (b) Developed HSQ mask on the CoFeB thin film. (c) Ion-beam etching process to fabricate (d) the artificial magnetic quasicrystal.

Nanotrough-based magnonic quasicrystal made of YIG for broadband spectroscopy and μ -BLS

1. Cleaning a GGG/YIG substrate by oxygen plasma etching process for 30 sec.
2. Evaporate Al/Ti (10/200 nm) on the GGG/YIG substrate using LAB 600H.
3. Spin coat HSQ on the substrate to obtain the thickness of 150 nm.
4. Expose e-beam on the HSQ coated GGG/YIG substrate (Fig. 3.2a).
5. Immerse the GGG/YIG substrate into MF-CD-26 for 30 sec to develop HSQ, and rinse it with DI water (Fig. 3.2b).
6. ICP Etch Al/Ti by STS multiplexer to form a mask of the quasicrystal patterns made of Ti (Fig. 3.2c).
7. Mill the exposed YIG/Al/Ti/HSQ pattern by ion-beam etching process using NEXUS IBE 350 (Fig. 3.2d and e).
8. Immerse the substrate into HF bath for 15 sec to etch out the Al/Ti mask.
9. Finish (Fig. 3.2f)

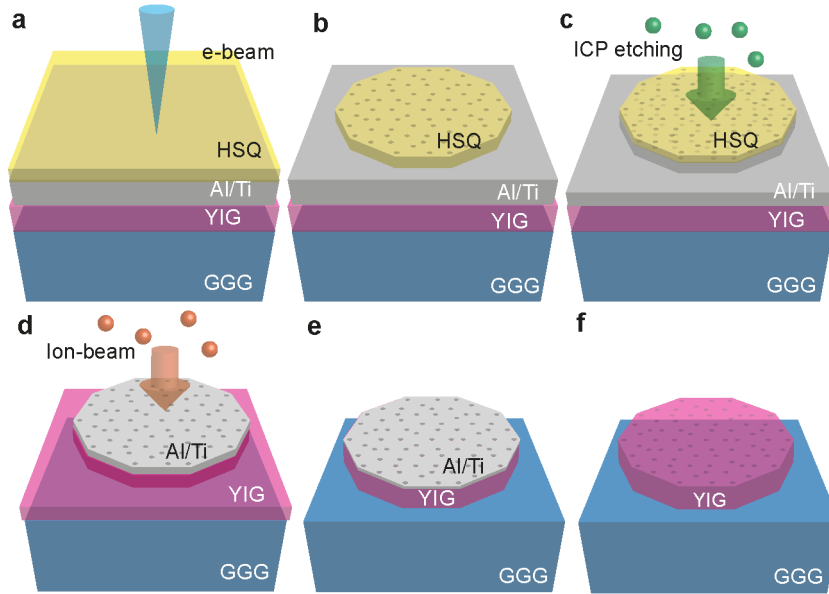


Figure 3.2: Schematic images of the fabrication process of nanotrough-based magnonic quasicrystals made of YIG. (a) E-beam exposure on an HSQ coated YIG/Al/Ti thin film on a GGG chip. (b) Developed HSQ mask on the YIG/Ti/Al thin film. (c) ICP etching process to form a Ti mask. (d) Ion-beam etching process to fabricate (e) the magnonic quasicrystal. (f) Magnonic quasicrystal after the removal of Al/Ti mask by HF etching.

Nanotrough-based magnonic quasicrystal made of YIG for STXM

1. Cleaning a GGG/YIG substrate by oxygen plasma etching process for 30 sec.
2. Evaporate Al/Ti (10/200 nm) on the GGG/YIG substrate using LAB 600H.
3. Spin coat CSAR-62 on the substrate to obtain the thickness of 125 nm and bake it for

- 5 min at 180 deg.
4. Expose e-beam on the HSQ coated GGG/YIG substrate (Fig. 3.3a).
5. Immerse the substrate into Amyl-Acetate for 2 mins for the development, and rinse it with MiBK:IPA solvent (mixing ratio 90:10) for 1 min (Fig. 3.3b).
6. Etch CSAR residuals by oxygen plasma cleaning for 10 sec.
7. ICP Etch Al/Ti by STS multiplexer to form a mask of the quasicrystal patterns made of Ti (Fig. 3.3c).
8. Mill the exposed YIG/Al/Ti/CSAR pattern on the chip using by ion-beam etching process using NEXUS IBE 350 (Fig. 3.3d and e).
9. Immerse the substrate into HF bath for 15 sec to etch out the Al/Ti mask (Fig. 3.3f).
10. Finish (Fig. 3.3f)

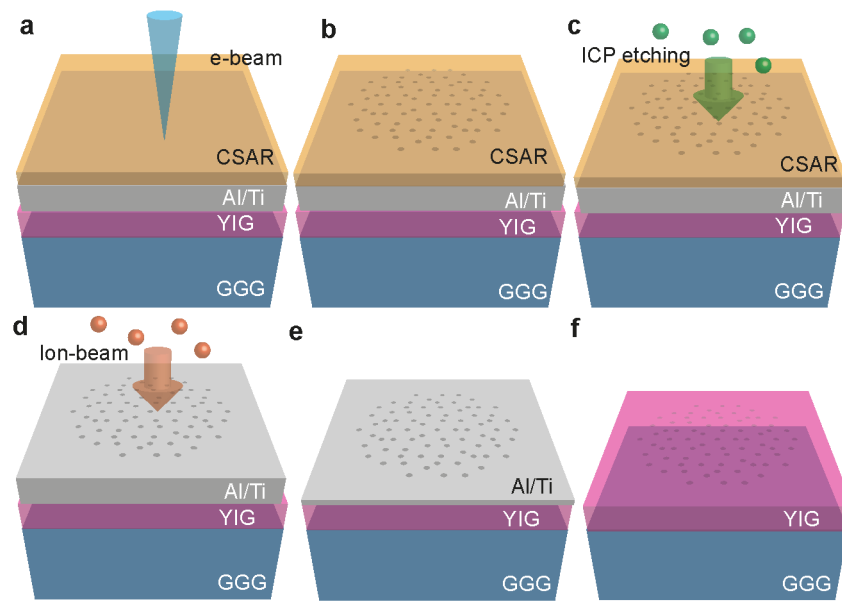


Figure 3.3: Schematic images of the fabrication process of nanotrough-based magnonic quasicrystals made of YIG. (a) E-beam exposure on a CSAR-62 coated YIG/Al/Ti thin film on a GGG chip. (b) Developed CSAR-62 mask on the YIG/Ti/Al thin film. (c) ICP etching process to form a Ti mask. (d) Ion-beam etching process to fabricate (e) the magnonic quasicrystal. (f) Magnonic quasicrystal after the removal of Al/Ti mask by HF etching.

3.3.2 Lift-off processing

Aperiodically arranged nanograting couplers made of Py nanopillars on a YIG film

1. Cleaning a GGG/YIG substrate by oxygen plasma etching process for 30 sec.
2. Spin coat MMA EL9/ PMMA 495 K bilayer positive resist on a YIG chip to obtain the thickness of 440/210 nm, respectively.
3. Sputter Au (10 nm) using DP650 sputtering system.
4. Expose e-beam on the MMA/ PMMA coated substrate (Fig. 3.4a).

Chapter 3. Sample fabrication

5. Au etching at wet bench.
6. Immerse the substrate into MiBK:IPA (mixing ratio 1:3) solvent for 1 min for the development, and rinse it with IPA for 1 min (Fig. 3.4b).
7. Etch MMA residuals by oxygen plasma cleaning for 10 sec.
8. Evaporate Py (100 nm) using LAB600H evaporator (Fig. 3.4c).
9. Immerse the substrate into Acetone until the lift-process is finished, and then wash it by DI water.
10. Finish (Fig. 3.4d).

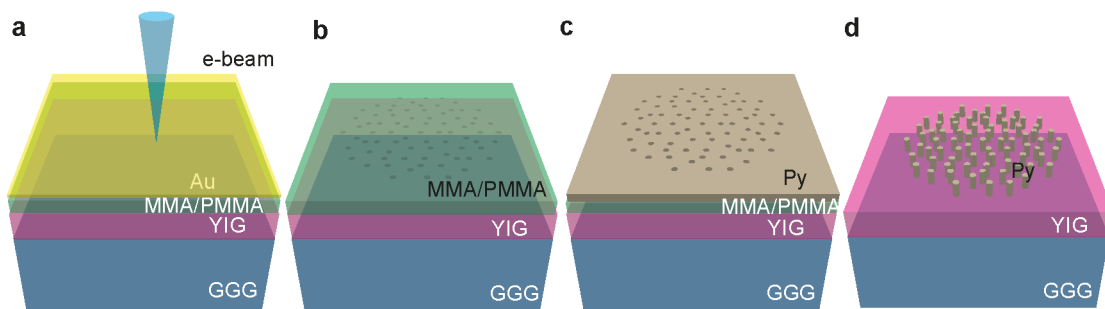


Figure 3.4: Schematic images of the fabrication process of magnonic grating couplers made of Py on a YIG thin film. (a) E-beam exposure on a MMA/PMMA coated YIG/GGG substrate with an Au conductive layer. (b) Developed MMA/PMMA positive resist. (c) Py evaporated onto GGG/YIG substrate with MMA/PMMA positive resist. (d) Magnonic grating couplers on the YIG thin film after lift-off processing.

Artificial spin ice made of Py nanobars on a Si wafer

1. Spin coat MMA EL9/ PMMA 495 K bilayer positive resist on a Si wafer to obtain the thickness of 440/210 nm.
2. Expose e-beam on the MMA/PMMA coated Si wafer (Fig. 3.5a).
3. Immerse the chip into MiBK:IPA (mixing ratio 1:3) solvent for 1 min for the development, and rinse the wafer with IPA for 1 min (Fig. 3.5b).
4. Evaporate Py/Al (25/3 nm) using LAB600H evaporator (Fig. 3.5c).
5. Immerse the wafer into Acetone until the lift-process is finished, and then wash the wafer with DI water.
6. Finish (Fig. 3.5d).

Artificial spin ice made of Ni nanobars on a YIG film

1. Cleaning a GGG/YIG substrate by oxygen plasma etching process for 1 min.
2. Spin coat MMA EL9/ PMMA 495 K bilayer positive resist on a YIG chip to obtain the thickness of 440/210 nm.
3. Sputter Au (10 nm) using DP650 sputtering system.

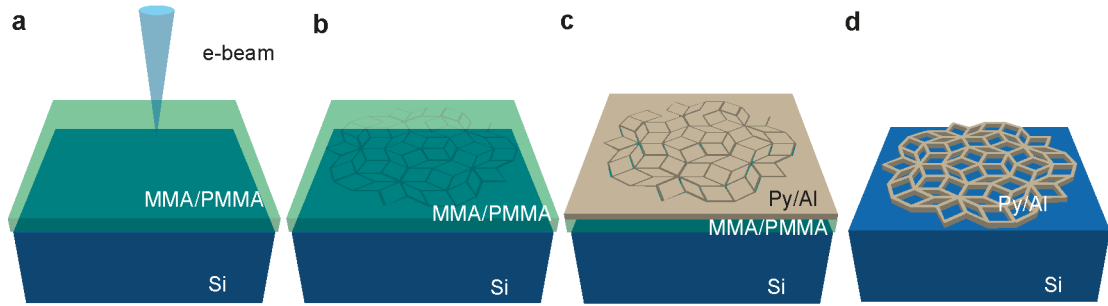


Figure 3.5: Schematic images of the fabrication process of artificial spin ice made of Py nano-bars. (a) E-beam exposure on a MMA/PMMA coated Si wafer. (b) Developed MMA/PMMA positive resist. (c) Py/Al evaporated on Si wafer with MMA/PMMA positive resist. (d) Artificial spin ice after the lift-off processing.

4. Expose e-beam on the MMA/ PMMA coated substrate (Fig. 3.6a).
5. Au etching at wet bench.
6. Immerse the chip into MiBK:IPA (1:3) solvent for 1 min for development, and rinse the chip with IPA for 1 min (Fig. 3.6b).
7. Etch MMA residuals by oxygen plasma cleaning for 10 sec.
8. Evaporate Ni (25 nm) using LAB600H evaporator (Fig. 3.6c).
9. Immerse the substrate into Acetone until the lift-process is finished, and then wash it with DI water.
10. Deposit Al_2O_3 to obtain a thickness of 37 nm using Atomic Layer Deposition BENEQ TFS200.
11. Finish (Fig. 3.6d).

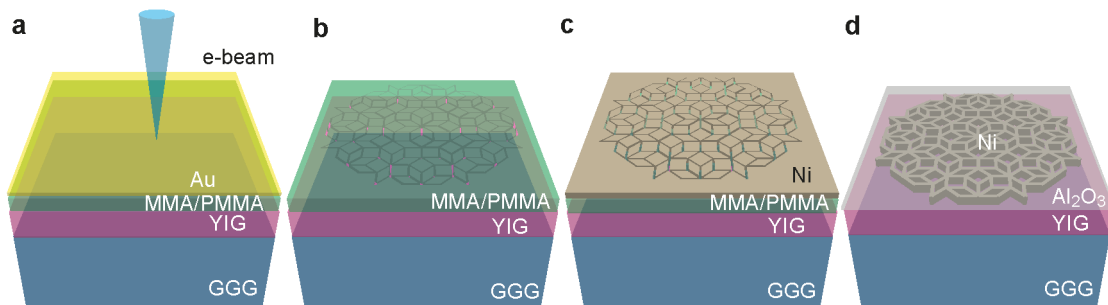


Figure 3.6: Schematic images of the fabrication process of artificial spin ice made of Ni on a YIG thin film. (a) E-beam exposure on a MMA/PMMA coated YIG/GGG substrate with an Au conductive layer. (b) Developed MMA/PMMA positive resist. (c) Ni evaporated GGG/YIG substrate with MMA/PMMA positive resist. (d) Artificial spin ice on the YIG thin film coated by Al_2O_3 .

Results and Discussion Part II

4 Worms and magnonic motifs in artificial ferromagnetic quasicrystals

Periodically arranged magnetic metamaterials, called magnonic crystals (MCs) [7] such as periodic antidot lattices (ADLs) with translational symmetry allow for tailoring the band structure for SWs [10, 11], and they offer multiple SW branches which have different directional properties of SWs due to the demagnetization field induced by nanoholes [14, 15, 62, 102]. Aperiodically arranged antidots based on the magnetic materials would provide different spatial distributions of SWs characterized by the position of nanoholes [30, 103].

In this chapter, we report new types of SW properties, i.e., magnon mode motifs and worm-like nanochannels, emerged in nanohole-based ferromagnetic CoFeB [72, 104] quasicrystals arranged on the Penrose P2 and P3 lattices [32]. We found magnonic mode motifs arising from the geometrical repetitive patches of the quasicrystalline structures. The aperiodic sequences of bends (Fibonacci sequences) gave rise to different wavelengths in the nanochannels and enabled a dense-wavelength division multiplexer (DWDM). This work appeared in *Advanced Functional Materials* [31].

4.1 Direct Observation of Worm-Like Nanochannels and Emergent Magnon Motifs in Artificial Ferromagnetic Quasicrystals

S. Watanabe, V. S. Bhat, K. Baumgaertl and D. Grundler

Adv. Funct. Mater., vol. 30, issue 36, 2001388 (2020).

doi.org/10.1002/adfm.202001388

Reproduced from *Adv. Funct. Mater.*, 30, 36, 2001388 (2020) with permission from Wiley. The layout of the manuscript was reformatted and the references were integrated into the thesis' bibliography. There is an additional term "(i.e., the total lateral size)" to clarify the meaning of "generation" in the introduction part in the following section.

Contribution I contributed to the manuscript as follows: Sample design preparation and experiments helped from K. B. Experimental and simulation data analysis together with V. S. B. and D. G. Note that micromagnetic simulation was performed by V. S. B.

Abstract

Quasicrystalline structures and aperiodic metamaterials find applications ranging from established consumer gadgets to potential high-tech photonic components owing to both complex arrangements of constituents and exotic rotational symmetries. Magnonics is an evolving branch of magnetism research where information is transported via magnetization oscillations (magnons). Their control and manipulation are so far best accomplished in periodic metamaterials which exhibit properties artificially modulated on the nanoscale. They give rise to functional components, such as band stop filters, magnonic transistors and nanograting couplers. Here, spin-wave excitations in artificial ferromagnetic quasicrystals created via aperiodic arrangement of nanoholes are studied experimentally. Their ten-fold rotational symmetry results in multiplexed magnonic nanochannels, suggesting a width down to 50 nm inside a so-called Conway worm. Key elements of design are emergent magnon motifs and the worm-like features which are scale-invariant and not present in the periodic metamaterials. By imaging wavefronts in quasicrystals, insight is gained into how the discovered features materialize as a dense wavelength division multiplexer.

Main Part

Introduction

Quasicrystals [105] are long-range ordered materials that exhibit aperiodicity and rotational symmetry forbidden in conventional crystals. [106] Aperiodicity makes the understanding of wave propagation a complex challenge as the Bloch theorem cannot be applied to quasicrystals. [107] Similar challenges exist for understanding their perfect growth and the generation of defects along the so-called Conway worms, that is, characteristic chains of tiles in 2D quasicrystals.[108, 109] The underlying mathematical concepts[33, 110, 111] and state-of-the-art nanofabrication techniques allow researchers nowadays to explore aperiodicity-induced effects based on a materials-by-design approach.[112] In photonics, artificial quasicrystals composed from nanoholes in thin dielectrics provoked distinct optical responses offering advanced manipulation of light waves.[35, 113, 114] In magnonics,[7] an evolving branch of magnetism exploring spin waves (SWs, magnons) to transmit and process information, periodically modulated magnetic materials have been explored to modify SWs and contributed to the realization of miniaturized microwave devices offering GHz signal processing. [4, 54] Magnonic crystals tailored the band structure of SWs and allowed one to create band stop filters. [7] Via non-linear magnon–magnon scattering in a magnonic crystal, all-magnon based information processing was realized. [115] Periodically arranged nanostructures on ferromagnetic thin films performed as microwave-to-magnon transducers. They provided reciprocal lattice vectors \mathbf{G} allowing to shorten wavelengths of microwave signals by several orders of magnitude.[16, 17]

There is a great interest in studying static and microwave magnetodynamics in artificial qua-

4.1 Direct Observation of Worm-Like Nanochannels and Emergent Magnon Motifs in Artificial Ferromagnetic Quasicrystals

quasicrystal spin ices made of connected or disconnected nanobars on Penrose and Ammann quasicrystal lattices.[73, 116, 117] From a fundamental physics perspective, quasicrystal artificial spin ices help towards answering the long-standing fundamental question of how aperiodicity influences the static and dynamic magnetic properties. From an application perspective, one of the main foci of the study of aperiodic quasicrystal spin ices is towards fabricating magnonic crystals with complete band gaps and omnidirectional grating couplers, enabled by the manifold rotational symmetries which go beyond the so far exploited periodic Bravais lattices. [16, 115] The arrays of circular nanoholes, in comparison to nanobar-based quasicrystal arrays, may offer distinct and additional insights into the aperiodic nature and related magnonics applications because of the following aspects: (1) the isotropic characteristics offered by a circularly shaped basis (via circular holes) as opposed to the two-fold symmetry of the nanobars; (2) interaction among nanobars greatly diminishes for separation greater than 100 nm, thereby making any aperiodic interaction driven application challenging to implement. Irregularities in nanobar shape, size, and placement greatly influence the underlying physical phenomena under investigation. The nanoholes offer enhanced domain wall pinning, [118] thereby causing an increased switching field, resulting in an increased stability of a device against magnetic field disturbances. Various shapes of holes have been studied on different periodic lattices, such as square shaped and circular holes on a square lattice. [102, 119, 120] Periodic hole lattices support two prominent types of spin-wave mode patterns: localized (confined) and de-localized modes which can form nanochannels [102] and artificially tailored magnonic minibands. [10, 11] The localized mode patterns occur in the directions perpendicular to the magnetic field and are mostly concentrated at edges of holes (edge modes) or between any two given holes (confined modes). The de-localized modes are connected throughout the ferromagnetic matrix between holes and are perpendicular to the magnetic field direction. These mode patterns appear in a periodic arrangement throughout the lattice. Spin-wave nanochannels exhibit periodically modulated widths. Antidot lattices consisting of periodically arranged holes have hence been investigated thoroughly. Experimental studies on hole arrays with a quasicrystalline arrangement are however missing. Relaxing the condition of periodicity allows one to directly probe the effect of aperiodicity on such type of patterns and explore their possible application (as reported in this article) due to increased spatial and rotational degrees of freedom. In contrast to photonics and plasmonics, [35, 113, 114] experimental studies on artificial ferromagnetic quasicrystals (AMQs) [30] which offer unconventional rotational symmetries and a great density of reciprocal vectors are in their infancy. [103, 117, 121] Corresponding dynamic magnetic responses in 2D quasicrystals have neither been classified nor fully exploited in view of manipulation and control of magnons.

In this paper, we report combined broadband SW spectroscopy, spatially resolved inelastic (Brillouin) light scattering (BLS) and micromagnetic simulations performed on 2D AMQs (Figure 4.1a,b). They were prepared from ferromagnetic $\text{Co}_{20}\text{Fe}_{60}\text{B}_{20}$ (CoFeB) thin films by etching out circular nanoholes on the vertices of Penrose P2 and P3 quasicrystalline tilings

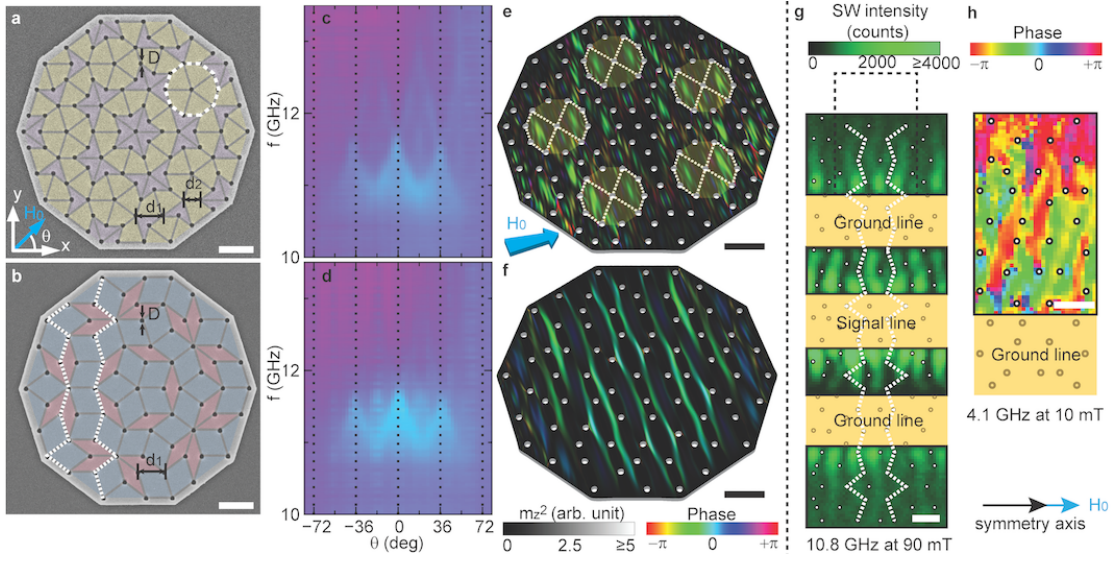


Figure 4.1: Scanning electron microscopy images of circular nanoholes (dark) patterned on a) Penrose P2 and b) Penrose P3 quasicrystal lattices. The white dotted line in (a) highlights a geometrical motif. The nanoholes are located at the vertices of (a) kites (yellow) and darts (purple), and (b) thick (blue) and thin (pink) rhombi. Colormaps showing experimental angular dependent SW spectra taken on 5th generation (with $D \approx 135$ nm) of c) Penrose P2 and d) Penrose P3 AMQs at $\mu_0 H_0 = 90$ mT. The cyan color indicates resonant absorption (SW modes). Simulated local power map of spinprecessional motion overlaid on top of corresponding phase maps for nanoholes with $D = 135$ nm on 3rd generation e) Penrose P2 (at $f = 11.72$ GHz) and f) Penrose P3 AMQ (at $f = 10.74$ GHz). The field of 90 mT was applied under $\theta = 18$ deg. White dashed lines and semitransparent yellow colored decagons illustrate mirror-symmetric SW motifs arising in the Penrose P2 AMQ in (e). The saturation (gray) and hue color scales in the legend indicate the simulated local power (m_z^2) and phase, respectively, for assumed uniform excitation (standing spin waves). g) Spatial distribution of spin precession (power map) excited at $f = 10.8$ GHz and imaged on a 9th generation Penrose P3 AMQ with $D = 163$ nm. The field of 90 mT was applied along a symmetry axis ($\theta = 0$ deg). Green (black) represents large (small) spin-precessional cone angle. h) Spatially resolved SW phase at $f = 4.1$ GHz propagating in $+y$ -direction in the quasicrystal (hue color) when excited inhomogeneously by the microwave antenna. The field of 10 mT was applied along the symmetry axis ($\theta = 0$ deg). Conway worms are indicated by white dotted lines in (b) and (g). Scale bars indicate $1 \mu\text{m}$.

[32, 122] (Figure 4.1 - A.3, Supporting Information). The CoFeB material was amorphous and magnetically isotropic. We prepared lattices of different generations (Experimental Section), that is, lateral extensions, and with mainly two different nanohole diameters D (Table 1). The arrangement of holes followed characteristic geometrical motifs that exhibited a long range order with ten-fold rotational symmetry. In Figure 4.1a one motif consists of a decagon (highlighted by a white dotted line) for which a central hole is surrounded by ten holes. The variation of the angle θ of an applied in-plane magnetic field H_0 induced SW branches of resonant microwave absorption that exhibited ten-fold angular symmetry (Fig-

4.1 Direct Observation of Worm-Like Nanochannels and Emergent Magnon Motifs in Artificial Ferromagnetic Quasicrystals

ure 4.1c,d). This symmetry is not known from periodic lattices with translational invariance and substantiates the quasicrystalline nature of the nanohole lattices. At fixed θ we observe multiple SW branches in experiments and simulations. We identify spin precession in fundamental motifs (Figure 4.1e) that do not depend on the generation (i.e., the total lateral size) and are distinctly different from the geometrical ones forming the tilings. Moreover, the aperiodic nanoholes give rise to stripe-like excitations in simulations (Figure 4.1f) and experiments (Figure 4.1g). These magnon nanochannels incorporate aperiodic sequences of bends. This aperiodicity is not known from previously investigated periodic hole lattices and might generate magnon band structures that vary from channel to channel, contrary to periodic counterparts. [102] The discovered aperiodic sequences of bends are similar to the Conway worms (white dotted lines in Figure 4.1b,g) which represent an established mathematical concept when modeling quasicrystals. These worms form aperiodic Fibonacci chains in the 2D Penrose tilings. [33, 110, 111] By BLS we obtain direct images of propagating magnons (Figure 4.1h) that exhibit irregular wavefronts across neighboring nanochannels which change with magnon frequency. These real-space images taken on a 2D analogue of a natural quasicrystal [122] thereby provide fundamental insight into the formation of wave-like states in quasicrystalline matter. The discovered magnon modes fuel a new class of metamaterials by which irregular worm-like channels transform into a real-world application such as a dense wavelength division multiplexer (DWDM). Going beyond photonics, the magnonic DWDM is ultra-compact, reconfigurable via a rotating field and driven by an electromagnetic wave at a single input frequency.

Result and Discussion

Standing Spin Waves in Artificial Ferromagnetic Quasicrystal

SW spectroscopy was performed by a vector network analyzer connected to a coplanar waveguide (CPW) integrated on top of ten nominally identical AMQs of a given generation (Figure A.2, Supporting Information). Penrose P2 and P3 AMQs (Figure 4.1a,b, and Table 1) both have ten-fold rotational symmetry but exhibit distinct differences concerning the prototiles used to construct them. In a P2 tiling (Figure 4.1a) the seed tiles are a kite and a dart. In a P3 tiling (Figure 4.1b) one considers thick and thin rhombi, [33] forming a 2D analogue of a natural icosahedral quasicrystal. [33] Two inter-vertex distances are present in a P2 tiling (we used $d_1 = 810$ nm and $d_2 = 500$ nm) as opposed to only one inter-vertex distance in Penrose P3 tiling (we used $d_1 = 810$ nm). The P2 tiling incorporates a lattice point (nanohole) density that is larger by 62% compared to P3. For the nanofabrication we kept the inter-vertex distances constant (see above) and thereby created AMQs covering larger and larger areas from generation to generation (Table 1). Figure 4.1a,b (Figure 4.1c,d) refer to AMQs P2_SH_3rdGen and P3_SH_3rdGen (P2_SH_5thGen and P3_SH_5thGen), respectively, with nanoholes (H) of small (S) diameter $D \approx 135$ nm located at the vertices of 3rd (5th) generation (AMQs of 5th generation P2 and P3 tilings are shown in Figure A.1, Supporting Information). The angle-dependent SW spectra in Figure 4.1c,d evidence magnetic anisotropy [1] and a tenfold rotational symmetry.

Chapter 4. Worms and magnonic motifs in artificial ferromagnetic quasicrystals

Table 4.1: The CoFeB films were 19 nm thick. The overall area of AMQs increases with the generation. Up to 5th generation, the CPW's signal line width was adjusted to fully cover the AMQs. Errorbars of diameter D of nanoholes indicate the 95% confidence interval of the diameters of ten nanoholes which were randomly chosen from the respective microscopy image.

Sample Name	Lattice	Generation	Area (μm^2)	Diameter D (nm)	Number of nanoholes
P2_S_3	P2	3rd	7.0×7.4	134 ± 6	121
P2_L_3	P2	3rd	7.0×7.4	227 ± 5	121
P2_S_4	P2	4th	11.0×11.6	137 ± 7	301
P2_L_4	P2	4th	11.0×11.6	216 ± 3	301
P2_S_5	P2	5th	17.5×18.5	144 ± 15	761
P2_L_5	P2	5th	17.5×18.5	215 ± 13	761
P2_S_9 ^{a)}	P2	9th	117.5×123.6	159 ± 6	34101
P2_L_9 ^{a)}	P2	9th	117.5×123.6	242 ± 6	34101
P3_S_3	P3	3rd	7.0×7.4	134 ± 6	76
P3_L_3	P3	3rd	7.0×7.4	219 ± 5	76
P3_S_4	P3	4th	11.0×11.6	133 ± 11	191
P3_L_4	P3	4th	11.0×11.6	218 ± 7	191
P3_S_5	P3	5th	17.5×18.5	137 ± 9	476
P3_L_5	P3	5th	17.5×18.5	221 ± 12	476
P3_S_9 ^{a)}	P3	9th	117.5×123.6	163 ± 5	21106
P3_L_9 ^{a)}	P3	9th	117.5×123.6	234 ± 4	21106

^{a)} The CPW signal line width was two microns and smaller than the lateral extension of the AMQ in case of 9th generation.

This rotational symmetry is expected for an infinitely large Penrose lattice. The pronounced variation of resonance frequencies f with θ reflects the variation of the effective magnetic field H_{eff} which enters the equation of motion of spin precession. [1] We note that according to the Curie principle,[123] we expect a ten-fold rotational symmetry of SW resonances also for small-area five-fold rotationally symmetric AMQs due to the linear polarization of the radio-frequency field in the CPW. This field is composed of, both, left- and right-circularly polarized electromagnetic waves. The two components allow us to excite gyrotropic spin precession for opposing directions of a magnetic field [1] and opposing spin-precessional motion in one and the same segment of the AMQ. Hence, SW resonances in a five-fold rotationally symmetric geometrical motif exhibit a tenfold rotational symmetry with respect to θ . [73]

Figure 4.2a,b shows field-dependent SW spectra for the 5th generation AMQ P2_SH_5thGen at $\theta = 0$ and 18 deg, respectively. Five prominent SW branches A_1 , B_1 , C_1 , D_1 , and E_1 for $\theta = 0$ deg and A_2 , B_2 , C_2 , D_2 , and E_2 for $\theta = 18$ deg are observed whose frequencies increase with H_0 (Figure 4.2c). We note that similar branches were detected when exploring AMQs of 3rd and 4th generation (Figures A.4 and A.5, Supporting Information). These branches exist independent

4.1 Direct Observation of Worm-Like Nanochannels and Emergent Magnon Motifs in Artificial Ferromagnetic Quasicrystals

of the total lateral size. Comparison of Figure 4.2a,b reveals that the SW resonances are “separated” more clearly from each other when the field was applied along $\theta = 18$ deg, that is, along an off-symmetry axis of the AMQ. Spectra taken on AMQ P3_SH_5thGen (Figure 4.2e,g) for $\theta = 0$ deg reveal four prominent branches F_1 , G_1 , H_1 , and I_1 . The resonances F_2 , G_2 , H_2 , and I_2 at small D (Figure 4.2f,g) are again partly better resolved for $\theta = 18$ deg compared to $\theta = 0$ deg. We note that resonances in the P3 AMQ (Figure 4.2f) were less well resolved compared to the P2 AMQ (Figure 4.2b). This was surprising as the Penrose P3 AMQ contained 62% less nanoholes that would act as scattering centers compared to P2 AMQ.

For AMQs with a large (L) hole diameter spectra are shown in Figure 4.2d,h (and in Figure A.5, Supporting Information). Clearer spectra also occurred for large hole diameters in P2 AMQs at 18 deg (Figure 4.2d). Some resonances are systematically shifted in frequency and are less pronounced in P2_LH (P3_LH) compared to P2_SH (P3_SH) AMQs. We attribute these observations to the larger nanohole diameter (i) modifying H_{eff} via the demagnetization effect and (ii) reducing the area covered by ferromagnetic material, respectively.

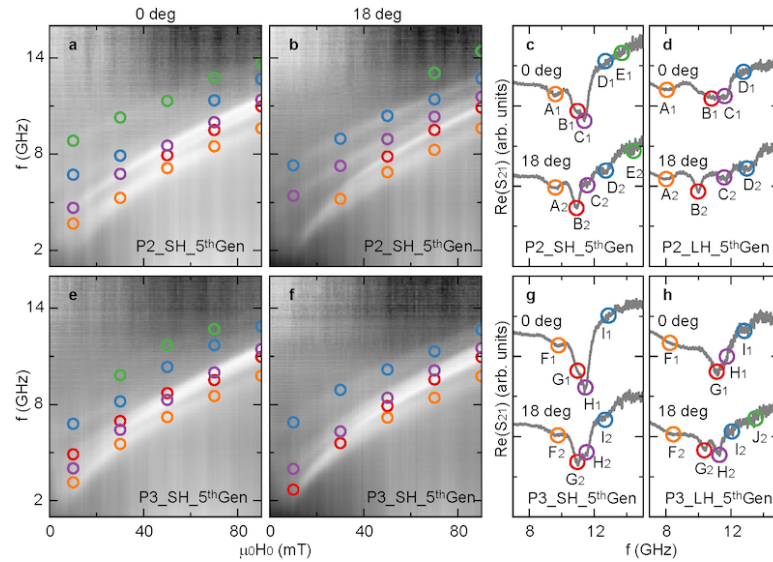


Figure 4.2: Field dependent spectroscopy on 5th generation Penrose AMQs. Grayscale-coded spectra for samples P2_SH_5thGen at a) $\theta = 0$ deg, and b) $\theta = 18$ deg; line spectra at 90 mT for c) P2_SH_5thGen, and d) P2_LH_5thGen at two angles; spectra for P3_SH_5thGen at e) $\theta = 0$ deg, and f) $\theta = 18$ deg; line spectra at 90 mT for g) P3_SH_5thGen, and h) P3_LH_5thGen at two different angles. Colored symbols in the experimental spectra in (c), (d), (g), (h) indicate the frequency values which are consistent with the different branches identified in the grayscale plots (a), (b), (e), (f).

Emergent Magnonic Motifs and Worm-Like Nanochannels Explored by Micromagnetic Simulation

To get a microscopic understanding of the experimental observations, we performed micro-

magnetic simulations. The simulated power spectrum for AMQ P2_SH_3rdGen at $\theta = 0$ deg suggests five distinct modes (Figure 4.3a). The number and frequencies agree well with SW resonance frequencies obtained experimentally (Figure S6, Supporting Information). Due to the inhomogeneous magnetic field created by the demagnetization effect (Figure A.7, Supporting Information), several spinwave modes of different eigenfrequencies are excited: Local phase and power maps indicate that branch A_1 reflects edge modes (not shown) with spin precession close to the edges of nanoholes. Branch B_1 (Figure 4.3b) contains stripe-like extended modes which remind one of modes seen in periodic nanohole lattices. However, in case of a P2 AMQ with a high density of vertices the stripe-like modes are multi-segmented as nanoholes selectively block spin precession at some places. Branch C_1 (Figure 4.3c) contains patches of pronounced excitations that appear to be confined between, for example, four holes (indicated by rhombi with dotted white lines). Note that the overall mode pattern exhibits a strict mirror symmetry with respect to the horizontal central axis of the AMQ, which is parallel to the applied field. Branches D_1 and E_1 are attributed to higher order confined modes (not shown). In the case of a P3_SH_3rdGen AMQ, we extract five salient modes (Figure 4.3d). Based on the simulations we classify them as follows: F_1 (edge mode), G_1 (extended modes shown in Figure 4.3e), H_1 (patches of confined modes shown in Figure 4.3f), I_1 and J_1 (higher order confined modes, not shown). Differences between P2_SH and P3_SH AMQs for a field along $\theta = 0$ deg are as follows: (1) stripe-like modes in P2 are blocked in many locations, whereas in P3 nanochannels extend more through the structure. (2) Patches highlighted with white dotted lines in Figure 4.3c,f represent a mode motif of magnons confined in thin rhombi. Importantly, AMQs with enlarged nanohole diameters repeat this rhombus-like mode motif confined between only four holes: For both P2 in Figure 4.3g and P3 in Figure 3h they are clearly visible; the additional holes in P2 compared to P3 suppress spin-precessional motion in large parts and reduce the magnon mode pattern to the rhombus-like motif almost completely (Figure 4.3g). We emphasize that the rhombus is a geometrical motif for P3, but not for P2. The observation of an identical magnon motif in P2 and P3 AMQs hints towards the emergence of magnon mode motifs different from the underlying geometrical motifs. (3) Simulated resonances in P2 (Figure 4.3a) are slightly better resolved as compared to P3 (Figure 4.3d) consistent with experiments.

For AMQ P2_SH_3rdGen (Figure 4.4a) and AMQ P3_SH_3rdGen (Figure 4.4e) with \mathbf{H}_0 applied at $\theta = 18$ deg we identify five modes in the corresponding simulations. The resonance frequencies are in good agreement with the experimentally observed branches at 90 mT (Figure A.6, Supporting information). The signal strengths of SW resonances B_2 to D_2 are comparable to one another in contrast to signals obtained for $\theta = 0$ deg on P2 (Figure 4.3a). In the experiments corresponding branches at $\theta = 18$ deg were indeed better resolved compared to $\theta = 0$ deg. Branch B_2 (Figure 4.4b) reflects stripelike modes extending in a direction transverse to the applied field direction. In Figure 4.4b–d we indicate the decagon-like geometrical motif enclosed by ten nanoholes which is highlighted by a white dotted line in Figure 4.1a. Thereby a one-to-one comparison between geometrical (structural) and mode motifs can be performed.

4.1 Direct Observation of Worm-Like Nanochannels and Emergent Magnon Motifs in Artificial Ferromagnetic Quasicrystals

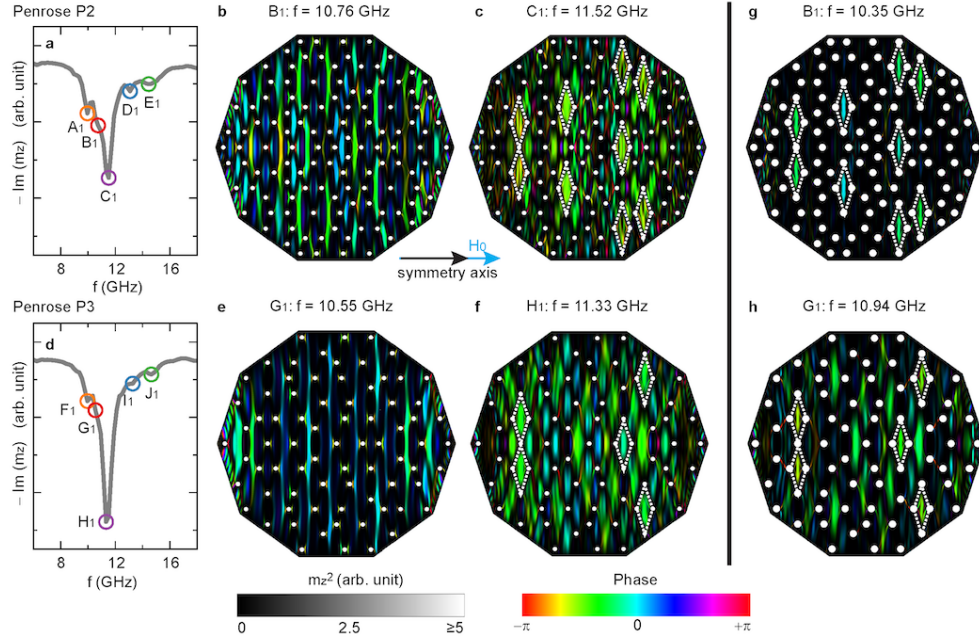


Figure 4.3: Micromagnetic simulations for an applied field of 90 mT along $\theta = 0$ deg (symmetry axis) of P2 and P3 AMQs and comparison of nanohole diameters. a) Simulated SW spectrum ($\text{Im}(m_z)$) of Penrose P2 AMQ with nanoholes of small diameter $D = 135$ nm. Circles and labels are chosen corresponding to resonance frequencies seen in experiments. Power (m_z^2) map overlaid on corresponding local phase maps indicating origins of modes b) B_1 (Penrose P2 AMQ), and c) C_1 (P2 AMQ). d) Spectrum of AMQ P3_SH_3rdGen, and maps of spin-precessional motion of modes e) G_1 (P3 AMQ), and f) H_1 (P3 AMQ). Dashed lines highlight spin precession surrounded by four nanoholes (rhombi). Gray and hue color scales represent the power and phase, respectively. In (b) and (e) an enhanced contrast is used to identify stripe-like SW excitations (nanochannels). Magnonic mode motifs found in (g) P2 and (h) P3 AMQ with large diameter ($D = 220$ nm).

In Figure 4.4b, close to the center of the geometrical motifs the modes exhibit bends. The bends imply that the aperiodically arranged nanoholes make propagation in SW nanochannels highly sensitive to the nanohole diameter (Figure A.8, Supporting Information). For P2 AMQs, we find the SW nanochannels to be multi-segmented. This is different for P3 AMQs: In Figure 4.1f (and P3_LH in Figure A.8 in the Supporting Information), long 1D nanochannels are identified that exhibit bends separated by different distances. Their appearances resemble worms whose bends vary from channel to channel. The aperiodicity prohibits identical sequences of holes within neighboring nanochannels suggesting channel dependent magnon states. The minimum width of a nanochannel analyzed along a Conway worm (highlighted by white dots in Figure 4.1b) amounts to 50 nm. Due to this confinement spin waves in the nanochannels are in the exchange-dominated regime, [1] and therefore the anisotropy of spin waves induced by the dipolar interaction in the long wavelength limit is not responsible for the existence of the worm-like nanochannels. We expect narrower nanochannels for further decreased inter-vertex distances in the Penrose tiling as the spin-wave dispersion relation is

isotropic in the exchange regime.[1] Furthermore, dissecting a Conway worm (Experimental Section) creates another Conway worm. [33] Interestingly there is always at least one Conway worm in the Penrose tiling produced by the matching rule, [33] which can propagate through the entire lattice. In case of low-damping material such nanochannels are expected to transmit spin-wave signals from edge to edge. Our experiment shows that inside the bulk of the AMQ there are many more aperiodic nanochannels guiding spin waves than these very long edge-connecting worms. We attribute our observation to the infinite set of worms of short and long ties that are expected for a regular Penrose tiling. [33] The worms are distributed according to the Fibonacci sequence.

Higher frequency excitations in P2 AMQ at $\theta = 18$ deg resemble narrow patches of pronounced spin-precessional motion as indicated by the white dotted lines in the simulation results: The patches appear within (Figure 4.1e and Figure 4.4c) or at the edges of the geometrical motifs (Figure 4.4d). The welldefined patches can be understood in analogy to periodic antidot lattices [102, 103] in which standing magnon modes reflected confinement and localization due to edges of nanoholes and inhomogeneities of H_{eff} , [124] respectively. We note that the emergent magnonic mode motifs seen in Figures 4.1e and 4.4b–d all exhibit a mirror symmetry axis being perpendicular to the applied field. A consistent mirror symmetry axis is found for mode patches of P3 at $\theta = 18$ deg (Figures 4.1f and 4.4f,g). Axes of mirror symmetries thus depend on the orientation of H_0 consistent with a report about nanobar-based quasicrystals. [73] Figure 4.4f,g substantiates that a SW motif identified in generation three of AMQ P3 (dashed white rhombus) occurs in generation four at structurally similar positions within the geometrical motif (highlighted by the yellow star). Emergent magnon motifs identified throughout this work thus reflect self-similar motifs reappearing in different generations of quasicrystals.

Wavelength Division Multiplexing Utilizing Worm-Like Nanochannels Using BLS microscopy (Figure A.3, Supporting Information) we evidenced spin-precessional motion in the aperiodically bent nanochannels (Figure 4.1g). Data were taken near a CPW by which we excited the magnons. In the experiment, we observed a minimum width of 300 nm which is larger than the predicted value of 50 nm. The discrepancy is attributed to the diffraction limit of micro-focus BLS as explained in ref. [79]. Regions of large spin-precessional motion varied as a function of frequency and field orientation as will be discussed in the following (see also Figures A.9 and A.10, Supporting Information). Large segments of worm-like nanochannels were resolved best at relatively low frequency consistent with simulations. BLS with phase resolution allows us to directly image the phase evolution of waves in the quasicrystalline structure when excited by the integrated microstructured CPW. We evidence irregular wavefronts of propagating SWs (Figures 4.1h and 4.5a–c) indicating that magnon states are different from nanochannel to nanochannel. The wavefronts vary significantly with excitation frequency. The lengths over which the phase $k(x, y) \times y$ varies by 2π in nanochannels vary with frequency (vertical bars in Figure 4.5a–c). $k(x, y)$ is the wave vector of spin waves which is not constant along a nanochannel as it depends on the aperiodically modulated effective field $H_{\text{eff}}(x, y)$. [1] The

4.1 Direct Observation of Worm-Like Nanochannels and Emergent Magnon Motifs in Artificial Ferromagnetic Quasicrystals

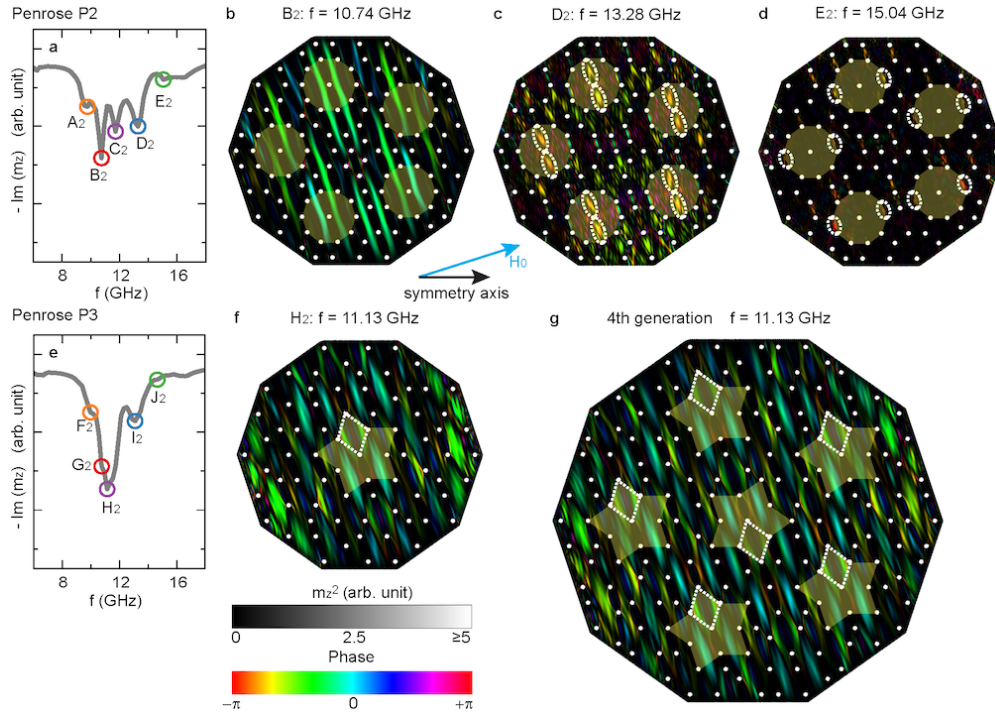


Figure 4.4: Micromagnetic simulations for an applied field of 90 mT along $\theta = 18$ deg (off-symmetry axis) of P2 and P3 AMQs and comparison of nanohole diameters. a) Simulated SW spectrum ($\text{Im}(m_z)$) of Penrose P2_SH_3rdGen with nanoholes of diameter $D = 135$ nm. Circles and letters are consistent with labels introduced for experimental data. Power maps (m_z^2) overlaid on corresponding local phase maps indicating regions of spin-precessional motion in P2 for branches b) B₂, c) D₂, d) E₂. e) Spectrum simulated for an AMQ P3_SH_3rdGen and spin-precessional motion of f) H₂ at $f = 11.13$ GHz in a 3rd generation AMQ. g) Spin-precessional motion at the same frequency in P3_SH_4thGen, that is, a 4th generation AMQ. A mirror symmetry becomes apparent for the localized mode patches (highlighted white dotted lines). The yellow semi-transparent decagons and stars revisit underlying geometrical motifs for P2 and P3, respectively.

irregular phase evolution (wavefront) is in contrast to 2D periodic antidot lattice magnonic crystals [102] for which spin waves in neighboring nanochannels are in phase and wavefronts are parallel to the CPW if the applied magnetic field direction is collinear with the CPW's signal line. The SW band structures for each nanochannel are identical due to the translational invariance of the magnonic crystals. In AMQs each SW nanochannel is modulated by a different sequence of nanoholes thanks to the quasicrystalline nature. Note that the arrangement of nanoholes is related to a 1D Fibonacci sequence, which suggests the formation of a specific spin-wave band structure. [125] For the same spin-precessional frequency differently propagating magnon states are thereby created on a single chip in neighboring nanochannels. They enable dense wavelength division multiplexing (Figure A.11, Supporting Information). In photonics, a DWDM allows one to exploit numerous wavelengths of light on a single optical fiber. For photons wavelength and frequency are coupled via the speed of light and hence a

corresponding number of different input frequencies is required. In the quasicrystal-based DWDM only a single input frequency is needed to generate different wavelengths. Going beyond photonics the configuration of the magnonic DWDM can be altered ("gated") by an applied magnetic field. Another gating device such as a phase shifter using local magnetic fields[38] could be used to tune wavefronts of spin waves in the quasicrystal, and in turn, the phase differences between neighboring nanochannels (Figure A.11, Supporting Information) would be modified. This would create a wave-based logic device with a large number of both processing units and outputs which offers an areal density much larger than the recently proposed (de)multiplexers. [126, 127] Thanks to the scale invariance of demagnetization fields, further downscaling of the size of the magnonic DWDM is possible. In Figure 4.5d we demonstrate the rotation of the extended modes in nanochannels experimentally by choosing $\theta = 90$ deg for BLS performed at an excitation frequency of 11.2 GHz. The observed rotation of channels goes beyond the photonic channels (waveguides) created by tailored defects in hyperuniform disordered solids which are fixed in space. [128] The extended magnon modes transform into localized excitations in the experiment when we increase the frequency to 12.9 GHz (Figure 4.5e). The transformation is predicted by simulations. Localized modes were found in theoretical studies also in bi-component magnonic AMQs.[30]

Conclusion

In our study, spin waves in 2D AMQs are thoroughly investigated using broadband all-electrical spectroscopy, spatially resolved inelastic light scattering and micromagnetic simulations. Scale invariant spin-wave spectra indicate the emergence of peculiar magnon mode patterns in 2D AMQs which we characterize by the simulations. They exhibit specific mirror symmetries different from the underlying quasicrystalline lattices. The mirror symmetry axis varies with the direction of the applied field H_0 and takes either zero or 90 deg with respect to H_0 . The unconventional rotational symmetries of AMQs is reflected in the angular dependent SW spectra. In analogy to their plasmonic counterparts, [113] the aperiodically arranged nanoholes could be exploited in grating couplers, that is, microwave-to-magnon transducers. Their unconventional rotational symmetries are advantageous in order to optimize multi-directional magnon emission relevant for integrated magnonic circuits. [16, 17] Particularly intriguing are the aperiodically bent nanochannels which we observed. For them we find a width down to 50 nm in simulations. Due to the quasiperiodic arrangement of the nanoholes, spin-wave states are expected to be different from nanochannel to nanochannel. Consistently we detect irregular wavefronts of spin waves in the AMQs using spatially resolved BLS. They are created due to an inhomogeneous internal field H_{eff} which is not active in photonics and plasmonics. The materials-by-design approach and imaging by a state-of-the-art microscopy technique allowed us to explore the implication of Conway worms defined for the theoretical description of quasicrystals concerning a real-world application. We propose a quasicrystal-based DWDM that can be operated at a single microwave frequency and is ultra-compact because of the significant wavelength reduction inherent to magnonics.

4.1 Direct Observation of Worm-Like Nanochannels and Emergent Magnon Motifs in Artificial Ferromagnetic Quasicrystals

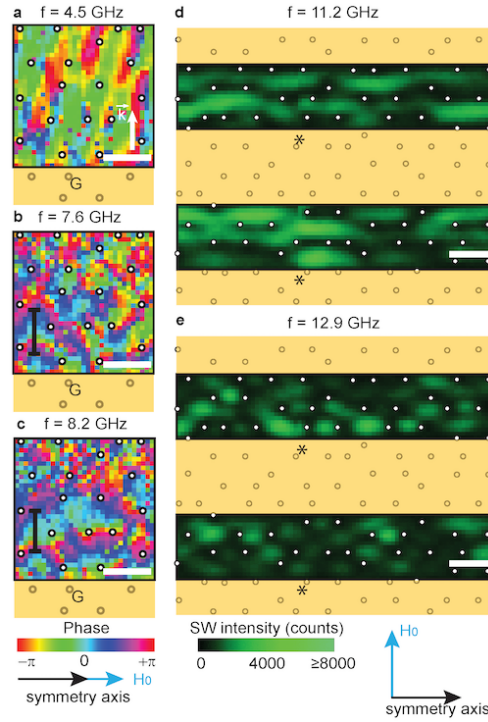


Figure 4.5: Phase-resolved magnon propagation in a quasicrystal and control of nanochannels. Spatially resolved phase evolution of spin waves propagating along k (white arrow in (a)) in the P3 quasicrystal of Figure 4.1h at a) 4.5 GHz, b) 7.6 GHz, and c) 8.2 GHz for 10 mT. The black vertical bars indicate a phase difference of 2π . The length of the bar can be attributed to the wavelength in the selected channel. d) Worm-like nanochannels (bright) imaged by BLS without phase resolution at an excitation frequency of 11.2 GHz for $\theta = 90$ deg and 90 mT. This angle is consistent with the channel configuration shown in Figure 4.1f. e) BLS imaging at an increased frequency of 12.9 GHz. The spin-precessional motion is found to be confined to narrow patches. The scale bars are $1\mu\text{m}$. The asterisk marks a position where there was a slight stitching error in the x, y positioning system.

Experimental Section

Creation of Penrose P2 and P3 AMQs: Figure A.12a, Supporting Information shows the methodology behind constructing Penrose P2 tilings of different generation (and overall size). The authors started with two prototiles, called kites and darts. A kite is a quadrilateral with four interior angles of 72° , 72° , 72° , and 144° ; a dart is a quadrilateral with four internal angles of 36° , 72° , 36° , and 216° . In this study, the authors began with the configuration formed by joining five kites at a common vertex; this configuration called “0th generation”. Next, each kite was dissected into two smaller kites and a dart, and rejoined according to the matching rule [33] to obtain the 1st generation tiling. Each application of such dissection rule generated a tiling of a higher generation containing a correspondingly larger number of prototypical elements. The 1st generation tiling was rescaled to make it the same size as the 0th generation tiling; kites and darts of the 1st generation were smaller in size, compared to those of the

0th generation. Continued dissection and rescaling produced higher-generation Penrose P2 tilings, and the deflation process was then terminated at desired finite generation.

In the case of Penrose P3 tilings (Figure A.12b, Supporting Information), it was started with two rhombi that have equal edges but different angles: (1) Thick rhombus with interior angles of 72° , 108° , 72° , and 108° . (2) Thin rhombus with interior angles of 36° , 144° , 36° , and 144° . Here, the authors started with the configuration formed by joining ten acute Robinson triangles (half of thin rhombi) at a common vertex; this configuration we termed “0th generation”. Two neighboring acute Robinson triangles were bisected into one thin and one thick rhombi that leads to “1st generation” P3 tiling. Subsequently, each thick rhombus was dissected into two thick and one thin rhombi; whereas thin rhombus got divided into one thick and thin rhombi, and were attached together according to matching rules, [33] producing next generation of Penrose P3 tiling. As in the case of P2 tiling, we rescaled the thick and thin rhombi so that the subsequent generation thick and thin rhombi were of smaller sizes as compared to ones in 0th generation. Finally, the edges of kites and darts were taken out and inserted nanoholes on vertices of kites and darts in P2 tiling. In the case of P3 tiling edges of rhombi were taken out and inserted nanoholes. The next step was to convert the final P2 and P3 tilings into a GDS file format that was imported into commercial electron beam lithography (EBL) software.

Sample Fabrication: A 19 nm thick amorphous CoFeB ($\text{Co}_{20}\text{Fe}_{60}\text{B}_{20}$) thin film was sputtered [94] on a Si substrate. The aperiodic nanohole masks were patterned on hydrogen silsesquioxane negative electron beam resists using EBL. Ion beam etching was then performed to form a decagonal mesa and open the nanoholes in the magnetic thin film to form different AMQs as summarized in Table 1. Consecutively, CPW were patterned via EBL, electron beam evaporation of Ti/Au, and lift-off processing. They covered ten nominally identical AMQs parallel to their symmetry axis. The saturation magnetization was determined using SW spectroscopy on a reference CoFeB film, and amounted to 1.8 T. The widths of the signal line of CPW were 9, 13, and $20\mu\text{m}$ for AMQs.

Broadband Spin-Wave Spectroscopy: SW excitations in AMQs were studied via all electrical SW spectroscopy. The two ends of the CPW (patterned on top of the AMQs, Figure A.2, Supporting Information) were connected to a vector network analyzer (VNA) to sweep the frequency and record the absorption spectra. The samples resided in a custom built 2D vector magnet assembly that allowed us to vary the in-plane angle θ of the applied field H_0 . A 2-port VNA allowed us to generate a microwave magnetic field with frequencies ranging from 10 MHz to 26.5 GHz. The applied microwave current generated an in-plane rf-magnetic field perpendicular to the long axis of the CPW. The microwave with a power of 0 dBm was applied at the port 1 of the CPW in order to excite magnetization precession. The precession-induced voltage was detected at port 2 via reading the scattering parameter S_{21} where the numbers 2 and 1 in the subscript denote the detection and excitation port. An external magnetic field $\mu_0 H_0$ of up to 90 mT was applied under an angle θ between the external field H_0 and the CPW’s long axis. In order to increase signal to noise ratio, $\Delta S_{21} = S_{21}(H_0)S_{21}(\text{Ref})$ was evaluated where

4.1 Direct Observation of Worm-Like Nanochannels and Emergent Magnon Motifs in Artificial Ferromagnetic Quasicrystals

$S_{21}(H_0)$ and $S_{21}(\text{Ref})$ represent scattering parameters measured at a given field H_0 and at 90 mT along $\theta = 90^\circ$, respectively.

Brillouin Light Scattering Microscopy: Spin-wave eigenmodes were imaged via Brillouin light scattering (BLS) microscopy with and without phase resolution at room temperature using a setup similar to refs. [76, 77]. Figure A.3, Supporting Information shows the experimental setup. The end of one CPW was electrically bonded to a printed-circuit board, which was connected to a signal generator applying a microwave current. The corresponding magnetic microwave field excited spin precession in the AMQ close to the CPW at a fixed frequency. The power was such that spin precession was excited in the linear regime. A magnetic field of 90 mT was applied under an angle θ via a permanent magnet for BLS measurement without phase resolution. For phaseresolved BLS measurement, a magnetic field of 10 mT was applied after that a field of 90 mT was applied in order to first saturate the AMQ. A lens with a numerical aperture of 0.85 was used to focus a 473 nm wavelength with a spot size of 300 nm onto the AMQ. Laser power was set to 1 and 0.85 mW for BLS measurement without and with phase resolution, respectively. Energy shifts of reflected laser light due to the inelastic magnon–photon scattering were detected by a triple-tandem Fabry–Pérot interferometer. The AMQ was positioned under the laser with a spot using x, y piezo-positioning system. The step size to acquire the images of Figures 4.1g,h and 4.5, Figures A.9 and A.10, Supporting Information was 100 nm. We exploited phase-resolved inelastic light scattering while exciting spin waves phase-coherently at the straight CPW. As the CPW was microstructured the excitation was inhomogeneous and generated propagating spin waves with a finite wave vector k . The acquisition time of inelastically scattered photons outside the CPW was chosen to be 2.14 times longer than in regions between signal and ground lines to compensate for the different excitation strength near a CPW. The 120 nm thick Au layer of the CPW did not allow us to monitor a signal from the magnonic channels underneath the ground and signal lines. The nanohole positions depicted in Figure 4.1g were reconstructed in that we overlaid (i) atomic force microscopy (AFM) images taken on the studied AMQ with (ii) the optical image taken in the BLS microscope, (iii) the BLS data, and (iv) the exposure masks for CPWs and electron beam lithography of nanoholes. Characteristic notches and dust particles identified in AFM and BLS microscopy data were used for a pre-alignment of the nanohole lattices. Finally we adjusted precisely the lattice of nanoholes given by the exposure mask relative to BLS data. Still we shifted this mask only within about 200 nm in lateral directions (i.e., by less than the diameter of the laser spot) to avoid that a maximum BLS intensity peak resided inside a hole with a diameter of about 200 nm.

Simulations: Micromagnetic simulations using OOMMF [88] were performed to obtain a microscopic insight into SW excitations in AMQs. A bitmap containing the required P2 and P3 geometry was imported into OOMMF and discretized on a grid of 10 nm \times 10 nm \times 19 nm. A global in-plane 90 mT DC magnetic field was applied along the x direction, and equilibrium magnetization configuration was determined. Subsequently, a spatially

homogeneous Gaussian pulse of 20 mT amplitude and 2.5 ps duration was applied along the z -axis (out of plane). In the simulation we explored the standing spin-wave modes due to uniform excitation. The perpendicular component of magnetization m_z was recorded as a function of x, y and the time step. A fast Fourier transformation (FFT) was performed on the magnetization of each pixel along the time axis to obtain the resonance spectrum. Then sums of power and phase of m_z were calculated to display the SW spatial profile for relevant frequencies. $\text{Im}(m_z)$ was then integrated over the whole geometry, and plotted as a function of frequency f in order to observe the microwave absorption. $\text{Im}(m_z)$ corresponds to the S_{21} observed in experiment. The input parameters used in the simulations were as follows: saturation magnetization $\mu_0 M_S = 1.8$ T, exchange constant $A = 13 \times 10^{-12}$ J m⁻¹, and damping constant 0.007. In simulations, the global magnetic field was fixed along x -axis and the relevant bitmap containing the geometry was oriented at 0° and 18°. To illustrate the spatial distribution of spin-precessional motion under uniform excitation we show maps of the local phase and power (square of the spin precessional amplitude m_z). The widths of nanochannels in simulations (experiments) were extracted in that we followed the amplitudes of spin-precessional motion along a Conway worm with a step size of 10 nm (100 nm). At each step we extracted the full width at half maximum of the local amplitude distribution in the corresponding spin-wave nanochannel.

Supporting Information

Supporting Information is available from the Wiley Online Library or from the author.

Acknowledgements

The research was supported by the SNSF via grant number 163016.

Conflict of Interest

The authors declare no conflict of interest.

Keywords

magnonics, metamaterials, nanomagnets, quasicrystals, spin waves Received: February 13, 2020 Revised: June 2, 2020

5 Magnon band structure in magnonic Penrose quasicrystal

Going beyond our previous study based on a ferromagnetic metal, we nano-engineered artificial magnetic quasicrystals AMQs from single crystalline and insulating yttrium iron garnet (YIG). YIG offers the lowest Gilbert damping parameter for magnons known to date, resulting in a long life time of SWs [5, 98]. This aspect boosts the development of YIG based magnonic devices for information processing compared to e.g., the ferromagnetic metal used in Sect. 4.1. Low damping enables sharper SW resonances, and thereby additional SW branches might be resolved. So far 1D magnonic crystals made of YIG have been actively investigated in magnonics [57, 58, 129]. Note that artificial magnetic quasicrystals, in which engineered magnonic band structures form, are called magnonic quasicrystals (MQCs) in the following.

In the first section of this chapter, we present the SW study on a 2D MQC made of YIG based on the Penrose P3 lattice [32]. Combining μ -BLS and broadband SW spectroscopy, we discovered multi-directional spin wave emission into the MQC, forbidden frequency gaps indicating the magnonic band formation, and the modified magnon density of states attributed to the backfolding and formation of a pseudo-Brillouin zone boundary [36]. The corresponding manuscript has been submitted to a journal.

The width of the worm-like nanochannels predicted for the artificial quasicrystals made of CoFeB was narrower than the diffraction limit of light for BLS [31]. For the characterization of such narrow nanochannels, we investigated a low-damping MQC using STXM at the MAXYMUS endstation at Helmholtz-Zentrum Berlin. We successfully imaged worm-like magnon nanochannels with irregularly varying widths down to 160 nm. Channelling occurred inside and, surprisingly, outside the MQC. Fast Fourier transformation analysis of SW images revealed that there was coherent back-scattering of SWs evidencing the formation of pseudo-Brillouin zone [36] for SWs in the quasicrystal.

5.1 Direct observation of multiband transport in magnonic Penrose quasicrystals via broadband and phase-resolved spectroscopy

S. Watanabe, V. S. Bhat, K. Baumgaertl, M. Hamdi and D. Grundler

Submitted to Science Advances.

Contribution I contributed to the work and the manuscript as follows: Design of the samples and planning of the experiments together with V. S. B and D. G. Sample fabrication of MC and MQC and integration of CPWs using clean room facilities (CMi). Experiments for broadband SW spectroscopy and BLS spectroscopy helped from K. B. and D. G. Analysis of experimental data together with D. G. Analytic calculation of MC and MQC using plane wave method by establishing calculation codes with help from. M. H.

The layout of the manuscript was reformatted and the references were integrated into the thesis' bibliography.

Abstract

Quasicrystals are aperiodically ordered structures with unconventional rotational symmetry. Their peculiar features have been explored in photonics to engineer band gaps for light waves. Magnons (spin waves) are collective spin excitations in magnetically ordered materials enabling non-charge-based information transmission in nanoscale devices. Here we report on a two-dimensional magnonic quasicrystal formed by aperiodically arranged nanotroughs in ferrimagnetic yttrium iron garnet. By phase-resolved spin wave imaging at GHz frequencies, multi-directional emission from a microwave antenna is evidenced allowing for a quasicontinuous radial magnon distribution, not observed in reference measurements on a periodic magnonic crystal. We observe partial forbidden gaps which are consistent with analytical calculations and indicate band formation as well as a modified magnon density of states due to backfolding at pseudo-Brillouin zone boundaries. The findings promise as-desired filters and magnonic waveguides reaching out in a multitude of directions of the aperiodic lattice.

Main Part

Since the discovery of quasicrystals over three and a half decades ago [105], their aperiodicity and unconventional rotational symmetries combined with long-range order have baffled physicists and material scientists alike. Recent advances in nanofabrication techniques have allowed researchers to explore the effects of aperiodicity using the materials-by-design approach [130]. The prime examples of this approach are the studies on artificial photonic crystals and plasmonic crystals [35, 113] based on the tenfold rotational symmetric Penrose tiling - a two dimensional (2D) analogue of three dimensional (3D) quasicrystals [122, 131]. Such photonic quasicrystals offered a complete band gap for light [36, 107, 132], whereas

5.1 Direct observation of multiband transport in magnonic Penrose quasicrystals via broadband and phase-resolved spectroscopy

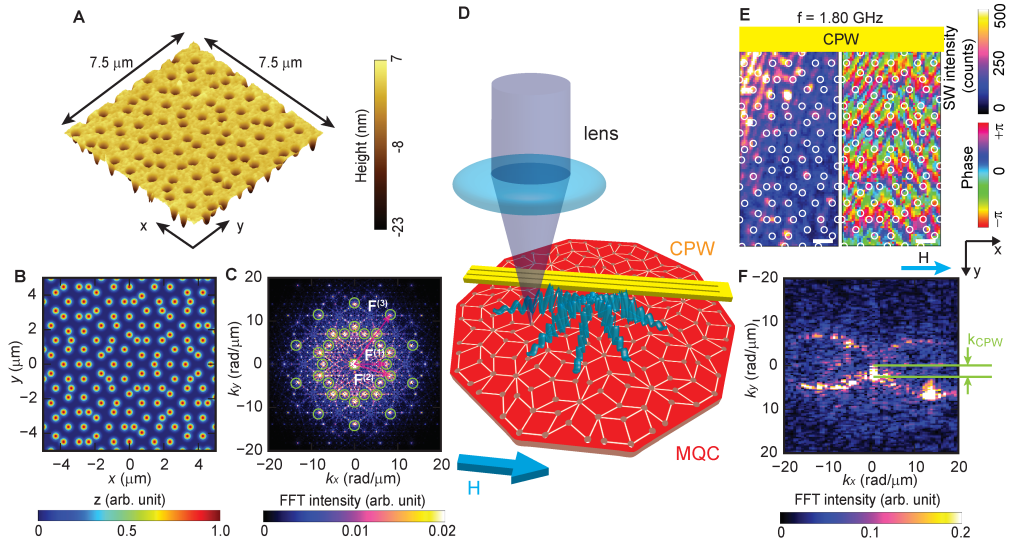


Figure 5.1: Omnidirectional spin wave emission in an aperiodic magnonic quasicrystal. (A) Atomic force microscopy image of magnonic quasicrystal based on the Penrose P3 lattice. Nanotroughs of a diameter of $D \sim 300 \text{ nm}$ were etched out from a 100 nm thick YIG thin film on the vertices of the Penrose P3 tiling. The virtual representation of Penrose P3 lattice in (B) real space and (C) reciprocal space. Light green circles indicate the reciprocal vectors of the Penrose lattice. (D) Schematic image of BLS experiment on the MQC. Integrated CPW on the MQC act as a SW emitter, and excited magnons are detected via magnon-photon scattering. (E) Spatial distribution of measured SWs in magnitude (left) and phase (right) at $f = 1.80 \text{ GHz}$ propagating in the $+y$ -direction in the MQC. The field of 10 mT was applied along the CPW long axis ($+x$ -direction). Scale bars indicate $1 \mu\text{m}$. Bright (dark) in the left image indicate large (small) spin-precessional cone angles, and the hue scale in the right image represents the phase of SWs. The white circles indicate the positions of nanotroughs. SW wavefronts are not only parallel to the CPW long axis but also along diagonal directions. (F) SW intensity in reciprocal space after Fourier transformation of the SW images of (E). The local maximum of SW intensity (bright) found close to $(k_x, k_y) = (0, 0)$ is attributed to the wave vector k_{CPW} provided by the CPW along the y -direction at the given frequency. Here, $\mathbf{k}_{\text{CPW}} \sim (0, 2.8 \pm 0.4) \text{ rad}/\mu\text{m}$ as indicated by the horizontal lines. A dumbbell-shape iso-frequency contour is observed indicating propagation of dipole-dominated SWs in an omnidirectional manner. Most likely the dumbbell is not closed at large values k because of the limited wave vector range of microfocus BLS. Note that FFT intensity of (C) and (F) is normalized with respect to the maximum intensity.

the observation of strong transmission peaks in artificial plasmonic quasicrystals refuted the conventional well-accepted view that periodicity is crucial for such observation [113]. Recently, novel insights were gained on the effect of aperiodicity in magnonic quasicrystals from the study of spin waves (SWs) [31, 117, 133]. The bicomponent magnonic quasicrystals based on a Fibonacci sequence (one dimension, 1D) and Penrose tiling (2D) exhibited a multilevel structure of magnonic band gaps in simulations [30, 133]. Such gaps and SW propagation in 1D quasicrystals were evidenced using Brillouin light scattering and X-ray

microscopy techniques [121, 125]. Furthermore, worm-like nanochannels discovered in 2D antidot quasicrystals gave rise to an unprecedented demultiplexing process with microwaves that showed distinct advantages over demultiplexing process in photonics [31]. Additionally, the reprogrammability of artificial quasicrystals [28, 117, 125] promised a novel data writing process. This makes the study of magnonic quasicrystals timely from the perspective of nanomagnonics, which is an evolving branch in magnetism exploring SWs [4]. On the nanoscale, magnon-based logic circuits are expected to transfer and process information efficiently [3]. One of the prominent limitations of earlier works are that they were based on ferromagnetic metals. Previous studies were done on materials for which their SW damping might have obscured further coherent SW back-scattering effects like the formation of a complete magnonic band gap. Such a gap is key for the creation of multi-directional magnonic waveguides and spin wave cavities inside a magnonic crystal by analogy with a photon cavity residing in a defect of a photonic crystal [134]. Due to the low rotational symmetry, the formation of a complete magnonic band gap is more challenging for magnonic crystals (MCs) based on periodic lattices [135] than for quasicrystals which can exhibit much higher rotational symmetry. The latter feature is advantageous also for multi-directional magnon emission in case of the magnonic grating coupler effect [16, 17, 19, 66], which however has not yet been reported for 2D quasicrystals.

In this article, we investigate SW properties of magnonic quasicrystals (MQCs). The MQCs were prepared from an yttrium iron garnet (YIG) thin film, a low-damping insulating ferrimagnet [98], by etching out circular nanotroughs at the vertices of Penrose P3 tiling (Fig. 5.1A). The SW damping in YIG is about 10^2 smaller as compared to previously studied NiFe and CoFeB films allowing us to explore further novel aperiodicity related effects on band structure. The Penrose lattice (Fig. 5.1B), due to its self-similarity and long-range ordered nature, shows sharp peaks (Bragg peaks) in reciprocal space that define specific reciprocal vectors \mathbf{F} (Fig. 5.1C). Subsequently coplanar waveguides (CPWs) integrated on the MQC allowed us to excite and characterize SWs using spatially resolved inelastic (Brillouin) light scattering (BLS) and broadband SW spectroscopy techniques (Fig. 5.1D). We observed SWs propagating in diagonal directions (Fig. 5.1E), in contrast to reference periodic lattice of nanotroughs in YIG (cf. Fig. 5.2). The Fourier transformation of complex SW images obtained on the quasicrystalline arrangement of nanotroughs (Fig. 5.1F) gives strong indication that the SWs are emitted in a truly omnidirectional manner. This has not been reported from the study of conventional magnonic grating couplers based on periodic structures. Moreover, we observed features consistent with a 2D pseudo-Brillouin zone (p-BZ) for SWs and a modified magnonic density of states (DOS) reflecting partial magnonic band gaps in the SW dispersion relation. Our experimental results suggest that a Penrose P3 tiling operates as a grating coupler inducing a manifold of both propagation directions and wavelengths. Such formation of magnonic minibands allows one to engineer magnonic waveguides by leaving out columns of nanoholes without the directional restrictions exhibiting distinct advantage over previously explored periodic nanohole lattices [12].

Results

Detection and imaging omnidirectional spin wave emission.

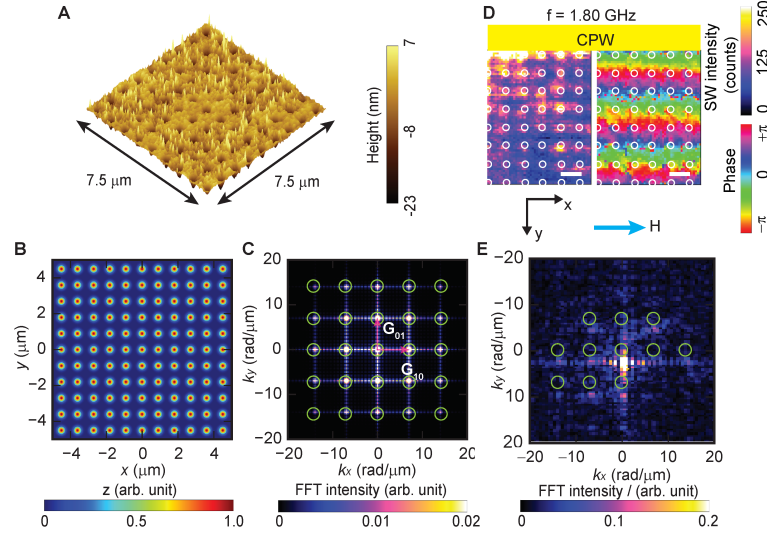


Figure 5.2: Multi-directional spin wave emission in a periodic magnonic crystal. (A) Atomic force microscopy image of magnonic crystal based on the square lattice of period $a = 900$ nm where nanotranches of a diameter of $D \sim 300$ nm were etched out from a YIG thin film. The virtual representation of the square lattice in (B) real space and (C) reciprocal space. Light green indicate the reciprocal vectors of the square lattice. (D) Spatial distribution of SWs in magnitude (left) and phase (right) at $f = 1.80$ GHz propagating in the $+y$ -direction in the MC. The field of 10 mT was applied along the CPW long axis ($+x$ -direction). Scale bars indicate $1 \mu\text{m}$. Bright (dark) in the left image indicate large (small) spin-precessional cone angles, and the hue scale in the right image represents the phase of SWs. The white circles indicate the positions of nanotranches. Green circles indicate calculated Bragg spots of reciprocal lattice vectors for comparison. (E) SW intensity in reciprocal space after FFT on the SW images of (D). Reciprocal lattice vectors \mathbf{G} are added to the SW mode excited with $\mathbf{k}_{\text{CPW}} = (0, 2.4 \pm 0.6)$ $\text{rad}/\mu\text{m}$ at $f = 1.8$ GHz by the CPW. The value of \mathbf{k}_{CPW} is extracted from the local intensity maximum near $(k_x, k_y) = (0, 0)$. FFT intensity of (C) and (E) is normalized with respect to the maximum intensity.

We first present BLS microscopy performed on the aperiodic Penrose P3 lattice (sample P3-MQC) (Fig. 5.1) and a reference periodic lattice (Fig. 5.2). Physical parameters and lattice characteristics are summarized in Tab. 5.1. BLS data were taken near the CPW by which we excited SWs, and an in-plane magnetic field H was applied parallel to the CPW and along the symmetry axis (x -axis) of P3-MQC. Here a bare CPW allows for the excitation of SWs that propagate along the y -direction. Before discussing MQC data in detail it is instructive to consider the SW imaging data taken on a magnonic crystal (Fig. 5.2A) incorporating a translationally invariant square lattice of nanotranches (sample SQ-MC).

Figure 5.2 (A to C), illustrates the periodic square lattice both in real and reciprocal space. The spatial distribution of SWs in SQ-MC at $f = 1.80$ GHz (Fig. 5.2D) show wavefronts of SWs

propagating parallel to the CPW. We analyzed the excited wave vectors of SWs for SQ-MC (Fig. 5.2E) by fast Fourier transformation (FFT) on complex-valued SW images. Here, the highest-intensity FFT peak close to $(k_x, k_y) = (0, 0)$ is observed at $\mathbf{k} = (k_x, k_y) \sim (0, 2.4) \text{ rad}/\mu\text{m}$. This wave vector is anticipated by the SW dispersion relation for Damon-Eschbach (DE) modes at $f = 1.80 \text{ GHz}$ in the unpatterned YIG thin film (fig. A.13A) and the wave vector is attributed to the CPW ($\mathbf{k}_{\text{CPW}} = (0, k_{\text{CPW}})$). In addition to this mode, sharp peaks appear periodically with spacings of $7.0 \text{ rad}/\mu\text{m} \sim 2\pi/(900 \text{ nm})$. The spacings correspond to reciprocal-lattice vectors \mathbf{G} of SQ-MC. In other words, we observe spin waves with wave vectors $\mathbf{k}_{\text{CPW}} + \mathbf{G}$, where $\mathbf{k}_{\text{CPW}} = (0, k_{\text{CPW}})$ is the wave vector imposed by the CPW at a given frequency. This set of peaks is consistent with the magnonic grating coupler effect [16]. It evidences coherent scattering of SWs and the backfolding of the SW dispersion via reciprocal-lattice vectors. In Ref. [11] it was argued that periodically modulated demagnetization fields induced by nanoholes in an MC served as scattering potentials for Bragg scattering of spin waves. At $f = 1.62 \text{ GHz}$ (Fig. 5.3A), the wavefronts display a longer wavelength in y -direction compared with that in Fig. 5.2D. At $f = 1.48 \text{ GHz}$ (Fig. 5.3B) the wavelength has increased further and the wavefronts appear to be distorted. Finally at $f = 1.22 \text{ GHz}$ (Fig. 5.3C) the wavelength in y -direction can no longer be extracted from the field of view ($\lambda \geq 10 \mu\text{m}$) and the wavefronts appear to be subdivided into channels extending parallel to the y -direction. Subsequently, the corresponding FFT results (Fig. 5.3 (D to F)) show that, beyond the pronounced mode with $(k_x, k_y) = (0, k_{\text{CPW}})$, the spin wave patterns contain excitations with reciprocal lattice vectors $(k_x, k_y) = (\pm p \cdot \frac{2\pi}{a}, k_{\text{CPW}} \pm p \cdot \frac{2\pi}{a})$ with $p = 0, 1$. In Fig. 5.3 (D and E) the wavelengths of SWs correspond to discrete k values in x and y -directions. At low frequency $f = 1.22 \text{ GHz}$ in Fig. 5.3F, FFT peaks are found near $(k_x, k_y) \sim (\pm 7.0, 0) \text{ rad}/\mu\text{m}$ instead of $(0, 0) \text{ rad}/\mu\text{m}$. Here SWs were elongated along the $+y$ -direction underneath nanotroughs, and standing SWs were confined in x -direction, which results in the formation of SW nanochannels [10]. The SW phase within neighboring nanochannels is almost identical while regions with large and small spin-precessional amplitudes are out of phase with each other.

The real-space SW map in the quasicrystalline structure (Fig. 5.1E) shows irregular SW wavefronts compared to SQ-MC at $f = 1.80 \text{ GHz}$. The corresponding FFT image (Fig. 5.1F) contains a dumbbell-shaped iso-frequency contour in k -space. Surprisingly such iso-frequency contour agrees with the anisotropic characteristics (dispersion relations) of SWs in an unpatterned YIG film (see figs. A.13B and A.14A). The data indicate that the microwave current in the CPW induces an inhomogeneous radiofrequency field h_{rf} that emits SWs into almost any direction at f . Reciprocal lattice vectors are not defined for an aperiodic Penrose P3 lattice; still, Bragg peaks are seen in diffraction pattern of a quasicrystal due to its self-similar and long-range ordered properties (Materials and Methods and Fig. 5.1C). The corresponding *reciprocal vectors* \mathbf{F} densely fill out the reciprocal space [36]. Such reciprocal vectors might provide the relevant Fourier components for h_{rf} to excite SWs in the nearly omnidirectional manner at fixed f as evidenced by the observed iso-frequency contour in k -space. This functionality is valid for a single frequency and thereby different from the previously reported grating couplers based on periodic lattices for which quasi-omnidirectional emission was claimed for SWs of different frequencies excited within a broad frequency band [16].

5.1 Direct observation of multiband transport in magnonic Penrose quasicrystals via broadband and phase-resolved spectroscopy

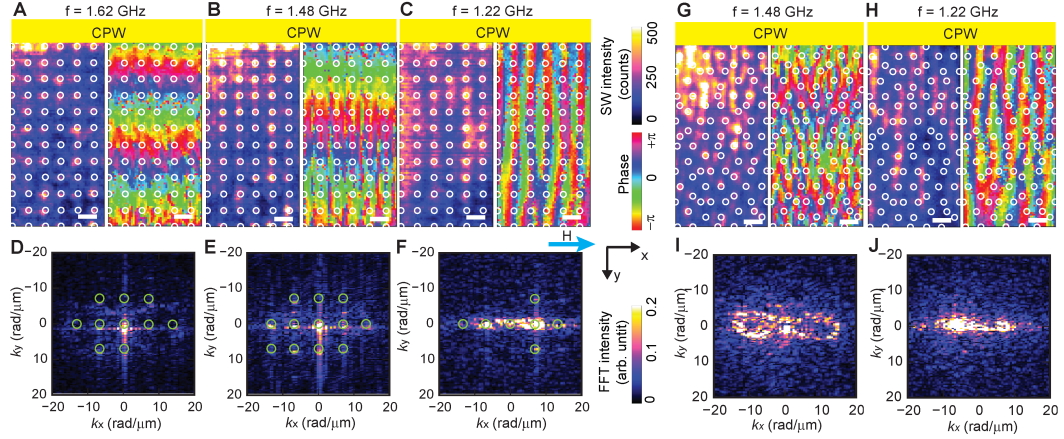


Figure 5.3: SW propagation in a periodic magnonic crystal and an aperiodic magnonic quasicrystal. Spatial distribution of SW magnitude (left) and phase (right) at (A) $f = 1.62$ GHz, (B) $f = 1.48$ GHz, and (C) $f = 1.22$ GHz, propagating in $+y$ -direction in sample SQ-MC. The field of 10 mT was applied along the CPW long axis ($+x$ -direction). Scale bars indicate $1 \mu\text{m}$. The bright (dark) in the left image indicates large (small) spin-precessional cone angle, and a hue scale in the right image represent SW phase. SW intensity in reciprocal space after a FFT performed on the SW images taken at (D) $f = 1.62$ GHz, (E) $f = 1.48$ GHz, and (F) $f = 1.22$ GHz. Green circles indicate calculated Bragg spots of reciprocal lattice vectors for comparison. Spatial distribution of SW magnitude (left) and phase (right) at (G) $f = 1.48$ GHz and (H) $f = 1.22$ GHz, propagating in $+y$ -direction in sample P3-MQC. SW intensity in reciprocal space after a FFT performed on the SW images taken at (I) $f = 1.48$ GHz and (J) $f = 1.22$ GHz. The wave vector \mathbf{k}_{CPW} extracted from BLS data in reciprocal space amounts to $(0, 1.5 \pm 0.4)$ rad/ μm at $f = 1.62$ GHz in (D), $(0, 0.9 \pm 0.4)$ rad/ μm and $(0, 0.9 \pm 0.5)$ rad/ μm at $f = 1.48$ GHz in (E) and (I), respectively, and $(0, 0 \pm 0.5)$ rad/ μm and $(0, 0 \pm 0.8)$ rad/ μm at $f = 1.22$ GHz in (F) and (J), respectively. FFT intensities of panels (D), (E), (F), (I), and (J) are each normalized with respect to their maximum intensity.

The wavelengths of SWs are found to increase in P3-MQC (Fig. 5.3 (G and H) for $f = 1.48$ GHz and $f = 1.22$ GHz, respectively) when the excitation frequency is reduced; this trend is similar to the SWs excited in SQ-MC. The extension of the dumbbell-shape iso-frequency contour at $f = 1.48$ GHz for P3-MQC (Fig. 5.3I and fig. A.14B) is smaller, since the anisotropy of SWs at $f = 1.48$ GHz involves smaller wave vectors compared to $f = 1.80$ GHz. The dumbbell-shape contour is now closed (Fig. 5.3I) as the maximum wave vector k resides in the sensitivity range of the BLS.

The FFT maps at $f = 1.22$ GHz for SQ-MC (Fig. 5.3F) and P3-MQC (Fig. 5.3J) show wide intensity distributions along k_x direction. These indicate that in real space the SW excitations are confined along x -direction, i.e., in both samples nanochannels are formed and extend in y -direction (orthogonal to \mathbf{H}). The nanochannel formation is due to the inhomogeneous internal field which takes locally small values because of the demagnetization effect of the nanotroughs, and occurs at correspondingly small excitation frequency. The nanochannels in P3-MQC appear to be irregular consistent with Ref. [31]. In the following we present broad-

band SW spectroscopy based on a Vector Network Analyzer (VNA) to explore the frequency dependence of SW absorption and transmission in P3-MQC in detail and compare the results with SQ-MC and a plane film.

Manifold spin wave emission.

We conducted angular-dependent SW spectroscopy in a rotating in-plane field H for the broadband characterization of SW properties in P3-MQC (Fig. 5.4). The field value of 90 mT was applied at various in-plane angles θ between the field direction and the CPW long axis. The SW resonances were determined using scattering parameters (S-parameters) in absorption and transmission configuration using a VNA (see Materials and Methods). In the transmission configuration, two CPWs were used: one for excitation and one for detection of propagating SWs. The propagating SWs induced microwave voltages (S_{21}), which in real and imaginary part oscillated as a function of frequency due to the phase accumulated by SWs between the CPWs. The period Δf of the oscillating S_{21} signal scales linearly with the group velocity v_g according to

$$v_g = \Delta f \cdot s \quad (5.1)$$

where s represents the distance between the two signal lines of the CPWs [15]. The most prominent excitation for the CPWs used in this work is centered around $k_1 = 1.92 \text{ rad}/\mu\text{m}$ (Fig. 5.4A). The second and third most prominent excitations of a bare CPW occur near k_2 and k_3 , respectively. In the following we present SW spectroscopy data taken by the VNA on three different samples: (i) an unpatterned YIG thin film (Fig. 5.4 (B and C)), (ii) the YIG film containing a periodic lattice (SQ-MC) of nanotroughs (Fig. 5.4 (D to F)) and (iii) quasicrystalline lattice (P3-MQC) of nanotroughs (Fig. 5.4 (G to I)). All the three samples were obtained from the same wafer.

The S_{21} signals obtained on the plane YIG film (PF) are displayed in Fig. 5.4B. The oscillating S_{21} signals of propagating SWs appear in three pronounced frequency bands reflecting the wave vector distribution of the CPW around \mathbf{k}_1 , \mathbf{k}_2 and \mathbf{k}_3 . The signals are most pronounced near $\theta = 0$ deg and the bands reside at the lowest frequency near $\theta = 90$ deg. The observed SW propagation modes follow the angular dispersion expected for dipole dominated SWs in a plane film. In Fig. 5.4C we show analytically calculated SW spectra considering the excitation spectrum of CPWs (Fig. 5.4A) and the dispersion relation of the YIG thin film [49]. Resonance frequencies of the prominent modes supported by the CPW follow a sinusoidal-like angular dependence due to the anisotropic dispersion relations of SWs. Oscillations in S_{21} vanish near $\theta \sim 55$ deg and 125 deg indicating a group velocity close to zero. Correspondingly the decay length $l_d = v_g \tau$ is small (τ is the life time of SWs), and, therefore, the amplitude of S_{21} measured at the detector CPW is low. SWs with wave vectors \mathbf{k}_1 , \mathbf{k}_2 and \mathbf{k}_3 are weak at $\theta = 180$ deg due to the non-reciprocity of the DE-type SWs in a YIG film [98]. The non-reciprocity parameter κ is defined in Ref. [136] as the ratio $\kappa = A_0(+H)/A_0(-H)$ of S_{21} oscillation amplitudes $A_0(H)$ for positive and negative fields H . The maximum κ amounts to $\kappa = A_0(+90 \text{ mT})/A_0(-90 \text{ mT}) = 25$ at $f = 4.8 \text{ GHz}$ in the unpatterned YIG plane film.

5.1 Direct observation of multiband transport in magnonic Penrose quasicrystals via broadband and phase-resolved spectroscopy

Considering previous studies on periodic antidot lattices and the magnonic grating coupler effect [16] we show in Fig. 5.4D relevant wave vectors (colored arrows) that are excited due to back-folding according to $\mathbf{k}_1 + \mathbf{G}_{ij}$ [\mathbf{k}_1 is the wave vector provided by the CPW (Fig. 5.4A) and $i, j = 0, \pm 1$]. Indeed, we detect more complex SW spectra on SQ-MC (Fig. 5.4E) compared to PF (Fig. 5.4B). Oscillating SW propagation signals in sample SQ-MC appear even at $\theta \sim 125$ deg (purple arrow) where the vanishing group velocity in PF prohibited a propagation signal. These additional propagation signals highlight the modified SW wave vectors due to the grating coupler effect. The colored arrows in Fig. 5.4E indicate modifications in SW spectra due to wave vectors displayed in Fig. 5.4D in the corresponding colors. Figure 5.4F displays the calculated angular dependencies of back-folded SW modes using a color code consistent with Fig. 5.4D, and compare these with the \mathbf{k}_i modes in the plane film (gray colored lines). The width of a line related to the grating coupler effect (colored line) represents the expected SW amplitude considering the non-reciprocity of SWs. At the intersections of \mathbf{k}_1 and \mathbf{k}_2 modes (gray) with the back-folded modes, angular-dependent SW propagation signals are expected to be modified strongly as observed in the experiments. Note that some back-folded modes such as $\mathbf{k}_1 + \mathbf{G}_{0(-1)}$, $\mathbf{k}_1 + \mathbf{G}_{1(-1)}$ and $\mathbf{k}_1 + \mathbf{G}_{(-1)(-1)}$ do not reach the detector CPW due to the propagation direction opposite to \mathbf{k}_1 . However, the CPW also offers $-\mathbf{k}_1$, and modes like $-\mathbf{k}_1 - \mathbf{G}_{ij}$ can be detected. Resonance frequencies of $\mathbf{k}_1 + \mathbf{G}_{ij}$ and $-\mathbf{k}_1 - \mathbf{G}_{ij}$ are identical. In Fig. 5.4G, we display the Bragg peaks (black circles) and color-coded vectors which represent $\mathbf{k}_1 + \mathbf{F}$ expected for P3-MQC. The Bragg peaks exhibit a manifold rotational symmetry and vectors \mathbf{F} are hence numerous. We focus on basic reciprocal vectors $\mathbf{F}^{(1)}$ and the second prominent reciprocal vectors $\mathbf{F}^{(2)}$ illustrated using differently colored arrows (compare Fig. 5.1C, and see Materials and Methods). Similarly colored arrows are used in Fig. 5.4H to highlight where SW modes $\mathbf{k}_1 + \mathbf{F}$ intersect with the \mathbf{k}_1 branch. Analytic calculations of a large set of SW modes corresponding to $\mathbf{k}_1 + \mathbf{F}$ where \mathbf{F} are different reciprocal vectors $\mathbf{F}^{(1)}$ and $\mathbf{F}^{(2)}$ are shown in Fig. 5.4I. Note that there are many additional reciprocal vectors \mathbf{F} of which the magnitudes are smaller than the basic reciprocal vectors $\mathbf{F}^{(1)}$ (Materials and Methods) [36], and therefore more back-folded modes are possible than we indicate in Fig. 5.4I. The detailed inspection of the data shown in Fig. 5.4H underlines that the aperiodic quasi-crystalline lattice allows one to excite SWs propagating in many more directions than the periodic SQ-MC which exhibits a lower rotational symmetry compared to P3-MQC.

Formation of magnonic band structure in MQC.

In the following we present absorption spectra. The absorption strength is known to scale with the frequency-dependent magnon DOS. Figure 5.5, (A, B and C) displays measured SW absorption spectra of PF, SQ-MC and P3-MQC, respectively (dark indicates large absorption). The overall sinusoidal characteristics of the dark bands of excited SWs are consistent with SWs expected for the plane YIG film. We find specific narrow regions for SQ-MC and P3-MQC (colored arrows in Fig. 5.5,B and C) where the signal strength is clearly reduced or vanishes. We attribute these features to forbidden frequency gaps in SQ-MC and P3-MQC which are not present in PF. Note that the modifications in the SW absorption spectra of SQ-MC and

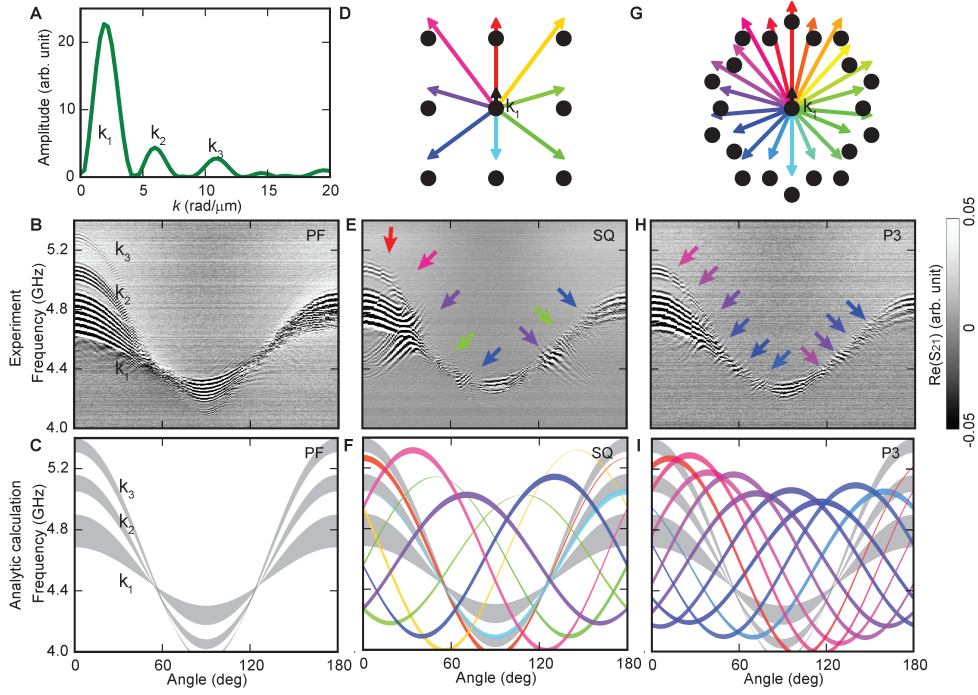


Figure 5.4: Angular-dependent SW spectra in transmission configuration. (A) Excitation spectrum by Fourier transformation of the CPW microwave magnetic field in y -direction. (B) Experimental and (C) calculated angular-dependent spin wave spectra of PF at a field of $\mu_0 H_0 = 93 \pm 3$ mT. (D) Reciprocal lattice points of the SQ lattice (black dots) including vectors of grating coupler induced modes $\mathbf{k}_1 + \mathbf{G}_{ij}$ shown in different colors. The similar combination of reciprocal lattice vectors \mathbf{G}_{ij} with a wave vector $-\mathbf{k}_1$ pointing in the opposite direction of \mathbf{k}_1 is possible as well. (E) Experimental and (F) calculated spectra of the SQ lattice. Gray bands represent the SW branches of \mathbf{k}_1 , \mathbf{k}_2 and \mathbf{k}_3 , and colored lines indicate the back-folded SW modes. Considering the full width at half maximum Δk_i for peaks labelled by k_i (with $i = 1, 2, 3$) in panel (A), the width of gray bands expresses the frequency band corresponding to $k_i - \Delta k_i/2 \leq k_i \leq k_i + \Delta k_i/2$. The thickness of the colored lines represents the amplitude of SW propagation spectra concerning the non-reciprocity of SWs. Arrows indicate the modified SW spectra. (G) Reciprocal lattice points of (D) the P3-MQC lattice. (H) Experimental and (I) calculated SW spectra of P3-MQC encoded and labeled in a consistent way with the SQ data. Colors in (E and F) and (F and I) highlight different SW resonance modes attributed to wave vectors defined in (D) and (G), respectively. In (B), (E) and (H) black and white represent the phase variation of SWs due to wave-vector dependent phase accumulation between two CPWs. The bands of pronounced oscillations are labeled by \mathbf{k}_1 , \mathbf{k}_2 and \mathbf{k}_3 in (B), consistent with the excitation spectrum of the CPW shown in (A).

P3-MQC are different.

In order to understand the origin of the forbidden frequency gaps, the DOS of SWs is calculated from the SW dispersion relation for each sample. Here the oscillator strength related to the projection of magnon eigenfunction and the excitation spectrum of the magnetic field h_{rf} is considered (see Materials and Methods). The angular-dependent weighted projected DOS

5.1 Direct observation of multiband transport in magnonic Penrose quasicrystals via broadband and phase-resolved spectroscopy

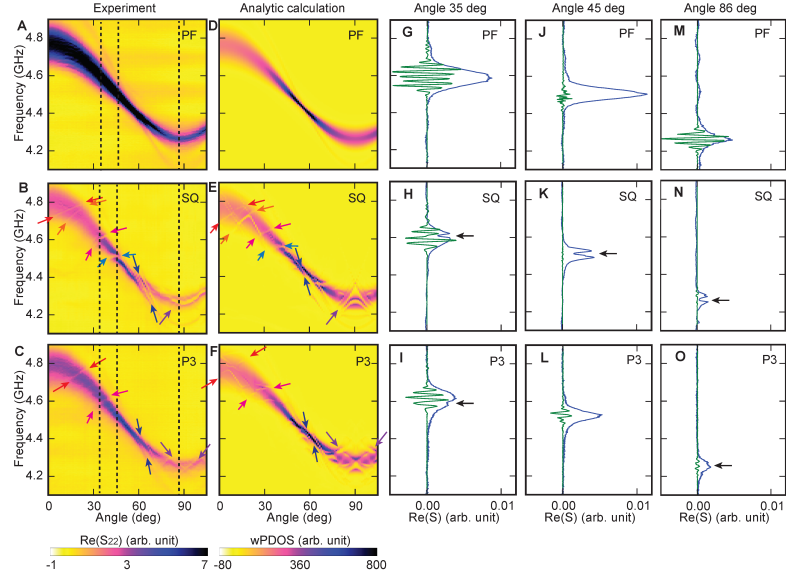


Figure 5.5: Angular-dependent SW spectra in reflection configuration. Angular-dependent SW spectra of (A) PF, (B) SQ-MC and (C) P3-MQC, respectively, in reflection geometry obtained with an applied field $\mu_0 H = 90$ mT. Dark (Bright) represents the SW absorption (background). Colored arrows indicate the modified SW absorption. Angular-dependent wPDOS for SWs of (D) PF, (E) SQ-MC and (F) P3-MQC. Dark (Bright) represents the high (low) value of wPDOS. Colored arrows represent the modified DOS corresponding to the forbidden frequency gaps in (B) and (C). Line cuts of SW spectra of (G) (J) (M) PF, (H) (K) (N) SQ-MC and (I) (L) (O) P3-MQC, respectively, at an angle of 35 deg (G) - (I), 45 deg (J) - (L) and 86 deg (M) - (O). Blue (green) line represents S-parameter in reflection (transmission) configuration. The amplitude of transmission spectra is multiplied by two in order to enhance the modification of the SW characteristics.

(wPDOS) for PF is shown in Fig. 5.5D. At $\theta \sim 55$ deg, the wPDOS is high as the slope of the SW dispersion relation in the dipolar regime is almost flat. The large wPDOS is consistent with the fact that the group velocity v_g at $\theta \sim 55$ deg is almost zero, consistent with the results discussed for Fig. 5.4B.

Gallardo *et. al* considered the plane-wave method [8] for calculating the dynamic response and band gaps of periodically modulated magnetic materials [61, 56]. We applied this method to our surface-modulated SQ-MC (see Materials and Methods). Figure 5.5E shows the wPDOS of SWs in SQ-MC when we consider the reciprocal-lattice vectors \mathbf{G}_{ij} where $i, j = 0, \pm 1, \pm 2, \pm 3$ for the basis set in magnon band calculations. Modifications of the DOS are indicated by arrows. These changes are traced back to the partial band gap openings in the SW dispersion due to the formation of BZs (see Methods and Materials). The calculated modifications are similar to the experimental results (displayed on the left), which indicates that the forbidden gaps observed in the experiments are derived from the back-folding effect and miniband formation in the periodically modulated MC.

Aperiodically arranged nanostructures do not possess Brillouin zones since reciprocal-lattice vectors \mathbf{G} do not exist in quasicrystals. However, one can still choose the reciprocal vectors \mathbf{F} of quasicrystals, and assume corresponding back-folding of the SW dispersion [56, 61]. For our calculation, we consider reciprocal vectors $\mathbf{F}^{(1)}$, $\mathbf{F}^{(2)}$ and $\mathbf{F}^{(3)}$ for the basis set. In the backward volume wave (BVW) regime near $\theta \sim 90$ deg, the modification of the wPDOS is pronounced (Fig. 5.5F). This is because the original SW dispersion relation of BVW is relatively flat, and thus, back-folded SW dispersion relations interact with the original SW dispersion strongly [56]. Consistent modifications are observed in the experiments on P3-MQC. The qualitative agreement indicates the formation of a pseudo-Brillouin zone in a real magnonic quasicrystal which has not been reported before. The resolved p-BZ is defined by the basic reciprocal vectors $\mathbf{F}^{(1)}$ shown in Fig. 5.1C [36]. The purple arrows indicate the angle-dependent modifications of SW absorption in the BVW regime.

Figure 5.5 (G, H and I) shows the line spectra of spin wave absorption and propagation signals at $\theta = 35$ deg for PF, SQ-MC and P3-MQC, respectively. The strong oscillation of $\text{Re}(S_{21})$ due to spin wave propagation between emitter and detector CPW is detected at the frequency for which the spin wave absorption peaks in sample PF (Fig. 5.5G) are large. According to Eq. 5.1 the group velocity is 0.30 km/s. In sample SQ-MC (Fig. 5.5H), mode \mathbf{k}_1 and a back-folded mode $\mathbf{k}_1 + \mathbf{G}$ coexist in the same frequency regime. Here, a dip is observed in the spin wave absorption spectra at $f = 4.6$ GHz, with a width of about 20 MHz. The oscillation signal of spin wave propagation at this frequency is modified as well. We attribute this modification to the partial gap opening of the magnonic band structure of SQ-MC. Group velocity of SWs for sample SQ-MC below and above $f = 4.6$ GHz are 0.26 and 0.36 km/s, respectively, which indicates that different modes dominate the SW propagation above and below the frequency. A similar type of modification is also seen in sample P3-MQC (Fig. 5.5I).

At $\theta = 45$ deg, observed modifications are of a different kind. In Fig. 5.5J we report a strong absorption peak for sample PF, but the amplitude of SW propagation is very small due to the low group velocity of 0.17 km/s. For SQ-MC (Fig. 5.5K), a clear dip occurs in the absorption spectrum. The dip is more than half of the SW absorption strength. The SW propagation appears to be completely suppressed, most likely due to a pronounced gap opening in the spin wave band. For sample P3-MQC (Fig. 5.5L) the measured absorption peak is feature-less and contrary to PF and SQ-MC a relatively strong SW propagation signal with a group velocity of 0.32 km/s is detected. We attribute this observation to back-folded modes forming an allowed miniband with an improved group velocity. At $\theta = 86$ deg, BVW-SWs with a group velocity of 0.28 km/s were emitted in PF. Similar to the angle 45 deg, SW absorption is suppressed at $f = 4.26$ GHz in sample SQ-MC. At the same frequency, a slight modification of SW absorption is detected in sample P3-MQC. Here, the SW group velocity amounts to 0.3 km/s. Note that sample SQ-MC shows a very similar group velocity of 0.31 km/s above the frequency of $f = 4.26$ GHz at which the absorption is suppressed.

Figure 5.6 displays spin wave band structures and wPDOS of SQ-MC and P3-MQC (blue curves) compared to the SW dispersion relation of the YIG film (red) at the field of the experiment applied with an angle of $\theta = 45$ deg. The diameter of dots forming the blue curves in Fig. 5.6 (A and C) represents the projection amplitude of the spin wave eigenfunction $|\Psi_{\mathbf{k}}\rangle$ onto a basis

5.1 Direct observation of multiband transport in magnonic Penrose quasicrystals via broadband and phase-resolved spectroscopy

plane-wave mode $|\mathbf{G}\rangle$ ($|\mathbf{F}\rangle$) corresponding to the reciprocal lattice vector \mathbf{G} (reciprocal vector \mathbf{F}) of the MC (MQC), relevant for backfolding wave vectors \mathbf{k} into the 1st BZ (p-BZ) according to $|P_{\mathbf{G}}(\mathbf{k})| = |\langle \mathbf{G} | \Psi_{\mathbf{k}} \rangle|$ ($|P_{\mathbf{F}}(\mathbf{k})| = |\langle \mathbf{F} | \Psi_{\mathbf{k}} \rangle|$) (see Materials and Methods, fig. A.15). The original spin wave dispersion relations (red dashed lines) fall onto a region with many back-folded modes in each of the two samples in Fig. 5.6(A and C). At the angle of 45 deg, the group velocity of plane-film spin waves is low. However, the numerous back-folded modes interact with the original dispersion relation and can possess higher group velocities than the original mode. Such back-folded modes then carry the pronounced spin wave propagation signals observed experimentally in SQ-MC and P3-MQC (Fig. 5.4(E and H)). At the same time hybridization of modes and novel allowed minibands form separated by small frequency gaps (highlighted by vertical arrows). Accordingly the wPDOS of SQ-MC and P3-MQC in Fig. 5.6B and D (light-blue colored area) show fine structures of local maxima and dips (horizontal arrow) while the unstructured film (dashed red line) exhibits a smooth wPDOS. (In fig. A.16 we depict for direct comparison the band structures and DOS calculated at the four angles 0, 35, 45 and 86 deg for SQ-MC and P3-MQC side by side.) In the experiments the absorption spectra do not feature all the predicted dips. We attribute this to SW damping in the real samples which was not considered for the calculations.

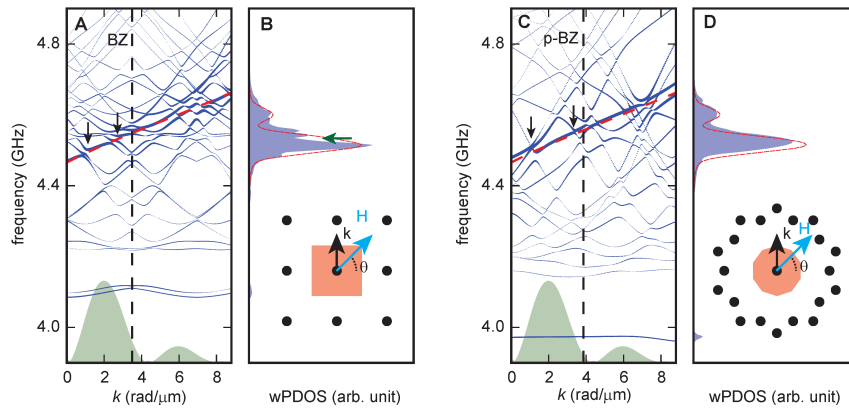


Figure 5.6: Band structures and density of states of the periodic and aperiodic lattice. (A) Band structure and (B) wPDOS of SWs of the SQ-MC. (C) Band structure and (D) wPDOS of SWs of the P3-MQC. In (A) and (C) the original spin wave dispersion relation of the YIG film is indicated by a red dashed line. Vertical arrows highlight band gap openings. The size of blue dots in band structure graphs indicate the corresponding projection amplitudes $|P_{\mathbf{G}}(\mathbf{k})|$ or $|P_{\mathbf{F}}(\mathbf{k})|$, which display the spin precession amplitudes. In green we show the excitation spectrum of the CPW microwave magnetic field in arbitrary units. A field value of 93 mT was assumed and applied at an angle of $\theta = 45$ deg. Insets of (B) and (D) display reciprocal lattice points (i.e. end points of reciprocal-lattice vectors \mathbf{G} and reciprocal vectors \mathbf{F}), the BZ and the p-BZ (orange areas) of SQ-MC and P3-MQC, respectively. The horizontal green arrow in (B) highlights the most prominent dip in the DOS induced by miniband formation. In (B) and (D) the wPDOS of SWs of the plain YIG film is indicated by a red dashed line.

Discussion

SWs in aperiodic P3-MQC are emitted quasi-omnidirectionally following the iso-frequency contour of the SW dispersion relation of the YIG film (fig. A.14). For the periodic SQ-MC we observe a strikingly different excitation pattern in k -space (fig. A.14 (C to E)); here, the Fourier transformed SW intensity display resonance peaks at $\mathbf{k} \pm \mathbf{G}$ which reside even outside the iso-frequency contour valid for an unpatterned film (yellow symbols in fig. A.14 (C to E)). The SWs were imaged in the region where SWs propagated in y -direction, and therefore we expected to see only FFT peaks with positive k_y values. But, for SQ-MC, FFT peaks with negative k_y values are also observed (Fig. 5.2E, and Fig. 5.3 (B and C)). This indicates the formation of the Bloch waves of SWs in the periodically modulated MC. According to the dispersion relation of the YIG film, the intensity of the SW modes $\mathbf{k} + \mathbf{G}_{i(-1)}$ ($i = 0, \pm 1, \pm 2$) is expected to be stronger than $\mathbf{k} + \mathbf{G}_{i1}$ at $f = 1.48, 1.62$ and 1.8 GHz (fig. A.17). However, the experimental results showed the opposite trend. This suggests that the coherent backscattering of SWs is modified by the grating. We assume the SW excitation at large absolute wave vectors to be allowed through the inhomogeneous broadening introduced by the unintentionally rough nanotroughs in the otherwise planar YIG film.

In Ref. [56] it was shown for periodically modulated films that the magnitude and width of forbidden gaps (dips) were tuned by the depth of nanotroughs. For the 1D surface-modulated MC of Ref. [56], the width of the 1st band gap for DE-type SWs increased with the depth of stripe-like grooves and the correspondingly enhanced dipolar fields induced by dynamic magnetic surface charges. We thus speculate that by deeper nanotroughs in P3-MQC more pronounced magnonic band gap openings can be created. Complete band gaps were realized for photonic quasicrystals. Here, the modification of individual elements induced a photonic waveguide [137]. Along an irregular path, light was guided and bent at sharp corners [138]. If complete band gaps were reached for SWs, magnonic quasicrystals would form an analogous basis for SW waveguides. A large out-of-plane magnetic field was required in Ref. [13] to generate a complete band gap in a periodic square lattice of antidots and exploit the isotropic forward volume waves propagating in a specific high symmetry direction. Quasicrystals possess however manifold rotational symmetries; therefore complete band gaps would allow one to create SW waveguides in a flexible manner and with a higher design degree of freedom concerning propagation directions.

In summary, we studied SW propagation and absorption in magnonic quasicrystals based on Penrose P3 tilings. We used BLS for phase-resolved SW microscopy and VNA for broadband SW spectroscopy. We obtained two important novel insights: (1) omnidirectional SW emission in the magnonic quasicrystal is observed by BLS microscopy and is attributed to the unconventional rotational symmetry of the Penrose P3 lattice; (2) using broadband spectroscopy by means of VNA, we evidenced band gap openings and correspondingly modified magnon DOS consistent with analytical calculations. The unconventional symmetries are advantageous for integrated magnonic circuits in that optimized multi-directional magnon emission is realized

5.1 Direct observation of multiband transport in magnonic Penrose quasicrystals via broadband and phase-resolved spectroscopy

at a single frequency and complete band gaps might enable flexible magnon wave guides without applying a large out-of-plane magnetic field.

Materials and Methods

Sample fabrication. The single-crystalline 100 nm thick YIG films were grown on (111) GGG substrate by liquid phase epitaxy (LPE) treated by the company Matesy GmbH in Jena, Germany. Al/Ti layers were evaporated on top of the YIG films with a thickness of 10/150 nm. The MCs and MQC masks were patterned on hydrogen silsesquioxane negative electron beam resists using electron beam lithography (EBL). Inductively coupled plasma (ICP) etching and ion beam etching (IBE) were performed to form a decagonal mesa and to introduce nanotroughs in the YIG film for the fabrication of the MCs and the MQC as summarized in Tab. 5.1.

Samples were immersed into Hydrofluoric Acid bath to remove Al/Ti completely. Consecutively, CPWs were patterned on the MCs and MQC via EBL, and Ti/Au (4/200 nm) were sputtered before lift-off processes. Symmetry axes of SQ-MC and P3-MQC are parallel to the long axis of the CPWs. The width of a signal line and ground lines of the CPWs are 800 nm, and the gap between the signal and ground lines is 640 nm. A center-to-center separation between two CPWs is 12 μm .

Note that SQ-MC used in SW spectroscopy and BLS experiments are different. As indicated in Tab. 5.1, the diameters and depths of nanotroughs are different for each sample while the characteristic length a stay same. SQ-MC used for BLS measurement misses a column of nanotroughs indicated in fig. A.18. As the missing column is far from the region of interest (ROI) for BLS experiment, we expect that the backfolding effect of the square lattice for SWs are still observed.

For the investigation of SW properties in quasicrystals, an identical P3-MQC was used. First of all, spin wave transport measurement was conducted by broadband SW spectroscopy technique. Afterwards, one of the CPW which used to be connected to port 2 of VNA was removed by injecting a large current. Then, spatial distribution of SWs were obtained by the BLS measurement. Note that a part of ROI is overlapped with the place where the CPW was mounted as shown in fig. A.19.

Broadband spin-wave spectroscopy. SW excitations/propagation were studied via all electrical SW spectroscopy. The two ends of the CPW (patterned on top of the devices, see fig. A.20) were connected to a VNA to apply microwaves. The in-plane angle θ of the applied field H was varied. A 2-port VNA allowed us to generate a microwave magnetic field with frequencies ranging from 10 MHz to 26.5 GHz. The microwave with a power of -25 dBm was applied at the port 1(2) of the CPW in order to excite magnetization precession. The precession-induced voltage was detected at port 2 via reading the scattering parameter S_{21} (S_{22}) where the numbers 2 and 1(2) in the subscript denote the detection and excitation port. An external magnetic field

Table 5.1: Parameters of prepared and investigated sample

Sample Name	equipment	Lattice	Type of lattice arrangement	Rotational symmetry in k -space	Characteristic length a (nm)	Diameter D (nm)	Depth t (nm)
PF	VNA	-	-	-	-	-	0
SQ-MC	VNA	Square	Periodic	4	900	288 ± 10	21.7 ± 1.5
SQ-MC	BLS	Square	Periodic	4	900	272 ± 23	8.8 ± 2.4
P3-MQC	VNA	Penrose	Aperiodic	10	900	299 ± 18	23.7 ± 2.1
	BLS	P3					

The YIG films were 100 nm thick. The overall area of the samples is $52.8 \times 50.2 \mu\text{m}^2$. The CPW signal line width was $0.8 \mu\text{m}$. Errorbars of diameter D and depth t of nanotroughs indicate the 95 % confidence interval of the diameters of 5 nanotroughs which were chosen from the respective microscopy image at the center of the samples.

H of up to 90 mT was applied under an angle θ between the external field H and the CPW's long axis. In order to increase signal-to-noise ratio, $\Delta S_{21} = S_{21}(H) - S_{21}(\text{Ref})$ was evaluated where $S_{21}(H)$ and $S_{21}(\text{Ref})$ represent scattering parameters measured at a given field H and at 90 mT along $\theta = 90$ deg, respectively.

Brillouin light scattering microscopy. Spin wave eigenmodes were imaged via BLS microscopy with/ without phase resolution at room temperature using a setup similar to Refs. [76, 77]. Figure A.21 shows a sketch of the experimental configuration. The end of the CPW was electrically bonded to a printed-circuit board, and the circuit board was connected to a signal generator for a microwave application. The microwave excited spin precession in the MC/MQC near the CPW at a fixed frequency. A magnetic field of 10 mT was applied parallel to the long axis of the CPW via a permanent magnet for BLS measurement after that a field of 90 mT was applied in order to first saturate the samples. A lens with a numerical aperture of 0.85 was used to focus a 473 nm wavelength laser with a spot size of 300 nm onto the samples. Laser power was set to 1 mW. Energy shifts of reflected laser light due to the inelastic magnon-photon scattering were detected by a triple-tandem Fabry-Pérot interferometer. The device was positioned under the laser spot using x, y piezo-positioning system. The step size to acquire the SW images was 100 nm. We exploited phase-resolved inelastic light scattering while exciting spin waves phase-coherently at the straight CPW. The nanotrough positions were reconstructed in that we overlaid (i) atomic force microscopy (AFM) images taken on the studied MC/MQC (ii) the BLS data and (iii) the exposure masks for CPWs and electron beam lithography of nanotroughs.

Bragg peaks of crystal/quasicrystal structure. Figure A.22 (A and B) shows the square and Penrose P3 lattice used for the fabrication of the MC and MQC, respectively. The Penrose P3 tiling is composed of acute and obtuse rhombi structures with a same side length a , and the real space are filled out with these rhombi in self-similar manner. The FFT of the crystal structure shows Bragg peaks as shown in fig. A.22A. Bragg peaks of the square lattice

5.1 Direct observation of multiband transport in magnonic Penrose quasicrystals via broadband and phase-resolved spectroscopy

correspond to its reciprocal lattice vectors \mathbf{G}_{ij} , which are expressed as follows:

$$\mathbf{G}_{ij} = i\mathbf{A} + j\mathbf{B} \quad (5.2)$$

where $\mathbf{A} = (2\pi/a, 0)$ and $\mathbf{B} = (0, 2\pi/a)$, i and j are integer numbers. The lines bisecting the reciprocal-lattice vectors \mathbf{G}_{10} , $\mathbf{G}_{(-1)0}$, \mathbf{G}_{01} , $\mathbf{G}_{0(-1)}$ form the square-shaped BZ boundary in square-lattice based crystals as shown in fig. A.22A. On the contrary to the periodic crystals, quasicrystals do not possess reciprocal-lattice vectors in k -space. A Bragg peak pattern is expressed with basic reciprocal vectors $\mathbf{C}_p = [2\pi/(a \cos(\pi/10))] \times (\cos(p\pi/5), \sin(p\pi/5))$ where $p = 0, 1, 2, 3, 4$. The reciprocal vectors are expressed by a linear combination of the basic reciprocal vectors,

$$\mathbf{F} = m_0\mathbf{C}_0 + m_1\mathbf{C}_1 + m_2\mathbf{C}_2 + m_3\mathbf{C}_3 + m_4\mathbf{C}_4 \quad (5.3)$$

which are chosen such that they: (i) are related to the strongest Fourier coefficients describing the distribution of the material parameters in the quasicrystal, (ii) cover the reciprocal space with the appropriate density, in order to describe the possible distribution of the magnon eigenmodes, and (iii) possess the rotational symmetry of the diffraction pattern [36]. m_p are integer numbers. Here $\mathbf{F}_{q=p}^{(1)} = \mathbf{C}_p$ and $\mathbf{F}_{q=p+5}^{(1)} = -\mathbf{C}_p$ where $q = 0, 1, \dots, 9$. Note that $\mathbf{F}_{q+5}^{(1)} = -\mathbf{F}_q^{(1)}$ and therefore $\mathbf{F}_{q+10}^{(1)} = \mathbf{F}_q^{(1)}$. The other intense peaks are expressed as $\mathbf{F}^{(0)} = (0, 0)$, $\mathbf{F}_q^{(2)} = \mathbf{F}_{q-1}^{(1)} + \mathbf{F}_{q+2}^{(1)}$ and $\mathbf{F}_q^{(3)} = \mathbf{F}_q^{(1)} + \mathbf{F}_{q+1}^{(1)}$ with the magnitude of $|\mathbf{F}^{(0)}| = 0$, $|\mathbf{F}^{(2)}| = 2\pi/(a \cos(\pi/5))$ and $|\mathbf{F}^{(3)}| = \pi/a$, respectively. The intensity of $\mathbf{F}^{(0)}$, $\mathbf{F}^{(2)}$ and $\mathbf{F}^{(3)}$ in diffraction patterns of the Penrose P3 lattice is higher than the intensity of the basic reciprocal vectors \mathbf{C}_p . Note that Bragg peaks of the Penrose P3 based quasicrystals exhibit ten-fold rotational symmetry. The lines bisecting the reciprocal vectors $\mathbf{F}_q^{(1)}$ form the decagon-shaped p-BZ boundary in Penrose P3 based quasicrystals as shown in fig. A.22B.

Calculation of density of state for MC/MQC. In order to calculate the DOS of SW, the band structure of SWs in the MCs and MQCs needs to be calculated. Considering Ref. [61, 56], the magnonic band structures for the MCs and MQCs are calculated using the plane wave method [8]. For calculating the magnon bands, 49 smallest reciprocal lattice vectors, \mathbf{G}_{ij} with $i, j = 0, \pm 1, \pm 2, \pm 3$ are considered for in the case of SQ-MC. In the case of P3-MQC, we considered 31 high intensity Bragg peaks, $\mathbf{F}^{(0)}$ and $\mathbf{F}_q^{(i)}$ with $i = 1, 2, 3$ and $q = 0, 1, \dots, 9$. The material and physical parameters used for the calculation are as follows: a saturation magnetization $M_s = 180$ mT, an exchange constant $A = 3.65 \times 10^{-12}$ J/m, a gyromagnetic ratio $\gamma/2\pi = 28.024$ GHz/T, characteristic length $a = 900$ nm, a diameter of nanotroughs $D = 295$ nm, a depth of nanotroughs $t = 23$ nm, and the thickness of the YIG film is 100 nm. The wave number of 1st BZ (p-BZ) boundary of sample SQ-MC (P3-MQC) is 3.49 rad/ μm (3.96 rad/ μm) along k_y -direction. An angular dependent external field $\mu_0 H(\theta) = (93 + 3 \cos(2\theta))$ mT is considered for the analytic calculation in order to match the results with experimental data. The Fourier coefficients for circle defined in Ref. [61] are used for the calculation of magnonic band structures. The calculation result of the band structure for SQ-MC inside the 1st BZ at $\mu_0 H = 93$ mT and $\theta = 45$ deg is shown in fig. A.15A. Eigenfrequencies $f_\eta(k)$ (η denotes the

back-folded mode number) from this calculation display the band structure of the SQ-MC. Gap openings in a SW band structure of 1D magnonic crystals in DE configuration only appear at the BZ boundary. Here, 2D magnonic crystals even possess partial band gaps inside the BZ due to the hybridization of the back-folded branches of the BVW mode. Using the projection of the magnon eigenfunction, $|\Psi_{\eta,\mathbf{k}}\rangle$, onto the plane wave mode $|\mathbf{G}\rangle$ ($|\mathbf{F}\rangle$) we calculated the projected DOS (PDOS) of SWs for the MC (MQC) as follows:

$$\rho_{\mathbf{G}(\mathbf{F})}(f) = \frac{-1}{\pi} \sum_{\eta} \int dk \text{Im} \left[\frac{|P_{\eta,\mathbf{G}(\mathbf{F})}(k)|^2}{f - f_{\eta}(k) + i0^+} \right] \quad (5.4)$$

where 0^+ is a positive infinitesimal value and $P_{\eta,\mathbf{G}(\mathbf{F})}(k) = \langle \mathbf{G}(\mathbf{F}) | \Psi_{\eta,\mathbf{k}} \rangle$ is the projection amplitude. Depending on the MC or MQC we either used \mathbf{G} or \mathbf{F} , respectively, in Eq.(5.4). η runs over the number of magnon bands (1 to 49 for MC and 1 to 31 for MQC). The limits of integration over k is 0 to $8.8 \text{ rad}/\mu\text{m}$. The size of blue dots in band structure graphs (see fig. A.15) indicate the projection amplitude $|P_{\eta,\mathbf{G}(\mathbf{F})}(k)|$, which corresponds to the spin precession amplitude. For the comparison to the SW spectra in reflection geometry using VNA, we consider the Fourier transformation of the excitation spectrum of the CPW induced microwave magnetic field, $I(k)$, (green transparent in Fig. 5.6A) as a weight factor and the weighted PDOS (wPDOS) is expressed as

$$\rho_{\mathbf{G}(\mathbf{F})}^w(f) = \frac{-1}{\pi} \sum_{\eta} \int dk \text{Im} \left[\frac{|P_{\eta,\mathbf{G}(\mathbf{F})}(k)|^2 |I(k)|^2}{f - f_{\eta}(k) + i0^+} \right]. \quad (5.5)$$

The range of the wave vectors covering the k_1 and k_2 modes of $I(k)$ is up to $8.8 \text{ rad}/\mu\text{m}$ which is beyond the wave vector of the boundary of the 1st BZ of the *periodic* SQ-MC. In order to extend the dispersion relation beyond its 1st BZ (fig. A.15), a magnon band structure with respect to the reciprocal lattice vectors \mathbf{G} is considered which are responsible for the backfolding of wave vectors \mathbf{k} into the 1st BZ (\mathbf{G}_{01} vector for our study, see fig. A.15C). Then, the results are concatenated to the original band structure (Fig. 5.6A and fig. A.15D). Figure 5.6B shows the calculated wPDOS of the SQ-MC at $\mu_0 H = 93 \text{ mT}$ and $\theta = 45 \text{ deg}$.

For the *aperiodic* P3-MQC, we calculated the dispersion relations in that we considered wave vectors $0 \text{ rad}/\mu\text{m} \leq k \leq 8.8 \text{ rad}/\mu\text{m}$ along the k_y -direction. The responsible reciprocal vector for the projection of magnon eigenfunctions was $\mathbf{F}^{(0)}$. Note that we could not simply extend the dispersion relation of P3-MQC by further concatenating the band structure due to the aperiodicity. Figure 5.6C shows the dispersion relation of the P3-MQC at $\mu_0 H = 93 \text{ mT}$ and $\theta = 45 \text{ deg}$. The most pronounced excitation around the k_1 mode of the CPW (Fig. 5.4A) covers the p-BZ (vertical dashed line in Fig. 5.6C). The number of SW branches and characteristics of the gaps are different from the ones of the MC (Fig. 5.6A). The corresponding wPDOS is displayed in Fig. 5.6D. The calculations have been performed for different field orientation angles θ for SQ-MC and P3-MQC. The angular-dependent densities of states considering our experimental setting are shown in Fig. 5.5 (E and F), respectively.

Acknowledgments

Funding

The research was supported by the SNSF via grant numbers 163016 and 177550. V.S. Bhat acknowledges support from the foundation for Polish Science through the IRA Programme financed by EU within SG OP Programme.

Author contributions

D.G., S.W. and V.S.B. planned the experiments, designed the magnonic crystals and quasicrystals. S.W. prepared the samples. S.W. performed the experiments supported by K.B. S.W. and D.G. analyzed and interpreted the data. S.W. performed the analytic calculation supported by M.H. S.W., V.S.B., M.H. and D.G. wrote the manuscript. All authors commented on the manuscript.

Competing interests

The authors declare that they have no competing interests.

Data and materials availability

All data needed to evaluate the conclusions in the paper are present in the paper and/or the Supplementary Materials. Additional data related to this paper may be requested from the authors.

5.2 Magnons in aperiodic worm-like nanochannels of 2D artificial magnetic quasicrystals

In the previous studies of both artificial magnetic quasicrystal (AMQ) based on CoFeB and MQC based on YIG, SWs propagating through nanochannels in quasicrystals were observed using the BLS technique. The diffraction limit of light used in the BLS experiments restricts the spatial resolution of SW images, and thus the physical parameters of nanochannels such as their width might be overestimated as indicated in [31]. In order to overcome the diffraction limit of visible light, we performed Scanning transmission X-ray microscopy (STXM) at the MAXYMUS endstation at Helmholtz-Zentrum Berlin. We investigated a magnonic quasicrystal prepared from a 100 nm thick YIG film, which taken from the same substrate of the samples reported in the previous section. Nanotroughs with a diameter of 190 nm and a depth of 17 nm were introduced at the vertices of the Penrose P3 tiling. The characteristic length of the Penrose tiling amounted to 900 nm. We used a positive resist mask (CSAR-62) fabricated by electron beam lithography (EBL) and ion beam etching (IBE) for the patterning. A CPW made

of Ti/Cu/Al (5 nm/120 nm/10 nm) was prepared on top of the quasicrystal using the lift-off technique. The substrate was mechanically thinned and then further thinned by focused ion beam etching from the back side in the form of a square window ($50 \times 50 \mu\text{m}^2$), which allowed us to conduct STXM measurements sensitive to the z -component of the dynamic magnetization. There are regions of the MQC and the plane YIG film inside the X-ray window. For the SW imaging (Fig. 5.7), continuous-wave microwaves were applied to the CPW ranging from 1.17 GHz to 2.25 GHz to induce SWs in the MQC while a magnetic field of +10 mT was applied parallel to the long axis of the CPW (+ x -direction). The three straight dark stripes represent the CPW (indicated by white dashed lines). The injected microwave power was set between -17 dBm and -18 dBm. Time-dependent magnetization precession was obtained stroboscopically. These time-dependent spin precession data allowed us to calculate the local oscillation amplitude and phase of the SW for each data point to create amplitude and phase maps (Fig. 5.7b and c, respectively). For the detailed understanding of the phase evolution of SWs as well as their amplitudes, those images are overlaid as shown in Fig. 5.7d.

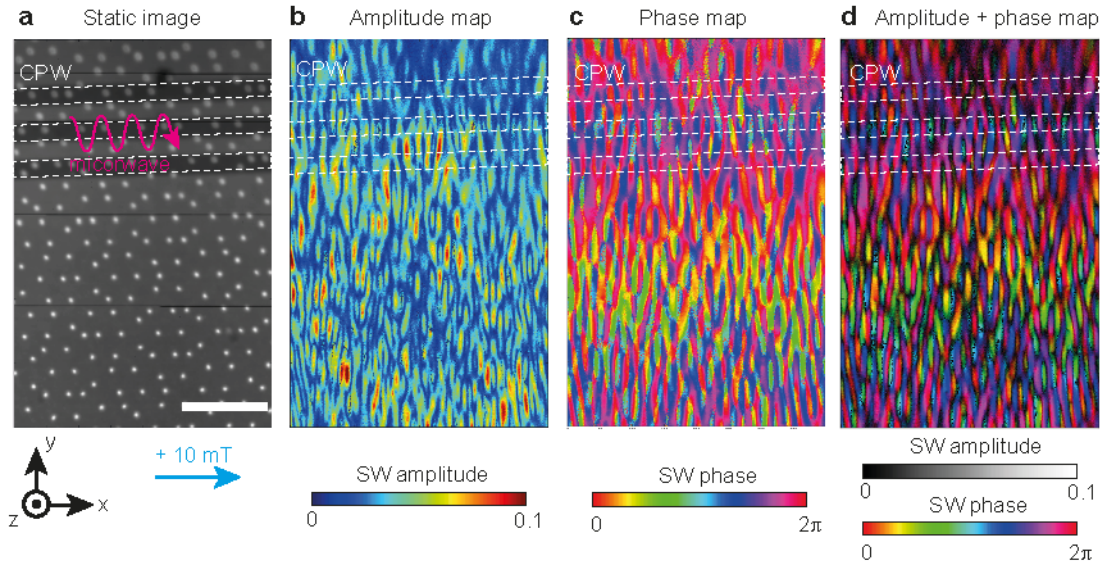


Figure 5.7: (a) Static image of MQC. Microwaves were applied to the CPW integrated on the MQC made of YIG. An external magnetic field of 10 mT was applied parallel to the long axis of the CPW (indicated by white dashed lines). X-rays with a nano-metre sized spot transmitted through the sample were detected while a continuous-wave microwave signal at 1.48 GHz was applied to the CPW, and spin dynamics were imaged. The scale bar represents $5 \mu\text{m}$. (b) SW intensity and (c) phase map. (d) Combined image of (b) and (c). Gray and hue color scales represent intensity and phase of SWs, respectively.

5.2 Magnons in aperiodic worm-like nanochannels of 2D artificial magnetic quasicrystals

Spin waves along a Conway worm

We imaged SWs in a region including a structural Conway worm (shown as zigzag white dashed lines in Fig. 5.8a) propagating through the entire quasicrystal. In the YIG-based MQC, we again observed SW nanochannels previously reported for CoFeB-based AMQs. The nanochannels were bent irregularly due to the aperiodic arrangement of nanotroughs, and the phases of SWs for each channel were found to be different (Fig. 5.8b). Here several nanochannels were investigated (channel 1: outside the Conway worm, channel 2 and 3: nearby the Conway and channel 4: inside the Conway worm). Solid white lines in Fig. 5.8b interconnect local maxima of SW amplitudes for each nanochannels. There are no identical bends of nanochannels. Inside each SW channel along y -direction, the full width at half maximum (FWHM) of the spin-precessional amplitudes are extracted as a function of y coordinate. The corresponding channel widths vary from 160 nm to 1000 nm along the Conway worm (Fig. 5.8c). Channel 3 near the Conway worm provides the narrowest channel width amounting to 160 nm, which is smaller than the diffraction limit of light used in the BLS experiment. Hence, an X-ray based imaging technique was essential to experimentally extract the SW nanochannel width. Note that the measured width of the spin precessional amplitude along a nanochannel does not vary periodically which one could expect for a periodic antidot lattice. The aperiodic width variation is different from nanochannel to nanochannel consistent with simulations reported for CoFeB based AMQs. The measured minimum width of 160 nm is larger than the minimum width predicted for the CoFeB-based AMQ, which was 50 nm [31]. XMCD based imaging on CoFeB-based AMQs was not possible in the course of this thesis.

Coherent scattering of SWs

Figure 5.9a shows further SW imaging data. Regions (A) and (B) indicate areas filled by the MQC and plane YIG film, respectively. The SWs propagated upwards and downwards with respect to the CPW (Fig. 5.9b and c). Interestingly, worm-like nanochannels at 1.22 GHz created inside the quasicrystal are observed outside the quasicrystal as well (Fig. 5.9b). This observation was not anticipated. Channel-like features changed by increasing the frequency, and the wavelength along the y -axis decreased (Fig. 5.9c). Figure 5.9d and e shows the FFT results processed on the SW images (A) inside and (B) outside of the quasicrystal at $f = 1.68$ GHz. Similar to the results in the previous section, dumbbell shaped iso-frequency contours are observed, corresponding to the anisotropic SW dispersion relation in the dipole-dominated regime. The FFT result inside the quasicrystal reveals that SWs propagate not only in $-y$ -direction imposed by the CPW but also in $+y$ direction (Fig. 5.9d), indicating the coherent back-scattering of SWs. The intensity distribution suggests the formation of a pseudo-Brillouin zone (p-BZ). On the contrary, the intensity of SW modes with positive k_y vectors partly vanishes outside the quasicrystal (Fig. 5.9e). We attribute this findings to the lack of scattering centers in the plain film. Line cuts of the SW intensity in reciprocal space at $k_x = +10.0$ rad/ μm inside and outside the MQC are shown in Fig. 5.9f and g, respectively.

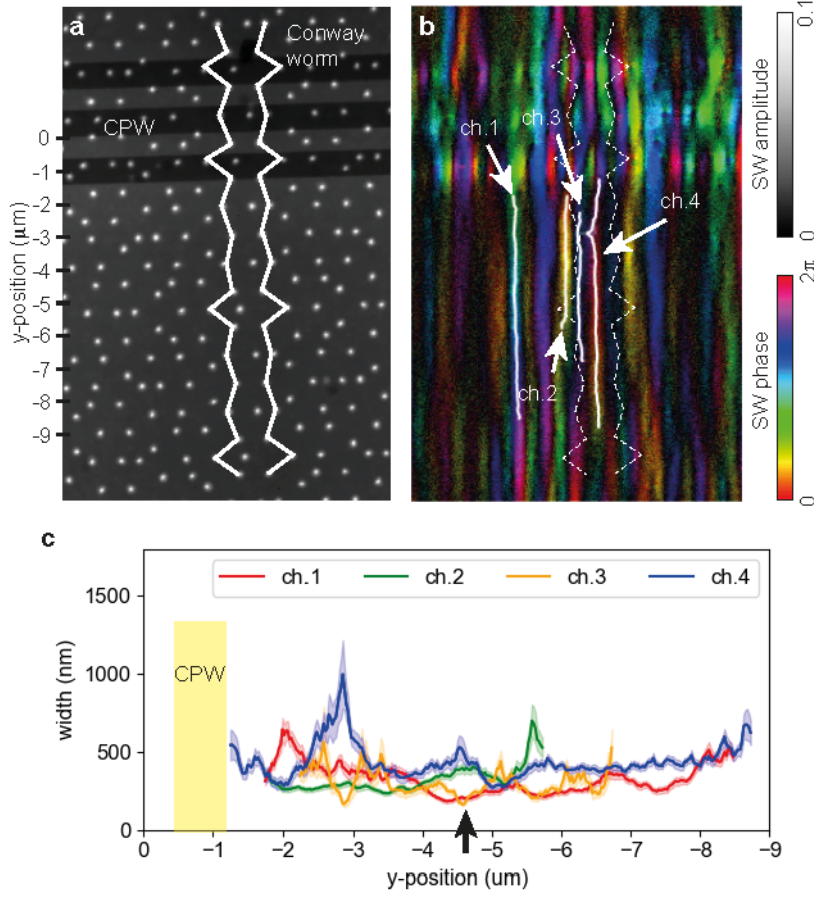


Figure 5.8: (a) Static and (b) dynamic transmission image of SWs at $f = 1.22$ GHz inside the MQC. Gray and hue color scales in (b) represent intensity and phase of SWs, respectively. White dashed lines indicate the Conway worm existing in the MQC. White solid lines in (b) indicate the local maxima of the spin precessional amplitudes along the selected channels (Channel 1 to 4). (c) Width profile of the selected SW nanochannels. Channel 4 indicates the SW nanochannel propagating inside the Conway worm. The black arrow indicates the narrowest width of observed SW nanochannels in the MQC.

The back-scattering effect is consistently observed at different frequencies above 1.48 GHz inside the MQC. The calculated back-scattering ratio A^+ / A^- , where A^+ and A^- represent the local maximum of the FFT intensity at positive and negative k_y , respectively, confirms the different strength of back-scattering. In principle, we would expect $A^+ = 0$ outside the MQC. However, we anticipate a locally varying membrane thickness introducing strain in YIG. This strain modifies the magnetic configuration at the boundary of the X-ray window, resulting in the reflection of SWs. Therefore, there are contributions from SWs with a positive k_y outside the MQC (Fig. 5.9e and g).

In order to investigate the SW properties of the MQC further, we have performed SW imaging

5.2 Magnons in aperiodic worm-like nanochannels of 2D artificial magnetic quasicrystals

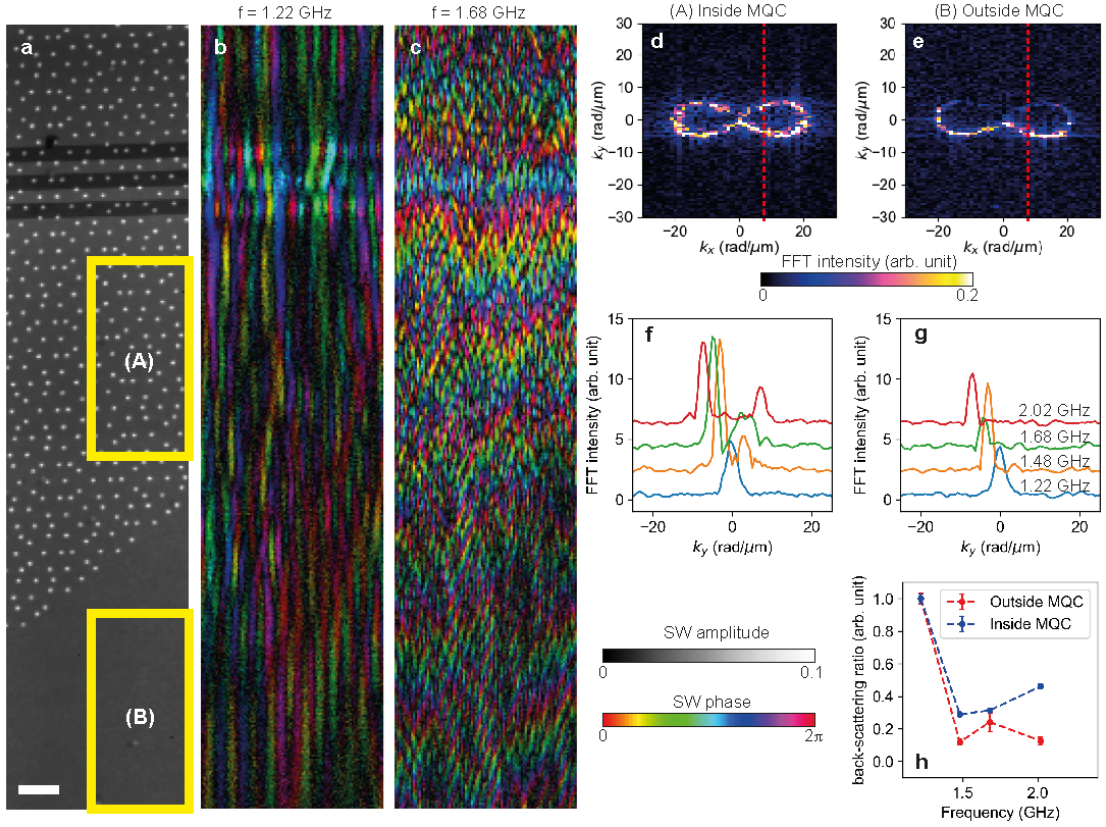


Figure 5.9: (a) Static X-ray transmission image of the MQC. SW images inside and outside the MQC at (b) $f = 1.22$ GHz and (c) $f = 1.68$ GHz. Gray and hue color scales represent intensity and phase of SWs, respectively. SW intensity in reciprocal space after Fourier transformation of the SW images (d) inside MQC (represented as region (A) in (a)) and (e) outside the MQC (represented as region (B) in (a)). Line cuts of the SW intensity in reciprocal space at $k_x = 10.0 \text{ rad}/\mu\text{m}$ (f) inside and (g) outside the MQC at several frequencies. (h) Back-scattering ratio of SW in $+k_y$ direction with respect to $-k_y$ at $k_x = 10.0 \text{ rad}/\mu\text{m}$.

on a relatively large area ($10 \mu\text{m}^2$). The applied frequency was varied from 1.17 GHz to 2.26 GHz. The CPW was at the center of the image so that we considered the SWs propagating upwards and downwards in a similar manner (Fig. 5.10a). Figure 5.10b taken at $f = 2.145$ GHz shows that the intensity of SWs propagating downwards is higher than upwards. This observation is attributed to the non-reciprocity of SWs. We performed FFT on the images and extracted the data at $k_x = 0.0 \text{ rad}/\mu\text{m}$ in order to obtain the k_y component of SWs. Figure 5.10c shows the experimentally extracted dispersion relation $f(k_y)$ of SWs propagating along the y -axis. Overall, the frequency of the SW modes increased with increasing absolute value of k_y . Interestingly, the amplitude of the SW branch was strongly suppressed at around 2.145 GHz in positive and negative k_y values. Indeed a partial gap opening at the p-BZ around 2.15 GHz was predicted by the theoretical calculation of the dispersion relation from the previous section (Fig. 5.10d). A complete gap opening in the band structure would be advantageous for a filter application and guiding of SWs by removing a specific line of nanotroughs. This theory

still predicts multiple bands crossing the observed gap opening. Further studies are needed to substantiate potential of quasycrystals for GHz-filter applications.

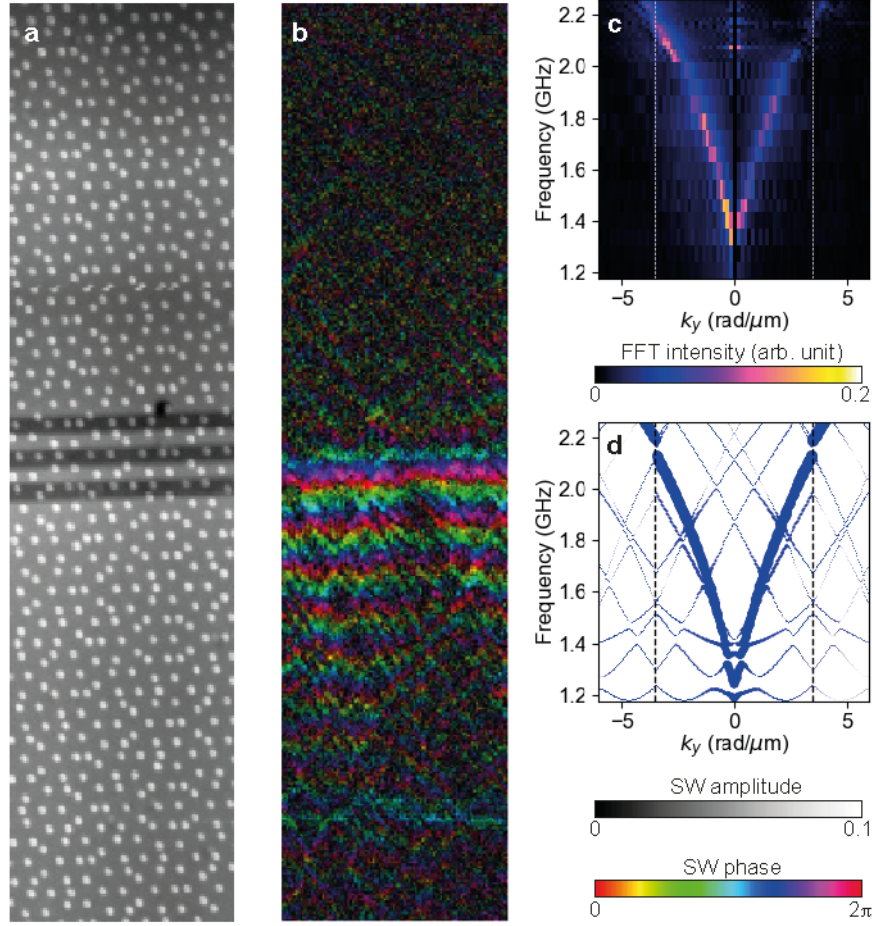


Figure 5.10: (a) Static and (b) dynamic transmission image of SWs at $f = 2.145$ GHz inside the MQC. Gray and hue color scales in (b) represent intensity and phase of SWs, respectively. (c) SW band structure at $k_x = 0$ rad/ μm . The white dashed lines indicate the pseudo-Brillouin zone boundary of the MQC. (d) Calculated band structure of the MQC. The black dashed lines indicate the p-BZ boundary

6 Magnonic nanogratings arranged on quasicrystalline lattice

The Magnonic grating coupler (MGC) effect enables the generation of short wavelength SWs, which is key for the performance of miniaturized magnonic devices [16, 17, 18, 19, 66]. Quasicrystals do not exhibit reciprocal lattice vectors \mathbf{G} in reciprocal space. However, Bragg peaks of a quasicrystalline structure densely fill reciprocal space in an omnidirectional fashion [36], and therefore aperiodically arranged magnonic grating couplers allow one to emit SWs with manifold propagation directions and wavelengths.

We fabricated grating couplers consisting of 100-nm-thick Py nanopillars in periodic and quasicrystalline arrangements on insulating YIG films. They operated as MGC. We observed magnon emission omnidirectionally into YIG with a broad range of wave vectors and frequencies of up to 25.3 GHz in an unprecedentedly small magnetic field. Short wavelength forward volume waves, which own isotropic propagation characteristic, were also successfully excited via MGC effect for the first time. Using two such emitters we evidenced constructive and destructive interference of sub-100 nm wavelength magnons at a separate detector antenna allowing for a binary 1/0 output operation. This study is important for future information processing via wave-logic on the nanoscale. A manuscript is under preparation.

6.1 Broadband nanograting coupler of multiple magnetic resonances approaching 5G telecommunication

S. Watanabe, V. S. Bhat, A. Mucchietto, S. Shan, E. N. Dayi and D. Grundler

Contribution I contributed to the manuscript as follows: Design of the sample and planing of experiment together with V. S. B and D. G. Sample fabrication of periodic and aperiodic GC samples using clean room facilities (CMI) together with E. N. D. Experiments for broadband SW spectroscopy. Data analysis of experimental data as well as simulation data supported by D. G. Note that simulation was performed by A. M. and S. S.

The layout of the manuscript was reformatted and the references were integrated into the

thesis' bibliography.

Abstract

Magnons are promising quanta used for transmission and processing of information for future communication devices. High frequency magnon excitation with a short wavelength is realized by the magnonic grating coupler effect. However, conventional magnonic grating elements have so far been resonant at a single frequency, and thus the condition to excite short wavelength spin waves were restricted. Here we study a broadband grating coupler effect using ferromagnetic nanopillars in a crystalline and quasicrystalline arrangement. Multiple magnon resonances in the ferromagnetic nanopillars serve as broadband grating elements. The quasicrystalline arrangement allows for spin wave emission omnidirectionally with a broad range of wave vectors. 25 GHz magnon entering 5G telecommunication is detected in square lattice-based grating coupler sample. Binary 1/0 output operation was performed by short wavelength spin wave interference. This study lays the groundwork for the fabrication of future magnonic devices for high frequency networking system.

Main Part

Magnons (spin waves, SWs) are collective spin excitations in magnetically ordered materials, used for transmission and processing information, without a flow of electrons [4]. In comparison to the complementary metal-oxide semiconductor (CMOS) circuits based on electron's charge used in current communication devices, wave-logic devices based on magnon efficiently work with low loss and high speed [3]. The wavelength of SWs, coupled to microwaves, is miniaturized by a factor of 10^5 with respect to a microwave wavelength in free space, e.g., sub 100 nm at 25 GHz used for 5G communication devices. Toward the fabrication of magnonic devices, efficient excitation of short wavelength magnons is key. A magnonic grating coupler (GC) effect found by H. Yu *et al.* used periodically arranged ferromagnetic nanobars (one dimension, 1D) and nanodisks (two dimension, 2D) integrated to a low damping SW propagation medium [16, 17, 18]. However, near 25 GHz SWs were not excited effectively as (1) the microwave frequency did not match the FMR frequency of grating elements and (2) the wavelength of SWs did not correspond to reciprocal lattice vectors \mathbf{G} , which restricted the width of frequency bands for communication technologies.

Apart from a FMR at which all spins in a magnetic material precess uniformly, a quantized magnon which forms standing spin wave in nanostructures would be excited at the different frequency of the FMR. Ferromagnetic thick dots made of $\text{Ni}_{81}\text{Fe}_{19}$ (Permalloy, Py) exhibited radially confined SW modes at different fields at a fixed frequency [140, 141]. By increasing the thickness of the dots, new axially confined SW modes between radially confined modes emerged [140]. In a vortex state of a ferromagnetic disk, azimuthal SW modes in a broad frequency range were detected [142]. These nanostructures exhibiting multiple resonance modes associated with quantized magnons would serve as grating elements operated in a broad frequency range. For the excitation of broadband wave vector SWs, quasicrystalline

6.1 Broadband nanograting coupler of multiple magnetic resonances approaching 5G telecommunication

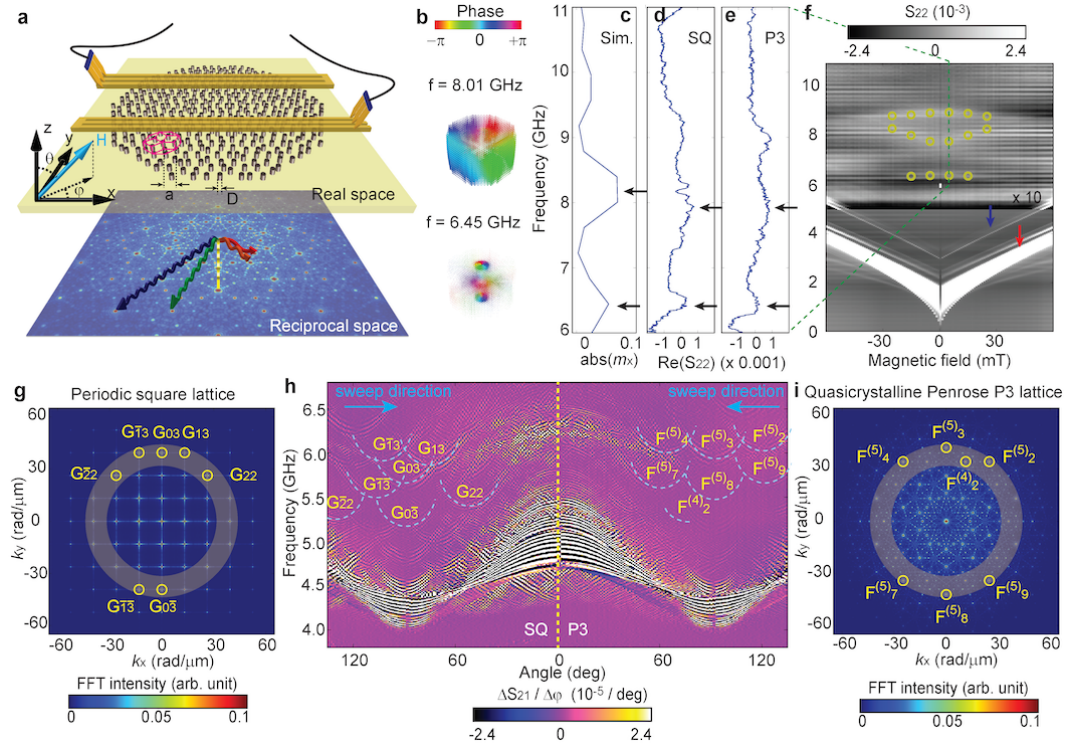


Figure 6.1: Broadband SW emission omnidirectionally using ferromagnetic grating nanopillars. (a) A schematic image of the experimental setup (top). Aperiodically arranged ferromagnetic nanopillars (brown) are fabricated on top of the YIG film (yellow), and SWs are excited by applying microwaves on the integrated CPWs. The magnetic field is applied either in-plane or out-of-plane. Via the grating coupler effect, SWs corresponding to the reciprocal vectors \mathbf{F} of the Penrose P3 lattice are emitted (bottom). (b) Spatial distribution of spin precession in a ferromagnetic nanopillar with a diameter of 155 nm imaged via Mayavi [139], and (c) SW spectrum simulated at the field of 5 mT applied in-plane. Experimental SW absorption spectra for (d) periodic SQ-ND155 and (e) aperiodic P3-ND155 taken at 5 mT. Black arrows in (c), (d) and (e) represent SW resonance peaks attributed to mode pattern shown in (b). (f) Field-dependent SW absorption spectra for sample P3-ND155. White (black) represents the large (small) spin precessional motion in the sample. Weak resonances are highlighted by circles. Horizontal black and white stripes are artifacts. (g) A false color plot of the square lattice in reciprocal space. Peaks corresponding to reciprocal lattice vectors \mathbf{G} appear periodically. (h) Angular dependent SW propagation spectra for SQ-ND95 (left) and P3-ND95 (right). Light blue dashed lines represent on-resonant grating coupler modes with a wave vector $k \approx 30$ rad/ μm . Black-white-black oscillations along the frequencies axis indicate SW propagation signals (i) A false color plot of the Penrose P3 lattice in reciprocal space. Yellow circles in (g) and (i) indicate \mathbf{G} and \mathbf{F} around 30 rad/ μm (indicated by a grayish ribbon) observed in (h).

arrangement of magnetic gratings is promising since reciprocal vectors \mathbf{F} of quasicrystals densely fills out the reciprocal space due to their self-similar property [113]. On top of this, SWs emit in a quasi-circular fashion thanks to their manifold rotational symmetry [143].

In this work, we study a broadband grating coupler effect using aperiodically arranged ferromagnetic nanopillars fabricated on insulating ferrimagnetic Yttrium iron garnet (YIG) films by means of GHz-SW spectroscopy [98] and micromagnetic simulation [89]. Ferromagnetic nanopillars made of Py are arranged at the vertices of Penrose P3 tiling, a 2D analogue of a natural quasicrystal [122, 144]. Coplanar waveguides (CPWs) are integrated on top of the GC samples to introduce microwaves for the excitation/detection of SWs, and wave vectors of SWs are related to the reciprocal vectors \mathbf{F} of the Penrose P3 lattice (Figure 6.1a) [36]. The magnetic field was applied either in-plane (with an azimuthal angle φ and polar angle $\theta = 90$ deg) or out-of-plane (at a polar angle of $\theta = 0$ deg). With a small magnetic field of 5 mT in $+x$ -direction, the vortex state is present in the ferromagnetic nanopillars. As shown in Fig. 6.1b,c, spin-precessional motion is excited at the center (perimeter) of the nanopillar at the frequency $f = 6.45$ GHz ($f = 8.01$ GHz). Higher eigenmodes forming standing waves with different wavelengths in the nanopillar are also excited (not shown). Such resonance frequencies are observed in the experimental SW absorption spectra obtained on the square lattice-based periodic (Fig. 6.1d) and Penrose P3 lattice-based aperiodic (Fig. 6.1e, f) GC samples. For the periodic GC sample, excited SWs possess wave vectors \mathbf{k} provided by the CPW plus the reciprocal lattice vectors \mathbf{G} (Figure 6.1g). In the angular dependent spectra, corresponding propagating GC modes are observed as oscillating black-white-black signals in Fig. 6.1h (left). The Penrose P3 lattice exhibits nearly isotropically distributed reciprocal vectors \mathbf{F} as seen in the diffraction pattern in Fig. 6.1i. SW modes with corresponding wave vectors are observed in Fig. 6.1h (right). Our study reveals omnidirectional SW emission with an unprecedentedly broad range of wave vectors and frequencies by utilizing nanopillars with internally confined magnon modes of high order. These nanopillar based grating elements are shown to operate up to 5G-compatible magnonic devices resonantly.

Omnidirectional spin wave emission

For the present study, we fabricated square lattice-based periodically and Penrose P3 lattice-based aperiodically arranged ferromagnetic nanopillars with a spacing of $a = 480$ nm on top of the 100 nm thick YIG film (Figure 6.1a). Ferromagnetic nanopillars are made of 100 nm thick Py with a different diameter D for each sample summarized in Tab. 5.II. CPWs are integrated on top of the GC samples with a spacing s of $12\ \mu\text{m}$. A Vector Network Analyzer (VNA) was connected to the CPWs in order to characterize SW properties in the GC samples by applying/detecting microwaves using scattering parameters (S-parameters, see Methods). The magnetic field was applied parallel to the CPW long axis (x -direction, in-plane) to characterize the eigenmodes of grating elements. Figure 6.1f displays the SW absorption spectra (S_{22} parameter) of sample P3-ND155 (aperiodically arranged ferromagnetic nanopillars with a

6.1 Broadband nanograting coupler of multiple magnetic resonances approaching 5G telecommunication

diameter of 155 nm). Below 6 GHz, field-dependent SW absorption spectra (white) in the YIG film are observed (indicated by arrows). The wave vector of SW at low frequency (red arrow) is \mathbf{k} imposed by the CPW due to the inhomogeneous microwave distribution (Supplementary Section A). At the higher frequency mode (blue arrow) corresponds to the perpendicular standing SW (PSSW). These excitation spectra are also observed in a plane YIG film (PF) sample (supplementary Section A). Additionally, several SW absorption peaks are detected for P3-ND155 at frequencies > 6 GHz at 5 mT (Figure 6.1e). These peaks are attributed to standing SWs in the ferromagnetic nanopillars. At the field of 5 mT applied in-plane, magnetic moments inside the nanopillars form a vortex (Supplementary Section B), and standing SWs are excited with the different spatial characteristics for the eigenmodes as shown in Fig. 6.1b,c. Convincingly, the resonances attributed to magnon resonances inside the nanopillars are observed independently of the lattice. Hence, they appear also in SQ-ND155 (Fig. 6.1d).

By increasing the magnetic field to 90 mT, the core of the vortex shifts from the center of the nanopillar (Supplementary Section B) to the rim and the ferromagnetic nanopillars stay operative as broadband grating elements. Figure 6.1h displays angular dependent SW propagation spectra (S_{21} parameter) with the field of 90 mT taken on samples SQ-ND95 and P3-ND95 (95 nm diameter). ΔS_{21} of reflecting difference in scattering parameter taken at successive angles are used in order to enhance signal-to-noise (SNR) ratio (see Methods). Oscillations of ΔS_{21} (black and white) originate from the phase accumulation between CPWs. Sinusoidal-like propagation spectra observed around 4.5 GHz all over the angle represent the angular dependence of SW modes characterized by \mathbf{k} reflecting the anisotropic dispersion of a thin YIG film (Supplementary Section A).

On-resonant GC modes at higher frequency are observed (dashed lines). Local minima of the angular dependent curves of GC modes are denoted by the corresponding reciprocal lattice vectors \mathbf{G} of the square lattice and reciprocal lattice vectors \mathbf{F} of the Penrose P3 lattice excited between 5.3 and 6.3 GHz relevant to the wave vectors of around $30 \text{ rad}/\mu\text{m}$ (Yellow transparent belts indicated in Fig. 6.1g,i). Due to the high rotational symmetry of the Penrose P3 lattice, the GC modes are emitted nearly isotropically [143]. SWs with $\mathbf{k} + \mathbf{G}$ and $\mathbf{k} + \mathbf{F}$ not parallel to \mathbf{k} travel longer from CPW to CPW than SWs with \mathbf{k} due to the different SW propagation distance s_{eff} , defined by the angle β between \mathbf{k} and $\mathbf{k} + \mathbf{G}$ or $\mathbf{k} + \mathbf{F}$, and is expressed as $s_{\text{eff}} = s/|\cos \beta|$ [66]. Attenuation is large for SWs propagating for long distance and GC modes with $|\beta|$ larger than 45° are barely detected. This is also true for modes with $-\mathbf{k} - \mathbf{G}$ and $-\mathbf{k} - \mathbf{F}$. Note that resonance frequencies of SWs with $\mathbf{k} + \mathbf{G}$ ($\mathbf{k} + \mathbf{F}$) and $-\mathbf{k} - \mathbf{G}$ ($-\mathbf{k} - \mathbf{F}$) are the same.

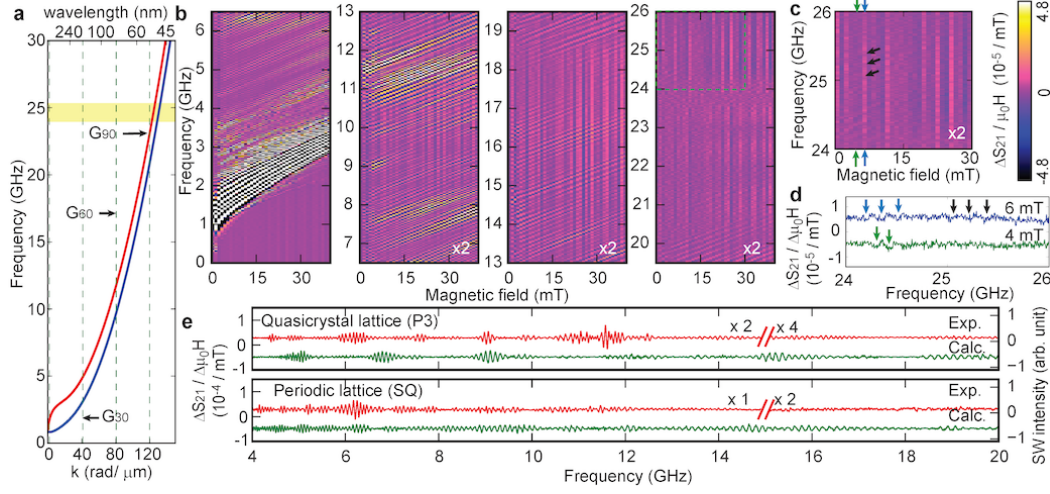


Figure 6.2: **Short wavelength spin wave coupled to higher order spin wave modes of grating elements.** (a) Dispersion relation of the 100 nm thick YIG film for Damon-Eschbach mode. (b) Field-dependent SW propagation spectra for sample SQ-ND155. The field of 5 mT is applied parallel to the long axis of the CPW. Black and white represents the oscillation of S_{21} , reflecting SW propagation from CPW 1 to the CPW 2. (c) Magnified image of (b) above 24 GHz, and (d) line cut of (b) at 4 mT and 6 mT. Oscillation signals of S_{21} are observed near 24.5 GHz and 25.3 GHz. (e) Line spectra ΔS_{21} of P3-ND155 (top) and SQ-ND155 (bottom) at 5 mT.

Broadband spin wave emission

In Fig. 6.2a, Damon Eschbach (DE)-type SW dispersion relation is shown. Figure 6.2b represents the field-dependent SW propagation spectra of sample SQ-ND155. SW propagation over a broad frequency range up to 22 GHz is clearly observed, in particular higher order eigenmodes in the nanopillars are excited at the high frequency regime of 5G above 25 GHz, SWs are excited around 5 mT as shown in Fig. 6.2c,d. According to the dispersion relation, the wavelength of SWs at 25.3 GHz corresponds to 52 nm shorter than the SW with a wave vector $|\mathbf{k} + \mathbf{G}_{90}| = 120 \text{ rad}/\mu\text{m}$, and the group velocity amounts to 2.0 km/s.

For quasicrystalline structures, reciprocal vectors \mathbf{F} are different compared to \mathbf{G} , and thus SW propagation amplitudes are different. Figure 6.2e and f shows SW line spectra at 5 mT for quasicrystalline P3-ND155 (top) and periodic SQ-ND155 (top) obtained by experiment, respectively. Sample P3-ND155 covers broader intervals of frequency almost continuously up to 16 GHz. SW propagation is also detected at 19 GHz (see also Supplementary Section C). This tendency is also observed by theoretical calculation result (bottom, see Section E). For SQ-ND155, SW propagation is observed over smaller frequency intervals. This is because the reciprocal lattice vectors \mathbf{G} are discrete. The reciprocal vectors \mathbf{F} of the Penrose P3 lattice densely fill the reciprocal space (see Methods).

In several integrals the propagation amplitude of the SWs is low. At a fixed frequency, SWs with several GC modes $\mathbf{k} + \mathbf{F}$ emit in different directions. Since (1) wave vectors of SWs and (2) effective SW propagation distance s_{eff} are different, the accumulated phase differences of the SWs at the detector CPW are different (dephasing), explaining the low SW propagation

amplitude.

Forward volume wave

Unlike SW modes for in-plane magnetization, forward volume waves (FVWs) with magnetization pointing perpendicular to the film surface show isotropic properties. Above a certain field, the low-field vortex state in the ferromagnetic nanopillars turns into a saturated state, and their magnetization vectors point along the z -direction. Due to the change of the magnetization configuration, the characteristics of standing SWs inside the nanopillars are also changed. In Fig. 6.3a, the magnetic field of 500 mT was applied along $+z$ direction in order to saturate the sample (Supplementary Section B), and then the field was swept down to 300 mT. In this field regime, both the ferromagnetic nanopillars and the YIG thin film were saturated. The field-dependent SW absorption spectra (S_{11} parameter) of sample SQ-ND95 show FVW-SWs whose resonance frequencies vary linearly. The peaks above 9 GHz at 500 mT are attributed to standing SWs in the saturated ferromagnetic nanopillars. Figure 6.3b shows that at the corresponding resonance frequencies SWs propagate through the YIG media via the resonant grating coupler effect. In the uniformly magnetized nanopillars, quantized SWs are excited in with a specific number of modes in radial (n_r), azimuthal (n_l) and longitudinal direction (n_z). In Fig. 6.3c, three dimensional (3D) representation of quantized SWs in a ferromagnetic nanopillar with a diameter of 95 nm for different frequencies are displayed. By increasing the diameter D of nanopillars, the resonance frequencies of eigenmodes are decreased as shown in Fig. 6.3c,d,e. For the fabrication of compact magnonic devices operated with high frequency microwaves in the regime of 5G telecommunication with a low-bias field: (1) decreasing the diameter D in order to increase the resonance frequency (Figure 6.3f), (2) increasing the thickness of the nanopillars to have uniform magnetization at low field, and (3) reducing the periodicity to excite short wavelength SWs, which is also helped by reducing the diameter D . Applying a bias-magnetic field slightly off-axis of the ferromagnetic nanopillars enlarges the line width of quantized SW modes [145] and thereby is advantageous to broaden the operation frequency bands. Utilizing ferromagnetic nanopillars as a grating element are of great potential for high frequency magnonic devices.

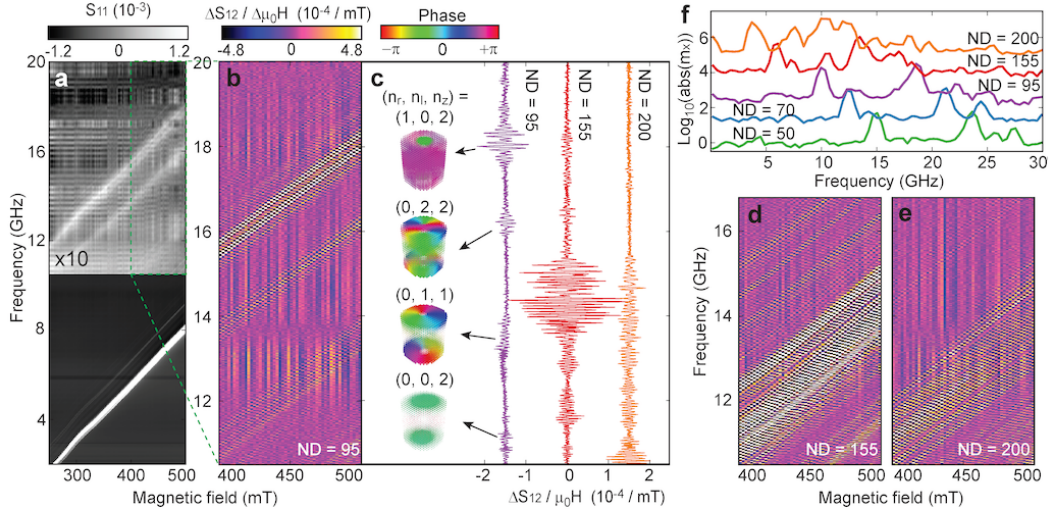


Figure 6.3: **Multiple eigenmodes of axially magnetized ferromagnetic nanopillars for different diameters.** (a) Field-dependent SW absorption spectra of SQ-ND95. White (Black) represents the large (small) SW absorption (S_{11} parameter). The field up to 500 mT is applied along $+z$ -direction. (b) Field-dependent SW propagation spectra (S_{21} parameter) of SQ-ND95. (c) SW propagation spectra of SQ-ND95 (left), SQ-ND155 (center) and SQ-ND200 (right) at 500 mT. Inset displays spatial distribution of spin precessional motion in a ferromagnetic nanopillar with a diameter of 95 nm for different frequencies where GC modes are observed. Field dependent SW propagation spectra of (d) SQ-ND155 and (e) SQ-ND200. (f) Amplitude of simulated spin precessional motion for ferromagnetic nanopillars with a different diameter D of 50, 70, 95, 155 and 200 nm.

logic operation of spin wave

Toward fabrication of miniaturized wave-based logic devices, superposition of short wavelength SWs is key. Three CPW antennas on top of the GC samples were connected to the VNA: Two CPWs (antenna 1 and antenna 3) for microwave inputs and one CPW (antenna 2) for the detection of interfered SWs (See Figure 6.4a). If the amplitude of input microwave voltage is the same (V_0) and there is a phase difference $\Delta\phi$ between two SWs from antenna 1 and 3, an oscillation amplitude of induced voltage by the superposed SWs at antenna 2 traveling from antenna 1 and 3 is expressed as follows:

$$V_s = V_0 \sqrt{2 + 2 \cos(\Delta\phi)}. \quad (6.1)$$

SWs interfere constructively (destructively) if the spins precess in-phase (out-of-phase). Sample SQ-ND155 rotated by 180 deg was used for the SW interference experiment with the field applied perpendicular to the CPW long axis ($\varphi = 90$ deg and $\theta = 90$ deg). The field amplitude is below 90 mT, and thus, the vortex is formed in the nanopillars. Note that phase difference of two microwave inputs $\Delta\phi_{\text{vna}}$ from the VNA contains a frequency dependent internal phase offset ϕ_0 due to a calibration specification of the VNA, and therefore phase difference of SWs is expressed as $\Delta\phi = \Delta\phi_{\text{vna}} - \phi_0$.

Figure 6.4b and c represent field-dependent SW propagation spectra at $\Delta\phi_{\text{vna}} = 280$ deg and 100 deg, respectively. Around $f = 19.2$ GHz, SW oscillation signal is clearly seen in Fig. 6.4b due to the constructive SW interference. On the contrary, SW propagation signal vanishes in Fig. 6.4c, as the superposed SW amplitude is close to zero. Figure 6.4d shows line cut spectra at $f = 19.2$ GHz for each $\Delta\phi_{\text{vna}}$, and one can extract the field-dependent SW oscillation amplitude between 4.8 and 8.8 mT using sinusoidal function (see Fig. 6.4e). The oscillation amplitude as a function phase difference $\Delta\phi_{\text{vna}}$ follows the Eq. 6.1 nicely, and $\phi_0 = -80$ deg is extracted from the fitting result.

At 19.2 GHz, SW possesses wave vector $\mathbf{k} + \mathbf{G} + \mathbf{k}_{\text{pssw}}$ with $\mathbf{G} = \mathbf{G}_{(-5)3}$ from CPW antenna 1 and \mathbf{G}_{53} from CPW antenna 3, and \mathbf{k}_{pssw} (Supplementary Section D). SWs propagate diagonally with respect to \mathbf{k} . The wavelength amounts to 70 nm. Superposition of diagonally propagated SWs is also observed for quasicrystal based grating coupler sample (Supplementary Section E). These experiments indicate that XOR and NAND circuits would be realized with four CPW antennas [146, 147] integrated on the GC samples, on which SW propagates diagonally with a short wavelength.

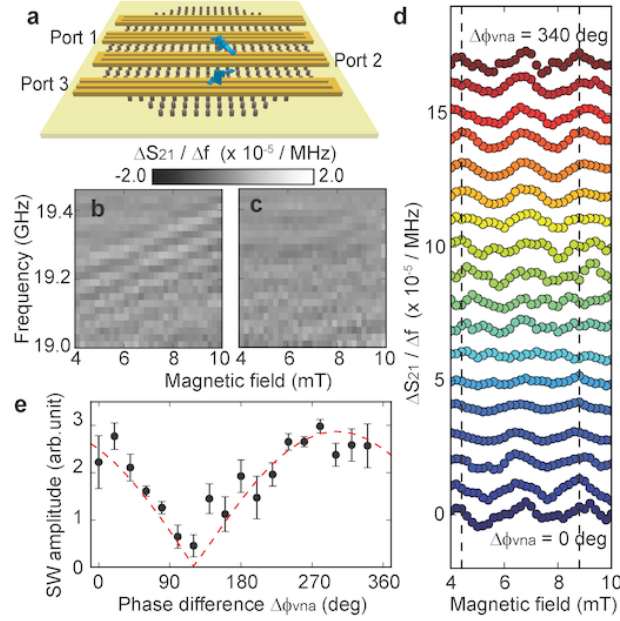


Figure 6.4: **Logic operation using short wavelength SW.** (a) Schematic image of SW interference experiment. Microwaves with a phase difference $\Delta\phi_{\text{vna}}$ are applied to two CPW antennas, and a voltage induced by interfered SWs underneath the other antenna is detected. Interfered SW data (frequency vs. magnetic field) at (b) $\Delta\phi_{\text{vna}} = 280$ and (c) 100 deg. At $\Delta\phi_{\text{vna}} = 280$ deg ($\Delta\phi_{\text{vna}} = 100$ deg), constructive (destructive) SW interference is observed. (d) Line cuts of interfered SW spectra taken at $f = 19.2\text{GHz}$ for each phase difference with a step of 20 deg. (e) Interfered SW amplitude as a function of the phase difference $\Delta\phi_{\text{vna}}$. Errorbars indicate fitting error of sinusoidal function on line cut spectra of d, and the dashed line represents the fitting result of interfered wave formula shown in Eq. 6.1

Conclusion

We demonstrated nearly isotropic SW emission in in-plane fields using aperiodically arranged nanogratings made of 100 nm thick Py ferromagnetic nanopillars mounted on insulating ferromagnetic YIG thin films. According to micromagnetic simulations, vortex states are stabilized in nanopillars in small in-plane fields, and several standing SW modes are observed over a large frequency range. These resonant modes in the grating elements allow for broadband SW excitations in the YIG film. SWs associated with discrete reciprocal lattice vectors \mathbf{G} of the periodic square lattice respond to the microwave discontinuously in frequency domain, while dense sets of reciprocal vector \mathbf{F} of the aperiodic Penrose P3 lattice allow SWs to be excited over wide frequency intervals. At a low field, SW propagation signals confirm that a high-frequency SW above 25 GHz (52 nm wavelength) propagates through the YIG film in the square lattice-based grating coupler samples.

Saturated ferromagnetic nanopillars exhibit different quantized magnon modes in radial, azimuthal and axial directions for different diameters D . The change of the diameter D of the nanopillars is relevant to the replacement of the material of grating elements. In the conventional grating coupler effect, high saturation magnetization materials, such as CoFeB and CoFe with saturation magnetization of 1.8 and 2.4 T, were used to excite short wavelength SWs in a high FMR frequency regime. SWs propagating even diagonal to the CPWs via the GC effect interfere constructively/ destructively depending on their phase difference, indicating the possibility of wave-based calculation with short wavelength SWs. Hybrid nanostructures composed of ferromagnetic nanopillars integrated on the low damping SW propagation media promise magnonic devices operated at high frequencies suitable for 5G telecommunication without applying large magnetic fields and using a standard ferromagnetic material like Py.

Table 6.1: Parameters of prepared and investigated grating coupler sample

Sample name	Lattice	Lattice arrangement	Rotational symmetry	Diameter D (nm)
PF	-	-	-	-
SQ-ND95	Square	Periodic	4	96.2 ± 3.1
SQ-ND155	Square	Periodic	4	154.9 ± 1.4
SQ-ND200	Square	Periodic	4	200.3 ± 3.9
P3-ND95	Penrose P3	Aperiodic	10	95.0 ± 3.5
P3-ND155	Penrose P3	Aperiodic	10	161.1 ± 2.8
P3-ND200	Penrose P3	Aperiodic	10	211.8 ± 6.0

The YIG films were 100 nm thick. The overall area of the samples is $52.8 \times 50.2 \mu\text{m}^2$. The CPW signal line width was $0.8 \mu\text{m}$. Errorbars of diameter D and depth t of nanotroughs indicate the 95 % confidence interval of the diameters of 5 nanotroughs which were chosen from the respective microscopy image at the center of the samples.

Method

Sample fabrication. The single-crystalline 100 nm thick YIG films were grown on (111) GGG substrate by liquid phase epitaxy (LPE) treated by the company Matesy GmbH in Jena, Germany. Using electron beam lithography (EBL) and lift-off processing, ferromagnetic nanopillars were prepared from evaporated Py after performing oxygen plasma cleaning to ensure the solid contact between ferromagnetic nanopillars and the YIG films. Physical parameter and arrangement of ferromagnetic nanopillars are summarized in Tab. 6.1. Subsequently, CPWs for each GC sample were patterned via EBL, and Ti/Au (4/120 nm) were evaporated before lift-off processes. Symmetry axes of the periodic and aperiodic GC samples are parallel to the long axis of the CPWs. The width of a signal line, ground lines of the CPWs and the gap between the signal and ground lines are 800 nm, 800 nm and 640 nm, respectively. A center-to-center separation s between two CPWs is 12 μm .

Broadband spin-wave spectroscopy. SW properties are studied via all electrical SW spectroscopy using VNA (Figure 6.1a), allowing us to generate a microwave with frequencies ranging from 10 MHz to 26.5 GHz. The microwave with a power of 0 dBm was applied at the port 1(2) of the CPW antenna 1 (2) in order to excite spin precession. Spin precessional motion induce voltages on CPWs, and therefore SW properties would be characterized electrically using Scattering parameter (S-parameter). S_{ij} represents the signal detected from the CPW antenna i with respect to the signal applied to the CPW antenna j . For example, S_{11} (S_{22}) indicates absorption spectra of spin precessional motion detected by CPW antenna 1 (2), and S_{21} (S_{12}) the SW propagation from CPW antenna 1(2) to CPW antenna 2 (1). For the spin wave interference experiment, CPW antenna 3 is connected to the VNA, and microwave signals from port 1 and port 3 were applied simultaneously with a phase difference $\Delta\phi_{\text{vna}}$. S_{21} represents the SW propagation signal from antenna 1 and 3.

An external magnetic field H was applied either (a) in-plane or (b) out-of-plane. (a) The field H of up to 90 mT was applied under an angle φ between the field H and the long axis of the CPWs. For field-dependent (angular dependent) SW spectroscopy, the angle φ (the field H) was fixed. (b) The field H of up to 500 mT was applied perpendicular to the film plane. There was no option to vary an angle θ in azimuthal direction.

In order to increase signal-to-noise (SNR) ratio of SW absorption spectra, $\Delta S_{ii} = S_{ii}(H) - S_{ii}(\text{Ref})$ was evaluated. $S_{ii}(H)$ is scattering parameters measured at a given field H , and $S_{ii}(\text{Ref})$ at (a) 90 mT along $\theta = 90$ deg for in-plane field and (b) 0 mT for out-of-plane field, respectively. For the same reason, field-derivative ($\Delta S_{ij} = S_{ij}(H) - S_{ij}(H - \Delta H)$) or angle-derivative ($\Delta S_{ij} = S_{ij}(\varphi) - S_{ij}(\varphi - \Delta\varphi)$) of SW propagation spectra is considered. ΔH is 1 mT and 2 mT for in-plane and out-of-plane fields, respectively, and $\Delta\varphi$ is 1 deg. In order to enhance SNR ratio of interfered SW, frequency-derivative ($\Delta S_{ij} = S_{ij}(f) - S_{ij}(f - \Delta f)$) is considered (Δf is 20 MHz)

Calculation of GC modes. Some wave vectors of SWs $\mathbf{k} + \mathbf{G}$ in 2D GC sample are not parallel

6.1 Broadband nanograting coupler of multiple magnetic resonances approaching 5G telecommunication

to \mathbf{k} imposed by the CPW, and thus several GC modes would be detected in SW propagation at a fixed frequency f . The phase of SWs for each GC mode is different since the amplitude of wave vectors \mathbf{k} and effective SW propagation distance s_{eff} are different. On top, the decay length l_d related to the group velocity v_g and damping parameter of YIG α play a role on the intensity of propagated GC modes. We modeled SW propagation spectra using the relevant lattice in reciprocal space as well as concerning the parameters mentioned above. Intensity of FFT peak is calculated from dots following gaussian profile with a diameter of D arranged in the lattices. SW intensity is calculated as follows: Iso-frequency contour at fixed frequency f derived from dispersion relation for SWs at 5 mT relevant to Fig. 6.2e and f is plotted on top of the FFT image shifted by $-\mathbf{k}_{\text{cpw}}$. Along the contour one acquires FFT intensity profile $I_{\text{fft}}(f, \varphi, k_{\text{cpw}})$, group velocity $v_g(f, \varphi)$, effective distance $s_{\text{eff}}(\varphi)$. Here SW relaxation time $\tau(f) = 1/2\pi\alpha f$ [1] contributes to the decay length $l_d(f, \varphi) = v_g(f, \varphi)\tau(f)$, and the decay amplitude $I_d(f, \varphi) = \exp(-s_{\text{eff}}(\varphi)/l_d(f, \varphi))$ is calculated. With concerning accumulated phase $\phi_a(f, \varphi) = \exp(ik(f, \varphi)s_{\text{eff}}(\varphi))$. Then SW propagation spectrum contributed from a fixed k_{cpw} is calculated as follows:

$$g_{\text{sw}}(f, k_{\text{cpw}}) = \sum_{\varphi} I_{\text{fft},f}(k, \varphi, k_{\text{cpw}}) I_d(f, \varphi) \exp(i\phi_a(f, \varphi)). \quad (6.2)$$

With considering weight factor $I_{\text{cpw}}(k_{\text{cpw}})$ (Excitation spectrum of \mathbf{k} , see Section A), SW propagation spectra is as follows:

$$G_{\text{sw}} = \sum_{k_{\text{cpw}}} I_{\text{sw}}(f, k_{\text{cpw}}) \times I_{\text{cpw}}(k_{\text{cpw}}). \quad (6.3)$$

Real part $\text{Re}(G_{\text{sw}})$ was plotted on Fig. 6.2e and f for the comparison with the experimental results. The amplitude of the wave vector k_{cpw} up to 4.0 corresponding to the edge of k_1 mode was considered.

Simulations. Micromagnetic simulations using MuMax [89] were performed to obtain a microscopic insight into SW excitations in ferromagnetic nanopillars. A grid of $2.5 \text{ nm} \times 2.5 \text{ nm} \times 5 \text{ nm}$ ($x \times y \times z$) was used. An global external field was applied either (a) in-plane or (b) out-of-plane: (a) A global in-plane 5 mT DC magnetic field was applied along the x -direction after that a field of 90 mT was applied, and equilibrium magnetization configuration \mathbf{M}_{eq} was determined. Note that misalignment angles $\theta = 89 \text{ deg}$ and $\varphi = 2 \text{ deg}$ were set. Subsequently, a spatially homogeneous sinc pulse of 0.15 mT with the frequency 30 GHz was applied along out-of-plane. (b) A DC magnetic field -500 mT was applied along the z -direction, and equilibrium magnetization configuration was determined. Misalignment angles $\theta = 2 \text{ deg}$ and $\varphi = 3 \text{ deg}$ were set. Subsequently, a spatially homogeneous sinc pulse of 0.15 mT with the frequency 30 GHz was applied along $+x$ -direction. Simulated \mathbf{M} is recorded 512 times every 5 ps. The input parameters of Py used in the simulations were as follows: saturation magnetization $M_s = 800 \text{ kA/m}$, exchange constant $A = 13 \times 10^{-12} \text{ J/m}$, and damping constant 0.01.

Dynamic magnetization $\mathbf{m} = (m_x, m_y, m_z) = \mathbf{M} - \mathbf{M}_{\text{eq}}$ was recorded as a function of x, y, z

in time domain. A fast Fourier transformation (FFT) was performed on the magnetization for each grid along the time axis to obtain the resonance spectrum in frequency domain by summing up a magnitude (a) m_z for in-plane bias field and (b) m_x for out-of-plane bias fields over all grid cells, respectively. For the illustration of spatial characteristics of quantized SW modes, we defined an amplitude and phase of SWs by the size of dots and color in hue, respectively, using Mayavi [139]. In this simulation, ferromagnetic nanopillar is in a vortex state (Supplementary Section B) for the in-plane field of 5 mT, and thus, m_z component is utilized to investigate the spatial profile of quantized magnon. For the saturated nanopillar by the out-plane field application, static magnetization points along z -direction (Supplementary Section B). The amplitude and phase of spin dynamics for the illustration are represented by $\mathbf{m}_{\parallel} = (m_x, m_y)$.

Bragg peaks of crystal/quasicrystal structure. Bragg peaks of the square lattice correspond to its reciprocal-lattice vectors \mathbf{G} , which is expressed as follow:

$$\mathbf{G} = i\mathbf{G}_{10} + j\mathbf{G}_{01} \quad (6.4)$$

where $\mathbf{G}_{10} = (2\pi/a, 0)$ and $\mathbf{G}_{01} = (0, 2\pi/a)$, i and j are integer numbers.

The Penrose P3 tiling is composed of acute and obtuse rhombi structures with a same side length a . Quasicrystals do not possess reciprocal-lattice vectors in reciprocal space while, Bragg peak pattern (Supplementary Section F) is expressed with basic reciprocal vectors $\mathbf{F}_p^{(1)} = (\cos(p\pi/5), \sin(p\pi/5)) \times 2\pi/(a \cos(\pi/10))$ where $p = 0, \dots, 9$, which is indicated by circles in Supplementary Section E. Note that $\mathbf{F}_p^{(1)} = -\mathbf{F}_{p+5}^{(1)}$. The other reciprocal vectors are expressed by linear combination of the basic reciprocal vectors,

$$\mathbf{F} = i\mathbf{F}_0^{(1)} + j\mathbf{F}_1^{(1)} + k\mathbf{F}_2^{(1)} + m\mathbf{F}_3^{(1)} + n\mathbf{F}_4^{(1)} \quad (6.5)$$

which fills out the reciprocal space densely and infinitely in theory (REF!). i, j, k, m and n are integer numbers. The other intense peaks are expressed as $\mathbf{F}_{p+1}^{(2)} = \mathbf{F}_p^{(1)} + \mathbf{F}_{p+3}^{(1)}$, $\mathbf{F}_p^{(3)} = \mathbf{F}_p^{(1)} + \mathbf{F}_{p+1}^{(1)}$, $\mathbf{F}_p^{(4)} = \mathbf{F}_{p-1}^{(1)} + \mathbf{F}_p^{(1)} + \mathbf{F}_{p+1}^{(1)}$, $\mathbf{F}_p^{(5)} = \mathbf{F}_{p-1}^{(1)} + \mathbf{F}_p^{(1)} + \mathbf{F}_{p+1}^{(1)} + \mathbf{F}_{p+2}^{(1)}$, with the magnitude of $|\mathbf{F}^{(2)}| = 2\pi/(a \cos(\pi/5))$, $|\mathbf{F}^{(3)}| = \pi/a$, $|\mathbf{F}^{(4)}| = 2\pi/a \times (2 + 1/(a \cos(\pi/10)))$ and $|\mathbf{F}^{(5)}| = 2\pi/(a \sin(\pi/10))$, respectively.

Acknowledgments

The research was supported by the SNSF via grant number 163016.

Author contributions

D.G., V.S.B. and S.W. planned the experiments. V.S.B. and S.W. designed the magnonic crystals/quasicrystals. S.W. prepared the samples together with E.N.D. S.W. took the data. A.M. and S.S. performed the micromagnetic simulation. S.W. and D.G. analyzed the data. S.W. and D.G. wrote the manuscript. All authors commented on the manuscript.

7 Engineering of artificial spin ice for magnonics

Periodically arranged interacting magnets called artificial spin ice (ASI) enable researchers to investigate experimentally geometrical frustration in magnetism, movement of monopoles and magnetic phase transitions. The bi-stable magnetism of macroscopic Ising magnets in an ASI might promise magnetization states which are reprogrammable via a global magnetic field. A global magnetic field does not seem to be suitable to induce deterministic switching (reprogramming) in a periodic ASI as the nucleation of reversed domains in a strictly periodic system should occur in a stochastic and non-reproducible manner. Here we study ASIs based on quasicrystalline arrangement in order to understand and characterize the mechanism of magnetization reversal. Dr. V. S. Bhat fabricated the ASI samples. Dr. V. S. Bhat, K. Baumgaertl and I performed X-ray photoemission electron microscopy (XPEEM) on the ASI samples supported by Dr. F. Kronast. I established data analysis codes with help of Dr. V. S. Bhat. Secondary, we integrate ASIs on YIG films to investigate the SW propagation underneath different magnetization configurations. These studies are important to further expand the possibility of ASI for reprogrammable magnonics [79, 59, 148].

7.1 Non-stochastic Switching in Aperiodic Nanomagnet Lattices Forming Reprogrammable Artificial Quasicrystals

One powerful avenue to gain novel insight resides in the materials-by-design approach making use of nanofabrication and imaging techniques [117]. Thereby unprecedented understanding of e.g. geometrical frustration in spin ice systems was achieved. The artificial spin ices (ASIs) consisted of either disconnected or interconnected ferromagnetic nanobars that were arranged on strictly periodic lattices with translational invariance [20, 69, 149]. In both ASI's cooperative phenomena were found and analyzed via spin ice rules, charge model and energy minimization via clockwise (CW) and counter-clockwise (CCW) flux-closure loops (FCLs) [67, 150]. For artificial magnetic quasicrystals (AMQs) comparable studies are in their infancy; however, un-conventional magnetic properties were reported [28, 116, 117, 151, 152]. The following questions are unanswered: (1) How do cooperative phenomena change when

one systematically varies the relative strength of exchange coupling with respect to dipolar interaction among nanobars on quasicrystalline lattices? (2) What is the origin of the knee-like anomalies which were reported for the magnetic hysteresis of a quasicrystalline Penrose P2 tilings? [117] (3) How do properties of ferromagnetic Penrose P2 and P3 tilings compare? They belong to the same class of five-fold quasicrystal lattices but consist of different geometric prototiles [32]. Here we report on nanostructured Penrose P2, P3 [32, 110, 153] and Ammann tilings [153] from the magnetically isotropic alloy $\text{Ni}_{81}\text{Fe}_{19}$ (Py) and address the open questions by performing magnetic imaging with high spatial resolution.

Method

We prepared artificial magnetic quasicrystals (AMQs) in the form of Py nanobars based on third generation Penrose P2 (Fig. 1.81a), Penrose P3, and second generation Ammann tiling (Fig. 7.1) using nanofabrication techniques. Penrose P2, P3 and Ammann tiling exhibited a five-fold, five-fold and eight-fold rotational symmetry, respectively. The width of nanobars, their thickness and intervertex spacing were 120 nm, 25 nm, and 810 nm, respectively. In order to tune the interaction at the vertex of the tilings, we created quasicrystals which consisted of (A) interconnected, (B) partially connected and (C) fully separated nanobars (C), respectively. The shape anisotropy fields for individual nanobars of lengths (A) 810 nm, (B) 609 nm, and (C) 408 nm were calculated to be 147 mT, 140 mT, and 117 mT, respectively [154].

We imaged the magnetic states in these AMQs using XMCD at the Fe L3-edge to detect the magnetization direction of a given nanobar via X-ray photoemission electron microscopy (XPEEM). XPEEM imaging was done at the SPEEM station located at the UE49/PGMa beamline at BESSY-II (Helmholtz Zentrum, Berlin). The samples were mounted on a sample holder which allowed us to apply magnetic field to the sample *in-situ*. The Penrose P2 and P3 AMQs were patterned on the same Si substrate, whereas Ammann AMQs were fabricated on another identical Si substrate. The nanomagnets displayed in blue (red) color in XPEEM images are considered to exhibit a magnetization component which is parallel (antiparallel) to the X-ray beam propagation direction (Fig. 7.1b). To study the magnetization reversal, a magnetic field was applied to the samples along $-x$ -direction at first (Fig. 7.1b) in that the integrated field coils with the maximum negative current of $I = -I_{\text{max}} = -2$ A was biased and the field $\mu_0 H = -52$ mT was generated. Second, a current $I > 0$ was applied, and an applied field pointed along $+x$ -direction. I was increased in a stepwise manner in order to induce the magnetization reversal. Application of an external magnetic field disturbs the electrons used for PEEM imaging, and therefore, imaging was performed at zero-field in that I was reduced to zero after each step of increased current [69]. In order to categorize magnetic states, we considered the shape anisotropy and bistability of nanobars and exploited the charge model (CM) explained in Sect. 1.4.3. The CM assigns a magnetic charge q to each of the vertices for evaluating the magnetic energy [67]. A vertex with a coordination number (CN) N can acquire a charge $Q = \sum q = +Nq \cdots -Nq$ which is the sum of individual charges q . For a given CN a vertex acquires the lowest possible charge Q in the ground state to minimize the total energy.

7.1 Non-stochastic Switching in Aperiodic Nanomagnet Lattices Forming Reprogrammable Artificial Quasicrystals

The total charge Q_{tot} of all the vertices in the minimum-energy state of P2, P3 (Fig. 7.2a to f) and Ammann tiling AMQs (Fig. 7.5a to c) would correspond to $|Q_{\text{tot}}| = 152, 86, \text{ and } 134$, respectively.

In order to analyze XMCD data, we first generated a cartoon image as shown in Fig. 7.1c containing the color (red or blue) for each nanobar based on Fig. 7.1b. The direction of magnetization for each nanobar is defined concerning the color of nanobars and X-ray direction (Fig. 7.1d). From the magnetization configuration map, the number of magnetic charge was calculated at each vertex (Fig. 7.1e) and the regions where microvortices were generated were evaluated (Fig. 7.1f). This process was iterated on all the XMCD data, and magnetization configuration as well as magnetic charges and microvortex states for each sample and applied external field were investigated.

Micromagnetic simulations were performed using the OOMMF code [88], and the Py parameters used in simulations were as follows: Exchange constant $A = 1.3 \times 10^{-11} \text{ J m}^{-1}$, saturation magnetization $M_s = 8 \times 10^5 \text{ A m}^{-1}$, magnetocrystalline anisotropy constant $K = 0$, gyromagnetic ratio $\gamma = 2.211 \times 10^5 \text{ m A}^{-1} \text{ s}^{-1}$, and dimensionless damping coefficient $\alpha = 0.01$. Different magnetic configurations were explored by initializing magnetization vectors of individual segments and relaxing the spin system at the given magnetic field. For this, we first created a colored bitmap (on a grid of $5 \text{ nm} \times 5 \text{ nm} \times 25 \text{ nm}$) where each segment was assigned a color corresponding to its assumed magnetization orientation. We then imported this colored bitmap into OOMMF and equilibrated it in the presence of a field that resided within the experimental switching regime.

Results and Discussion

P2 and P3 AMQs

In Fig. 7.2a to f we show the XMCD-PEEM topography images of six studied P2 and P3 AMQs. In Fig. 7.2g to l we show representative XPEEM data obtained on magnetic states of the P2 and P3 AMQs after initiating partial reversal as described above. Each image thus displays a remnant state obtained in a minor loop of the magnetic hysteresis. The lattices reported here can be decomposed into three types of nanobars, i.e., Type I, Type II, and Type III based on the angle ϕ that the nanobars take with respect to the magnetic field H : Type I exhibits $\phi = 0 \text{ deg}$, Type II $\phi = \pm 36 \text{ deg}$, and Type III $\phi = \pm 72 \text{ deg}$ for Penrose P2 and P3 tilings. Note that the maximum field $|\mu_0 H_{\text{max}}| = 52 \text{ mT}$ that we were able to apply in the XPEEM microscope was smaller than the calculated anisotropy fields H_{ani} . Considering the curling process for incoherent reversal [155], the applied field H was even not large enough to fully saturate or reverse individual non-interacting nanobars of Type III that exhibited $\phi = \pm 72 \text{ deg}$ and did not interact with other magnets. The calculated nucleation field for incoherent reversal via curling amounted to about 70 mT . This value was also the lower limit for the reversal field expected for coherent rotation. For all scenarios the applied field alone was not large enough to initiate

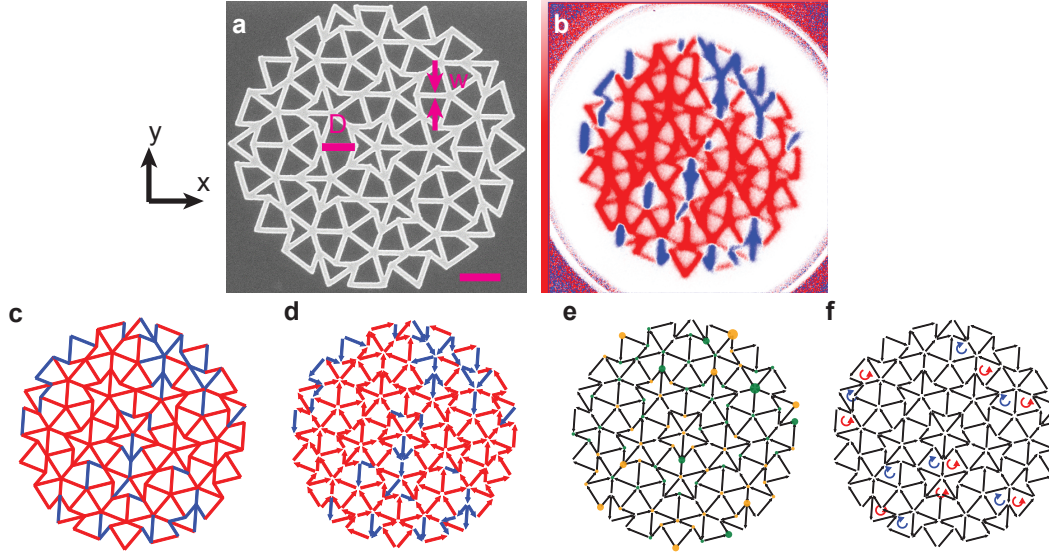


Figure 7.1: (a) SEM image of interconnected Py nanobars (bright) on a Penrose P2 tiling on Si (dark). The length a and w of a nanobar are 810 nm and 120 nm, respectively. Scale bar represents 1 μm . (b) XMCD data for P2A taken after applying a magnetic field $\mu_0 H = 32.5$ mT. (c) Cartoon image of XMCD data. The color (red or blue) for each nanobar is given based on (b). (d) Map of magnetization vector, (e) magnetic charges and (f) microvortices. Orange (green) color in (e) indicates negative (positive) charge. Red (blue) arrows in (f) indicate the CCW (CW) FCLs.

the reversal of an individual Type III nanobar.

Remnant states of P2A in Fig. 7.2g and P3A in Fig. 7.2j of a minor loop show that these AMQs with interconnected nanobars contain large-area domains or chains of reversed nanobars (blue) next to large-area domains in which nanobars remained in the original orientation (red). The reversed domains and chains are found to include reversed nanobars of Type III despite their large anisotropy field. The detection of reversed Type III nanobars reflects a cooperative phenomenon in the magnetic hysteresis of corresponding quasicrystals as the reversal is not triggered by relatively weak external field alone. The reversal is attributed to the additional interaction with neighboring nanobars which exhibit $|\phi| \leq 36$ deg. The analysis in terms of the CM (Fig. 7.2m and p) shows that vertices formed by the interconnected nanobars exhibit overall small values of Q in their remnant states (the maximum value amounts to $Q = 3$ in Fig. 7.2m and p). AMQs from partially and fully separated nanobars imaged as P2B (Fig. 7.2h), P2C (Fig. 7.2i), P3B (Fig. 7.2k), and P3C (Fig. 7.2l) show numerous reversed magnets that are (more) randomly distributed over the whole AMQ compared to interconnected AMQs. In the former cases, the arrangements of opposing nanobar magnetization directions look fragmented. From XPEEM images taken for many different magnetic histories (not shown) we found that switching events in the form of avalanches were seen in the interconnected P2A and P3A samples but were not seen in the disconnected P2C and P3C samples.

7.1 Non-stochastic Switching in Aperiodic Nanomagnet Lattices Forming Reprogrammable Artificial Quasicrystals

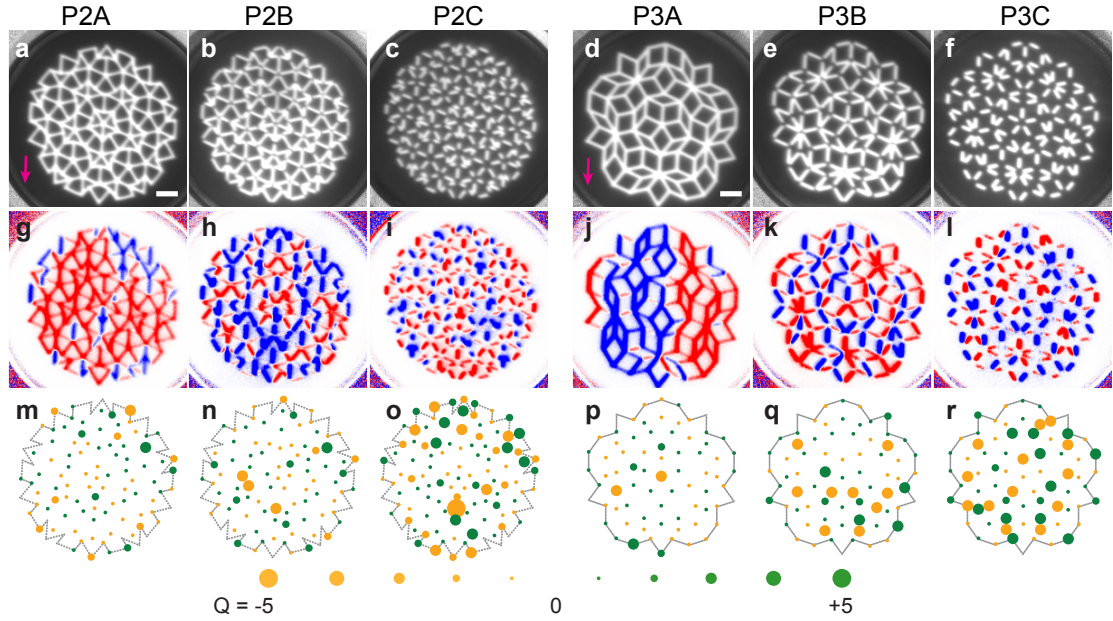


Figure 7.2: (a) - (f) XMCD-PEEM topography images for six different quasicrystals as labelled in the graphs. Bright (dark) regions correspond to magnetic (non-magnetic) material. The scale bar given in (a) and (d) corresponds to 1 μm . The arrows in (a) and (d) represent the X-ray direction and the magnetic field direction. Selected magnetic images of remnant states using PEEM after applying different field values $\mu_0 H$ (given in parenthesis) for (g) P2A (32.5 mT), (h) P2B (41.6 mT), (i) P2C (42.64 mT), (j) P3A (36.4 mT), (k) P3B (42.9 mT), and (l) P3C (48.1 mT) representing the switching of 44 %, 51 %, 46 %, 56 %, 44 %, and 55 % type I nanobars, respectively. Blue (red) colors represent magnetization parallel (opposite) to the X-ray direction. Blue color indicates a reversed nanobar. The images represent the states attained when about 50 % of Type I nanobars switched. Notice the weak contrast in case of nanobars which do not point along the X-ray direction. (m) – (r) CM analysis of the XMCD experimental data shown in (g) – (l). The green and orange filled circles at the vertices represent positive and negative vertex charges, respectively. Here the circles with smallest and largest diameter represent charges $|Q| = 0$ and $|Q| = 5$, respectively. When quasicrystals consist of disconnected nanobars a large charge of up to $|Q| = 5$ can be found.

We analyze the reversal in the AMQs in greater detail in Fig. 7.3. In Fig. 7.3a to f the relative numbers of reversed nanobars are depicted as extracted from a series of XPEEM microscopy images taken at remnance after applying different magnetic fields H displayed on the x -axis. For P2A and P2B reversals start from Type I nanobars, for the other AMQs Type II nanobars switch first. Once Type I or Type II nanobars reverse in P2A or P3A composed of fully interconnected nanobars, Type III nanobars follow in their cases. A less pronounced successive reversal of Type III nanobars is found for P2B and P3B. Here, the number of reversed Type III nanobars is much smaller compared to the interconnected P2A and P3A samples. In P2C and P3C consisting of completely disconnected nanobars we do not find the reversal of Type III nanobars in the accessible field regime. In Fig. 7.3g to l the total charge Q_{tot} extracted from XPEEM images is displayed. In P2 AMQs the onset of reversal is accompanied by a small

global minimum in Q_{tot} . In case of P2A and P2B Q_{tot} regains a value close to the initial state at large H . This is different for P2C for which Q_{tot} grows with increasing reversal field. A comparable growth of Q_{tot} is observed for P3B and P3C. For Penrose P3 tilings, Q_{tot} stays small at large H for P3A only.

In Fig. 7.3m to r, the number of FCLs present in the XPEEM images is summarized. For P2 AMQs the minimum in Q_{tot} is accompanied by a maximum of FCLs. The maximum in number of FCLs roughly occurs when about 50 % of Type I and Type II nanobars have undergone switching. For P3B a pronounced maximum in FCLs is found as well. For P3A and P3C the variation is small. Note that P2B, P2C and P3B exhibit a large number of FCLs already before pronounced switching has taken place. We attribute this observation to the limited field strength (52 mT) that was available to define the initial magnetic state. The maximum field was not large enough to saturate Type III nanobars that were not connected to neighboring nanobars.

In Fig. 7.3s to x we depict the number of individual vertices that exhibit the maximum charge Q for $N = 3$, $N = 4$ and $N = 5$, i.e., $Q = 3$, $Q = 4$ and $Q = 5$, respectively. For P2A and P2B the number of vertices with $Q = 4$ and $Q = 5$ is negligible. Strikingly, the number of vertices with $Q = 3$ takes its lowest value when the maximum number of FCLs is reached in P2A. A similar behavior is observed for P2B and P3A. P2C, P3B, and P3C behave differently in that the number of vertices with $Q = 3$ does not go through a global minimum as a function of reversal field. In case of the disconnected P2C and P3C samples the number grows with H . A considerable number of vertices with $Q = 4$ ($Q = 5$) is found only in P3B and P3C (P3B). Large individual vertex charges hence occur in Penrose P3 tilings with disconnected nanobars, but not for P2 and P3 tilings with interconnected AMQs. A large vertex charge indicates the violation of the ice rule [156, 157]

To gain further insight into the violation of spin ice rules we have simulated low- and high-energy vertex states for connected and disconnected nanobars (Fig. 7.4a to h). The five (four) interconnected nanobars joining in the vertices illustrated in Fig. 7.4a and b (e and f) are both exchange and dipolarly coupled. Separated nanobars shown in Fig. 7.4c and d (g and h) are dipolarly coupled only. Possible magnetic configurations of nanobars in vertices and the corresponding charges Q are illustrated. We see that for interconnected nanobars found e.g. in P2A, the total vertex energy increases by about 80 % from Fig. 7.4a ($Q = -1$) to Fig. 7.4b ($Q = -5$), respectively, considering a vertex with $N = 5$. The vertex configuration with large $|Q|$ stabilized in micromagnetic simulations in Fig. 7.4b and f have not been observed in the reversal regime. The AMQ lattices made from interconnected nanobars avoided these high-energy configurations and instead formed FCLs. We argue that the exchange interaction in the vertices of the interconnected P2A and P3A samples plays the major role for the observed cooperative magnetization reversal which included Type III nanobars. Precursors for the AMQ reversal are the Type I and Type II nanobars that meet at a vertex exhibiting a relatively large charge (e.g. $Q = 2$ for $N = 4$). On the contrary, a violation of the spin ice rule ($Q = -5$ in Fig. 7.4d) causes an energy higher by only 7 % compared to Fig. 7.4c ($Q = -1$) for the

7.1 Non-stochastic Switching in Aperiodic Nanomagnet Lattices Forming Reprogrammable Artificial Quasicrystals

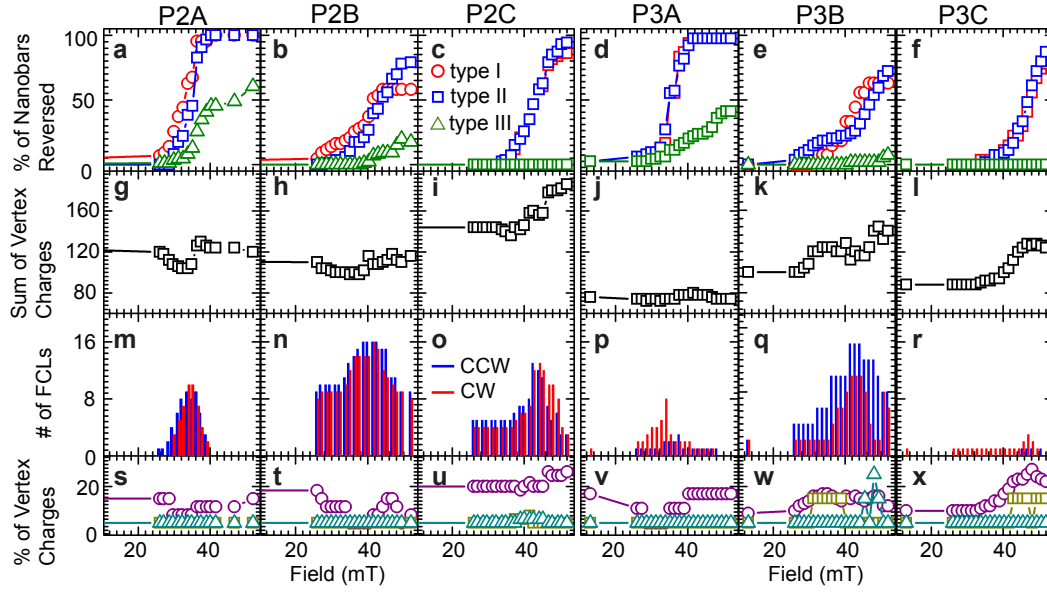


Figure 7.3: (a) - (f) Field-dependent reversal of Type I (red circle), Type II (blue square) and Type III (green triangle) in AMQs P2A, P2B, P2C, P3A, P3B, and P3C, respectively. (g) - (l) Total charge Q_{tot} for P2A, P2B, P2C, P3A, P3B, and P3C, respectively. (m)-(r) Number of FCLs for P2A, P2B, P2C, P3A, P3B, and P3C, respectively. (s) - (x) Evaluation of relative amounts of maximum possible individual vertex charges Q in P2A, P2B, P2C, P3A, P3B, and P3C, respectively. The purple, dark yellow, and dark cyan colored symbols represent charges 3 (for $N = 3$), 4 (for $N = 4$), and 5 (for $N = 5$), respectively. The values in (s)-(w) were multiplied by 3 for better visualization using a unique y scale for all graphs. Notice the presence of charges $|Q| = 5$ in P3B for $N = 5$ vertices.

disconnected nanobars relevant e.g. in P2C. The effect of how weak nanobars interact is observed via the violation of the local ice rule (i.e., occurrence of large Q). Consistent energy variations with Q are also found for vertices with $N = 4$ in Fig. 7.4e to h. Figure 7.3s to x reveals that ice rule violations are pronounced (small) in disconnected (interconnected) samples, evidencing weak interaction in case of disconnected nanobars.

Ammann AMQs

We summarize the experimental data obtained on Ammann tilings (AT) consisting of interconnected (ATA), partially connected (ATB) and disconnected nanobars (ATC) shown in Fig. 7.5a, b and c, respectively. For the Ammann tilings, nanobars of Type I, II and III make angles $\phi = 0$ deg, $\phi = \pm 45$ deg, and $\phi = \pm 90$ deg, respectively, with the field applied in the XPEEM experiments (Fig. 7.5d to 4f). We detect a large central domain of reversed nanobars for the interconnected ATA sample while the reversed nanobars are more distributed over ATB and ATC. In analogy to disconnected Penrose AMQs the analysis based on the CM provides a tendency towards slightly larger vertex charges when going from interconnected ATA to disconnected ATC. Still this tendency is less significant in the graphs of Fig. 7.5g to i compared to the Penrose

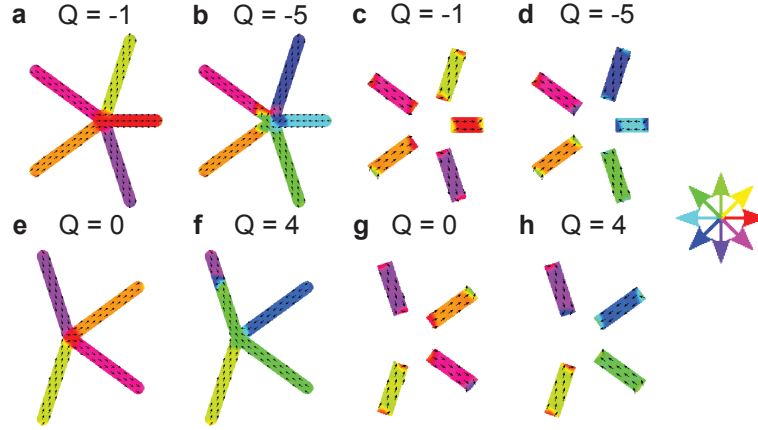


Figure 7.4: Simulated magnetization directions (black arrows and color wheel) for representative connected and disconnected bars on Penrose (a)-(d) P2 and (e)-(h) P3 tilings. The total energies in units of 10^{-16} J are (a) 1.01, (b) 1.85, (c) 1.20, (d) 1.30, (e) 0.83, (f) 1.51, (g) 0.96, and (h) 1.03, respectively. The values Q depicted in the graphs indicate the total charge of the respective input magnetization configuration.

AMQs. Analyzing all our XPEEM datasets we find that almost all of Type III nanobars with $\phi = \pm 90$ deg do not undergo switching in Ammann AMQs. Studying the reversal of Type I and Type II nanobars in detail (Fig. 7.5j to l) the interconnected ATA sample shows a narrower switching field distribution for these nanobars compared to the interconnected P2A and P3A samples. About 40 % of Type I and Type II nanobars of ATA undergo reversal within a span of 7.5 mT (Fig. 7.5j), i.e., within a field regime smaller than for P2A and P3A. Full reversal of the Type I and Type II nanobars is seen at about 34 mT. The corresponding nanobars that are disconnected require a field of up to about 52 mT for full reversal. One can suppose that the narrow field distribution for switching in ATA reflects a cooperative reversal phenomenon like an avalanche (compare the blue chain-like domain in Fig. 7.5d). The analysis of total charges Q_{tot} is depicted in Fig. 7.5m to o. In all three Ammann tilings we observe a minimum in Q_{tot} when Type I and Type II nanobars undergo the reversal process. The drop in Q_{tot} is accompanied by an increased number of FCLs (Fig. 7.5p to r). In the magnetization reversal of ATB (Fig. 7.5k) the switching seems to take place in two separate steps (see the increases in the number of reversed nanobars at 28 mT and 42 mT in Fig. 7.5k). Consistent with these features, there are local minima (a shoulder and a maximum) in Q_{tot} (FCLs). We also see that the maximum in FCLs coincides with the minimum in the sum of charges. The slope of reversal in ATC (Fig. 7.5l) resembles the high-field slope of ATB in Fig. 7.5k and the ones seen in P2B, P2C and P3C. We argue that the high-field reversal processes which are detected over a broad field regime reflect the disconnected nanobars in all three samples. In this field regime we find the spin ice rule violations for ATB and ATC (Fig. 7.5t and u, respectively) in that the maximum vertex charge $Q = 3$ is present in case of $N = 3$. This large vertex charge is not observed in the reversal of ATA (Fig. 7.5s).

7.1 Non-stochastic Switching in Aperiodic Nanomagnet Lattices Forming Reprogrammable Artificial Quasicrystals

As discussed before, the large energy cost for a spin ice rule violation found in simulations for interconnected nanobars favors low vertex charges which are consistent with the spin ice rule. Indeed we experimentally detected low- Q states in the interconnected P2A, P3A and ATA samples in the reversal regime. Once present, high energy (high- Q) vertices in interconnected AMQs act as nucleation sites for the reversal. They give rise to non-stochastic switching [28], presumably causing the staircase-like jumps or knee anomalies [117]. High- Q vertices render AMQs into a novel class of reprogrammable magnonic crystal as compared to previously studied periodic magnonic crystals [6]. Once vertices consist of disconnected nanobars they accommodate large Q thereby violating the spin ice rule.

7.1.1 Conclusion

In our work presented here, we varied the exchange and dipolar interactions in Penrose P2, P3, and Ammann tiling based AMQs, and imaged ferromagnetic reversal in these exotic ASI structures using XPEEM. Our data show compliance with ice rules in the exchange coupled nanobars. Ice rule violation occurs prominently in the systems without exchange coupling among the disconnected nanobars. Using micromagnetic simulations we highlight the reasons behind such observation. We observed the narrowest distribution of reversal fields in an exchange mediated Ammann tiling, followed by the exchange mediated Penrose P2 and P3 tilings. Here reversal is triggered by vertices whose charge Q deviates from the ground state. The magnetization reversal is drastically different for disconnected arrays owing to the asymmetric and aperiodic arrangements of nanobars around a vertex. Nanobars taking the same angle with the applied field have significantly different switching behavior depending on their local environment. Magnetodynamics studies on periodic ASI have shown that the local environment due to magnetic defects distinctly affected the resonance frequency and thereby fueled the idea of reprogrammable magnonic metamaterials [25, 158, 159]. The quasicrystals reported here that host built-in aperiodic variations in local environment in even their saturated state hence give rise to a novel class of magnonic crystals which obey dynamic responses reprogrammable via the global magnetic field. In the following section we will investigate this aspect further based on an interconnected Ammann tiling.

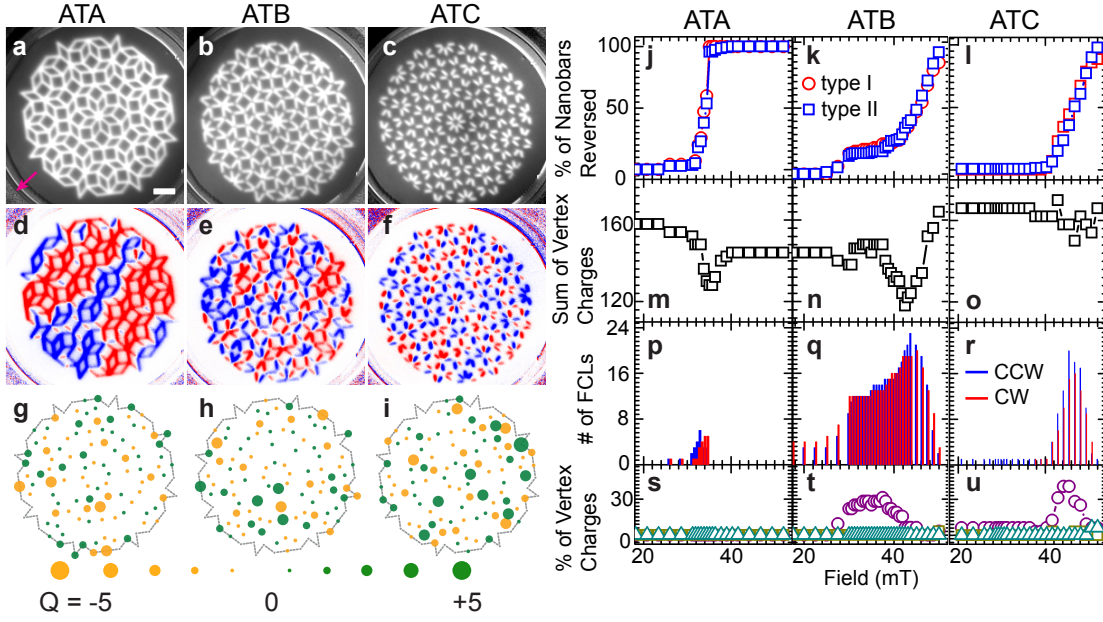


Figure 7.5: (a) XMCD-PEEM topography image for (a) ATA ($\mu_0 H = 34$ mT), (b) ATB (at 47 mT), and (c) ATC (at 47 mT) representing the switching of 47 %, 47 %, and 53 % Type I nanobars. Bright (dark) regions correspond to magnetic (non-magnetic) regions. The scale bar corresponds to $1 \mu\text{m}$. The arrow represents the field direction. The X-ray direction was misaligned by 22 deg to optimize the detection of nanobars of all the different orientations. (d) - (f) XMCD data of topography images shown in (a) - (f). Blue (red) colors represent magnetization parallel (opposite) to the X-ray direction. Blue color indicates a reversed nanobar. Notice the weak contrast of nanobars whose orientation deviates from the X-ray direction. (g) - (i) CM analysis of XMCD experimental data shown in (d) - (f). The green and orange filled circles at the vertices represent positive and negative vertex charges, respectively. Here the circles with smallest and largest diameter represent charge $|Q| = 0$ and $|Q| = 5$, respectively. (j) - (l) Classification of reversal in terms of switching of Type I and II of nanobars for ATA, ATB, and ATC, respectively. Legends I and II represent nanobars of Types I and II. (m) - (o) Total charge count for ATA, ATB, and ATC, respectively. (p)-(r) Number of FCLs (see the inset in (p) for their definition) for ATA, ATB, and ATC, respectively. (s) - (u) Charge depiction for ATA, ATB, and ATC, respectively. The purple, dark yellow, and dark cyan colored symbols represent charges 3 ($N = 3$), 4 ($N = 4$), and 5 ($N = 5$), respectively.

7.2 Toward reconfigurable magnonic waveguide based on artificial spin ice integrated YIG film

Dynamic properties of artificial spin ice also gather attention in the field of magnonics [21, 22, 160]. Broadband spin wave spectroscopy combined with micromagnetic simulation revealed the magnetization configuration dependent SW properties [161]. Band structures of square-lattice-based ASIs would be tunable both by external magnetic fields and the configuration of individual nanomagnets [162]. SW channels were tailored in a ferromagnetic thin film combined with artificial spin ice in simulations [23].

7.2 Toward reconfigurable magnonic waveguide based on artificial spin ice integrated YIG film

In this section, we explore SW properties of hybrid magnetic nanostructures consisting of an interconnected Ammann ASI, which shows exotic cooperative switching phenomena via global magnetic fields in the previous section, and a square lattice ASI integrated on YIG thin films. These hybrid ASI systems exhibit a manifold rotational symmetry reflecting its lattice symmetry. Here we report a tunable grating coupler effect by the different magnetization configurations of the ASI on the YIG underlayer. We also control the spin wave properties in the remnant state via application of global magnetic fields and the magnetic history.

7.2.1 Method

We fabricated square (SQ) tiling-based periodically and Ammann (AM) tiling-based aperiodically arranged artificial spin ices (ASIs) on top of 126-nm-thick YIG films as shown in Fig. 7.6a and b, respectively. ASIs were composed of interconnected nanobars made of Ni with the saturation magnetization of 0.62 T. The width w , thickness t and intervertex spacing a of nanobars were kept at 175 nm, 25 nm, and 810 nm, respectively. Coplanar waveguides (CPWs) were integrated on top of the ASI samples with a spacing s of 12 μm . The CPW signal line width was 0.8 μm , and the same as for CPWs in Sect. 5.1. Thus the most prominent excitation by the CPW was centered at $k_1 = 1.92 \text{ rad}/\mu\text{m}$. Between the ASIs and the CPWs, an Al_2O_3 layer with a thickness of 37 nm was inserted to insulate CPWs from the metallic ASIs. For the ASIs based on both the square tiling (SQ-ASI) and Ammann tiling (AM-ASI), the CPW's long axis was parallel to one of their symmetry axes. Therefore nanobars took angles $\varphi = 0$ or ± 90 deg for SQ-ASI and $\varphi = 0, \pm 45$ or ± 90 deg for AM-ASI. A Vector Network Analyzer (VNA) was connected to the CPWs in order to characterize SW properties in the ASI samples by detecting spin waves using scattering parameters (S-parameters). S_{21} (S_{22}) represents SW absorption (SW propagation) spectra. The microwave power was set to 0 dBm. The magnetic field was applied in-plane to characterize the eigenmodes of the ASIs and YIG. The terms SQ-ASI-YIG and AM-ASI-YIG are used to express the ASI and YIG hybrid nanostructures in order to distinguish them from the ASIs without the YIG underlayer.

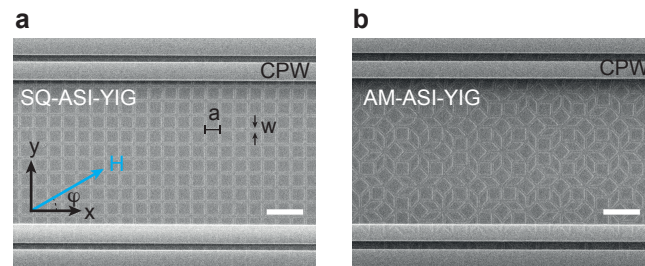


Figure 7.6: SEM images of (a) SQ-ASI-YIG and (b) AM-ASI-YIG (bright) prepared from Ni on YIG thin films (dark). CPWs (horizontal leads) are integrated in order to excite and detect SWs. In-plane fields were applied. Scale bars indicate 2 μm .

7.2.2 Result and discussion

Manifold rotational symmetry of SW absorption

We performed angular dependent SW spectroscopy in a rotating field H for periodic SQ-ASI-YIG and quasicrystalline AM-ASI-YIG (Fig. 7.7a and b, respectively). The external field was kept at 90 mT. The most prominent SW absorption band exhibited two-fold rotational symmetry. These branches (bright bands in Fig. 7.7a and b) are attributed to the k_1 mode excited by the CPW in the YIG thin film. Below 4.2 GHz, the weaker SW absorption features show four-fold and eight-fold rotational symmetries for SQ-ASI-YIG and AM-ASI-YIG, respectively, reflecting their lattice symmetries [31, 73]. The frequency of the weaker SW spectra at ± 90 deg for the periodic SQ-ASI-YIG sample corresponds to 3.4 GHz, which is lower than the lowest SW mode in the magnon band (4.0 GHz) according to the dispersion relation of the YIG film with the field of 90 mT.

Demagnetization factors for their width, thickness, and length amounts to $N_w = 0.148$, $N_t = 0.822$, and $N_a' = 0.030$, respectively if we neglect the vertices of interconnected nanobars ($a' = a - w$) [154], and the coercive field of the nanobars to be magnetized perpendicularly is calculated to $\Delta N M_s = (N_w - N_a') M_s = 73$ mT concerning the Stoner-Wohlfarth model [163]. Figure 7.7c and d shows angular dependent SW spectroscopy for SQ-ASI-YIG with rotating a field of 30 mT below the coercive field in the clockwise and counter-clockwise directions, respectively. We observe the weaker SW absorption features below 2.0 GHz which is the lowest frequency shown in the dispersion relation of the YIG film with the corresponding field. The insets illustrate the applied fields and expected magnetization directions of the SQ-ASI. These branches exhibit the hysteretic behavior, such that the shifts of their resonance frequencies near the symmetry axis of the SQ-ASI occur ($\varphi = 0, \pm 90$ and ± 180 deg). According to the magnetization configurations and the fields, we argue that the weaker modes are governed by the magnetization configuration of ferromagnetic nanobars which orient perpendicular to the external field. Due to the application of the external fields, the Ni nanobars might modify the magnetization configuration of the YIG film via stray field [164] and/or magnetostriction [101]. In order to understand this mode, further investigations such as micromagnetic simulations are needed.

Grating coupler effect and spin wave guiding

We have performed field-dependent SW spectroscopy at $\varphi = 0$ deg (DE-configuration). The field was swept from 90 mT to 0 mT. Figure 7.8a and b shows SW absorption and propagation spectra of SQ-ASI-YIG, respectively. Dark indicates the SW absorption and black-white oscillations represent the SW propagation from CPW to CPW (Fig. 7.8a and b, respectively). Above the k_1 mode, there are several SW absorption branches, attributed to the spin precessional motion in the nanobars oriented parallel to the field. The reciprocal lattice vectors read $\mathbf{G}_{ij} = (i, j)2\pi/a$ where $i, j = 0, \pm 1, \pm 2, \dots$. Correspondingly, magnonic grating coupler (MGC) modes are indicated by sky blue dashed lines in Fig. 7.8b. Below the k_1 mode, the

7.2 Toward reconfigurable magnonic waveguide based on artificial spin ice integrated YIG film

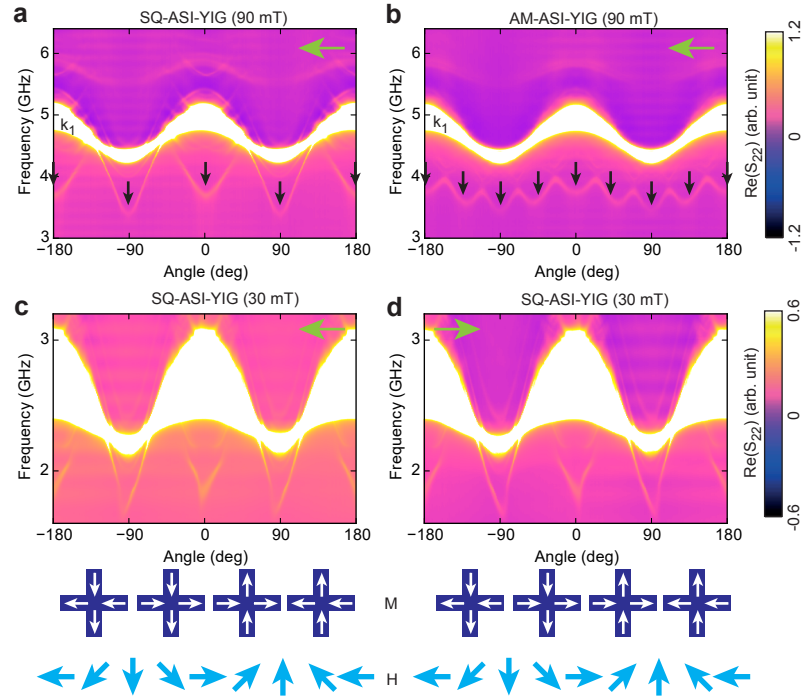


Figure 7.7: Angular-dependent SW absorption spectra of (a) SQ-ASI-YIG and (b) AM-ASI-YIG at a field of 90 mT. Bright (Dark) represents the SW absorption (background). Black arrows represent local minima of SW branches exhibiting four- and eight-fold rotational symmetry for the SQ-ASI-YIG and AM-ASI-YIG samples, respectively. Angular-dependent SW absorption spectra of SQ-ASI-YIG at a field of 30 mT rotated in the (c) clockwise and (d) counter-clockwise directions. Insets illustrate the field directions (light blue arrows), and the corresponding magnetization configurations of the SQ-ASI (white arrows). Light green arrows represent the angle scanning directions.

low frequency SW absorption mode shows the change of the slope around 45 mT in Fig. 7.8a. SW propagation of the corresponding mode is clearly resolved only below 45 mT in Fig. 7.8b. According to the discussion in the previous subsection, the nanobars orient perpendicular to the field induce the low frequency mode in YIG. It might be possible that the nanobars form domains in the YIG underlayer, and steer magnons in reconfigurable manner [23].

SW absorption originating from the nanobars of AM-ASI-YIG is also observed in Fig. 7.8c. MGC modes in Fig. 7.8d are resolved weakly, indicated by a black parenthesis. Since the reciprocal vectors of quasicrystalline Ammann tiling densely fills out the reciprocal space, the MGC modes were detected over a broad range of frequency. The SW mode below the k_1 branch is detected also in AM-ASI-YIG as well as the change of its slope df/dH near 45 mT. However, the oscillation signal in Fig. 7.8d is hardly resolved. The reason might be because (1) magnons in the YIG underlayer were not steered at the vertex of the AM-ASI or the (2) phase of the magnon for each steered nanochannel is different as observed for the worm-like nanochannels in nanohole-based artificial magnetic quasicrystal [31]. In order to further

understand the magnon-steering mode, it is interesting to perform μ -BLS measurement.

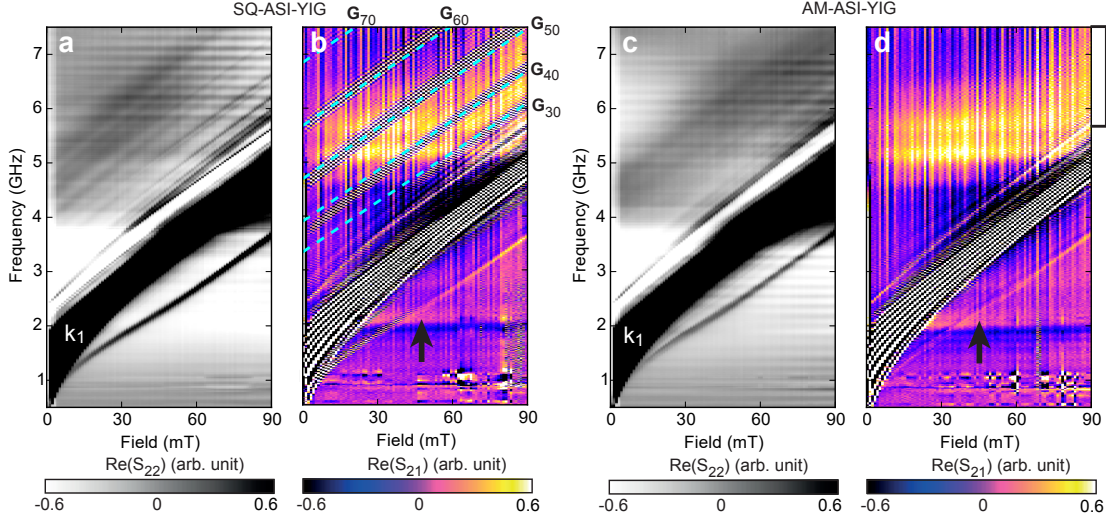


Figure 7.8: Field-dependent SW spectra of (a) and (b) SQ-ASI-YIG and (c) and (d) AM-ASI-YIG at $\varphi = 0$ deg. The field was swept from +90 mT to 0 mT. (a) and (c) Dark (Bright) represents the SW absorption (background) in (a) and (c). Black-white oscillations represent the SW propagation in (b) and (d). Sky blue dashed lines indicate the expected MGC modes for SQ-ASI-YIG in (b). Black parenthesis highlights a series of MGC modes with a dense set of reciprocal vectors of Ammann tiling in (d). Black arrows represent the frequency where a slope of the relevant SW resonance is changed.

The coercive field of nanobars in the ASIs is larger than the YIG film thanks to their shape anisotropy, and the anti-parallel alignment of the YIG film magnetization and nanobar magnetization is possible. Figure 7.9a and b shows the field-dependent SW absorption and propagation spectra for SQ-ASI-YIG, respectively. Note that the microwave amplitude was set to -10 dBm. The field was swept from -90 mT to 90 mT, and the spectra for $\mu_0 H > 0$ mT are shown. SW absorption associated with GC modes is resolved below and above 10 mT. At 10 mT the frequencies of the corresponding branches show a discontinuity. We attribute this to the reversal of Ni nanomagnets consistent with Ref. [18]. In Ref. [18], the authors agreed that below the discontinuity the magnetization vectors in YIG and grating coupler elements were anti-parallel, and above they were parallel. The notable switching of the ASI is also observed for AM-ASI-YIG (Fig. 7.9c). We did not resolve the MGC mode in parallel state and anti-parallel state of YIG and Ni due to the low signal-to-noise ratio caused by the low microwave power. With an increased microwave power, the MGC modes were resolved, and at the same time, the coercive field of the ASI was decreased most likely due to microwave assist switching [26].

7.2 Toward reconfigurable magnonic waveguide based on artificial spin ice integrated YIG film

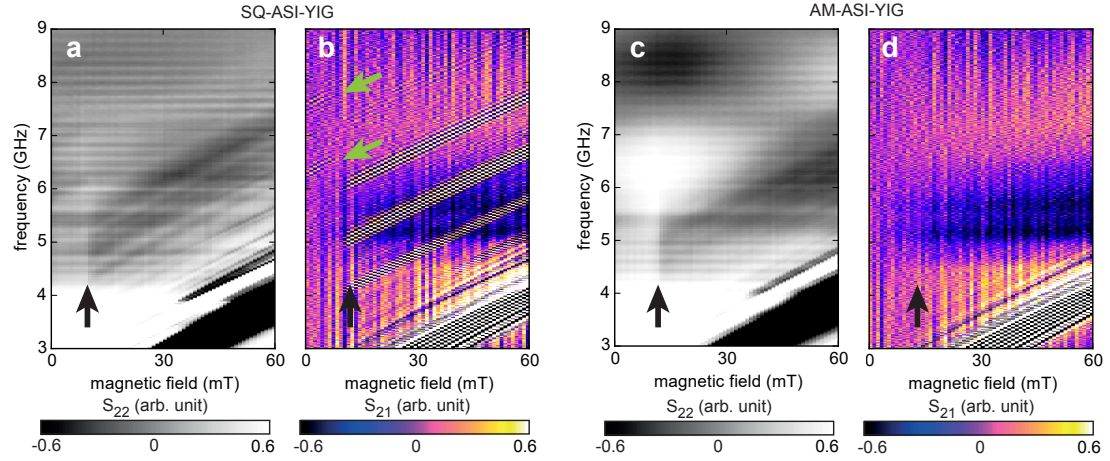


Figure 7.9: Field-dependent SW spectra of (a) and (b) SQ-ASI-YIG and (c) and (d) AM-ASI-YIG at $\varphi = 0$ deg. The field was swept from -90 mT to 90 mT. (a) and (c) Dark (Bright) represents the SW absorption (background) in (a) and (c). Black-white oscillations represent the SW propagation in (b) and (d). Light green arrows indicate MGC modes detected below 10 mT in (b). Black arrows indicate the switching field of the ASIs.

Reconfigurable magnonics

With the absence of an external magnetic field, one might expect that a YIG plane film would form a multi-domain state, and SWs would not propagate efficiently. Figure 7.10a (b) shows the field-dependent SW spectroscopy of AM-ASI-YIG with the field applied along the y -direction and swept from $+90$ mT to -90 mT (-90 mT to $+90$ mT). Before the field was swept, a field of 90 mT was applied along the $+x$ -direction. With the presence of the external field applied along the y -direction, the backward volume wave (BVW) modes were excited. However, surprisingly large amplitude SWs are detected in the remnant state when $\mu_0 H = 0$. Note that a large amplitude SW propagation was not observed for the YIG plane film sample at $\mu_0 H = 0$. These facts indicate that a large domain in the YIG film underneath the Ni AM-ASI might be formed. The group velocity of the SWs at $\mu_0 H = 0$ after the application of positive and negative fields is 2.3 km/s and 1.8 km/s, respectively. The magnetization direction of the YIG film is expected to be 30 - 35 deg and 50 - 55 deg, respectively, with respect to the CPW long axis according to the calculated group velocities of the 126 -nm-thick YIG thin film.

For a detail understanding, SW spectra of AM-ASI-YIG were detected in the remnant state after the following field protocol: A magnetic field of $+20$ mT was applied along x -direction, and the field was reduced to zero. Afterwards the magnetic field of (i) 90 mT was applied in $+y$ -direction and then a field H_r in $-y$ -direction was applied and (ii) *vice versa*. The SW propagation spectra at $\mu_0 H = 0$ following protocol (i) and (ii) are shown in Fig. 7.10c and d, respectively. For protocol (i), the large SW propagation spectra are observed at $\mu_0 H = 0$ for field $\mu_0 H_r \geq -10$ mT, which corresponds to the switching field detected in Fig. 7.9c. Below $\mu_0 H_r = -10$ mT, the amplitude of propagating SWs is vanishingly small. On the contrary, large propagating SW amplitudes are seen for (ii) for $\mu_0 H_r \geq 11$ mT (Fig. 7.10d). We consider that

the magnetization configuration of AM-ASI below (above) $\mu_0|H_r| = 10$ mT for protocol (i) and above (below) $\mu_0|H_r| = 10$ mT for protocol (ii) would be similar to the remnant state of Fig. 7.10a (Fig. 7.10b). From $\mu_0 H_r = 11$ mT to $\mu_0 H_r = 12$ mT for protocol (ii) in Fig. 7.10d, the SW properties are in the transition state from ASI saturated at -90 mT to 90 mT. Considering Fig. 7.5d, chain-like magnetization switching might happen in the AM-ASI sample. This transition state might realize the channeling of SWs in the YIG underlayer along the chain-like domains of the ASI in its remnant state.

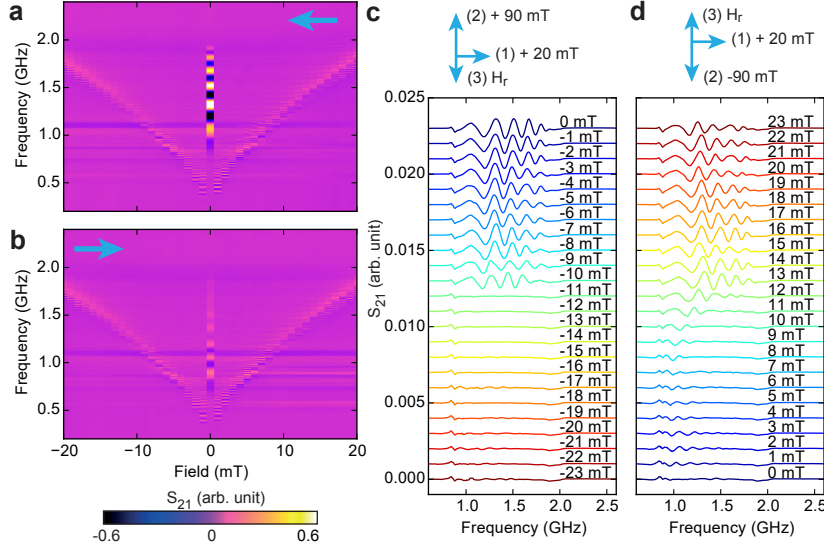


Figure 7.10: Field-dependent SW propagation of AM-ASI at $\varphi = 90$ deg from (a) $+90$ mT to -90 mT and (b) -90 mT to $+90$ mT. Black-white oscillations represent SW propagation through the YIG film. (c) and (d) SW propagation of AM-ASI-YIG at $\mu_0 H = 0$ after following the field protocol of (i) and (ii) illustrated by the insets: (1) A magnetic field of $+20$ mT was applied along x -direction, and the field was set to zero. (2) The magnetic field of 90 mT was applied along the y -axis, and then (3) the field of H_r was applied in the opposite direction. The field values inside the graphs indicate H_r before going back to $\mu_0 H = 0$ and measuring the SW propagation signals.

Conclusion

We investigated SW propagation of 126 -nm thick YIG films underneath square tiling and Ammann tiling based ASIs prepared from Ni. Angular dependent SW spectra exhibited manifold rotational symmetry, which reflected the rotational symmetry of each ASI. Grating coupler modes relevant to the reciprocal vectors of the ASIs were resolved. SQ-ASI showed the magnetization configuration dependent GC modes. We found SW propagation mode below the lowest frequency of the magnon band, and the mode might be induced by the ASI. In AM-ASI, magnetization-configuration-dependent SW propagation spectra are observed at $\mu_0 H = 0$. The ASIs integrated on the YIG thin film hence realize reconfigurable magnonic waveguides with and without the presence of external magnetic fields.

8 Summary and Outlook

In this thesis, static and dynamic properties of artificially engineered quasicrystals based on ferro- and ferri-magnetic thin films are investigated by means of broadband spin wave spectroscopy, Brillouin light scattering (BLS) technique, X-ray magnetic circular dichroism (XMCD), and micromagnetic simulation. In the following, a summary of the thesis work and an outlook on possible future studies are given.

Worms and magnon motifs in artificial ferromagnetic quasicrystals

We fabricated artificial magnetic quasicrystals (AMQs). The quasicrystals based on Penrose P2 and P3 lattices were made of amorphous CoFeB with a thickness of 19 nm. The characteristic length of the Penrose lattices was kept at 810 nm, and the width of nanoholes varied from 135 nm to 220 nm. Angular-dependent SW spectroscopy revealed that the SW spectra exhibited ten-fold rotational symmetry reflecting the lattice symmetry of the AMQs. Scale-invariant SW properties of AMQs implied the excitation of magnonic mode motifs arising from their geometrical repetitive patches, which was confirmed by micromagnetic simulations. The simulation results also indicated the existence of worm-like SW nanochannels extended through the Penrose P3 based quasicrystal, which were directly observed by SW imaging. The phase-resolved BLS evidenced that the phase front of nanochannels was irregular in the AMQ, implying that the SW states were different from channel to channel. The nanohole-based AMQs would be a new class of dense wavelength division multiplexers, which would be gated via rotation of an external magnetic field.

Formation of band structure in magnonic Penrose quasicrystal

Previously investigated AMQs were made of relatively high damping metallic CoFeB, which made the investigation of long-range SW propagation challenging. In order to overcome the difficulty, we fabricated nanotroughs based artificial quasicrystals made of 100-nm-thick insulating ferrimagnetic YIG via an etching process. The characteristic length of the Penrose P3 lattice was kept at 900 nm and a decagonal mesa was formed. By phase-resolved BLS

technique and broadband SW spectroscopy, we discovered multi-directional SW emission attributed to the unconventional rotational symmetry of the quasicrystals and a dense set of reciprocal vectors. The SW absorption spectra exhibited forbidden frequency gaps and a corresponding modification of the magnon density of states thanks to the formation of a magnonic band structure. The backfolding effect at the pseudo-Brillouin zone boundary of the quasicrystal was also observed in analytic calculations. The omnidirectional SW emission is advantageous for the fabrication of magnonic circuits. The formation of the pseudo-Brillouin zone would allow for the realization of a perfect magnonic band gap for forward volume wave (FVW) SW in magnonic quasicrystals.

Micromagnetic simulation predicted that the width of worm-like nanochannels in AMQs made of CoFeB amounted to 50 nm, which was beyond the diffraction limit of light for BLS measurements. In a collaboration with researchers from Max-Planck-Institute and Helmholtz Zentrum Berlin, we explored SW states in an AMQ by scanning transmission X-ray microscopy. The observed long-range nanochannels had different widths and phases. Intriguingly, SW propagated in nanochannels inside and outside of the AMQ. The Fourier transformation of SWs revealed that there were back-scattered SWs inside the quasicrystal giving rise to the formation of a band structure. Dispersion relations of the SWs in the AMQ in the experiment and simulations suggested the gap openings at the pseudo-Brillouin zone boundary.

Quasiperiodically/ periodically arranged magnonic grating couplers

We fabricated Py nanopillars on an insulating YIG thin film to excite short-wavelength SWs by the magnonic grating coupler (MGC) effect. The 100-nm-thick nanopillars with different diameters were arranged on a quasiperiodic Penrose P3 lattice and periodic square lattice. Ferromagnetic nanopillars were found to be multiply resonant grating elements by the formation of standing SWs in a vortex state and saturated state. Both periodic and quasiperiodic MGC samples exhibited MGC modes associated with their reciprocal lattice vectors (RLVs) \mathbf{G} and reciprocal vectors (RVs) \mathbf{F} , respectively, investigated by angular dependent SW spectroscopy. In the Penrose MGC SWs were excited in a broad frequency range thanks to the RVs \mathbf{F} , which densely filled all reciprocal space. The periodic MGC sample allowed SWs to be transmitted at the operation frequency of up to 25.3 GHz, corresponding to a wavelength of 52 nm. Short wavelength FVWs were excited with out-of-plane external fields, which saturated ferromagnetic nanopillars along their axial direction. Short wavelength SWs simultaneously excited by two emitters interfered constructively/destructively at a separate detector antenna, allowing for a 1/0 binary output operation. These hybrid nanostructures of ferromagnetic nanopillars with insulating YIG thin films would promise the miniaturized magnonic circuits operated for broadband 5G-communication technologies.

According to simulation results, the resonance frequencies of the grating elements were raised by reducing their diameter thanks to the increased axial anisotropy. Grating elements with reduced diameter can densely fill the space, which enlarges the magnitude of RVs (RLVs) of the gratings, and allows SWs to be excited with a shorter wavelength at a higher operation fre-

quency. The usage of high saturation magnetization materials such as CoFeB and CoFe would be also beneficial. This improvement might also cause strong dipolar interaction between nanopillars, and artificial spin ice as well as magnonic crystal properties might emerge, which might be beneficial for the advanced controls of SWs.

Magnonic engineering of artificial spin ice

We fabricated artificial spin ices (ASIs) made of Py ferromagnetic nanobars arranged on aperiodic Penrose P2, P3 and Ammann tilings. The intervertex distance for each tiling was kept at 810 nm while the length of nanobars were varied from 408 nm (isolated nanoislands) to 810 nm (interconnected network) in order to tune the dipolar interaction and exchange interaction at the vertices. Magnetization configurations of ASIs in the remnant state after applying in-plane magnetic field were imaged by photo electron emission microscopy (PEEM) using XMCD performed at Helmholtz Zentrum Berlin. The magnetization switching phenomena were analyzed using the dumbbell model and charge model. The compliance in the ice rule with interconnected ASIs and violation of the ice rules in the isolated ASIs indicated that exchange interaction played a dominant role in magnetization switching and cooperative reversal. We found that high magnetic charges at the vertices deviating from their ground state triggered the magnetization reversal in the interconnected ASIs. Notably, magnetization switching in the Ammann tiling based ASI was associated with chain-like domains. The reported ASIs based on the quasicrystalline arrangement might be a new class of reprogrammable magnonic crystals manipulated via the global magnetic field.

Toward realization of reconfigurable magnonics, we integrated ASIs made of Ni nanobars on a YIG thin film. The ASIs with an intervertex spacing of 810 nm were arranged on quasiperiodic Ammann and periodic square tilings. By angular SW spectroscopy we discovered SW resonances reflecting their lattice-symmetry. The field-dependent SW spectra showed grating coupler modes and SW guiding mode arising from the ferromagnetic nanobars parallel and vertical to the external field, respectively. The magnetization configuration of the ASI with respect to the YIG film tuned the resonance frequency of MGC modes. In the absence of an external field, SW propagation with large amplitude in the quasiperiodic ASI-integrated YIG film was observed unlike the unpatterned YIG film. Interestingly, the amplitude of propagating SWs was modified depending on the remnant state of the ASIs controlled by the global field. For the detailed understanding of the SW propagation in the remnant state, further investigations considering the orientation of the bias-magnetic field are necessary. Instead of a saturated state (Fig. 8.1a), the chain-domain state in an Ammann-tiling-based ASI confirmed from PEEM experiment would be utilized for guiding SWs, which would be explored by (phase-resolved) BLS microscopy as illustrated in Fig. 8.1b. A replacement of Ni with Py might be advantageous as (i) large stray field effects might be induced and (ii) the static magnetization configuration would be accessible by means of magnetic force microscopy.

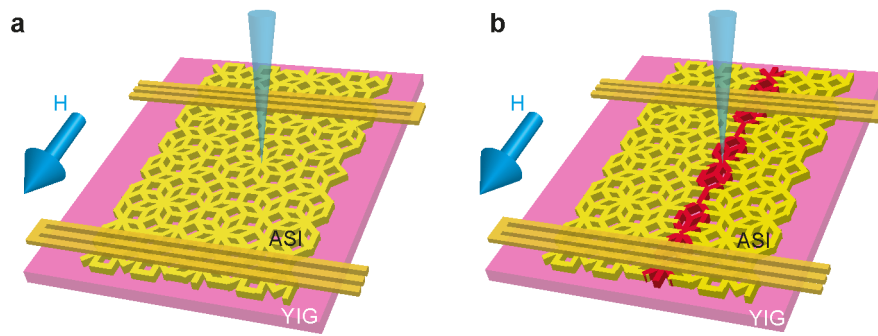


Figure 8.1: Schematic images of BLS experiments on a YIG thin film incorporating an Ammann tiling based ASI. Depending on (a) the saturated state and (b) the unsaturated state with a chain-like domain, the SW properties in the YIG film might be different.

A Appendix

This Chapter contains supporting information (SI). Supplementaries of published/submitted paper have been reformatted, the content was not modified.

A.1 SI-Direct Observation of Worm-Like Nanochannels and Emergent Magnon Motifs in Artificial Ferromagnetic Quasicrystals

This section provides supporting information for published manuscript reprinted in Section 4.1.

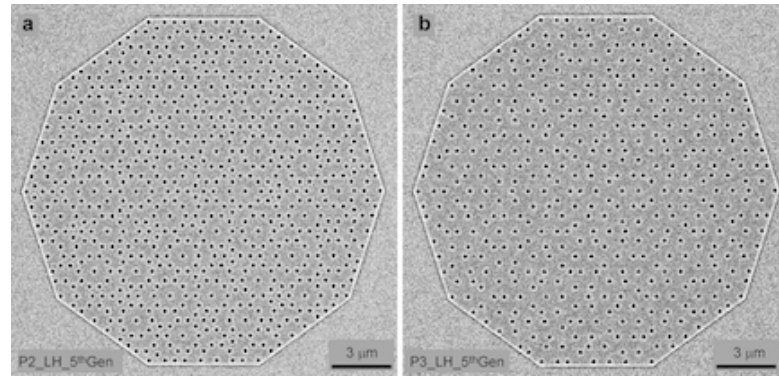


Figure A.1: Scanning electron microscopy images. AMQs of 5th generation incorporating nanoholes (dark) following (a) Penrose P2 and (b) P3 tilings. Nanoholes exhibit a diameter $D = 215 \pm 13$ nm and 221 ± 12 nm in (a) and (b), respectively. AMQs are fabricated from 19 nm thick CoFeB film. Nanoholes are etched at the vertices of the Penrose tiling.

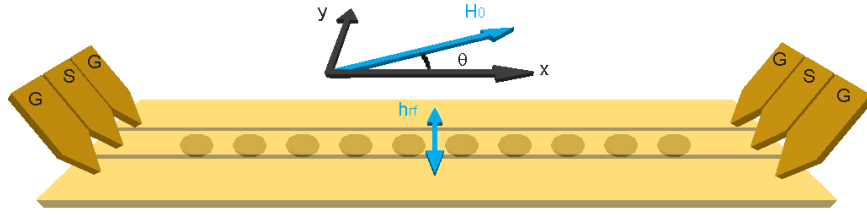


Figure A.2: Experimental setup of all electrical spin wave spectroscopy on artificial magnetic quasicrystals (AMQs). Sketch of experimental setup illustrating the THRU-coplanar waveguide (CPW) with ground (G) - signal (S) - ground (G) lines. The CPW was integrated on ten nominally identical AMQs prepared from CoFeB. AMQs are aligned with their symmetry axes parallel to the long axis of the CPW. The in-plane component of the radio-frequency magnetic field \mathbf{h}_{rf} is sketched.

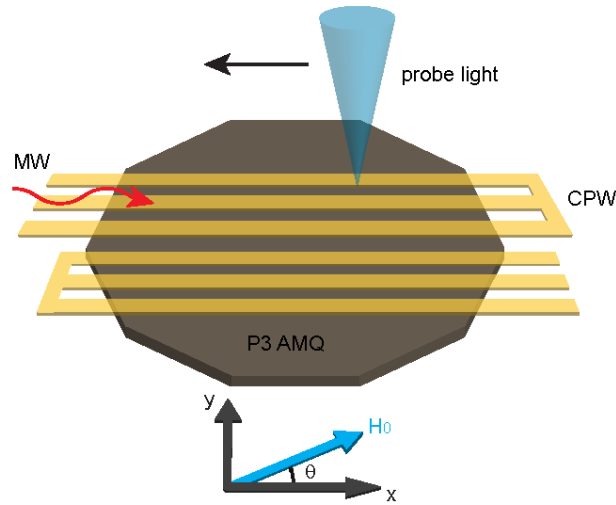


Figure A.3: Experimental set up of Brillouin light scattering microscopy on P3 AMQ. Schematic image of experimental setup for spin wave imaging via inelastic magnon-photon interaction. Two SHORT-type CPWs were fabricated on top of the P3 AMQ and were symmetric with respect to the center of the AMQ. The CPWs' long axes are parallel to the symmetry axis of the AMQ. A microwave (MW) signal is applied to one of the CPW to generate a radio-frequency magnetic field in order to excite spin-precessional motion in the AMQ.

A.1 SI-Direct Observation of Worm-Like Nanochannels and Emergent Magnon Motifs in Artificial Ferromagnetic Quasicrystals

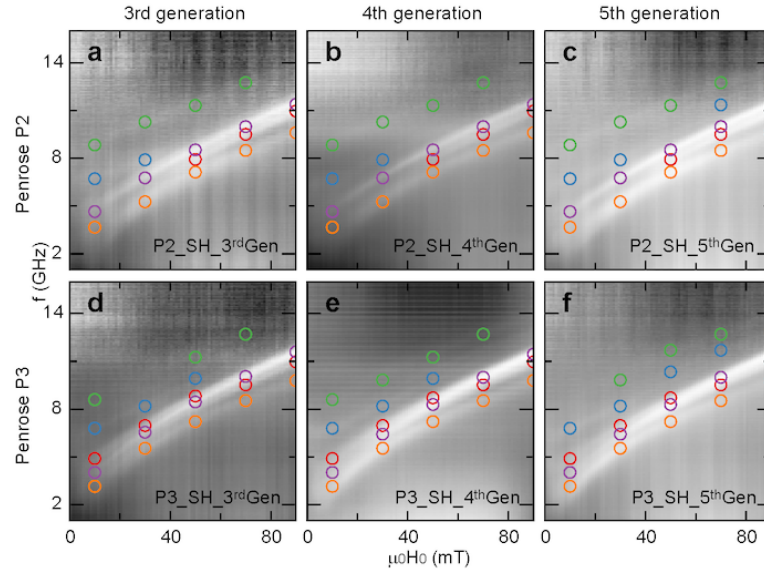


Figure A.4: Spin wave spectra obtained on AMQs with small (S) nanohole diameters. Field dependent spin-wave spectroscopy on AMQs of 3rd [shown in (a) and (d)], 4th [shown in (b) and (e)] and 5th [shown in (c) and (f)] generation of Penrose P2 [top row, (a), (b) and (c)] and P3 lattices [bottom row, (d), (e) and (f)] at $\theta = 0$ deg. The hole diameters for each AMQ are specified in Table 1 of the Methods section. Bright indicates microwave absorption. Colored symbols are guides to the eye highlighting individual branches.

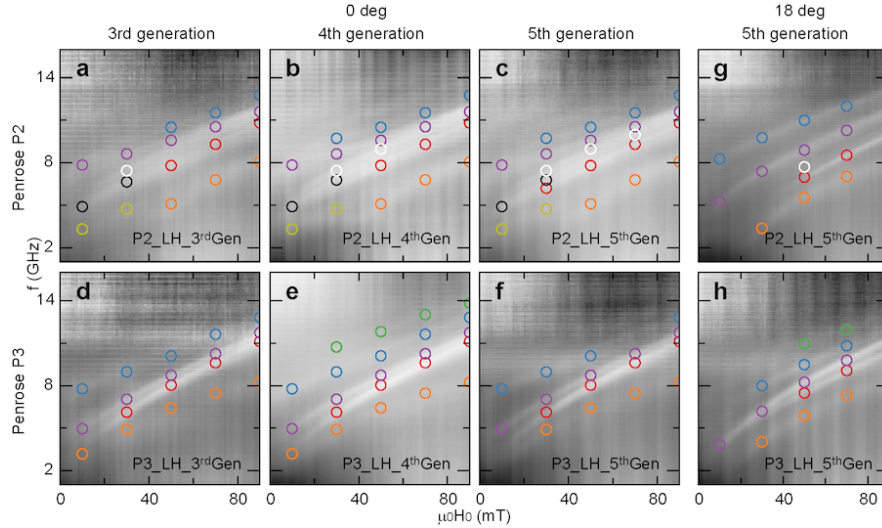


Figure A.5: Spin wave spectra obtained on AMQs with large (L) nanohole diameters. Field dependent spin-wave spectroscopy on AMQs of 3rd [shown in (a) and (d)], 4th [shown in (b) and (e)] and 5th [shown in (c) and (f)] generation of Penrose P2 [top row, (a), (b) and (c)] and P3 lattices [bottom row, (d), (e) and (f)] at $\theta = 0$ deg. Spin wave spectra obtained on AMQs of 5th generation of (g) Penrose P2 and (h) Penrose P3 lattices at $\theta = 18$ deg. The hole diameters for each AMQ are specified in Table 1 of the Methods section. Bright indicates microwave absorption. Colored symbols are guides to the eye highlighting individual branches.

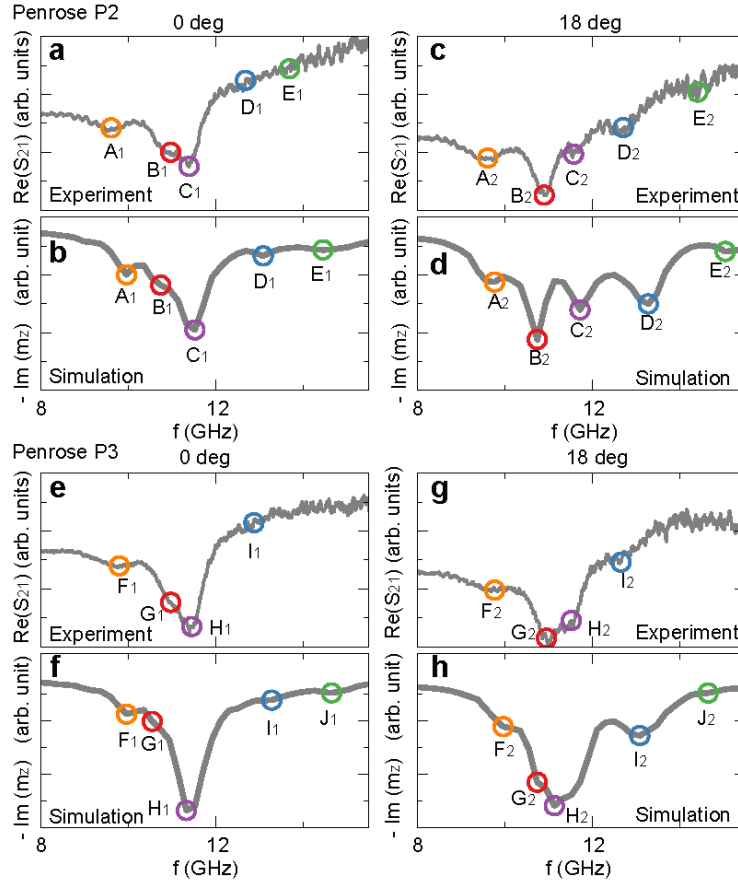


Figure A.6: Line spectra measured at 90 mT for P2_SH_5thGen [shown in (a) and (c)] and P3_SH_5thGen [shown in (e) and (g)] at $\theta = 0$ deg [shown in (a) and (e)] and $\theta = 18$ deg [shown in (c) and (g)]. Simulated SW spectrum ($\text{Im}(m_z)$) at 90 mT for Penrose P2 [shown in (b) and (d)] and Penrose P3 [shown in (f) and (h)] at $\theta = 0$ deg [shown in (b) and (f)] and $\theta = 18$ deg [shown in (d) and (h)] with nanoholes of small diameter $D = 135$ nm. Colored symbols in the experimental spectra indicate the frequency values which are consistent with the different branches identified in the grayscale plots shown in Figure 2. The frequency resolution of the SW spectra in the experiment was 10 MHz, which was better compared to 200 MHz provided by the simulation.

A.1 SI-Direct Observation of Worm-Like Nanochannels and Emergent Magnon Motifs in Artificial Ferromagnetic Quasicrystals

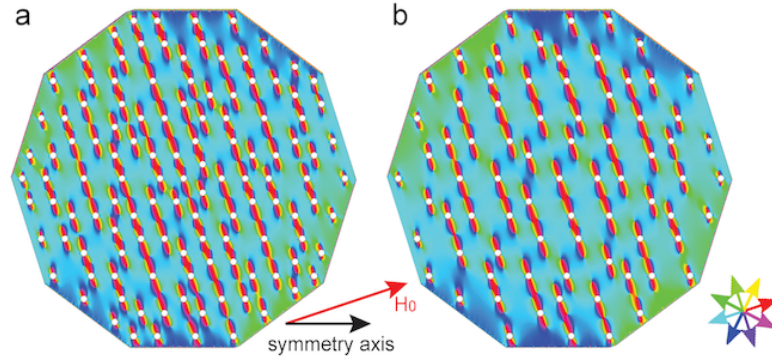


Figure A.7: Spatial distribution of the local demagnetization field direction for the AMQ with $D = 135$ nm in (a) a Penrose P2 and (b) P3 lattice. The simulation results shown in Figure 4.1e and 4.1f, respectively, are relevant. A magnetic field of 90 mT is applied at an angle $\theta = 18$ deg. Hue color represents the direction of the demagnetization field as indicated by the color wheel at the right bottom. Note that the light blue color indicates a demagnetizing field which is antiparallel to the applied field. As a consequence, the internal field is small in the correspondingly colored regions.

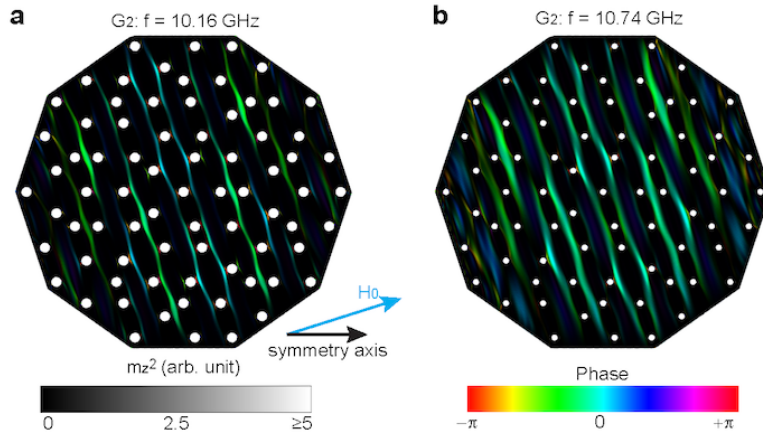


Figure A.8: Spatial distribution of spin-precessional motion (channel-like spin waves) for AMQs with different hole diameters. Mode profiles of AMQs with (a) $D = 220$ nm and (b) $D = 135$ nm in Penrose P3 lattices at (a) $f = 10.16$ GHz and (b) $f = 10.74$ GHz. The simulation result shown in Figure 4.1f of the main text is replotted for direct comparison. A magnetic field of 90 mT is applied at an angle $\theta = 18$ deg. Saturation and hue scales represent the power and phase of the dynamical magnetization component m_z , respectively.

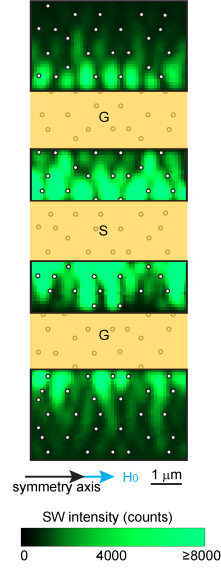


Figure A.9: Imaging of spin waves in the P3 AMQ for an applied field of 90 mT along $\theta = 0$ deg (symmetry axis). Measured spatial distributions of intensities of spin precession in the P3 AMQ with nanohole diameter $D = 163$ nm obtained near a CPW. The microwave signal was applied to the CPW at $f = 11.4$ GHz. Rectangles of semi-transparent yellow color represent signal (S) and ground (G) lines of the CPW.

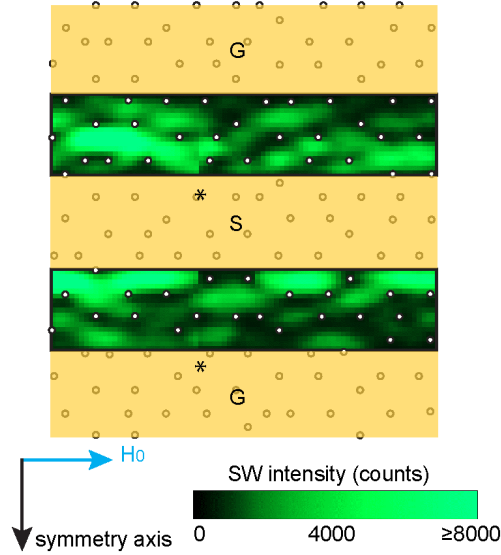


Figure A.10: SW imaging for an applied field of 90 mT of P3 AMQ along $\theta = 90$ deg (off-symmetry axis). Measured spatial distributions of intensities of spin precession (legend) in P3 AMQ with a nanohole diameter $D = 163$ nm obtained near a CPW. The microwave signal was applied at $f = 11.7$ GHz. Rectangles of semi-transparent yellow color represent signal and ground lines of the CPW. The discontinuity in the SW image (intensity) indicated by the asterisk is attributed to a stitching error of the XY piezo-positioning system.

A.1 SI-Direct Observation of Worm-Like Nanochannels and Emergent Magnon Motifs in Artificial Ferromagnetic Quasicrystals

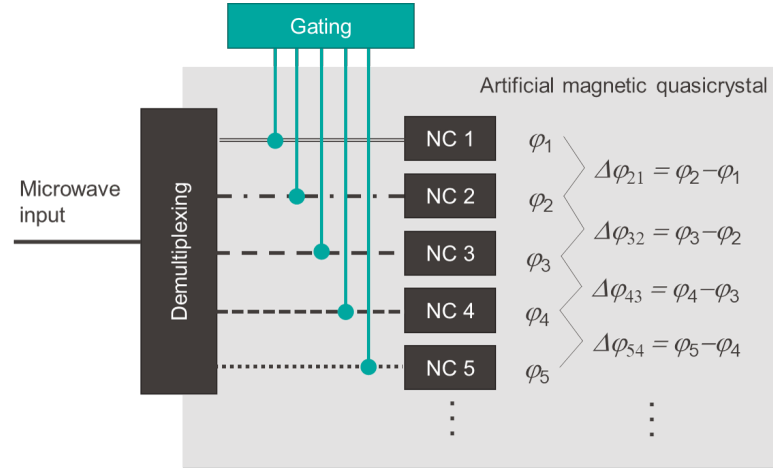


Figure A.11: Schematic image of the demultiplexing functionality of a quasicrystal with nanochannels (NCs) as observed in the manuscript. The solid line on the left represents the microwave signal at a single frequency. The different lines indicate the different spin wave nanochannels supporting locally different wavelengths λ . After the same length x in horizontal direction the spin waves exhibit specific but different phases $\varphi_i = 2\pi x/\lambda_i$. The accumulated phase per nanochannel could be modified by a gating system (central part), thereby allowing for wave-based logics with the high areal density offered by the AMQ-induced nanochannels. The read out could be performed by individual detectors or combined detection making use of interference effects and gated phase differences (right column) between nanochannels.

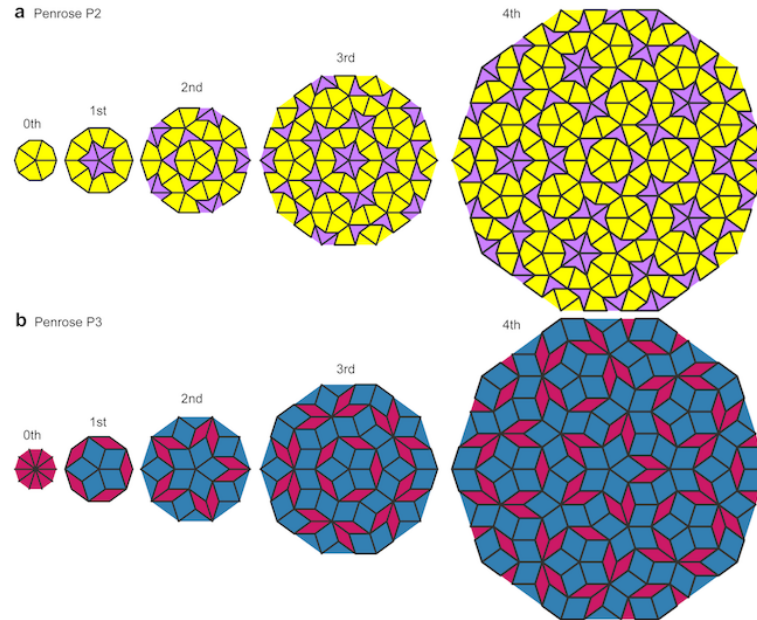


Figure A.12: Deflation of Penrose tiling. Both (a) Penrose P2 and (b) P3 tilings are composed of two different prototiles, and thereby the self-similar aperiodic tilings are fabricated.

A.2 SI-Direct observation of multiband transport in magnonic Penrose quasicrystals via broadband and phase-resolved spectroscopy

This section provides supporting information for submitted manuscript reprinted in Sec. 5.1.

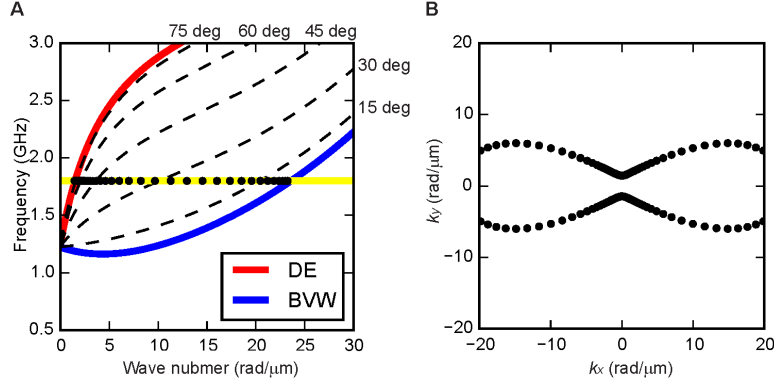


Figure A.13: **Angular dependence of spin wave dispersion relations and isofrequency contour.** (A) SW dispersion relation for unpatterned YIG thin film (100 nm thickness). Red and blue lines represent the DE and BVW modes, respectively. Dashed line indicates the dispersion relation of YIG at different wave vector orientation θ with respect to the field. Black dots indicate the wave vector of SWs at fixed frequency ($f = 1.80$ GHz) marked by the yellow line. (B) Isofrequency contour of SWs at $f = 1.80$ GHz. The wave vector magnitude and angle is calculated by dispersion relation of the YIG film as shown in (A).

A.2 SI-Direct observation of multiband transport in magnonic Penrose quasicrystals via broadband and phase-resolved spectroscopy

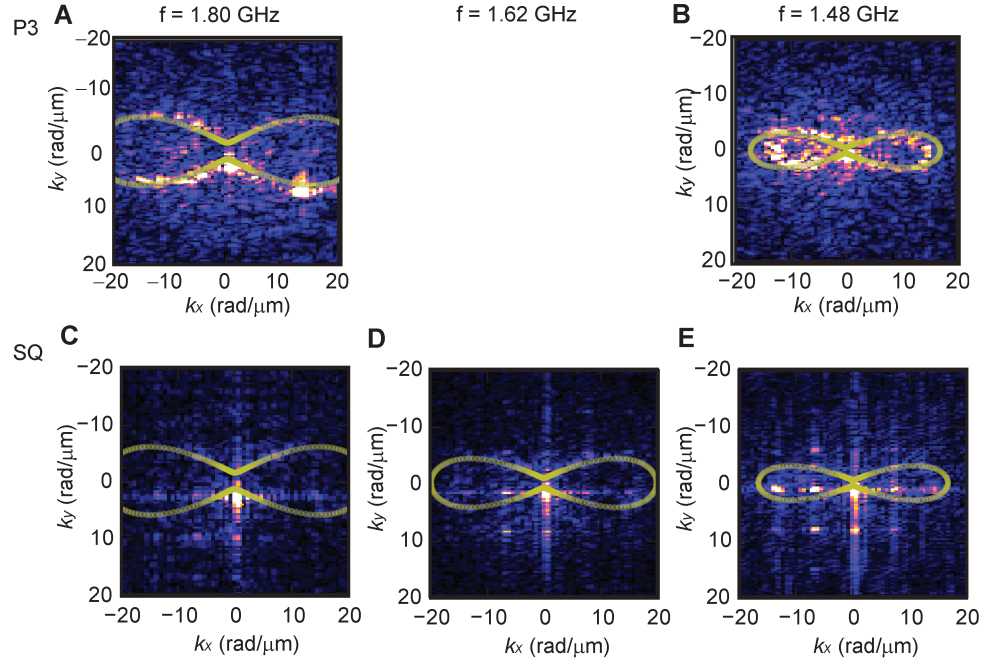


Figure A.14: **Spin waves in reciprocal space.** SW intensity in reciprocal space after a FFT performed on the SW images in Fig. 1, 2, 3 and 4 for (A) (B) P3-MQC and (C) (D) (E) SQ-MC at (A) (C) $f = 1.80$ GHz, (D) $f = 1.62$ GHz and (B) (E) $f = 1.22$ GHz. Isofrequency contours of SWs for corresponding frequencies are plotted with yellow dots.

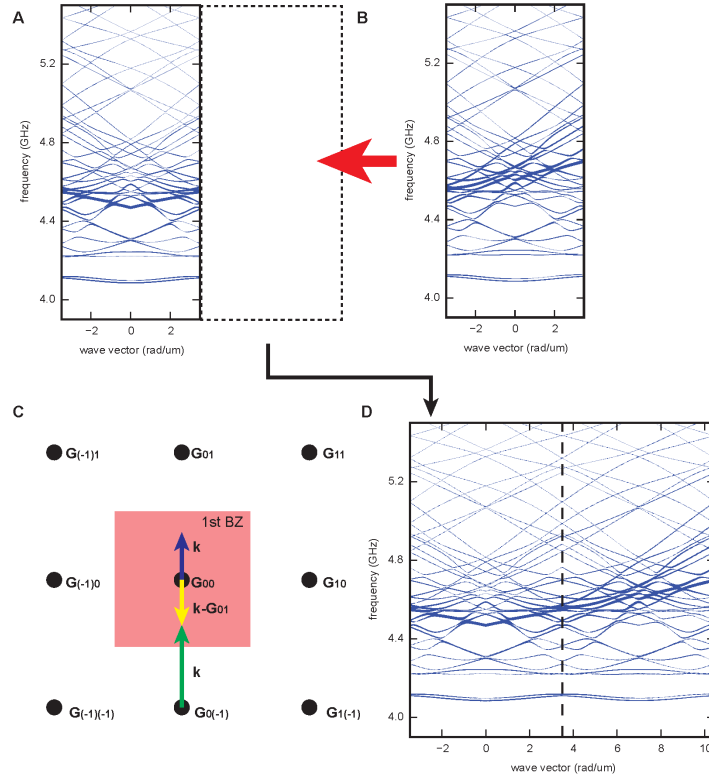


Figure A.15: **Extension of dispersion curves beyond Brillouin zone boundary.** A band structure of SQ-MC with a field value of 93 mT for $\theta = 45$ deg with projection of the magnon wavefunction on the corresponding plane wave modes of (A) G_{00} and (B) G_{01} responsible for backfolding wave vectors \mathbf{k} into 1st BZ. The thickness of blue dots represents the projection amplitude of the back-folded modes. (C) A reciprocal lattice of SQ-MC (dots) and 1st BZ (red). Blue and green arrows indicate wave vectors \mathbf{k} with an amplitude smaller and larger than 1st BZ boundary, respectively. The yellow arrow indicates the back-folded wave vectors $\mathbf{k} - \mathbf{G}_{01}$. (D) An extended band structure of SQ-MC by concatenating (A) with (B). The black dashed line represents the 1st BZ boundary.

A.2 SI-Direct observation of multiband transport in magnonic Penrose quasicrystals via broadband and phase-resolved spectroscopy

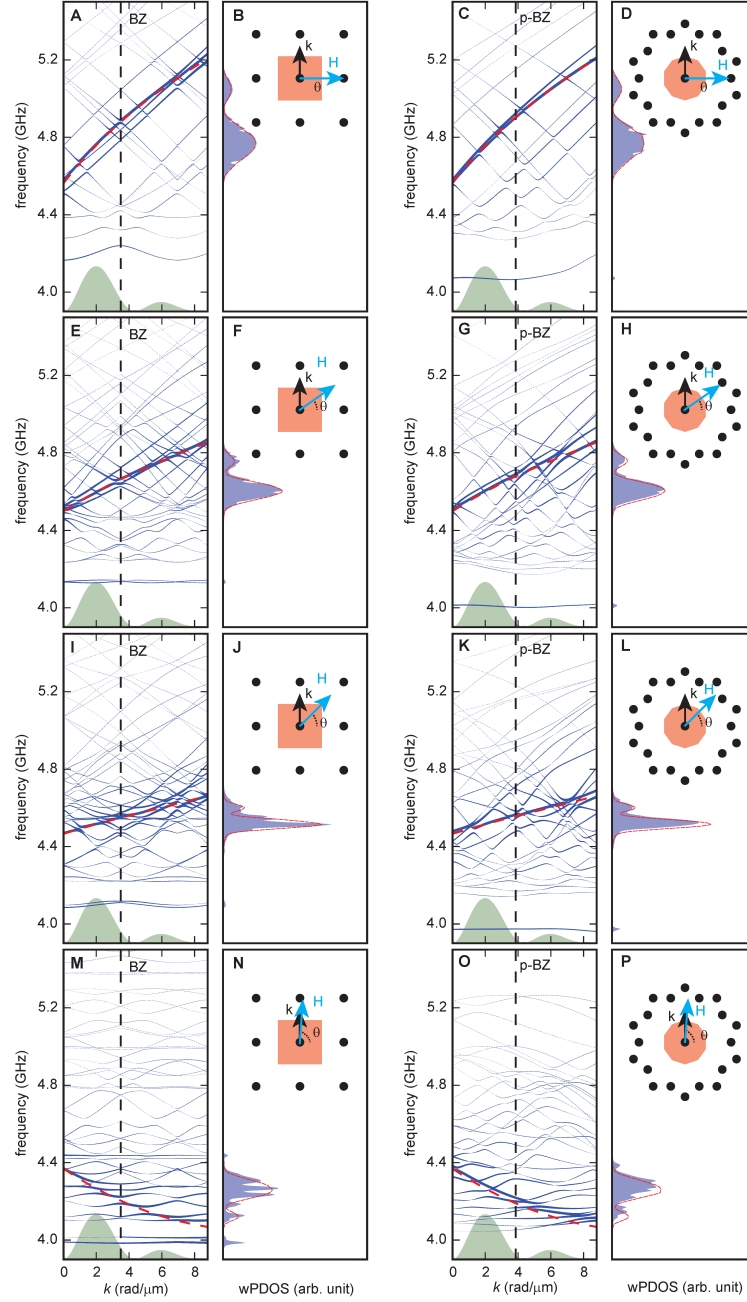


Figure A.16: Band structure and density of states in a magnonic crystal and quasicrystal. Band structure of (A) (E) (I) (M) SQ and (C) (G) (K) (O) P3 compared to the original spin wave dispersion relation of the YIG film (red dashed line). The diameter of blue dots forming lines represents the weight of the back-folded modes including the original dispersion. In green we show the excitation spectrum of the CPW microwave magnetic field in arbitrary units. wPDOS of SWs of (B) (F) (J) (N) SQ-MC and (D) (H) (L) (P) P3-MQC for $\theta = 0, 35, 45, 86$ deg with a field value of 96, 94, 93, 90 mT, respectively, is shown in blue. The red line represents the wPDOS of SWs of PF as a reference. Insets display reciprocal lattice points (i.e., the end points of reciprocal lattice vectors \mathbf{G} and reciprocal vectors \mathbf{F} and the BZ and the p-BZ (orange areas) of SQ-MC and P3-MQC, respectively).

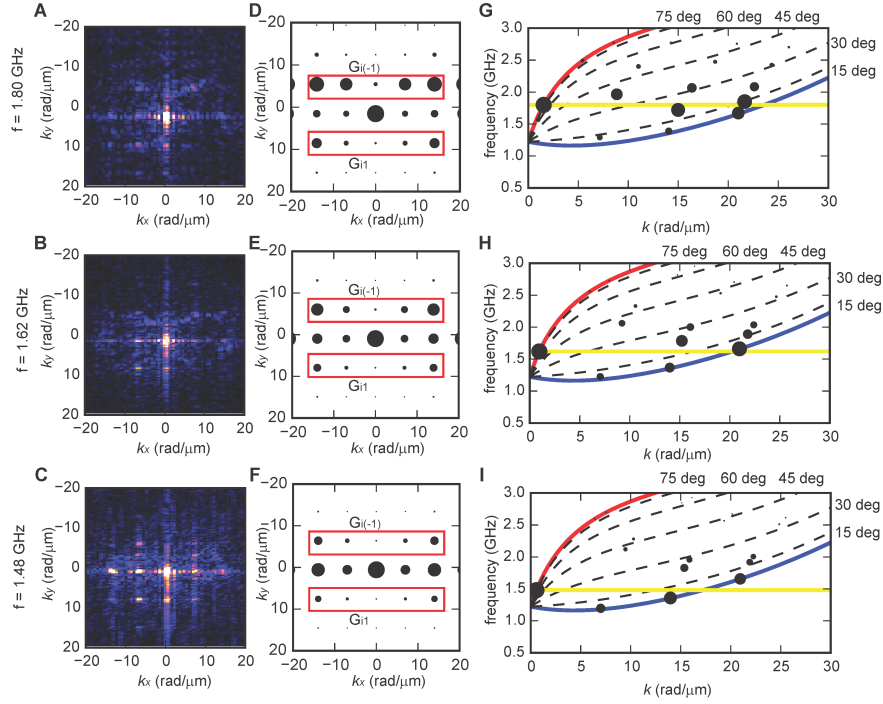


Figure A.17: Spin waves in reciprocal space and calculated grating coupler modes. SW intensity in reciprocal space after a FFT performed on the SW images in Fig. 2 and 3 for SQ-MC at (A) $f = 1.80$ GHz, (B) $f = 1.62$ GHz, and (C) $f = 1.48$ GHz. Simulated Bragg peaks expected in the FFT result of SW images taken at (D) $f = 1.80$ GHz, (E) $f = 1.62$ GHz and (F) $f = 1.48$ GHz. The size of dots represents how close the resonance frequency of SW modes ($\mathbf{k} + \mathbf{G}_{ij}$) is with respect to the corresponding microwave frequency expected from the dispersion relation shown in (G) (H) and (I). Red and blue lines in dispersion relations represent the DE and BVW modes, respectively. Dashed line indicates the dispersion relation of YIG at different wave vector orientation θ with respect to the field. Yellow line indicates the applied microwave frequency.

A.2 SI-Direct observation of multiband transport in magnonic Penrose quasicrystals via broadband and phase-resolved spectroscopy

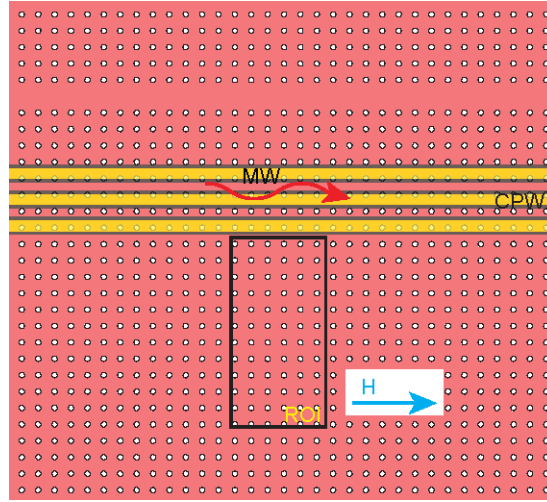


Figure A.18: **Magnonic crystal for BLS measurement.** Schematic image of SQ-MC used for the BLS measurement. Circles indicate the positions of nanotroughs. One column of nanotroughs is missing in the MC. The region of interest (ROI) for the BLS measurement does not include the column, and thus we expect that the back-folded modes in the MC is still observed. The magnetic field was applied along the long axis of the CPW.

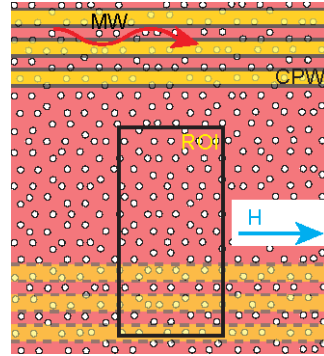


Figure A.19: **Magnonic quasicrystal for BLS measurement.** Schematic image of P3-MQC used for the BLS measurement. After SW spectroscopy, one of the CPWs indicated by the dashed line was removed, and BLS experiment was conducted at the region of interest (ROI) including the place where CPW was mounted. Circles indicate the positions of nanotroughs. The magnetic field was applied along the long axis of the CPW.

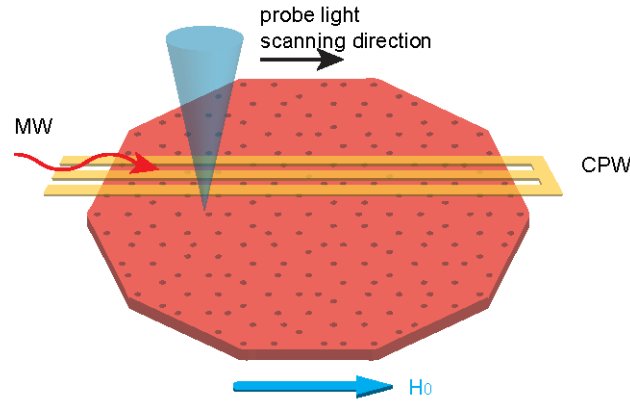


Figure A.20: **Experimental set up of Brillouin light scattering microscopy.** Schematic image of experimental setup for spin wave imaging via inelastic magnon-photon interaction. A SHORT-type CPW were fabricated on top of the MC/MQC. The CPWs' long axis are parallel to the symmetry axes of both MC and MQC. A microwave (MW) is applied to the CPW to generate a radio-frequency magnetic field in order to excite spin-precessional motion in the MC/MQC. The magnetic field is always applied along the long axis of the CPW. A probe light always scans along the CPW long axis.

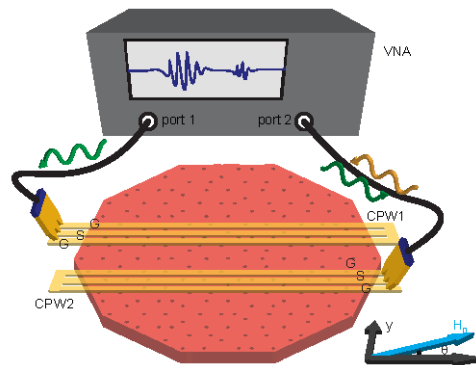


Figure A.21: **Experimental setup of all electrical spin wave spectroscopy.** Sketch of experimental setup illustrating the SHORT-coplanar waveguides (CPWs) with ground (G) - signal (S) - ground (G) lines. The CPWs were integrated on the MC/MQC prepared from YIG. The MC/MQC were aligned with their symmetry axes parallel to the long axis of the CPWs. Both CPWs were connected to the VNA. The S_{21} (S_{22}) parameter represents the SW propagation (absorption) by applying microwaves from port 1 (2). The signal was always detected at port 2. The magnetic field was applied in-plane.

A.2 SI-Direct observation of multiband transport in magnonic Penrose quasicrystals via broadband and phase-resolved spectroscopy

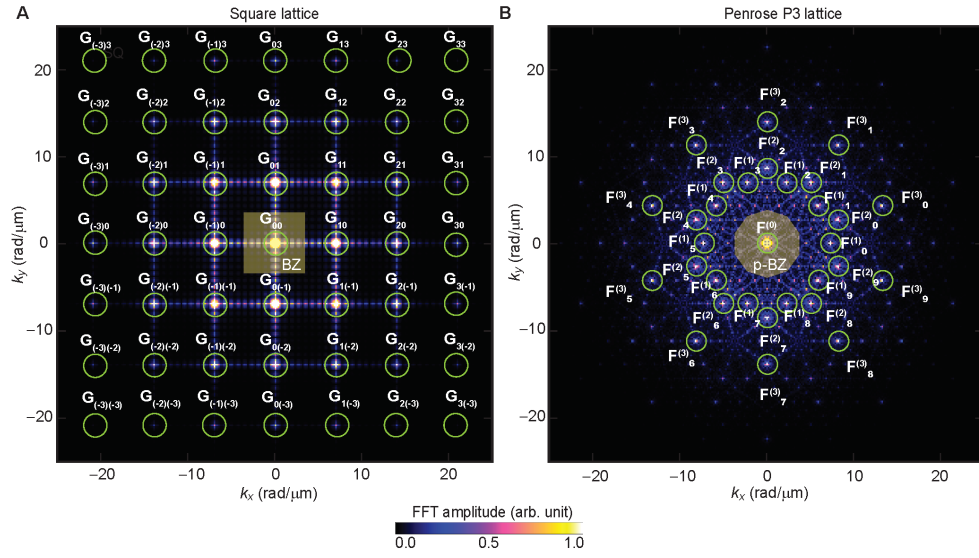


Figure A.22: **Bragg diffraction patterns of 2D periodic and aperiodic lattices.** The virtual representation of (A) square lattice and (B) Penrose P3 lattice in reciprocal space. Light green circles indicate the reciprocal lattice vectors \mathbf{G} of square lattice and reciprocal vectors \mathbf{F} of Penrose P3 lattice used for the calculation of magnon band structure of SQ-MC and P3-MQC, respectively. Transparent yellow represents the square-shaped 1st BZ of square lattice and decagonal shaped p-BZ of Penrose P3 lattice.

A.3 SI-Broadband magnonic nanograting coupler approaching 5G telecommunication

This section provides supporting information for a manuscript, which is intended to submit to a journal, reprinted in Section 6.1.

Excitation spectrum of microwave magnetic field and spin wave excitation in YIG thin film

For the excitation of SWs, microwaves are applied to a CPW. Excitation spectrum in real space and reciprocal space of microwave magnetic fields h_x is shown in Fig. A.23a,b, respectively. There are several peaks denoted as k_i with integer number i . Field-dependent SW absorption spectra S_{22} of a YIG plane film for in-plane magnetic field along $+x$ -direction are shown in Fig. A.23c. Field-dependent SW excitation associated with k_i and $k_i + k_{PSSW}$ are clearly seen. Similarly, angular dependent SW propagation mode associated with k_i and $k_i + k_{PSSW}$ are detected (Fig. A.23d).

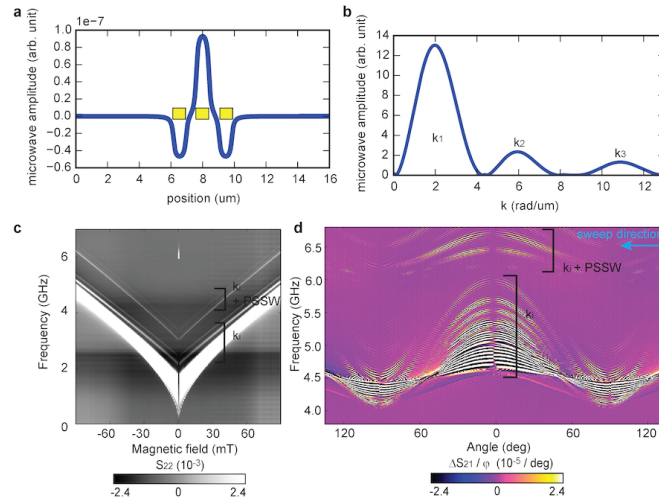


Figure A.23: Excitation spectrum (a) in real space and (b) reciprocal space of microwave magnetic fields h_x . (c) Field-dependent SW absorption spectra S_{22} of a YIG plane film for in-plane magnetic field along $+x$ -direction. (d) Angular dependent SW propagation spectra with a field value of 90 mT.

Magnetization configuration of ferromagnetic nanopillars

Magnetization configuration of ferromagnetic nanopillars for each diameter D is in a vortex state with a small in-plane magnetic field 5 mT. By applying further magnetic field (90 mT), a core of the vortex shifts along y -axis. Magnetic moments in the nanopillar points $-z$ direction (saturated) when the external magnetic field of -500 mT in z -direction for each sample.

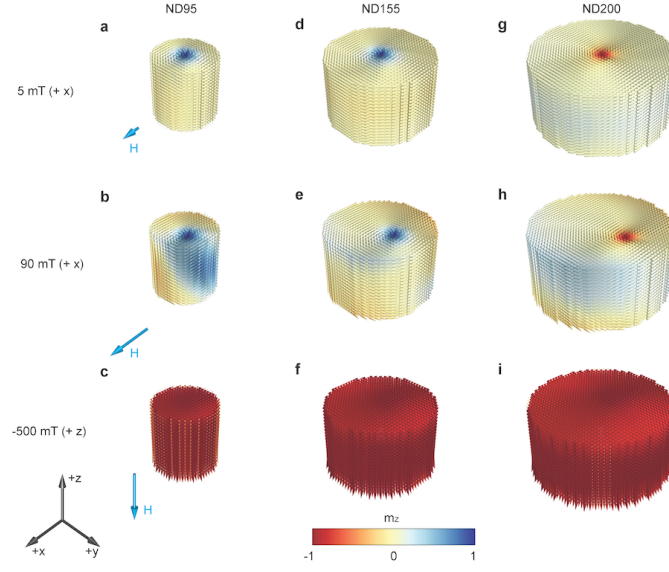


Figure A.24: Static magnetization configuration of ferromagnetic nanopillars for (a)(b)(c) ND95, (d)(e)(f) ND155 and (g)(h)(i) ND200 for in-plane magnetic field with a value of (a)(d)(g) 5 mT and (b)(e)(h) 90 mT and (c)(f)(i) out-of-plane magnetic field of -500 mT .

Field-dependent SW propagation spectra of aperiodically arranged GC sample

Magnetic field is applied along the long axis of the CPW of sample P3-ND155. Black and white represent the oscillation of S_{21} signal. The field is applied parallel to the long axis of the CPWs. White dashed circle represents the SW propagation spectra at 19 GHz. The line cut of the SW propagation spectra is shown in Fig. 6.2e in the main text.

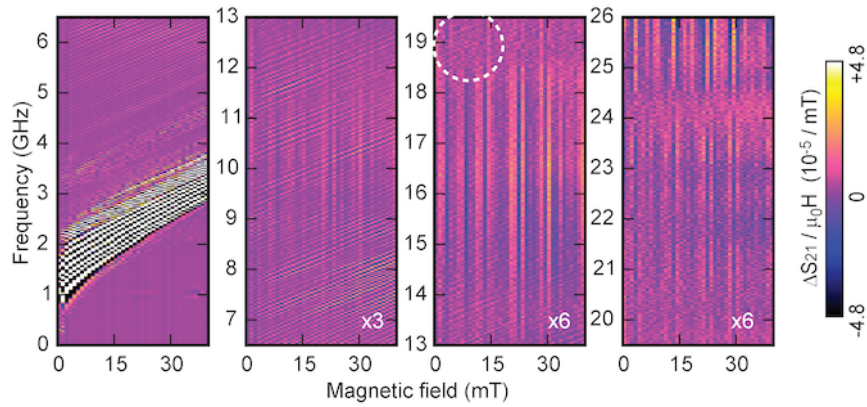


Figure A.25: Static magnetization configuration of ferromagnetic nanopillars for (a)(b)(c) ND95, (d)(e)(f) ND155 and (g)(h)(i) ND200 for in-plane magnetic field with a value of (a)(d)(g) 5 mT and (b)(e)(h) 90 mT and (c)(f)(i) out-of-plane magnetic field of -500 mT .

Angular dependent SW propagation spectra of periodically arranged GC sample

Magnetic field is applied on sample SQ-ND155 in-plane at 10 mT. Black and white represent the oscillation of S_{21} and S_{23} signal. Light green arrows represent the GC modes ($\mathbf{G}_{(-5)3} + \mathbf{k}_{PSSW}$ for S_{21} and $\mathbf{G}_{53} + \mathbf{k}_{PSSW}$ for S_{21}) used in the SW interference experiment (Fig. 6.4). Those GC modes propagate through the SQ lattice sample diagonally (not perpendicular to the long axis of the CPW).

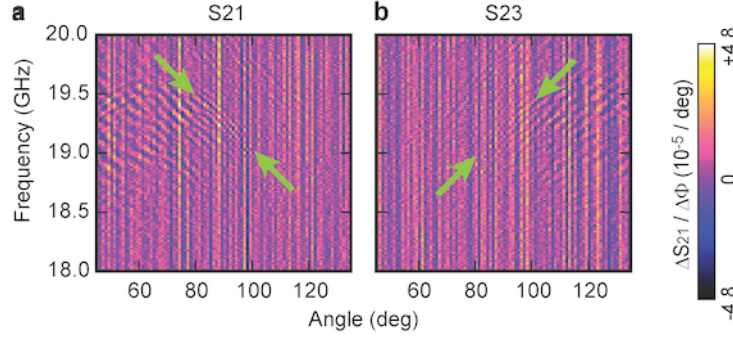


Figure A.26: Angular dependent SW propagation spectra of SQ-ND155 sample. SWs were emitted from (a) CPW antenna 1 (S_{21}) and (b) CPW antenna 3 (S_{23}) and propagated to CPW antenna 2.

Logic operation using short wavelength SW for aperiodically arranged GC sample

Magnetic field is applied at $\varphi = 54$ deg to sample P3-ND95 in order to excite $\mathbf{F}_7^{(5)}$ mode shown in Fig. 6.1h. Microwaves with a phase difference ϕ_{vna} are applied to two CPW antennas (CPW antenna 1 and 3), and a voltage induced by interfered SWs underneath the other antenna (CPW antenna 2) is detected. Black and white represent the oscillation of S_{21} signal as shown in Fig. A.27b and c. At 5.55 GHz SWs are interfered constructively at $\phi_{vna} = 280$ deg and destructively at $\phi_{vna} = 100$ deg.

Bragg diffraction pattern of 2D quasicrystal

Reciprocal vectors \mathbf{F} of the Penrose P3 lattice are expressed with a linear combination of basic reciprocal vectors $\mathbf{F}^{(1)}$. $\mathbf{F}^{(1)}$, $\mathbf{F}^{(2)}$, $\mathbf{F}^{(3)}$, $\mathbf{F}^{(4)}$ and $\mathbf{F}^{(5)}$ are described in Fig. A.28. The intensity of the Bragg peaks corresponding to $\mathbf{F}^{(2)}$ and $\mathbf{F}^{(3)}$ is larger than of $\mathbf{F}^{(1)}$.

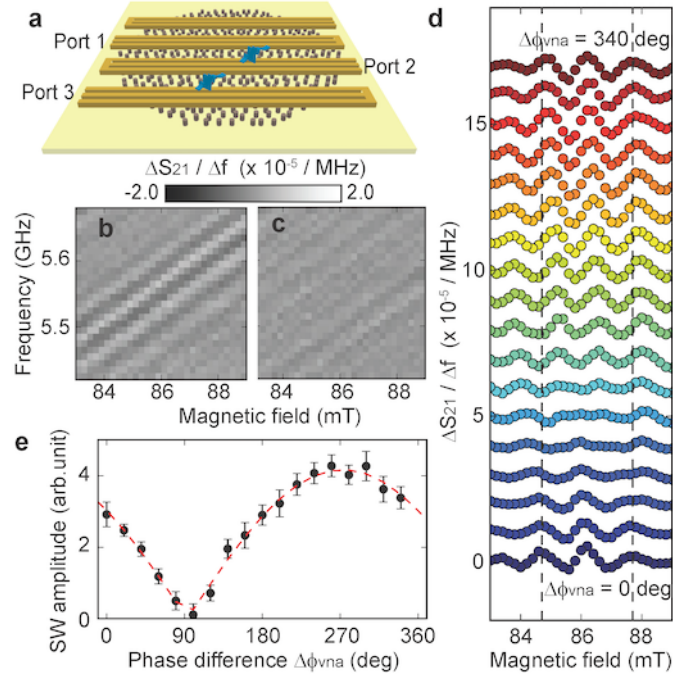


Figure A.27: (a) Schematic image of SW interference experiment. Interfered SW spectra (b) at $\phi_{vna} = 280$ deg and (c) at $\phi_{vna} = 100$ deg. (d) Line cuts of interfered SW spectra taken at $f = 5.55$ GHz for each phase difference with a step of 20 deg. (e) Interfered SW amplitude as a function of the phase difference ϕ_{vna} . Errorbars indicate fitting error of sinusoidal function on line-cut spectra of (d), and the dashed line represents the fitting result of interfered wave formula shown in Eq. (1).

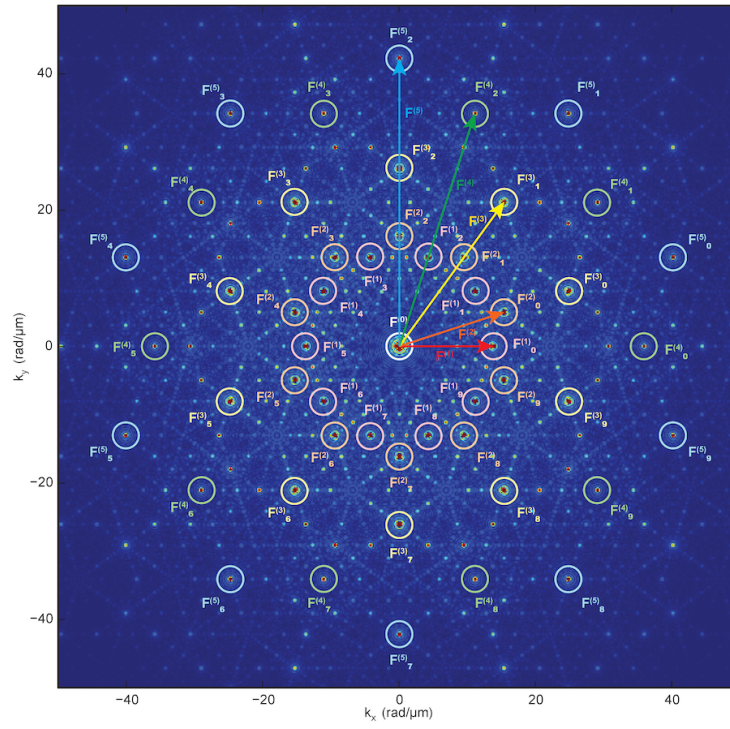


Figure A.28: Penrose P3 lattice in reciprocal space.

Bibliography

- [1] A.G. Gurevich and G.A. Melkov. *Magnetization oscillations and waves*. CRC press, Boca Raton, Florida, 1996.
- [2] J. Gubbi, R. Buyya, S. Marusic, and M. Palaniswami. Internet of things (IoT): A vision, architectural elements, and future directions. *Future Generation Computer Systems*, 29(7):1645–1660, 2013.
- [3] A. Khitun, M. Bao, and K.L. Wang. Magnonic logic circuits. *Journal of Physics D: Applied Physics*, 43(26):264005, 2010.
- [4] V.V. Kruglyak, S.O. Demokritov, and D. Grundler. Magnonics. *Journal of Physics D: Applied Physics*, 43(26):264001, 2010.
- [5] A.A. Serga, A.V. Chumak, and B. Hillebrands. YIG magnonics. *Journal of Physics D: Applied Physics*, 43(26):264002, 2010.
- [6] M. Krawczyk and D. Grundler. Review and prospects of magnonic crystals and devices with reprogrammable band structure. *Journal of Physics: Condensed Matter*, 26(12):123202, 2014.
- [7] A.V. Chumak, A.A. Serga, and B. Hillebrands. Magnonic crystals for data processing. *Journal of Physics D: Applied Physics*, 50(24):244001, 2017.
- [8] M. Krawczyk and H. Puzkarski. Plane-wave theory of three-dimensional magnonic crystals. *Physical Review B*, 77(5):054437, 2008.
- [9] M. Krawczyk, S. Mamica, M. Mruczkiewicz, J.W. Klos, S. Tacchi, M. Madami, G. Gubbiotti, G. Duerr, and D. Grundler. Magnonic band structures in two-dimensional bi-component magnonic crystals with in-plane magnetization. *Journal of Physics D: Applied Physics*, 46(49):495003, 2013.
- [10] S. Neusser, G. Duerr, S. Tacchi, M. Madami, M.L. Sokolovskyy, G. Gubbiotti, M. Krawczyk, and D. Grundler. Magnonic minibands in antidot lattices with large spin-wave propagation velocities. *Physical Review B*, 84(9):094454, 2011.

- [11] R. Zivieri, S. Tacchi, F. Montoncello, L. Giovannini, F. Nizzoli, M. Madami, G. Gubbiotti, G. Carlotti, S. Neusser, G. Duerr, and D. Grundler. Bragg diffraction of spin waves from a two-dimensional antidot lattice. *Physical Review B*, 85(1):012403, 2012.
- [12] T. Schwarze and D. Grundler. Magnonic crystal wave guide with large spin-wave propagation velocity in CoFeB. *Applied Physics Letters*, 102(22):222412, 2013.
- [13] T. Schwarze, R. Huber, G. Duerr, and D. Grundler. Complete band gaps for magnetostatic forward volume waves in a two-dimensional magnonic crystal. *Physical Review B*, 85(13):134448, 2012.
- [14] S. Tacchi, B. Botters, M. Madami, J. W. Kłos, M. L. Sokolovskyy, M. Krawczyk, G. Gubbiotti, G. Carlotti, A. O. Adeyeye, S. Neusser, and D. Grundler. Mode conversion from quantized to propagating spin waves in a rhombic antidot lattice supporting spin wave nanochannels. *Physical Review B*, 86(1):014417, 2012.
- [15] S. Neusser, G. Duerr, H.G. Bauer, S. Tacchi, M. Madami, G. Woltersdorf, G. Gubbiotti, C.H. Back, and D. Grundler. Anisotropic propagation and damping of spin waves in a nanopatterned antidot lattice. *Physical Review Letters*, 105(6):067208, 2010.
- [16] H. Yu, G. Duerr, R. Huber, M. Bahr, T. Schwarze, F. Brandl, and D. Grundler. Omnidirectional spin-wave nanograting coupler. *Nature Communications*, 4(1):2702, 2013.
- [17] H. Yu, O. d’Allivy Kelly, V. Cros, R. Bernard, P. Bortolotti, A. Anane, F. Brandl, F. Heimbach, and D. Grundler. Approaching soft X-ray wavelengths in nanomagnet-based microwave technology. *Nature Communications*, 7(1):11255, 2016.
- [18] C. Liu, J. Chen, T. Liu, F. Heimbach, H. Yu, Y. Xiao, J. Hu, M. Liu, H. Chang, T. Stueckler, et al. Long-distance propagation of short-wavelength spin waves. *Nature Communications*, 9(1):738, 2018.
- [19] K. Baumgaertl, J. Gräfe, P. Che, A. Mucchietto, J. Förster, N. Träger, M. Bechtel, M. Weigand, G. Schütz, and D. Grundler. Nanoimaging of ultrashort magnon emission by ferromagnetic grating couplers at GHz frequencies. *Nano letters*, 20(10):7281–7286, 2020.
- [20] R.F. Wang, C. Nisoli, R.S. Freitas, J. Li, W. McConville, B.J. Cooley, M.S. Lund, N. Samarth, C. Leighton, V.H. Crespi, et al. Artificial ‘spin ice’ in a geometrically frustrated lattice of nanoscale ferromagnetic islands. *Nature*, 439(7074):303–306, 2006.
- [21] S.H. Skjærvø, C.H. Marrows, R.L. Stamps, and L.J. Heyderman. Advances in artificial spin ice. *Nature Reviews Physics*, 2(1):13–28, 2020.
- [22] S. Gliga, E. Iacocca, and O.G. Heinonen. Dynamics of reconfigurable artificial spin ice: Toward magnonic functional materials. *APL Materials*, 8(4):040911, 2020.
- [23] E. Iacocca, S. Gliga, and O.G. Heinonen. Tailoring spin-wave channels in a reconfigurable artificial spin ice. *Physical Review Applied*, 13(4):044047, 2020.

-
- [24] F. Montoncello, S. Tacchi, L. Giovannini, M. Madami, G. Gubbiotti, G. Carlotti, E. Sirotkin, E. Ahmad, F.Y. Ogrin, and V.V. Kruglyak. Asymmetry of spin wave dispersions in a hexagonal magnonic crystal. *Applied Physics Letters*, 102(20):202411, 2013.
- [25] V.S. Bhat, F. Heimbach, I. Stasinopoulos, and D. Grundler. Magnetization dynamics of topological defects and the spin solid in a kagome artificial spin ice. *Physical Review B*, 93(14):140401, 2016.
- [26] V.S. Bhat, S. Watanabe, K. Baumgaertl, A. Kleibert, M.A.W. Schoen, C.A.F. Vaz, and D. Grundler. Magnon modes of microstates and microwave-induced avalanche in kagome artificial spin ice with topological defects. *Physical Review Letters*, 125(11):117208, 2020.
- [27] V.S. Bhat, J. Sklenar, B. Farmer, J. Woods, J.T. Hastings, S.J. Lee, J.B. Ketterson, and L.E. De Long. Controlled magnetic reversal in permalloy films patterned into artificial quasicrystals. *Physical Review Letters*, 111(7):077201, 2013.
- [28] V.S. Bhat, B. Farmer, N. Smith, E. Teipel, J. Woods, J. Sklenar, J.B. Ketterson, J.T. Hastings, and L.E. De Long. Non-stochastic switching and emergence of magnetic vortices in artificial quasicrystal spin ice. *Physica C: Superconductivity and its Applications*, 503:170–174, 2014.
- [29] V.S. Bhat, F. Heimbach, I. Stasinopoulos, and D. Grundler. Angular-dependent magnetization dynamics of kagome artificial spin ice incorporating topological defects. *Physical Review B*, 96(1):014426, 2017.
- [30] J. Rychły, S. Mieszczak, and J.W. Kłos. Spin waves in planar quasicrystal of penrose tiling. *Journal of Magnetism and Magnetic Materials*, 450:18–23, 2018.
- [31] S. Watanabe, V.S. Bhat, K. Baumgaertl, and D. Grundler. Direct observation of worm-like nanochannels and emergent magnon motifs in artificial ferromagnetic quasicrystals. *Advanced Functional Materials*, 30(36):2001388, 2020.
- [32] R. Penrose. Pentaplexity a class of non-periodic tilings of the plane. *The mathematical intelligencer*, 2(1):32–37, 1979.
- [33] M. Gardner. *Penrose Tiles to Trapdoor Ciphers: And the Return of Dr Matrix*. The Mathematical Association of America, Washington, DC, revised edition, 1997.
- [34] D. Shechtman, I. Blech, D. Gratias, and J.W. Cahn. Metallic phase with long-range orientational order and no translational symmetry. *Physical Review Letters*, 53(20):1951, 1984.
- [35] Z.V. Vardeny, A. Nahata, and A. Agrawal. Optics of photonic quasicrystals. *Nature Photonics*, 7(3):177, 2013.

Bibliography

- [36] M.A. Kaliteevski, S. Brand, R.A. Abram, T.F. Krauss, R.D. Rue, and P. Millar. Two-dimensional Penrose-tiled photonic quasicrystals: from diffraction pattern to band structure. *Nanotechnology*, 11(4):274, 2000.
- [37] M.E. Zoorob, M.D.B. Charlton, G.J. Parker, J.J. Baumberg, and M.C. Netti. Complete photonic bandgaps in 12-fold symmetric quasicrystals. *Nature*, 404(6779):740–743, 2000.
- [38] K. Edagawa. Photonic crystals, amorphous materials, and quasicrystals. *Science and technology of advanced materials*, 15(3):034805, 2014.
- [39] J.M.D. Coey. *Magnetism and Magnetic Materials*. Cambridge University Press, Cambridge, England, 4th printing edition, 2014.
- [40] C.M. Hurd. Varieties of magnetic order in solids. *Contemporary Physics*, 23(5):469–493, 1982.
- [41] D. Rüffer. Magnetic states and spin-wave modes in single ferromagnetic nanotubes. PhD thesis No. 6316, EPFL, 2014.
- [42] R. Becker and F. Sauter. *Electromagnetic fields and interactions*, volume 1. Dover Publications, Mineola, New York, 1982.
- [43] C. Herring and C. Kittel. On the theory of spin waves in ferromagnetic media. *Physical Review*, 81(5):869, 1951.
- [44] G.S. Abo, Y.K. Hong, J. Park, J. Lee, W. Lee, and B.C. Choi. Definition of magnetic exchange length. *IEEE Transactions on Magnetics*, 49(8):4937–4939, 2013.
- [45] L.D. Landau and E. Lifshitz. On the theory of the dispersion of magnetic permeability in ferromagnetic bodies. *Phys. Zs. Sowjet.*, 8:153, 1935.
- [46] A. Abragam and B. Bleaney. *Electron paramagnetic resonance of transition ions*. Oxford University Press, Oxford, England, 2012.
- [47] T.L. Gilbert. A Lagrangian formulation of the gyromagnetic equation of the magnetization field. *Physical Review*, 100:1243, 1955.
- [48] C. Kittel. On the theory of ferromagnetic resonance absorption. *Physical Review*, 73(2):155, 1948.
- [49] B.A. Kalinikos and A.N. Slavin. Theory of dipole-exchange spin wave spectrum for ferromagnetic films with mixed exchange boundary conditions. *Journal of Physics C: Solid State Physics*, 19(35):7013, 1986.
- [50] R. Ammann, B. Grünbaum, and G.C. Shephard. Aperiodic tiles. *Discrete & Computational Geometry*, 8(1):1–25, 1992.

-
- [51] S. Fischer, A. Exner, K. Zielske, J. Perlich, S. Deloudi, W. Steurer, P. Lindner, and S. Förster. Colloidal quasicrystals with 12-fold and 18-fold diffraction symmetry. *Proceedings of the National Academy of Sciences*, 108(5):1810–1814, 2011.
- [52] S.P. Gorkhali, J. Qi, and G.P. Crawford. Switchable quasi-crystal structures with five-, seven-, and ninefold symmetries. *Journal of the Optical Society of America B*, 23(1): 149–158, 2006.
- [53] S. Walter and S. Deloudi. *Crystallography of quasicrystals: concepts, methods and structures*, volume 126. Springer, Berlin and Heidelberg, Germany, 2009.
- [54] P. Tailhades S. A. Nikitov and C. S. Tsai. Spin waves in periodic magnetic structures magnonic crystals. *Journal of Magnetism and Magnetic Materials*, 236(3):320–330, 2001.
- [55] M. Kostylev, P. Schrader, R.L. Stamps, G. Gubbiotti, G. Carlotti, A.O. Adeyeye, S. Goolaup, and N. Singh. Partial frequency band gap in one-dimensional magnonic crystals. *Applied Physics Letters*, 92(13):132504, 2008.
- [56] R.A. Gallardo, T. Schneider, A. Roldán-Molina, M. Langer, J. Fassbender, K. Lenz, J. Lindner, and P. Landeros. Dipolar interaction induced band gaps and flat modes in surface-modulated magnonic crystals. *Physical Review B*, 97(14):144405, 2018.
- [57] A.V. Chumak, A.A. Serga, B. Hillebrands, and M.P. Kostylev. Scattering of backward spin waves in a one-dimensional magnonic crystal. *Applied Physics Letters*, 93(2):022508, 2008.
- [58] H. Qin, G.J. Both, S.J. Hämäläinen, L. Yao, and S. van Dijken. Low-loss YIG-based magnonic crystals with large tunable bandgaps. *Nature Communications*, 9(1):5445, 2018.
- [59] J. Topp, D. Heitmann, M.P. Kostylev, and D. Grundler. Making a reconfigurable artificial crystal by ordering bistable magnetic nanowires. *Physical Review Letters*, 104(20):207205, 2010.
- [60] M. Okuda, T. Schwarze, J.C. Eloi, S.E.W. Jones, P.J. Heard, A. Sarua, E. Ahmad, V.V. Kruglyak, D. Grundler, and W. Schwarzacher. Top-down design of magnonic crystals from bottom-up magnetic nanoparticles through protein arrays. *Nanotechnology*, 28(15):155301, 2017.
- [61] R.A. Gallardo, A. Banholzer, K. Wagner, M. Körner, K. Lenz, M. Farle, J. Lindner, J. Fassbender, and P. Landeros. Splitting of spin-wave modes in thin films with arrays of periodic perturbations: theory and experiment. *New Journal of Physics*, 16(2):023015, 2014.
- [62] S. Neusser, B. Botters, M. Becherer, D. Schmitt-Landsiedel, and D. Grundler. Spin-wave localization between nearest and next-nearest neighboring holes in an antidot lattice. *Applied Physics Letters*, 93(12):122501, 2008.

- [63] L. Eurenium, C. Häggglund, E. Olsson, B. Kasemo, and D. Chakarov. Grating formation by metal-nanoparticle-mediated coupling of light into waveguided modes. *Nature Photonics*, 2(6):360–364, 2008.
- [64] Z. Xiao, F. Luan, T.Y. Liow, J. Zhang, and P. Shum. Design for broadband high-efficiency grating couplers. *Optics letters*, 37(4):530–532, 2012.
- [65] G. Quaranta, G. Basset, O.J.F. Martin, and B. Gallinet. Recent advances in resonant waveguide gratings. *Laser & Photonics Reviews*, 12(9):1800017, 2018.
- [66] S. Maendl and D. Grundler. Multi-directional emission and detection of spin waves propagating in yttrium iron garnet with wavelengths down to about 100 nm. *Applied Physics Letters*, 112(19):192410, 2018.
- [67] C. Castelnovo, R. Moessner, and S.L. Sondhi. Magnetic monopoles in spin ice. *Nature*, 451(7174):42–45, 2008.
- [68] S. Zhang, I. Gilbert, C. Nisoli, G.W. Chern, M.J. Erickson, L. O’Brien, C. Leighton, P.E. Lammert, V.H. Crespi, and P. Schiffer. Crystallites of magnetic charges in artificial spin ice. *Nature*, 500(7464):553–557, 2013.
- [69] E. Mengotti, L.J. Heyderman, A.F. Rodríguez, F. Nolting, R.V. Hügli, and H.B. Braun. Real-space observation of emergent magnetic monopoles and associated dirac strings in artificial kagome spin ice. *Nature Physics*, 7(1):68–74, 2011.
- [70] A. Farhan, P.M. Derlet, A. Kleibert, A. Balan, R.V. Chopdekar, L. Wyss, M. and Anghinolfi, F. Nolting, and L.J. Heyderman. Exploring hyper-cubic energy landscapes in thermally active finite artificial spin-ice systems. *Nature Physics*, 9(6):375–382, 2013.
- [71] S. Gliga, G. Hrkac, C. Donnelly, J. Büchi, A. Kleibert, J. Cui, A. Farhan, E. Kirk, R.V. Chopdekar, Y. Masaki, et al. Emergent dynamic chirality in a thermally driven artificial spin ratchet. *Nature Materials*, 16(11):1106–1111, 2017.
- [72] H. Yu, R. Huber, T. Schwarze, F. Brandl, T. Rapp, P. Berberich, G. Duerr, and D. Grundler. High propagating velocity of spin waves and temperature dependent damping in a CoFeB thin film. *Applied Physics Letters*, 100(26):262412, 2012.
- [73] V. S. Bhat and D. Grundler. Angle-dependent magnetization dynamics with mirror-symmetric excitations in artificial quasicrystalline nanomagnet lattices. *Physical Review B*, 98(17):174408, 2018.
- [74] M. Bailleul, D. Olligs, and C. Fermon. Propagating spin wave spectroscopy in a permalloy film: A quantitative analysis. *Applied Physics Letters*, 83(5):972–974, 2003.
- [75] C.S. Chang, M. Kostylev, E. Ivanov, J. Ding, and A.O. Adeyeye. The phase accumulation and antenna near field of microscopic propagating spin wave devices. *Applied Physics Letters*, 104(3):032408, 2014.

-
- [76] T. Sebastian, K. Schultheiss, B. Obry, B. Hillebrands, and H. Schultheiss. Micro-focused Brillouin light scattering: imaging spin waves at the nanoscale. *Frontiers in Physics*, 3: 35, 2015.
- [77] V. E. Demidov and S. O. Demokritov. Magnonic waveguides studied by microfocus Brillouin light scattering. *IEEE Transactions on Magnetics*, 51(4):1–15, 2015.
- [78] F. Fohr, A.A. Serga, T. Schneider, J. Hamrle, and B. Hillebrands. Phase sensitive brillouin scattering measurements with a novel magneto-optic modulator. *Review of Scientific Instruments*, 80(4):043903, 2009.
- [79] K. Wagner, A. Kakay, K. Schultheiss, A. Henscijke, T. Sebastian, and H. Schultheiss. Magnetic domain walls as reconfigurable spin-wave nanochannels. *Nature Nanotechnology*, 11(5):432–436, 2016.
- [80] P.A. Fleury, S.P.S. Porto, L.E. Cheesman, and H.J. Guggenheim. Light scattering by spin waves in FeF_2 . *Physical Review Letters*, 17(2):84, 1966.
- [81] S.O. Demokritov, B. Hillebrands, and A.N. Slavin. Brillouin light scattering studies of confined spin waves: linear and nonlinear confinement. *Physics Reports*, 348(6):441–489, 2001.
- [82] K. Baumgärtl. Magnonic crystals with reconfigurable magnetic defects for spin-based microwave electronics. PhD thesis No. 7854, EPFL, 2020.
- [83] Z.Q. Qiu and S.D. Bader. Surface magneto-optic Kerr effect (SMOKE). *Journal of magnetism and magnetic materials*, 200(1-3):664–678, 1999.
- [84] J. McCord. Progress in magnetic domain observation by advanced magneto-optical microscopy. *Journal of Physics D: Applied Physics*, 48(33):333001, 2015.
- [85] B.T. Thole, P. Carra, F. Sette, and G. van der Laan. X-ray circular dichroism as a probe of orbital magnetization. *Physical Review Letters*, 68(12):1943, 1992.
- [86] P. Carra, B.T. Thole, M. Altarelli, and X. Wang. X-ray circular dichroism and local magnetic fields. *Physical Review Letters*, 70(5):694, 1993.
- [87] D. Kumar and A.O. Adeyeye. Techniques in micromagnetic simulation and analysis. *Journal of Physics D: Applied Physics*, 50(34):343001, 2017.
- [88] M.J. Donahue and D.G. Porter. OOMMF user guide, version 1.0. *Interagency Report NISTIR 6376*, 1999.
- [89] A. Vansteenkiste, J. Leliaert, M. Dvornik, M. Helsen, F. Garcia-Sanchez, and B. Van Waeyenberge. The design and verification of mumax3. *AIP advances*, 4(10): 107133, 2014.

- [90] Y.C. Chen, D.S. Hung, Y.D. Yao, S.F. Lee, H.P. Ji, and C. Yu. Ferromagnetic resonance study of thickness-dependent magnetization precession in $\text{Ni}_{80}\text{Fe}_{20}$ films. *Journal of Applied Physics*, 101(9):09C104, 2007.
- [91] D.J. Twisselmann and R.D. McMichael. Intrinsic damping and intentional ferromagnetic resonance broadening in thin permalloy films. *Journal of Applied Physics*, 93(10):6903–6905, 2003.
- [92] C. Berk, M. Jaris, W. Yang, S. Dhuey, S. Cabrini, and H. Schmidt. Strongly coupled magnon–phonon dynamics in a single nanomagnet. *Nature Communications*, 10(1):2652, 2019.
- [93] R. Gontarz, H. Ratajczak, and P. Šuda. Magnetostriction of thin Ni-films. *Phys. Stat. Sol. b*, 6(3):909–912, 1964.
- [94] D. Rüffer, M. Slot, R. Huber, T. Schwarze, F. Heimbach, G. Tütüncüoglu, F. Matteini, E. Russo-Averchi, A. Kovács, R. Dunin-Borkowski, R. R. Zamani, J.R. Morante, J. Arbiol, A. Fontcuberta i Morral, and D. Grundler. Anisotropic magnetoresistance of individual CoFeB and Ni nanotubes with values of up to 1.4% at room temperature. *APL Materials*, 2(7):076112, 2014.
- [95] C. Berk, Y. Yahagi, S. Dhuey, S. Cabrini, and H. Schmidt. Controlling the influence of elastic eigenmodes on nanomagnet dynamics through pattern geometry. *Journal of Magnetism and Magnetic Materials*, 426:239–244, 2017.
- [96] C. Bilzer, T. Devolder, J.V. Kim, G. Counil, C. Chappert, S. Cardoso, and P.P. Freitas. Study of the dynamic magnetic properties of soft CoFeB films. *Journal of Applied Physics*, 100(5):053903, 2006.
- [97] X. Liu, W. Zhang, M.J. Carter, and G. Xiao. Ferromagnetic resonance and damping properties of CoFeB thin films as free layers in MgO-based magnetic tunnel junctions. *Journal of Applied Physics*, 110(3):033910, 2011.
- [98] H. Yu, O. d’ Allivy Kelly, V. Cros, R. Bernard, P. Bortolotti, A. Anane, F. Brandl, R. Huber, I. Stasinopoulos, and D. Grundler. Magnetic thin-film insulator with ultra-low spin wave damping for coherent nanomagnonics. *Scientific Reports*, 4(1):6848, 2014.
- [99] Y. Sun, Y.Y. Song, H. Chang, M. Kabatek, M. Jantz, W. Schneider, M. Wu, H. Schultheiss, and A. Hoffmann. Growth and ferromagnetic resonance properties of nanometer-thick yttrium iron garnet films. *Applied Physics Letters*, 101(15):152405, 2012.
- [100] M.C. Onbasli, A. Kehlberger, D.H. Kim, G. Jakob, M. Kläui, A.V. Chumak, B. Hillebrands, and C.A. Ross. Pulsed laser deposition of epitaxial yttrium iron garnet films with low Gilbert damping and bulk-like magnetization. *APL Materials*, 2(10):106102, 2014.
- [101] K. An, A.N. Litvinenko, R. Kohno, A.A. Fuad, V.V. Naletov, L. Vila, U. Ebels, G. de Loubens, H. Hurdequint, N. Beaulieu, et al. Coherent long-range transfer of angular momentum between magnon Kittel modes by phonons. *Physical Review B*, 101(6):060407, 2020.

-
- [102] S. Neusser, B. Botters, and D. Grundler. Localization, confinement, and field-controlled propagation of spin waves in $\text{Ni}_{80}\text{Fe}_{20}$ antidot lattices. *Physical Review B*, 78(5):054406, 2008.
- [103] S. Choudhury, S. Barman, Y. Otani, and A. Barman. Efficient modulation of spin waves in two-dimensional octagonal magnonic crystal. *ACS nano*, 11(9):8814–8821, 2017.
- [104] A. Conca, J. Greser, T. Sebastian, S. Klingler, B. Obry, B. Leven, and B. Hillebrands. Low spin-wave damping in amorphous $\text{Co}_{40}\text{Fe}_{40}\text{B}_{20}$ thin films. *Journal of Applied Physics*, 113(21):213909, 2013.
- [105] D. Shechtman. Nobel lecture, Stockholm, 8 December 2011, The Nobel Prize organisation.
- [106] D.P. DiVincenzo, editor. *Quasicrystals: the state of the art*, volume 16 of *Series on directions in condensed matter physics*. World Scientific Publishing Company, Singapore, 1999.
- [107] M. Bayindir, E. Cubukcu, I. Bulu, and E. Ozbay. Photonic band gaps and localization in two-dimensional metallic quasicrystals. *EPL (Europhysics Letters)*, 56(1):41, 2001.
- [108] D. P. DiVincenzo. *Physical models of perfect quasicrystal growth*, volume 229 of *NATO ASI Series B: Physics*, page 133. Plenum Press, New York and London, 1990.
- [109] M. Ronchetti, M. Bertagnolli, and M.V. Jaric. *Generation and dynamics of defects in two-dimensional quasicrystals*, volume 229 of *NATO ASI Series B: Physics*, page 141. Plenum Press, New York and London, 1990.
- [110] H. Au-Yang and J.H.H. Perk. Quasicrystals—the impact of N.G. de Bruijn. *Indagationes Mathematicae*, 24(4):996, 2013.
- [111] F. Fang, D. Hammock, and K. Irwin. Methods for calculating empires in quasicrystals. *Crystals*, 7:304, 2017.
- [112] P.J. Steinhardt, P.M. Chaikin, and W. Man. Quasicrystalline structures and uses thereof. U.S. Patent No. 8,064,127, 11 2011.
- [113] T. Matsui, A. Agrawal, A. Nahata, and Z.V. Vardeny. Transmission resonances through aperiodic arrays of subwavelength apertures. *Nature*, 446(7135):517–521, 2007.
- [114] J.M. Dubois. So useful, those quasicrystals. *Israel Journal of Chemistry*, 51:1168, 2011.
- [115] A.V. Chumak, A.A. Serga, and B. Hillebrands. Magnon transistor for all-magnon data processing. *Nature Communications*, 5(1):4700, 2014.
- [116] D. Shi, Z. Budrikis, A. Stein, S.A. Morley, P.D. Olmsted, G. Burnell, and C.H. Marrows. Frustration and thermalization in an artificial magnetic quasicrystal. *Nature Physics*, 14(3):309, 2018.

Bibliography

- [117] V. S. Bhat, J. Sklenar, B. Farmer, J. Woods, J. T. Hastings, S. J. Lee, J. B. Ketterson, and L. E. De Long. Controlled magnetic reversal in permalloy films patterned into artificial quasicrystals. *Physical Review Letters*, 111(7):077201, 2013.
- [118] X. Zhou, G.L. Chua, N. Singh, and A.O. Adeyeye. Large area artificial spin ice and anti-spin ice $\text{Ni}_{80}\text{Fe}_{20}$ structures: Static and dynamic behavior. *Advanced Functional Materials*, 26(9):1437–1444, 2016.
- [119] M.J. Pechan, C. Yu, R.L. Compton, J.P. Park, and P.A. Crowell. Direct measurement of spatially localized ferromagnetic-resonance modes in an antidot lattice. *Journal of Applied Physics*, 97(10):10J903, 2005.
- [120] J. Sklenar, V.S. Bhat, L.E. DeLong, O. Heinonen, and J.B. Ketterson. Strongly localized magnetization modes in permalloy antidot lattices. *Applied Physics Letters*, 102(15):152412, 2013.
- [121] F. Lisiecki, J. Rychły, P. Kuświk, H. Głowiński, J.W. Kłos, F. Groß, N. Träger, I. Bykova, M. Weigand, and M. and others Zelent. Magnons in a quasicrystal: Propagation, extinction, and localization of spin waves in Fibonacci structures. *Physical Review Applied*, 11(5):054061, 2019.
- [122] L.A. Bursill and P.J. Lin. Penrose tiling observed in a quasi-crystal. *Nature*, 316(6023):50–51, 1985.
- [123] K. Brading and E. Castellani. *Symmetries in physics: philosophical reflections*. Cambridge University Press, Cambridge, England, 2003.
- [124] J. Jorzick, S. O. Demokritov, B. Hillebrands, M. Bailleul, C. Fermon, K. Y. Guslienko, A. N. Slavin, D. V. Berkov, and N. L. Gorn. Spin wave wells in nonellipsoidal micrometer size magnetic elements. *Physical Review Letters*, 88(4):047204, 2002.
- [125] F. Lisiecki, J. Rychły, P. Kuświk, H. Głowiński, J.W. Kłos, F. Groß, I. Bykova, M. Weigand, M. Zelent, E.J. Goering, et al. Reprogrammability and scalability of magnonic Fibonacci quasicrystals. *Physical Review Applied*, 11(5):054003, 2019.
- [126] K. Vogt, F.Y. Fradin, J.E. Pearson, T. Sebastian, S.D. Bader, B. Hillebrands, A. Hoffmann, and H. Schultheiss. Realization of a spin-wave multiplexer. *Nature Communications*, 5(1):3727, 2014.
- [127] F. Heussner, G. Talmelli, M. Geilen, B. Heinz, T. Brächer, T. Meyer, F. Ciubotaru, C. Adelman, K. Yamamoto, A. A. Serga, et al. Experimental realization of a passive gigahertz frequency-division demultiplexer for magnonic logic networks. *Phys. Stat. Sol. RRL*, 14(4):1900695, 2020.
- [128] M. Florescu, P.J. Steinhardt, and S. Torquato. Optical cavities and waveguides in hyper-uniform disordered photonic solids. *Physical Review B*, 87(16):165116, 2013.

-
- [129] A.V. Chumak, A.A. Serga, S. Wolff, B. Hillebrands, and M.P. Kostylev. Scattering of surface and volume spin waves in a magnonic crystal. *Applied Physics Letters*, 94(17):172511, 2009.
- [130] C. Nisoli, R. Moessner, and P. Schiffer. Colloquium: Artificial spin ice: Designing and imaging magnetic frustration. *Review of Modern Physics*, 85(4):1473, 2013.
- [131] A.L. Mackay. Crystallography and the Penrose pattern. *Physica A: Statistical Mechanics and its Applications*, 114(1-3):609–613, 1982.
- [132] M.C. Rechtsman, H.C. Jeong, P.M. Chaikin, S. Torquato, and P.J. Steinhardt. Optimized structures for photonic quasicrystals. *Physical Review Letters*, 101(7):073902, 2008.
- [133] J. Rychły, J. W. Kłos, M. Mruczkiewicz, and M. Krawczyk. Spin waves in one-dimensional bicomponent magnonic quasicrystals. *Physical Review B*, 92(5):054414, 2015.
- [134] Y. Akahane, T. Asano, B.S. Song, and S. Noda. High-Q photonic nanocavity in a two-dimensional photonic crystal. *Nature*, 425(6961):944–947, 2003.
- [135] S. Mamica, M. Krawczyk, and D. Grundler. Nonuniform spin-wave softening in two-dimensional magnonic crystals as a tool for opening omnidirectional magnonic band gaps. *Physical Review Applied*, 11(5):054011, 2019.
- [136] J.H. Kwon, J. Yoon, P. Deorani, J.M. Lee, J. Sinha, K.J. Lee, M. Hayashi, and H. Yang. Giant nonreciprocal emission of spin waves in Ta/Py bilayers. *Science Advances*, 2(7):e1501892, 2016.
- [137] C. Jin, B. Cheng, B. Man, Z. Li, D. Zhang, S. Ban, and B. Sun. Band gap and wave guiding effect in a quasiperiodic photonic crystal. *Applied Physics Letters*, 75(13):1848–1850, 1999.
- [138] Y. An, Z. Gao, and Z. Ouyang. Surface wave photonic quasicrystal. *Applied Physics Letters*, 116(15):151104, 2020.
- [139] P. Ramachandran and G. Varoquaux. Mayavi: 3d visualization of scientific data. *Computing in Science & Engineering*, 13(2):40–51, 2011.
- [140] X. Zhou, D. Kumar, I.S. Maksymov, M. Kostylev, and A.O. Adeyeye. Axially and radially quantized spin waves in thick permalloy nanodots. *Physical Review B*, 92(5):054401, 2015.
- [141] G. Carlotti. Pushing down the lateral dimension of single and coupled magnetic dots to the nanometric scale: Characteristics and evolution of the spin-wave eigenmodes. *Applied Physics Reviews*, 6(3):031304, 2019.
- [142] K. Schultheiss, R. Verba, F. Wehrmann, K. Wagner, L. Körber, T. Hula, T. Hache, A. Kákay, A.A. Awad, V. Tiberkevich, et al. Excitation of whispering gallery magnons in a magnetic vortex. *Physical Review Letters*, 122(9):097202, 2019.

Bibliography

- [143] S. Watanabe, V.S. Bhat, K. Baumgaertl, and D. Hamdi, M. and Grundler. Direct observation of multiband transport in magnonic penrose quasicrystals via broadband and phase-resolved spectroscopy. *unpublished*.
- [144] R. Penrose. The role of aesthetics in pure and applied mathematical research. *Bulletin of the Institute of Mathematics and Its Applications*, 10:266–271, 1974.
- [145] S.A. Bunyaev, V.O. Golub, O.Y. Salyuk, E.V. Tartakovskaya, N.M. Santos, A.A. Timopheev, N.A. Sobolev, A.A. Serga, A.V. Chumak, B. Hillebrands, and G.N. Kakazei. Splitting of standing spin-wave modes in circular submicron ferromagnetic dot under axial symmetry violation. *Scientific Reports*, 5(1):18480, 2015.
- [146] S. Klingler, P. Pirro, T. Brächer, B. Leven, B. Hillebrands, and A.V. Chumak. Spin-wave logic devices based on isotropic forward volume magnetostatic waves. *Applied Physics Letters*, 106(21):212406, 2015.
- [147] T. Fischer, M. Kewenig, D.A. Bozhko, A.A. Serga, I.I. Syvorotka, F. Ciubotaru, C. Adelmann, B. Hillebrands, and A.V. Chumak. Experimental prototype of a spin-wave majority gate. *Applied Physics Letters*, 110(15):152401, 2017.
- [148] D. Grundler. Reconfigurable magnonics heats up. *Nature Physics*, 11(6):438, 2015.
- [149] Y. Qi, T. Brintlinger, and J. Cumings. Direct observation of the ice rule in an artificial kagome spin ice. *Physical Review B*, 77(9):094418, 2008.
- [150] W.R. Branford, S. Ladak, D.E. Read, K. Zeissler, and L.F. Cohen. Emerging chirality in artificial spin ice. *Science*, 335(6076):1597–1600, 2012.
- [151] V. Brajuskovic, F. Barrows, C. Phatak, and A.K. Petford-Long. Real space observation of magnetic excitations and avalanche behavior in artificial quasicrystal lattices. *Scientific Reports*, 6(1):34384, 2016.
- [152] B. Farmer, V.S. Bhat, A. Balk, E. Teipel, N. Smith, J. Unguris, D.J. Keavney, J.T. Hastings, and L.E. De Long. Direct imaging of coexisting ordered and frustrated sublattices in artificial ferromagnetic quasicrystals. *Physical Review B*, 93(13):134428, 2016.
- [153] B. Grünbaum and G.C. Shephard. *Tilings and patterns*. Dover Publications, Mineola, New York, 2nd edition, 1987.
- [154] A. Aharoni. Demagnetizing factors for rectangular ferromagnetic prisms. *Journal of Applied Physics*, 83(6):3432–3434, 1998.
- [155] D.M. Burn, M. Chadha, and W.R. Branford. Angular-dependent magnetization reversal processes in artificial spin ice. *Physical Review B*, 92(21):214425, 2015.
- [156] S. Ladak, D.E. Read, G.K. Perkins, L.F. Cohen, and W.R. Branford. Direct observation of magnetic monopole defects in an artificial spin-ice system. *Nature Physics*, 6(5):359–363, 2010.

-
- [157] S. Ladak, D. Read, T. Tyliczszak, W.R. Branford, and L.F. Cohen. Monopole defects and magnetic coulomb blockade. *New Journal of Physics*, 13(2):023023, 2011.
- [158] S. Gliga, A. Kákay, R. Hertel, and O.G. Heinonen. Spectral analysis of topological defects in an artificial spin-ice lattice. *Physical Review Letters*, 110(11):117205, 2013.
- [159] L.J. Heyderman and R.L. Stamps. Artificial ferroic systems: novel functionality from structure, interactions and dynamics. *Journal of Physics: Condensed Matter*, 25(36):363201, 2013.
- [160] S. Mamica, X. Zhou, A. Adeyeye, M. Krawczyk, and G. Gubbiotti. Spin-wave dynamics in artificial anti-spin-ice systems: Experimental and theoretical investigations. *Physical Review B*, 98(5):054405, 2018.
- [161] A. Ghosh, F. Ma, J. Lourembam, X. Jin, R. Maddu, Q.J. Yap, and S. Ter Lim. Emergent dynamics of artificial spin-ice lattice based on an ultrathin ferromagnet. *Nano letters*, 20(1):109–115, 2019.
- [162] E. Iacocca, S. Gliga, R.L. Stamps, and O. Heinonen. Reconfigurable wave band structure of an artificial square ice. *Physical Review B*, 93(13):134420, 2016.
- [163] E. C. Stoner and E.P. Wohlfarth. A mechanism of magnetic hysteresis in heterogeneous alloys. *Philosophical Transactions of the Royal Society of London. Series A, Mathematical and Physical Sciences*, 240(826):599–642, 1948.
- [164] P. Che, K. Baumgaertl, C. Kúkol’ová, A. and Dubs, and D. Grundler. Efficient wavelength conversion of exchange magnons below 100 nm by magnetic coplanar waveguides. *Nature Communications*, 11(1):1445, 2020.

Sho Watanabe

Route du bois 57,
CH-1024 Ecublens

Phone :

+41 78 652 65 97

E-mail :

sho.d.watanabe@gmail.com

**Education**

07/2016–present	Doctoral program EPFL, Switzerland <ul style="list-style-type: none">- Study emphasis: Nanoscale Magnetic Materials and Magnonics- PhD thesis title: "Magnons, worms and nanogratings in artificial magnetic quasicrystals"- Program: EDMX Material Science and Engineering– Thesis supervisor: Prof. Dirk Grundler
03/2013 - 03/2016	Double degree program TUM and Keio
10/2013 - 09/2015	Master of Science , Technische Universität München (TUM), Germany <ul style="list-style-type: none">- Study emphasis: Magnetism- Master thesis title: "Circularly polarized microwaves for magnetic resonance experiments"– Supervisor: PD Sebastian T. B. Goennenwein– Final grade: 2.0 (in German system)
10/2015 - 03/2016, 04/2013 - 09/2013	Master of Science , Keio University , Japan <ul style="list-style-type: none">- Study emphasis: Spintronics– Thesis supervisor: Prof. Nozaki Yukio– Final grade: 3.9 (on a scale of 4, GPA)
10/2013 - 09/2015	Bachelor of Science , Keio University , Japan <ul style="list-style-type: none">- Study emphasis: Spintronics- Master thesis title: "Fast switching of magnetization in a NiFe particle with an assistance of non-local spin injection"– Thesis supervisor: Prof. Nozaki Yukio– Final grade: 3.4 (on a scale of 4, GPA)

Research projects

2016–present

"Magnons, worms and nanogratings in artificial magnetic quasicrystals" Laboratory of Nanoscale Magnetic Materials and Magnonics (LMGN), EPFL

Doctoral Thesis | Supervisor: Prof. Dirk Grundler. Funded by SNF grant 163016. Nanofabrication of magnetic materials at clean room facility. Characterization of artificial magnetic materials by means of broadband GHz spectroscopy, Brillouin light scattering spectroscopy, X-ray-based microscopy, and magnetic force microscopy. Data analysis with Python.

Publications

- "Direct Observation of Worm-Like Nanochannels and Emergent Magnon Motifs in Artificial Ferromagnetic Quasicrystals"; S. Watanabe, V. S. Bhat, K. Baumgaertl, and D. Grundler *Advanced Functional Materials* **30** 2001388 (2020).
- "Magnon Modes of Microstates and Microwave-Induced Avalanche in Kagome Artificial Spin Ice with Topological Defects."; V. S. Bhat, S. Watanabe, K. Baumgaertl, A. Kleibert, M. A. W. Schoen, C. A. F. Vaz, and D. Grundler *Physical Review Letters* **125** 117208 (2020).
- "Phase control of spin waves based on a magnetic defect in a one-dimensional magnonic crystal"; K. Baumgaertl, S. Watanabe, and D. Grundler; *Applied Physics Letters* **112**, 142405 (2018).

Teaching

Lecturer

Teaching assistant for courses

- Lecture on "Magnetic materials for modern technologies (2017 and 2019)" by Prof. Dr. Grundler
- Lab course of "Crystallography (2018)" by Dr. Drezet

Supervisor for Master theses

- "Modeling of GHz dynamics in nanomagnet lattices", Master thesis, Shan Shixuan (2020)

Supervisor for semester projects

- "Coupling between charge transport and magnetization in $\text{Co}_8\text{Zn}_8\text{Mn}_4$ ", Richa Agrawal (2020).
- "Magnetic Force Microscopy applied to nanopatterned ferromagnetic quasicrystals", Clément Jean-Michel Patrice Cardon (2019).

- "Characterization of magnetization configuration of ferromagnetic nanotubes", Julien Gay (2018).
- "Magnetic states in nanostructured metallic magnets explored by magnetic force microscopy and image analysis", Qi Huang (2017).

Skills

Programming skills

- Python: semi-automatic image registration to analyze several 1,000 X-ray images and visualization of 2D and 3D data taken by experiments and simulations.
- Labview: automation of measurement routines.

Experimental skills

- Broadband GHz spectroscopy with vector network analyzer (frequency domain) and time domain reflectometry (time domain)
- Brillouin light scattering microscopy
- Atomic force microscopy and magnetic force microscopy
- Sample fabrication (E-beam lithography, photolithography, evaporation, sputtering, wet/dry etching, Scanning electron microscopy)

Software

- Illustrator, Photoshop: Image construction for thesis, manuscripts and reports
- Solidworks: Design mechanical items for experiments

Languages

- | | |
|------------|--|
| – Japanese | Native |
| – English | Full professional proficiency |
| – German | Limited working proficiency (CEFR: B1) |
| – French | Elementary proficiency (CEFR: A1/A2) |